STUDIES OF ACTIVE LAYER MORPHOLOGY IN BULK-HETEROJUNCTION POLYMER BASED SOLAR CELLS USING OPTICAL AND FORCE MICROSCOPY METHODS

A Thesis Submitted in Partial Fulfillment of
The Requirements of the Degree of

DOCTOR OF PHILOSOPHY

By

Sabyasachi Mukhopadhyay

Chemistry and Physics of Materials Unit
Jawaharlal Nehru Centre for Advanced Scientific Research
Bangalore, Karnataka – 560064, INDIA
May 2012

DECLARATION

I hereby declare that the matter embodied in this thesis is the result of the work carried out by me under the supervision of Prof. K. S. Narayan, at Molecular Electronics Laboratory, in Chemistry and Physics of Materials Unit, Jawaharlal Nehru Centre for Advanced Scientific Research, Bangalore, India. It has not been submitted for the award of any degree or diploma or associateship of any other university or institute.

In keeping with the general practice in reporting scientific observations, due acknowledgment has been made whenever the work described is based on the findings of other investigators.

(Sabyasachi Mukhopadhyay)

Candidate

JAWAHARLAL NEHRU CENTRE FOR ADVANCED SCIENTIFIC RESEARCH
Jakkur, Bangalore – 560064, India

K. S. NARAYAN
Professor
Dean (Research and Development)
PHONE: +91 80 2208 2822/2548
E-mail: narayan@jncasr.ac.in
Fax: +91 80 2208 2766

May, 2012

I hereby certify that the matter embodied in this thesis entitled "*Studies of active layer morphology in bulk-heterojunction polymer based solar cells using optical and force microscopy methods*" has been carried out by Mr. Sabyasachi Mukhopadhyay at the Molecular Electronics Laboratory, Chemistry and Physics of Materials Unit, Jawaharlal Nehru Centre for Advanced Scientific Research, Bangalore, India, under my supervision and it has not been submitted elsewhere for the award of any degree or diploma.

Prof. K. S. Narayan

(Research Supervisor)

Dedicated to

Swami Amiteshananda

And to my teacher

Sri Khitish Chandra Acharya

Acknowledgment

This thesis is the result of work through which I have been mentored, assisted, accompanied and supported my many people. I take this opportunity to express my sincere gratitude to all of them.

It is my great pleasure to express my sincere gratitude to my research supervisor, Prof. K. S. Narayan, for introducing me to the scientific community, and guiding me during various phases with constant encouragement and simulating discussions throughout. His immense passion for science is infectious and has made my journey all the more exciting. I am especially thankful to him for introducing me to the various research fields and also to the world of photovoltaic.

I would like to express my heartfelt gratitude to Dr. Raja, faculty of Theoretical Studied Unit. His constant guidance has immensely helped in my progress. Thank you Sir, for all the things, you have done for me. I thank Prof. Chandrabhas Narayana for his excellent molecular spectroscopy course, and for allowing me to use his lab facilities, various suggestions, and supports during the optics experiments.

I thank the Chairman of Chemistry and Physics of Materials Unit, Prof. G.U. Kulkarni (past) and Prof. Balasubramanian Sundaram (present) for their constant encouragement and help throughout my doctoral study. I specially thank Prof. C. N. R. Rao for his encouraging support and for allowing me to use his lab facilities. I thank all the faculty members of CPMU for making AMRL a wonderful research place. I acknowledge the support from Mr. Arokianathan, CPMU workshop for his constant help during NSOM set-up.

I am thankful to Prof. S. Ramakrishnan, IPC, IISc, for his keen interest in my progress, for effective suggestions during my work and also for various conjugated polymer samples.

I would like to express my heartfelt gratitude to Prof. Aaron Lewis, founder of Nanonics Inc, Israel and Mrs. Chaya Lewis for their wonderful hospitality during my trainee days at Jerusalem. I am also thankful to all the staffs of Nanonics Imaging Inc, Nanonics supertips Inc., especially, Devid Lewis, Hesham Thane, Rimma, Yogev for their wonderful support and help. My interaction with them has inspired me to pursue a research carrier on near field optics and scanning probe microscopy field. Their constant support throughout my PhD study has immensely helped in my progress. Prof. Lewis has promoted me for a 2 week training which helped me to learn advanced techniques on scanning probe technology and gift probe sets have greatly contributed towards my research.

I am thankful to the present and past members of JNC office, library, academic section, computer lab, dining hall, purchase section and JNC hostel for their endeavors to providing excellent facilities at JNC. I acknowledge JNC for granting me fellowship and Nano-science and Technology Initiative by Department of Science and Technology, Govt. of INDIA for NSOM instrument. I thank NCBS, for their confocal facilities and IISc for advanced facilities at Nanoscience Center.

I thank to my past and present lab members, Dr. Manoj, Dr. Soumya, Dr. Dinesh, Dr. Dhritiman, Dr. Arun, Dr. Manohar, Dr. Balraju, Dr. Srinidhi, Dr. Monojit, Dr. Kishore, Dr. Utpal S. Joshi, Shruti, Jasmeet, Hemant, Arun, Anshuman, Vini, Satyaprasad, Ravichandran, Prashant, Azashar, Vijay, Nishit, Madhu. They are wonderful people who have given all the support to sail through the high and low in the lab. A big “thank you” to Srinidhi and Rashmi without whom it was impossible to complete this thesis work smoothly. Thanks to all my lab juniors for their help and for maintaining high spirit of the lab. Spacial thanks to Monojit, a great friend with whom I have discussed not only the science but share all things under the Sun. Thanks to Shiladitya and Vishwash for their support and help during presentation preparation. Special thanks to Sayantan, Pralayda and Rahulda, true friend and well-wishers. I am thankful to my IISc–friends Dibyendu, Saptarshi, Barun, Gautam, Saroj, Sayak, Shaon, Atin, Sandeep and … for their support.

I acknowledge support from my batch mates Pranab, Kalyan, Mukti, Laxmi Narayan, Pankaj, Shigdhadip, Avhishek, Arup, and Madhura. Staying in JNC hostel was memorable and I thank all my friends – especially Prakash, Sudip, Arpan, Rana, Debu, Ritesh, Dibyajyoti, Gautam, Babhru, Pralok, Partha, Soumik, Amrit, Sudeshna, Sananda, Sutapa, Mounitadi, Surbhi and many more…

I take this opportunity to thank my teachers at IIT Kharagpur who guided me during my venture to the wonderful world of physics and materials science. Thanks to all the faculties of Department of Physics and Meteorology, for their guidance and inspiration. I also acknowledge Prof. A. Saha and his family, Nanditadi for their help and guidance. I thank my wonderful teachers from Ramakrishna Mission Vidyamandira for guidance.

I thank my presents and other family members for their constant encouragement and support throughout my life. They are the source of constant imprison for me to dream big and achieve the goal through hard work. I pay my deepest respect to my belated grandparents, who had most influence on my life. Special thanks to Dada, Boudi and Tatai for their love and encouragement and to make my stay at Bangalore more memorable.

May, 2012

JNCASR, Bangalore **SABYASACHI MUKHOPADHYAY**

List of Publications

In this thesis:

---

1. *Sabyasachi Mukhopadhyay*, Anshuman Das, K. S. Narayan, Studies of bulk-heterojunction morphology in polymer-small molecule based solar cells utilizing optical and force microscopy methods, (manuscript under preparation)
2. *Sabyasachi Mukhopadhyay*, K. S. Narayan, Rationalization of donor-acceptor ratio in bulk heterojunction solar cells using lateral photocurrent studies, *Applied Physics Letters, 100, 163302,* ***2012***
3. *Sabyasachi Mukhopadhyay*, Srinidhi Ramachandra, and K. S. Narayan, Direct observation of charge generating regions and transport pathways in bulk heterojunction solar cells with asymmetric electrodes using Near Field Photocurrent Microscopy, *Journal of Physical Chemistry C, 115, 17184,* ***2011***
4. *Sabyasachi Mukhopadhyay*, Rakesh Voggu, C. N. R. Rao, N. S. Vidhyadhiraja, and K. S. Narayan, Lateral Photocurrent Scanning of Donor and Acceptor Polymers on Graphene Coated Substrates, *Japanese Journal of Applied Physics, 50, 061602,* ***2011***
5. Anshuman Das, *Sabyasachi Mukhopadhyay*, and K. S. Narayan, Characteristic noise features in light transmission across membrane protein undergoing photocycle, *Journal of Chemical Physics, 134, 07510,* ***2011***
6. Narasimhan Arun, *Sabyasachi Mukhopadhyay*, and K. S. Narayan, Monitoring intermediate states of bacteriorhodopsin monolayers using near-field optical microscopy, *Applied Optics, 49, 1131-1138,* ***2010***
7. Dhritiman Gupta, *Sabyasachi Mukhopadhyay*, and K. S. Narayan, Fill factor in organic solar cells, *Solar Energy Materials & Solar cells, 94, 1309-1313,* ***2010***

Conference Presentations:

Conference on Photonic Materials/Active Organic Materials, IUMRS-ICAM-2007, Bangalore, **October 2007** (Poster Title - *Charge transport under carrier grating in semi-conducting polymer films*)

11th International Conference on Near-field Optics, Nanophotonics and related Techniques (NFO-11), Beijing, China, **September 2010**, (Talk - *Imaging Purple Membrane with near field optics*)

Synopsis

Polymer-fullerene based bulk heterojunction solar cells (BHJ-PSCs) are turning out to be attractive energy options due to the ease of processability and reasonable power conversion efficiency. The limiting processes in BHJ-PSCs have been attributed to a wide variety of factors ranging from molecular level to macroscopic sources. It has been observed in BHJ-PSCs which consist of tailored donor-acceptor molecules to form an optimized interface for charge transfer and separation, factors such as donor-acceptor domain size and inter-domain connectivity limit the performance. Optimizations of these performance limiting issues present a considerable challenge in the efforts to realize efficient polymer based solar cells. The thesis largely addresses these issues by introducing specific techniques to probe the role of heterojunction morphology. These studies were carried out as a function of annealing conditions, effect of solvents and the ratio of constituent donor and acceptor materials which apparently govern the heterojunction microstructure.

Correlation of morphology and device performance demands high resolution microscopy techniques on working devices. In general, high resolution techniques such as transmission electron microscopy or photo-conducting atomic force microscopy, which are capable of imaging electrode-less heterojunction films, provide insufficient evidence for correlating heterojunction morphology with device performance. In this context, near field transmission and photocurrent mapping technique along with atomic force microscopy based near field scanning optical microscope (NSOM) is useful to establish the correlation.

In BHJ films, donor-acceptor phase separation is observed at meso-scale regime with the inter-domain distance of the order of 10 nm to 500 nm. Differences in the optical absorption of donor and acceptor material result in local optical transmission contrast. This local contrast can be followed by NSOM based techniques. This methodology of imaging via near field scanning optical microscopy is emphasized in Chapter-two and the technique is demonstrated for imaging single dye molecules and polymer nanoparticles.

The following Chapter focuses on PC studies in BHJ films upon local illumination and form the basis of the PC mapping method. The PC which decays as a function of spatial distance from the electrode periphery can be utilized to obtain the local information. The decay length scale is quite informative in evaluating the microscopic charge and spatial anisotropy. The technique involves the measurement of the spatially varying PC generated at the photo-active layer sandwiched between a patterned substrate and a top electrode, where the narrow-incident light beam scans regions beyond the overlapping electrodes.

In Chapter-four, the results obtained from near field current-contrast-optical scanning microscopy studies on heterojunction films with different blend ratios and processing conditions are discussed. The quasi-periodic length scale present in the contrast images is obtained from the 2-dimensional fast Fourier transform and power spectral density analysis of these images. This method has been employed to follow changes in bulk-heterojunction morphology with the variation in donor-acceptor ratio in the blend and thermal annealing conditions. Correlations between the changes in heterojunction morphology with carrier generation and transport pathways are clearly established from these studies. The presence of peak spatial frequencies in power spectrum renders the existence of quasi-periodic length scales which prevail in these binary mixtures. The variations in peak spatial frequencies upon thermal annealing are exploited to quantify the formation of nano-crystalline domains on film surface, the elongation in donor-acceptor domain size and the improvement in inter-domain connectivity.

Chapter-five of the thesis deals with the rationalization process of donor-acceptor ratio towards optimum device performance. During the performance optimization of BHJs consisting of crystalline or amorphous donor polymer blended with small molecule acceptor, it was observed that highly efficient devices were obtained from dissimilar donor-acceptor ratios for two systems. In this chapter, the requirement of different donor-acceptor ratio for different blend families from the microstructure perspective is discussed. Optimum donor-acceptor phase separation length scale and bicontinuous interpenetrating network for continuous carrier percolation to the electrodes are the prerequisite conditions for higher device performance. The effect of acceptor concentration on percolation transport is obtained by employing lateral PC decay measurements. The results demonstrate that an optimized blend composition leads to a balanced ambipolar transport that yields maximum device efficiency. The power spectral analyses of near field transmission contrast images demonstrate that for the crystalline polymer, the optimum length scale is formed at low acceptor concentration, whereas for the amorphous blend, optimum length scale is obtained at higher acceptor concentration. So, the phase-separation process which develops an interpenetrating network in heterojunction films evolves with the crystalline nature of donor polymer. The study predicts a universal rule that dictates the role of donor polymer structure on optimum blend ratio for efficient device performance.

The last Chapter deals with miscellaneous but relevant problems involving modification of transparent electrode by depositing graphene film on it. The lateral PC decay measurements on graphene coated substrates demonstrate the consequences of graphene on ambipolar transport for both acceptor and donor type polymers. The presence of graphene layer significantly alters the unipolar PC decay profile at the electrode edge. The variation in decay profile is then correlated to microscopic transport processes in the polymer system by employing a spreading impedance model. It is observed that the granularity of the graphene layer has a significant influence on the carrier transport network formation in polymer films.

•

Table of Content

List of Figures

Notations/Abbreviations

Abbreviations	**Details**
DOS	Density of states
HOMO	Highest occupied molecular orbital
LUMO	Lowest unoccupied molecular orbital
2D	Two dimensional
3D	Three dimensional
PP	Polaron pair
D-A	Donor-Acceptor
BHJ	Bulk-heterojunction
PCE	Power conversion efficiency
PC	Photocurrent
NSOM	Near field scanning optical microscope
NPC	Near field photocurrent
PSF	Point spread function
FFT	Fast-Fourier transform
PSD	Power spectral density
PDF	Probability density function

Chapter 1

General Introduction

1.1 Introduction

Photovoltaics deal with harnessing sunlight and subsequent conversion into electrical energy. Efficient photovoltaic solar cells based on inorganic semiconductors have developed considerably [1] since the first realization of silicon solar cells in 1954 from Bell Laboratory [2]. To date, silicon based cells with power conversion efficiency up to 30 – 40% are still leading technology in the photovoltaic market. However, the costs of silicon based cells are still not comparable to other conventional sources of energy, primarily due to the large-area requirement of harnessing the sunlight. An approach for roll to roll production of solar cells at low cost is to utilize as organic semiconducting materials that can be processed under less demanding conditions. Research on organic based photovoltaics have been pursued for more than 20 years, however, within the last decade this research field has made considerable improvement with higher efficiency and reliability to make it commercially feasible [3, 4], [5].

Organic electronics research started with the discovery of dark conductivity in halogen doped organic compounds [6]. It was followed by both experimental and theoretical studies on charge transport properties of photo-responsive polymers and small molecule systems [7]. Conductivity in carbon-based semiconductor arises due to extensive π-conjugation of the carbon backbone [8]. The isomeric effect of these π electrons results in high electron polarizability. Due to the Peierls instability (alternating single and double bond structure) delocalized states are formed in long conjugated polymer chains. It constitutes two different electronic energy states, the highest occupied molecular orbital (HOMO) and the lowest unoccupied molecular orbital (LUMO) [9, 10]. HOMO and LUMO are separated by a bandgap ~ 1 - 3 eV, resulting in conjugated polymers being semiconductors. Energy states have a direct implication on optical properties and charge carrier transport in these amorphous materials. The accessibility of modifying optoelectronic properties following different synthesis methods accompanied by low cost large scale production makes conjugated polymers a very interesting choice for photovoltaic applications [11].

First generation organic solar cells were based on the hole conducting organic layer sandwiched between two metal electrodes of different work functions (Figure 1.1a) [9], [12]. The conversion efficiencies for this device structure was generally poor ($\eta \sim 10^{-3}$ to 10^{-1} %), with very low photovoltage (0.2 - 0.4 V). In this context, second generation organic solar cell (bilayer cell) was reported by *Tang* and *co-workers* [13] consisting of donor and acceptor layer, and achieved a power conversion efficiency ~ 1%. The typical device configuration is shown in Figure1.1b.

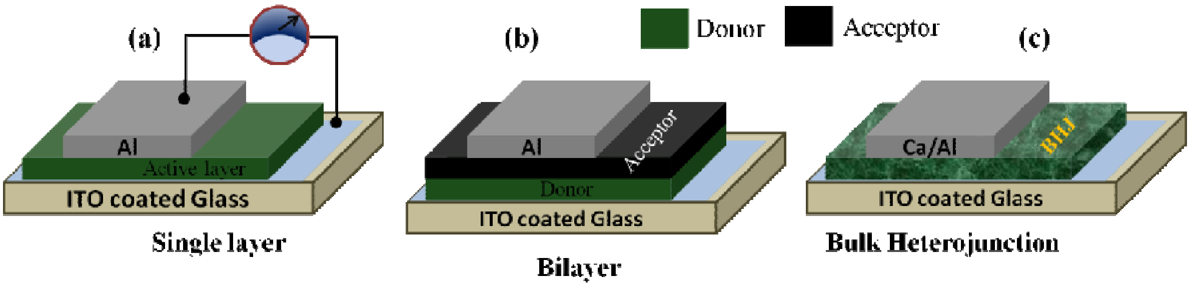

Figure 1.1: Different polymer solar cell architectures

The concept of bulk heterojunction polymer solar cell (BHJ-PSC) was introduced with the discovery of photovoltaic effect in an intermixed polymers network [14]. This approach, shown in Figure 1.1c, features a distributed junction between the donor and the acceptor material. BHJ concept is implemented by spin coating a polymer–fullerene blend solution on conducting glass substrate. Bulk heterojunction has an advantage of being able to dissociate primary photo-excitation very efficiently, thus generating electron–hole pairs throughout the active layer. It has been extensively shown that the choices of solvent, thermal annealing, and additive solvent have a profound effect on the heterojunction morphology and the performance of the solar cells [15]. It elucidates that a good control over the morphology is very important for an efficient bulk heterojunction solar cell (~ 3%). The choice of solvent as well as post-annealing of the solution-processed polymer-fullerene thin film, leads to a more favourable bulk structure in view of the dissociation of bound electron–hole pairs and the subsequent charge transport [16], [17]. Indeed, optimization by novel routes is an ongoing research, and over the last five years, further steps in improving power conversion efficiency have been made. Efficiency between 5% and 8% had been achieved by the use of novel materials as well as additives optimizing the D-A phase separation [18, 19]. It is imperative to understand the fundamentals of opto-electronic properties (photophysics) of polymers before exploring the ramifications of morphology on BHJ device performance.

1.2 Photophysics of Semiconducting Polymers

Conjugated polymers have anisotropic, quasi-one-dimensional electronic structure with π electrons coupled to the polymer backbone. This extensive π electron conjugation along a rigid backbone confers extraordinary coherence lengths on wave functions. Chains are typically broken into conformational subunits consisting of planar π-electron systems by 2 to 12 repeat units. These are the primary absorbing units, or chromophores, [20, 21] as shown for poly[2-methoxy-5-(2-ethyl-hexyloxy)-1,4-phenylene-vinylene] (MEH-PPV) chain (Figure 1.2b). The overlapping of π (also π*) electron wave functions form a valence band (conduction band) with a gap size of typically 2.7 eV, corresponding to the conventional semiconductor gap. The electronic structure of semiconducting polymers were described by *Su et al.* in terms of a quasi-one-dimensional tight binding model [22]. Upon photoexcitation self-localized excitations are formed in the polymer chains — solitons, polarons, or bipolarons, depending on the ground-state degeneracy [23, 24]. *In degenerate ground-state (trans- polyacetylene), solitons are the important nonlinear excitations, whereas in non-degenerate ground-state systems, including most of the conjugated polymers such as poly(p-phenylene vinylene), polypyrrole and polythiophene, polarons and bipolarons are the responsible charge-storage excitations* (Figure 1.2a) [23]. Photophysics of conjugated polymer chains are ascertained by the formation and properties of such nonlinear excitations. Photoexcitation *i.e.* perturbing charges onto the polymer backbone by direct optical pumping above the π-π* energy gap with an intensive external light source, reveals the physical properties of non linear excitations in conjugated polymers. Depending on strength of the electron-electron interactions relative to the band width and the electron-phonon interactions, these elementary excitations are generated as mobile charge carriers (charged polarons) or bound neutral excitons.

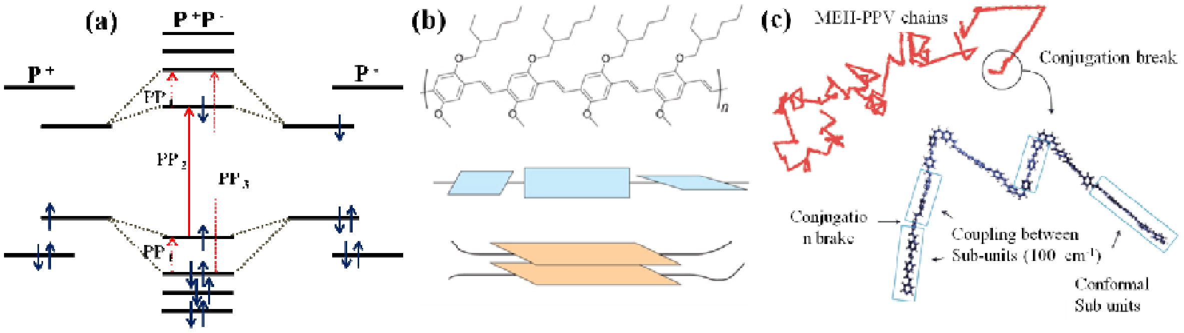

Figure 1.2: (a) Natural excitations from non-degenerate ground-states polymers (polaron pairs) (b) Chemical structure of poly(2-methoxy 5-[2'-ethylhexyloxy]-p-phenylene vinylene(MEH-PPV). Rectangles represent twisted conjugated polymer segments. (c) Schematic of chromophores along a conjugated polymer backbone (adapted from Science 2009, 323, (5912), 369-373. Reprinted with permission from AAAS).

These electronic coupling interactions dictate the energy transport between conformational subunits. Two basic types of electron energy transport (EET) have been identified: intrachain and interchain [25-27]. The former consists of energy migration along the backbone between adjacent segments (Figure 1.2c). The latter is described as energy hopping among segments coupled through space, either because the chains are near to each other in a solid film or because the chain is folded back on itself (Figure 1.2c). Interchain interaction in printed or solid film modifies the optical property of chain with red–shift in photoluminescence. In this respect the optical properties of individual segments can be found by studying optical properties of diluted solution [28]. In polymer film, energy migrations through polymer chains demonstrate the electrical transport in conjugated polymer, which is discussed in the next section.

1.3 Charge Transport in Disordered Semiconducting Polymers

Unlike the crystalline materials, charge transport in amorphous semiconducting polymers is governed by structural and energetic disorders which arise from positional disorders and fluctuations in local conjugation length [29]. The hopping mechanism of charge carrier transport between different energy sites is one of the most important factors in understanding and developing organic semiconductors based devices. The density of state (*DOS*) distribution of HOMO and LUMO energy levels in organic semiconductor is well represented by a Gaussian-like distribution of localized states [29-33]. It reflects the energetic spread of the charge transport sites as -

$$DOS(E) = \frac{N_V}{\sqrt{2\pi}.\sigma} exp\left[-\left(\frac{E-E_0}{\sqrt{2\pi}.\sigma}\right)^2\right] \quad (1.1)$$

where E is the energy, E_0 the Gaussian centre; N_V is the DOS and σ the Gaussian variance (Figure 1.3). In a disordered organic system with a Gaussian density of states of width σ, the charge density under steady state conditions thermalizes near to $-\sigma^2/k$T, below the centre of the density of state distribution at a given temperature (Figure 1.3).

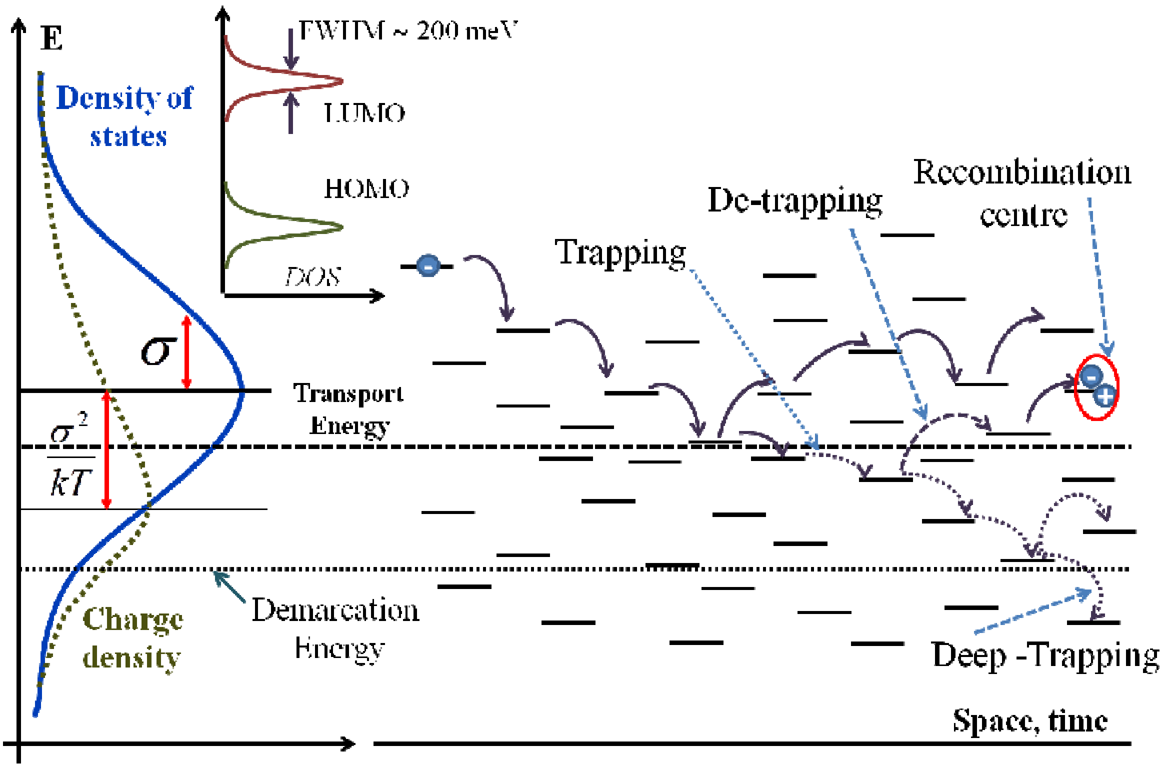

Figure 1.3: Schematic of DOS, charge carrier density distribution and transport process in a disordered system.

Electrical transport in these amorphous materials is always accompanied by frequent capture of involved carriers in localized states (Figure 1.3). Such trapped carriers are released after a specific retention period forming a trap centre or may recombine with the carriers of opposite charge by forming a recombination centre. These trap states originate from impurities, structural defects, geminate pairs and sometimes self-trapping. To distinguish between the trap states and regular transport sites, temperature dependent transport energy (E_t) concept was introduced by *Monroe et al.* for amorphous semiconductors [34]. According to the multi-trapping and releasing model, a carrier in a deep tail state will most probably escape to a state of energy E_t, independent of its initial energy in the tail. Consequently, states below the E_t are trap states, while the states above the transport energy are regular transport sites. During transport, carriers are repeatedly trapped in localized states and released by the thermal excitations to the transport energy [35-37]. As transport energy varies with temperature, a state acting as trap state at room temperature may become a transport state at lower temperature. The rate of carrier release from a trap with binding energy E at temperature T is defined as $\omega_0 exp(-E/kT)$, where ω_0 is an attempt to escape prefactor which is order of 10^{12} s^{-1} and relates to the demarcation energy E_D(t) as $E_D(t) = kTln(\omega_0 t)$ [36]. Trapped carriers at shallower trap states release within a short time compared to those from deeper states which have much lower in concentration and excitation probability [38]. Indeed carriers are predominantly excited from the states near E_D at any time; hence E_D represents average trap energy with respect to the transport energy at temperature T (Figure 1.3). So total carrier concentration is a sum of the mobile, conductive charge carriers n_c and immobile charge carriers n_t trapped in a tail of the Gaussian density of states. Gaussian centre, width and functional form of the DOS for semiconducting conjugated polymer can be obtained from their optical absorption and emission spectroscopy, whereas demarcation energy is associated with the carrier activation energy. These measurements are limited to the optically accessible electronic states of DOS. Investigation on MEH-PPV polymer demonstrates that Gaussian DOS (LUMO) is centered (E_0) at 2.86 ± 0.03 eV with a variation (σ) of 60 meV [39]. Macroscopic charge transport in organic semiconductor based devices was determined by a theoretical model (*Gaussian disorder model*) based on the thermally assisted intermolecular variable range hopping of charges from one site to next [40, 41]. The Gaussian disorder model (GDM) is purely based on cubic lattice arrangement of charge transport sites as assumed by Bässler *et. al* [42]. These sites are represented either by entire small molecules, or the conjugated segments of polymers. According to the Marcus model (*effective medium approximation*) [43, 44], the hopping transport between two sites ($i \rightarrow j$) depends on the transfer integral of corresponding wave functions and a thermally activated process which describes the local charge transport as

$$\nu_{ij} = \frac{|I_{ij}|^2}{\hbar}\sqrt{\frac{\pi}{\lambda kT}}\, exp\left(-\frac{\left(\Delta G_{ij}+\lambda\right)^2}{4\lambda kT}\right) \tag{1.2}$$

Here, I_{ij} is the transfer integral, λ is the reorganization energy related to the polaron relaxation, and ΔG_{ij} is the energy difference between these two particular sites.

Considering spatial disorder, tunneling and thermal activation even more explicitly, a charge positioned at point *i* on this lattice will hop to a neighboring point *j* with a rate ν_{ij} that is defined by Miller-Abrahams expression [45]

$$\nu_{ij} = \nu_o exp\left(-\gamma r_{ij}\right)\begin{cases} exp\left(-\frac{\Delta E_{ij}}{kT}\right), \Delta E_{ij} > 0\ (up\ hop) \\ 1, \Delta E_{ij} \leq 0\ (down\ hop) \end{cases} \tag{1.3}$$

where ν_o is frequency pre-factor, ν_{ij} the maximum hopping rate, γ the inverse localization radius which is proportional to the transfer integral and r_{ij} the distance of the site *i* and *j*. Then by computing the motion of charges across the lattice with Kinetic Monte Carlo algorithm, the expression of carrier mobility with temperature was simulated [46]. These calculations, over a range of lattices, temperatures T and electrical fields *E*, reveal an empirical expression for experimentally measured mobility (μ). In presence of an applied electric field, the potential drop between the sites is calculated as the distance between the sites time the applied electric field. The occupation probability of the state at energy E_i at a certain site is determined by the Fermi-Dirac distribution $f(E_i)$. So the hopping current from site *i* to the site *j* is

$$j_{ij} = [DOS(E_i)f(E_i,E_F)] \times \left[DOS(E_j)\left(1-f(E_j,E_F)\right)\right]\nu_{ij}\vec{r}_{ij}\cdot\hat{E} \tag{1.4}$$

Therefore, the total hopping current can be expressed as [12]

$$J = \int_{-\infty}^{\infty} dE_i \int_{-\infty}^{\infty} dE_j \int_{\Re}^{\infty} d\vec{r}_{ij}\,[DOS(E_i)f(E_i,E_F)] \times \left[DOS(E_j)\left(1-f(E_j,E_F)\right)\right]\nu_{ij}\vec{r}_{ij}\cdot\hat{E} \tag{1.5}$$

The temperature and low field dependent charge carrier mobility was derived from GDM formalism as a function of the degree of disorder [42, 46]

$$\mu_{GDM}(\sigma, \Sigma, E) = \mu_{\infty} exp\left(-\left(\frac{2\sigma}{3kT}\right)^2\right) \times \begin{cases} exp\left(C_0\left[\left(\frac{\sigma}{kT}\right)^2 - \Sigma^2\right]\sqrt{E}\right), \Sigma \geq 1.5 \\ exp\left(C_0\left[\left(\frac{\sigma}{kT}\right)^2 - 2.25\right]\sqrt{E}\right)\ \Sigma < 1.5 \end{cases} \tag{1.6}$$

where μ_0 and C_0 are constants. GDM successfully reproduced many of the features of charge mobilities that were observed in disordered organic solids, in particular their dependence on the temperature and field [47-49]. Disorder in Bässler model is incorporated by choosing ν_{ij} and $\varepsilon_i - \varepsilon_f$ from Gaussian distributions of width $\sqrt{2\Sigma}$ and $\sqrt{2\sigma}$ respectively [29, 50].

Conventional carrier transport, which is defined by the *Einstein relation* between the diffusion coefficient (D) and the carrier mobility (μ), $D/\mu = kT/e$, is not well adequate to establish carrier transport in organic semiconductor. A generalized relation can be derived considering the generalized DOS and charge carrier distribution (P) as $D/\mu = P/e\frac{\partial P}{\partial E_F}$, where $P = \int_{-\infty}^{\infty} DOS(E)f(f)dE$ and E_F represent chemical potential. Accounting Gaussian density of state distribution in organic semiconducting materials, the generalized *Einstein relation* is represented as

$$\frac{D}{\mu} = \frac{kT}{q} \frac{\int_{-\infty}^{\infty} exp\left[-\left(\frac{E - E_0}{\sqrt{2}\sigma}\right)^2\right] \frac{1}{1 + exp\left(\frac{E - E_F}{kT}\right)} dE}{\int_{-\infty}^{\infty} exp\left[-\left(\frac{E - E_0}{\sqrt{2}\sigma}\right)^2\right] \frac{\exp\left(\frac{E - E_F}{kT}\right)}{\left[1 + exp\left(\frac{E - E_F}{kT}\right)\right]^2} dE} \eta \tag{1.7}$$

where η assumed to be larger than one for any practical charge density and the effect is more pronounced for high disordered materials (larger σ value) [51].

1.4 Principles of Organic BHJ Photovoltaics

Conversion of sunlight into the electric current in an organic photovoltaic cell can be summarized by five successive processes: (i) Absorption of a photon leading to the formation of an excited state, exciton or the tightly bounded electron-hole pair (ii) exciton diffusion to the D-A interface region, (iii) charge transfer process at the interface (iv) charge transfer complex dissociation and (v) finally free carriers transport to the anode (hole) and cathode (electron) [5]. The electric current delivered by the photovoltaic device corresponds to the number of charges collected at the electrodes [52, 53]. The overall internal quantum efficiency (IQE) of photovoltaic devices (η) is determined by *a*) the fraction of photon absorbed (η_A), *b*) the fraction of dissociated electron-hole pairs (η_{ED}), *c*) fraction of separated charge that reached to the electrodes (η_{CT}) and *d*) the fraction collected at the electrodes (η_{CC}) [54].

$$\eta = \eta_A \eta_{ED} \eta_{CT} \eta_{CC} \tag{1.8}$$

η_A can be calculated from the Beer-Lambert law accounting for the absorption spectrum, absorption coefficient (α) and film thickness (t) of the active material with internal multiple reflections from two metal electrodes (R)

$$\eta_A = (1 - R)(1 - e^{-\alpha t}) \tag{1.9}$$

η_{ED} is determined by whether the excitons diffuse to the region where the charge separation occurs, or on the charge separation probability. η_{CT} is directly related to the film morphology, which yields the percolation pathways to the carrier transport and η_{CC} is determined by band bending at the metal-polymer interface. Carrier concentration gradient at the interface results in a field induced drift and diffusion currents and drives the carriers to the electrode [55, 56]. Detailed numerical analyses of charge carrier distributions over film depth depicts that thin film devices (≤ 100 nm) are mostly dominated by the field drift whereas thicker devices are more dominated by the diffusion of charge carriers in the concentration gradient at the selective contact [57, 58]. In characterization process, PC action spectrum of solar cells, *i.e.* incident photon to current conversion efficiency (IPCE) or the external quantum efficiency (EQE), represents ratio of the PC to the incident photon flux as a function of the excitation wave length,

$$IPCE(\lambda) = EQE(\lambda) = \frac{n_{electron}}{n_{photon}} = \frac{J/_{e}}{P/_{h\upsilon}} = \frac{J}{P}\frac{hc}{e\lambda} = \frac{J}{P}\frac{1240}{\lambda(nm)} \tag{1.10}$$

where J is the measured PC in A/m^2 and P is incident light power in W/cm^2. EQE is obtained by recording PC at different wavelengths (λ) of incident light and is a measure of efficiency of photon to electron conversion. The current density-voltage characteristics (yellow line) of a typical polymer solar cell are presented in the Figure 1.4 and 1.5 in dark and under illumination (100 mW/cm^2) respectively. Under illumination condition, separated charges drift in this electric field, electron move to the metal with low work function and holes move to the opposite electrode.

A certain applied voltage balances the built-in field and no current flows through the circuit. This open circuit condition known as “Flat-band-condition” and applied voltage is called open circuit voltage (V_{OC}). In dark condition, no current flows through the circuit, until charges are injected heavily at forward bias for voltages larger than V_{OC}.

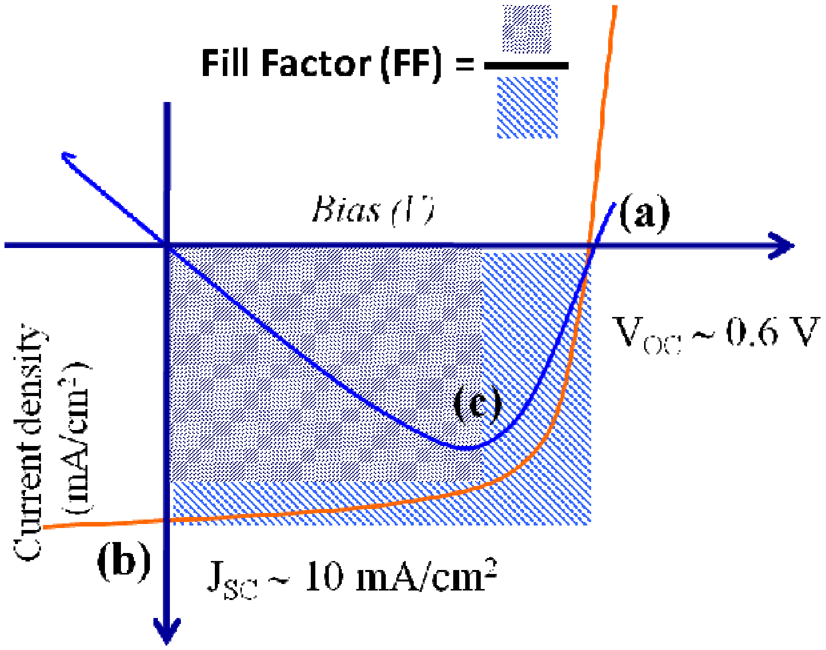

Figure 1.4: Schematic of current density-voltage characteristic of typical bulk heterojunction solar cells

Under illumination, current flows in the opposite direction to the injected current. In Figure 1.4 at point (a), the drift and diffusion PC currents are balanced to zero and maximum PC (b) flows under the short-circuit condition. The device generates power (J×V) in the fourth quadrant and the performance of a solar cell is described by the power conversion efficiency (PCE) or η. At point (c) in J-V response, J×V product hence the power output is largest, which denotes as a maximum power point (MPP). PCE is represents in terms of open circuit voltage V_{OC}, short circuit current density J_{SC} ($J_{SC} = I_{SC}$/active area) and fill factor FF. Assuming that organic layer is thick enough to absorb all photons in the wavelength range from λ_1 to λ_2, the maximum value of J_{SC} can be obtained as

$$J_{SC} = \frac{e}{hc}\int_{\lambda_1}^{\lambda_2} P_{inc}\, EQE(\lambda)\, \lambda\, d\lambda \tag{1.11}$$

Fill factor is calculated as FF = $V_{MPP} \times J_{MPP} / (V_{OC} \times J_{SC})$ and determines the part of the generated power that can be used. The power conversation efficiency of solar cell devices is defined as

$$\eta_{POWER} = \frac{P_{OUT}}{P_{IN}} = \frac{I_{MPP} . V_{MPP}}{P_{IN}} = \frac{FF . I_{SC} . V_{OC}}{P_{IN}} \quad (1.12)$$

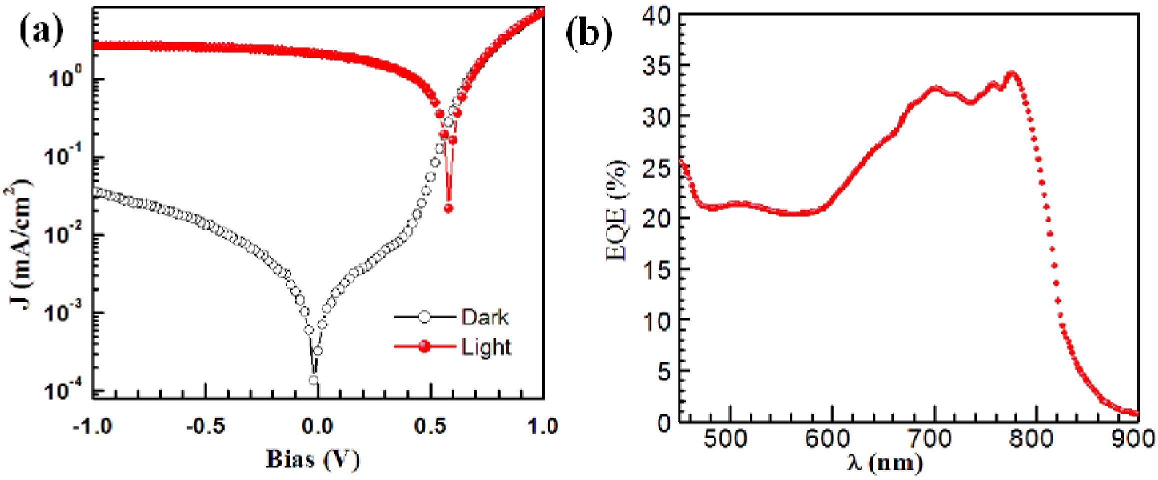

Figure 1.5: (a) Semi-logarithmic J-V measurements of P3HT: PCBM (1:1) plastic solar cell under (AM 1.3) solar spectrum simulator (light) and in dark. (b) EQE spectra of typical BHJ solar cell.

The efficiency of the polymer solar cells is strongly dependent on cell temperature, incident light intensity and its' spectral content. The standard reporting protocols for efficiency measurement are specified as [55]

Light Intensity	1000 W/m^2
Sun Spectrum	AM 1.5 Global (IEC 904-3)
Sample Temperature	25° C

The measurement procedure requires use of solar simulator (E_S) with a light spectrum approximate to the AM 1.5 global spectrum ($E_{1.5G}$) with calibrated reference cell. Due to the difference in spectral response of test devices (S_T) with calibrated cell (S_R), a spectral mismatch factor is defined as

$$M = \frac{\int E_{1.5G}(\lambda)S_R(\lambda)d\lambda}{\int E_S(\lambda)S_R(\lambda)d\lambda}\frac{\int E_S(\lambda)S_T(\lambda)d\lambda}{\int E_{1.5G}(\lambda)S_T(\lambda)d\lambda} \tag{1.13}$$

The conversion efficiency $\eta_{\mathrm{AM}\ 1.5}$ of the photovoltaic devices measured with a simulator is giving by

$$\eta_{AM\ 1.5} = \frac{P_{OUT}}{P_{IN}}M = FF\frac{I_{SC}.V_{OC}}{P_{IN}}M \tag{1.14}$$

Various solar cells parameters such as influence of leakage current and the degree of different recombination losses can be quantified from *J-V* characteristics (Figure 1.5a). In general *J-V* characteristics of organic solar cell are described using Shockley equation [59, 60]. In order to account for a real solar cell, the ideal Shockley equation is extended by two resistors. A series resistor R_S, which is in series with the ideal diode describes the contact resistances, such as injection barriers and the sheet resistance. In contrast, the parallel resistance R_P represents the influences of the local shunts between two electrodes. The total current density for a practical solar cell, therefore, consists of three contributions, photoinduced short circuit current, diode current and parallel current through R_P, where j_0 is the reverse saturation current density and n denotes the diode identity factor [55].

$$j(V) = j_{ph} + j_0\left[exp\left(\frac{q(V - jR_S)}{nkT}\right) - 1\right] - \frac{V - jR_S}{R_P} \tag{1.15}$$

However, certain devices show a strong field-dependent PC behavior in the third quadrant, and maximum PC is not reached under short circuit condition but only at more negative bias. This reduces the fill factor and consequently the solar cell efficiency. These features of the current density-voltage curve cannot be explained properly by diode equation. Such *J-V* response can be attributed to the field dependence dissociation of Coulomb-bound electron-hole pair.

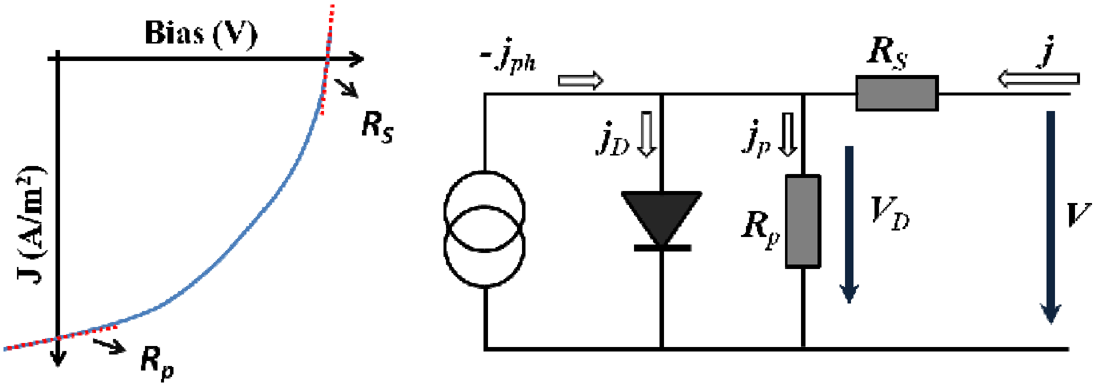

Figure 1.6: Schematic of current density (J)-bias voltage (V) characteristic of polymer-small molecule solar cells. The equivalent circuit representation of practical solar cell (left).

For small deviations from the ideal values $R_S \rightarrow 0$ and $R_P \rightarrow \infty$, the influence of both losses on the *J*-*V* curve can be derived analytically by differentiating with respect to bias (*V*). In a particular modes of operation such as V $(j = 0) \Rightarrow$ V_{OC} and V $(j = j_{SC}) \Rightarrow 0$, assuming $R_S \langle\langle R_P$ -

$$\frac{\partial V}{\partial j}|_{j=0} = R_S + \frac{R_P}{1 + \frac{j_0 R_P}{nkT} exp \frac{V_{OC}}{nkT}} \approx R_S \qquad (1.16)$$

and

$$\frac{\partial V}{\partial j}|_{V=0} = R_S + \frac{R_P}{1 + \frac{j_0 R_P}{nkT} exp\left(-\frac{j_{SC} R_S}{nkT}\right)} \approx R_S + R_P \approx R_P \qquad (1.17)$$

So the reciprocal derivatives of the *J*-*V* curve under illumination at the open circuit and short circuit represent a series and parallel resistances R_S and R_P respectively. Due to diode non-linearity, these parameters are not constant but vary with illumination level, reverse saturation current (J_0) and cell temperature.

1.5 Morphology Driven BHJ Performance

Conjugated polymer-fullerene bulk heterojunction (BHJ) is the benchmark architecture for current polymer material based solar cells with the possibility of achieving high external quantum efficiencies [61]. The dispersed interface throughout the bulk film improves the exciton dissociation rate and charge separation within the different phases and reduces the back recombination to a certain extent. The bicontinuous and interpenetrating network of donor and acceptor components yield percolation pathways for hole and electron transport to the metal contacts. *Therefore, the bulk heterojunction devices are more sensitive to their morphology of blend film. This idea of correlating morphology to device performance is the central theme of the thesis.*

1.5.1 Phase separation process in blend films

In the BHJ-PSC, both the excitons dissociation and the carrier transport are facilitated by the presence of a quasi-bicontinuous, interpenetrating network of electron donor (conjugated polymers) and acceptor (e.g., fullerene) domains [62-64]. But the origin and structure of bicontinuous phase separation in polymer-fullerene systems had been neglected for years. Recently temperature-composition phase diagram for donor polymer-small molecule acceptor solvent mixture was computed using the *Flory-Huggins* (F-H) *model* [65-70]. Particularly, acceptor solubility limit is an important thermodynamic parameter to control phase separation and morphology in a blend film. Furthermore, the correlations of phase behavior with electrical transport facilitates better understanding of structure-property relationships in polymer-fullerene blends and allows to develop rational strategies for improving polymer solar cell performance.

In a dilute limit, polymer-polymer blends in a common solvent behave as single phase system. During spin-coating, rapid solvent evaporation essentially increases the density and eventually leads the condensed film states where small-scale phase segregation is observed. In polymer-fullerene blend, phase segregation morphology is governed by the solubility limit of fullerene acceptor (~ 9-47 mg/ml) and two-phase liquid-liquid demixing kinetics [71, 72]. The surface directed demixing between two components mainly develops from the polymer-fullerene interaction at liquid-liquid phase regime [73]. In this thesis, resulting morphology of spin coated polymer-polymer and polymer-fullerene blends are studied closely as a function of (i) different type of donor polymer (ii) different weight ratio of the blend and (iii) processing condition (*Chapter 4 and 5*). An amorphous or dispersion of fullerene nanocrystal are formed in film in spin-coating process of polymer-fullerene blend [74]. With rapid solvent evaporation (thermal annealing) the composition of the liquid phase is reached to the higher fullerene concentration beyond the equilibrium limit, which finally end up with rapid nucleation and growth of fullerene crystals which was observed under high resolution optical microscope [75], while with increasing fullerene concentration, fullerene island formation was clearly observed in heterojunction film [76]. During the thermal annealing process, fullerene diffusion and pure crystalline domain formation is generally explained by Fick's diffusion process

$$\frac{\partial \Phi}{\partial t} = -D\frac{\partial^2 \Phi}{\partial x^2} \tag{1.18}$$

where Φ and D represent the fullerene concentration (in volume) and diffusion coefficient respectively [77]. The approach described in the thesis presents the observed segments of this aggregation. *Various fundamental processes governed by the phase separated morphology, which directly influence the performance of heterojunction solar cells are briefly discussed below.*

1.5.2 Exciton generation, diffusion and formation of charge-transfer states

In an organic D-A solar cell, light is usually absorbed by the donor materials, *i.e.* conjugated polymer which exhibits very high absorption coefficients (~ 10^5 cm^{-1}). Absorbed photon generates Coulomb-bound electron-hole pairs or excitons in the organic semiconductor. The binding energy of these excitons is larger compared to the activated thermal energy in the organic semiconductor [78]. The photogenerated excitons dissociation process is confined at the D-A interfacial area of active film. So the excitons, which are produced at the distance shorter than their diffusion length (10 -20 nm), have the good probability to reach D-A interface where charge carriers are formed. Hence, in polymer bulk heterojunction solar cell, exciton diffusion length (L_{Diff}) is an important parameter since diffusion process dictates the photoexcitation energy transfer to the D-A interface. Once the exciton reaches the interface, it transfers electron to the electronegative acceptor. This charge transfer is extremely fast and in order of tens of femtosecond [79]. Recent studies demonstrate that the charge generation process consists of exciton generation mostly at the polymer, energy transfer to acceptor molecule and subsequent hole transfer to the polymer [80]. The intermediate step is ascribed to the Förster resonant energy transfer [81]. This charge transfer process is much faster compared to any loss processes such as photoluminescence or inter-system crossing, associated with the transition from the singlet to triplet exciton [82, 83]. The exciton will dissociate after electron transfer, if its energy is larger compared to the energy of electron-hole pair which is often known as polaron pair (positive polaron on the donor material and negative polaron on the acceptor) or charge transfer complex (CTC) [84, 85], [86]. Along with the donor conjugated polymer, acceptor material also absorbs light, although the exciton generation rate is much lower as compared with the polymer [87]. A substituent charge transfer to the polymer from fullerene acceptor has been also observed experimentally [88].

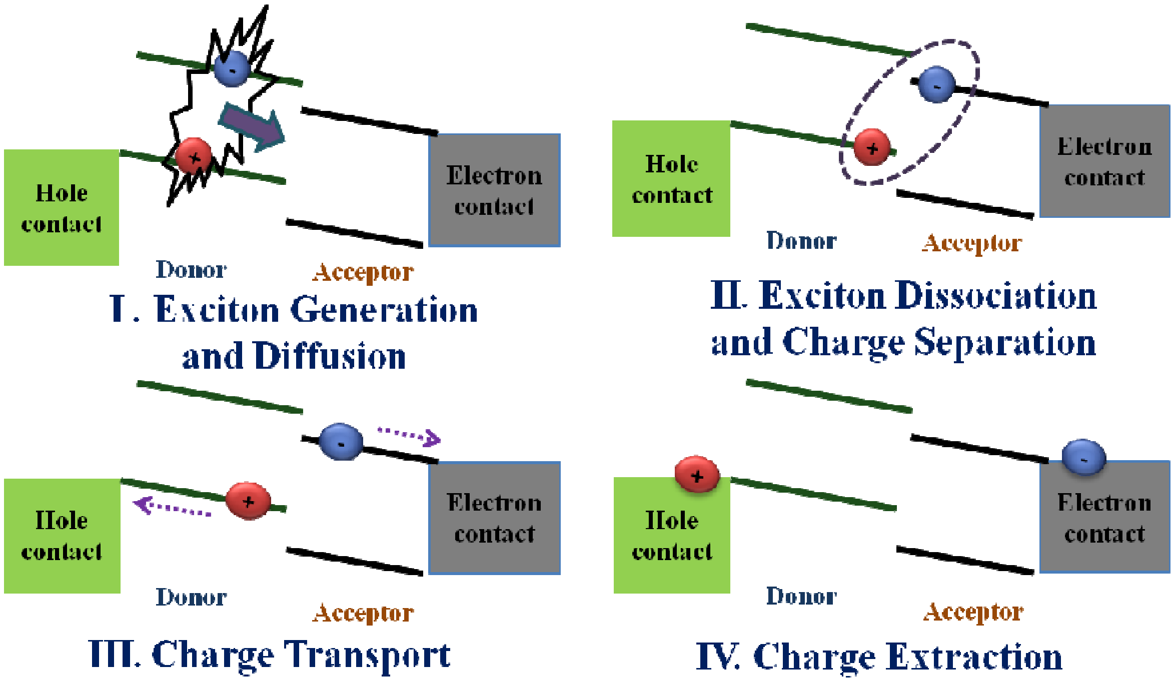

Figure 1.7: Cartoon representation of exciton generation, diffusion, dissociation and PC generation in a bulk heterojunction solar cell.

1.5.3 Charge carrier pair dissociation

After dissociation of exciton at the interface, electron and hole resides on the acceptor and donor respectively, but they are still Coulomb bound as a polaron pair. The dissociation of polaron pair produces free and mobile charge carriers [89, 90]. A cartoon representation of the polaron pair separation is shown in Figure 1.8 Polaron pair dissociation in the context of photogeneration in BHJ-PSC has been appropriately described by Braun-Onsager model [91, 92]. This model accounts for the finite lifetime of the initial bound states and has been successfully applied to the charge transfer states dissociation in D-A systems. The polaron pair (PP) can either dissociate to the free charges with the rate k_{PPd} or recombine to the ground state with a constant rate, given by inversed of its life time $k_{\mathrm{PPf}} = \tau_{\mathrm{pp}}^{-1}$.

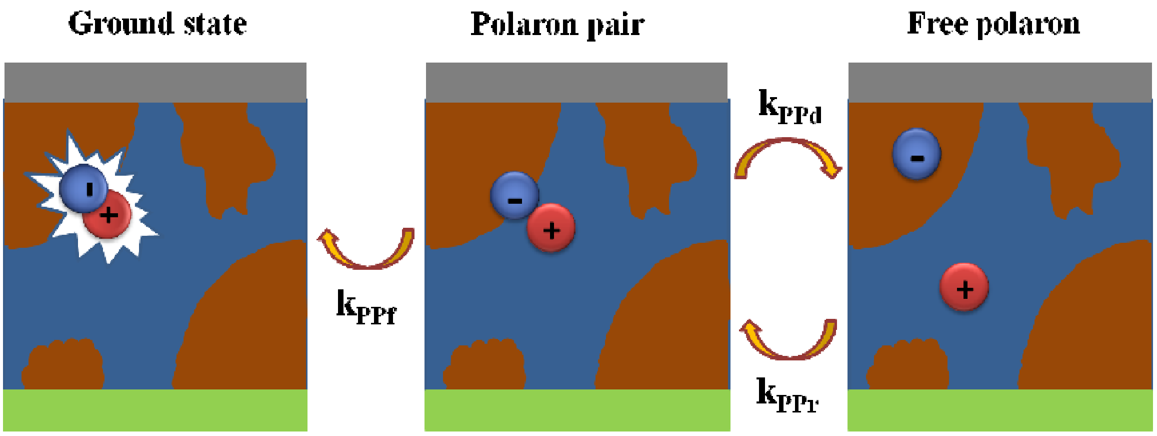

Figure 1.8: Schematic of polaron pair dissociation at the donor-acceptor interface. Dissociation rate of polaron pair to free charges with represents as k_{PPd} *and reverse process of free recombination rate as* k_{PPr}*.* k_{PPf} *is the recombination rate of the polaron pair to ground state.*

On other side, free charges can also recombine and generate bound polaron pairs again with a rate k_{PPr}. At a balance situation, the detailed expression of dissociation rate k_{PPd} can be obtained considering Langevin recombination rate [93]. According to this model the local electric field dependent (E) dissociation probability is expressed as

$$P(E) = \frac{k_{PPd}(E)}{k_{PPd}(E) + k_{PPf}} \tag{1.19}$$

and the field dependent dissociation rate k_{PPd} as

$$k_{PPd}(E) = \frac{3\gamma}{4\pi r_{pp}^3} exp\left({}^{E_b}\!/_{kT} \right) \frac{J_1\left(2\sqrt{-2b}\right)}{\sqrt{-2b}} \tag{1.20}$$

where $\gamma = q(\mu_e+\mu_h)/\varepsilon\varepsilon_0$, is the Langevin recombination factor, r_{pp} the initial polaron pair radius, $E_b = e^2/(4\pi\varepsilon\varepsilon_0 r_{pp})$ the Coulomb binding energy of the pair, and $b = e^3E/(8\pi\varepsilon\varepsilon_0(kT)^2)$ [94]. The fraction of polaron pairs which are not able to dissociated, can recombine geminately in a monomolecular process, being proportional to the polaron pair concentration not on the product of the electron and hole densities [95]. In a very fine-grained phase separated BHJ film, polaron pairs cannot escape their mutual influence and electron back transfer from the acceptor to the triplet exciton state takes over [96]. These studies demonstrate the significance of BHJ morphology on polaron pair dissociation process.

1.5.4 Charge carrier recombination

In BHJ solar cell, carrier recombination processes mainly depend on the internal electric field and the carrier concentrations. A monomolecular recombination process is approximated by n/τ, where n is the carrier density and τ represents average lifetime. Recombination of free polarons that originates from different excitons is called nongeminate. Such a nongeminate process in low mobility materials is considered as bimolecular or second-order process, where the recombination rate R is expected to be proportional to the electron concentration (n) times the hole concentration (p) – $R \propto \gamma(np - n_i^2)$ [97, 98]. According to the experimental observations, thermally activated recombination rate in BHJ can be expressed as

$$R_{Langevin} = \zeta\gamma(np - n_i^2) \tag{1.21}$$

where n (p) is the free electron and hole density, n_i (p_i) the intrinsic electron (hole) density and γ the Langevin recombination factor [7]. For a pristine material γ can be expressed as $\gamma = e(\mu_e + \mu_e)/\epsilon$, where ε is the dielectric constant and $\mu_{e(h)}$ the temperature dependent electron (hole) mobility [51, 99]. However there are many possibilities to consider recombination process at different stages of the device geometry. A detail summary of different recombination processes is as follows –

a) *Recombination of the exciton before it reaches the interface* – an exciton generated in the polymer could recombine with a hole by an Auger process and similarly an exciton in the acceptor can also recombine with an electron. These are bimolecular recombination mechanisms since the rate depends on the product of the exciton and free carrier concentration, both of which are proportional to the optical generation rate [100].

b) *Field ionization of the geminate CTE* – when exciton reaches the interface, it splits into an electron in the acceptor and a hole in the polymer, which are presumed to form a bound geminate electron-hole pair (CTE). The internal electric field in the cell reduces the barrier for electron-hole separation and separated bound carrier can again form localized exciton [101]. In polaron-pair recombination, if electron and hole pair is generated from one common precursor state, i.e. singlet exciton, the transition of the polaron pair to the ground state is called geminate recombination, and is a monomolecular or first-order decay [102].

c) *Non-geminate recombination of the charge-transfer exciton* – there is a high probability that a free electron and a free hole will meet at the interface and recombine as a charge-transfer exciton, with each carrier on an either side of the interface. The difference in recombination kinetics arises because the geminate pair originates from one initial exciton and the non-geminate pair originates from two different excitons. This is a *bimolecular* mechanism [103].

d) *Recombination through interface states in the middle of the interface gap* – the defect or impurity states at the D-A interface can trap electrons and holes, and hence allow recombination. The states are in a narrow energy band or broadly distributed across the gap. The recombination adopts a monomolecular kinetics, provided that the density of states is larger than the density of carriers. In a general way, trap-assisted recombination involves trapping of one type of carrier at defect states within a donor or acceptor phase and its subsequent recombination with free carriers present at different phase. This trap-assisted recombination rate follow Shockley-Read-Hall (SRH) mechanism at low light intensity [104, 105]. The trap assisted Shockley-Read-Hall (SRH) recombination mechanism in BHJ at ultralow optical intensity is defined as

$$R_{SRH} = \frac{C_n C_p N_t (np - n_i^2)}{C_n (n + n_i) + C_p (p + n_i)} \tag{1.22}$$

where C_n and C_p are the capture coefficients of electrons and holes respectively, N_t the density of traps, n and p the electron density at the LUMO and hole density at the HOMO [106-108].

e) *Reverse diffusive recombination at the contacts* – free carriers can diffuse against the internal field, and therefore could recombine at the metal contacts. This mechanism plays a significant role when the carriers are created very close to the contact as the diffusion length exceeds the drift length for these carriers [9].

However, in BHJ organic solar cell, carriers created near the heterojunction and diffusive recombination at the interface is mainly dominated by trap-assisted non-geminate bimolecular recombination [109, 110]. Experimentally, non-linear recombination rate is evaluated from the illumination light intensity dependent V_{OC}, J_{SC} and fill factor [111-114] and it reveals that the order of the decay is not constant at a value of 2 but varies between the 2.5 to 3.5, depending on the processing conditions. Thus experimentally found recombination dynamic follows:

$$R_{Experiment} \propto \bar{n}^{2-3.5} = (np - n_i^2)^{2-3.5}/_2 \tag{1.23}$$

These non-linear exponents mainly originate from influence of the dynamic trapping in the tail state *i.e.* trap-assist recombination [115].

1.5.5 Carrier transport in BHJ-PSC

Microscopic current density (*J*) in OPVs is composed of a drift and a diffusion component-

$$\vec{J}_i = q\mu_i n_i \vec{E} + qD_i \vec{\nabla} n_i \tag{1.24}$$

where μ is the carrier mobility, *n* the carrier density, *E* the applied electric field, *D* the diffusion coefficient and *i* indicates negative (*e*) or positive (*h*) charge carrier [114]. The charge carrier dynamics in BHJ is given by the continuity equation,

$$\frac{dn}{dt} = -\frac{1}{q}\frac{dj_n}{dx} + G - R \tag{1.25}$$

where, *G* and R represent optical generation and recombination rate respectively. Similarly, continuity equation for polaron pair in BHJ solar cells can be represented as[105]

$$\frac{\overline{pp}}{dt} = G_{\overline{pp}} - k_{PPr}\overline{pp} - \underbrace{k_{PPd}\overline{pp}}_{G} + R \tag{1.26}$$

where $G_{\overline{pp}}$ is the polaron pair generation rate (singlet generation rate) and R the recombination of free carriers which leads to the generation of polaron pairs. Under steady-state conditions $\frac{\overline{pp}}{dt} \rightarrow 0$, the continuity equations (1.25 and 1.26) lead to

$$\frac{dn}{dt} = -\frac{1}{q}\frac{dj_n}{dx} + \eta_{PPd}G_{\overline{pp}} - (1 - \eta_{PPd})R \tag{1.27}$$

The factor (1-η_{PPd}) can be interpreted as free electron and hole recombination in a blend system which creates a bound electron-hole pair as a reverse process.

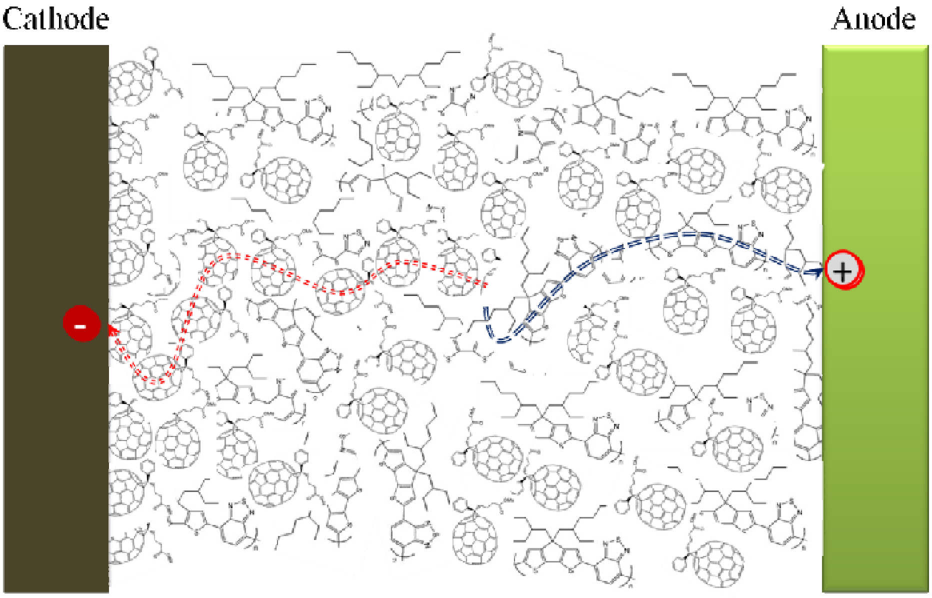

Figure 1.9: Schematic of electron and hole percolation paths in a bulk heterojunction solar cell.

At working condition, net diffusion current in BHJ solar cells dominates over drift component and amplitude depends on the random distribution of D-A phases [116]. The diffusion current gets modified depending on the donor or acceptor domain connectivity which often contains dead-ends or percolating pathways for each components to the respective electrodes [117].

1.5.5.1. Percolation model

Interpenetrating phase separated D-A network composites, i.e. bulk heterojunction appear to be ideal the photovoltaic composite. Simultaneously a bicontinuous network is required to enhance the carrier collection efficiency of the electrode. Schematic (Figure 1.9) shows the onset of percolation transport in polymer-fullerene BHJ cell. Carrier transport in the BHJ film depends on the properties of individual component, but recombination and trapping at phase separated components drastically influence the carrier lifetime. Carrier transport by thermally assisted hopping transitions between the spatially separated sites in an interpenetrating network can be inferred from the percolation theory [42, 45, 118, 119]. According to the classical percolation model, the conductance between the sites m and n is given by

$$Z_{mn}^{-1} = Z_0^{-1} exp\left(-2\alpha\left|\vec{R}_m - \vec{R}_n\right|\right) \times exp\left(-\frac{|E_m - E_F| + |E_n - E_F| + |E_n - E_m|}{kT}\right) \tag{1.28}$$

Here, Z_0 is a prefactor, α the Bohr radius of the localized wave functions, R_m denotes the position of the m^{th} site and E_m the energy of the carriers at site m. The first part of the equation 1.28 represents tunneling term and the second one is the thermal activation term ~ Boltzmann term.

According to the percolation theory, the average conductivity of each component in BHJ film can be expressed as $\sigma = \frac{1}{l} Z_c^{-1}$. Here, l is the characteristic length scale depending on the network-connectivity between the domains, while Z_c represents lowest average resistance. The efficiency enhancement at certain fullerene concentration can be attributed to the enhancement the percolation connectivity in two ways: Firstly, the higher acceptor concentration decreases l, and secondly, new paths with a lower resistance Z_c are formed.

1.5.6 Charge extraction

After successfully surviving in exciton dissociation and polaron pair separation, free charge carriers, which have been transported to their respective electrodes avoiding recombination, can finally be extracted. Charge extraction at the electrode involves surface recombination, carrier transfer rate from photovoltaic bulk to the electrodes and directly modify solar cell *J-V* characteristic [120]. Charge extraction at metal electrodes sometimes gets modified by the dipoles present at the metal-polymer interface, which is reflected as *S*-shape current density-voltage characteristic.

1.5.7 Open circuit voltage (V_{OC}) in BHJ-PSC

Open circuit voltage is an important factor in understanding process and performance optimization of organic photovoltaic devices [121]. In bulk heterojunction devices, V_{OC} is mainly governed by effective energy gap $E_{g,\,DA}$ ($\leq E_{donor}^{HOMO} - E_{acceptor}^{LUMO}$). A fine intermixing blend shows a flatter potential distribution, and a weaker band bending at D-A interface, which leads to an enhancement in the open circuit voltage. Theoretically V_{OC} is determined by energy difference of the quasi-Fermi levels at zero net current flow. So the energy of the polaron pair or charge transfer state (CTC) is the maximum possible V_{OC} that can be obtained from a device [122]. Moreover, the quasi-Fermi levels are influenced by the injection barrier at the anode ($\Delta\Phi_A$) and cathode ($\Delta\Phi_B$). The influences can be summarized as

$$V_{OC} = \frac{E_{g,DA}}{q} + BB_A + BB_D - \Delta\Phi_A - \Delta\Phi_D \tag{1.29}$$

where BB_A and BB_D correspond to the band bending at the donor and acceptor layers (Figure 1.10).

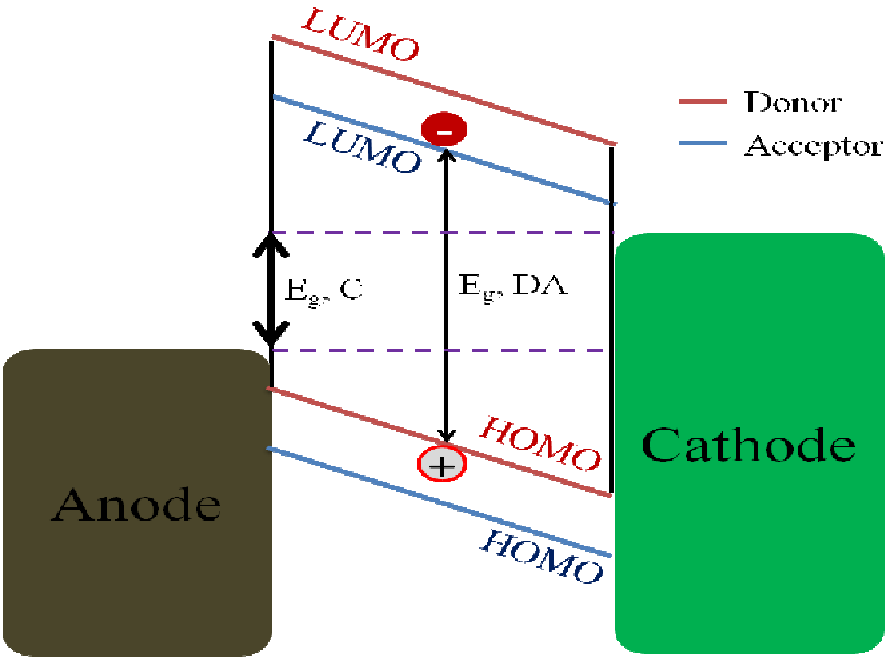

Figure 1.10: Schematic of the BHJ solar cells open circuit voltage.

Calculation by *Cheyns et al.* accounting to the injection mechanism, demonstrated that the band bending cancels the effect of the injection barriers and V_{OC} can be expressed as [123] –

$$V_{OC,Cheyns} = \frac{E_{g,DA}}{q} - \frac{kT}{q} ln\left(\frac{N_D N_A}{pn}\right) - \frac{1}{e}\varepsilon_L \tag{1.30}$$

Here N_D and N_A is the donor and acceptor effective density of states, p, n are the hole and electron, concentration respectively. The third term represents the sum of all additional free-energy losses during carrier transport [124]. A series of studies were carried out by *Brabec et. al* and *Gadisa et. al.* on different polymers in combination with fullerene acceptor in order to conclude the influence of effective bandgap on V_{OC} [125, 126]. These studies depict almost a linear correlation of V_{OC} with D-A effective bandgap. Accounting carrier continuity equation (equation 1.27), *Koster et al.* [127] presented a description of V_{OC} derived from the quasi-Fermi level difference as

$$V_{OC} = \frac{E_{g,DA}}{q} - \frac{kT}{q} ln\left(\frac{(1-\eta_{PPd})\gamma N_{DOS}^{2}}{\eta_{PPd} G}\right) - \frac{1}{e}\varepsilon_{L} \qquad (1.31)$$

Here, η_{PPd} is the probability of exciton dissociation to free charge, G the exciton generation rate, γ the Langevin recombination rate, and N_{DOS} represent effective density of state. Investigations show that the effect of injection barriers can be neglected for a wide range of cathode metals on donor polymer-fullerene cells [128]. So for a specific cathode-anode combination, the maximum V_{OC} is mainly determined by the effective bandgap of the D-A blend [124].

Fourier transforms PC spectroscopy measurements by *Vandewal et al.* provide more insight into the origin of effective bandgap dependent V_{OC} [128]. It was demonstrated that polaron pair energy depends directly on the D-A properties and blend morphology [129], and the effective bandgap reduces to 0.3 eV below the corresponding $HOMO_D - LUMO_A$ energy. Also, the quasi-Fermi level splitting corresponding to the V_{OC} turns out to be about 0.4 to 0.5 eV below the effective bandgap [96]. This discrepancy is assigned to the band-banding at D-A interface due to the carrier diffusion, energetic disorder and the energy required for polaron pair dissociation. The determined experimental V_{OC} is given as

$$V_{OC} = {}^{1}/_{q}\,(HOMO_{D} - LUMO_{A}) - 0.43\ V \qquad (1.32)$$

In order to optimize V_{OC}, the difference between the polaron pair energy and V_{OC} should be reduced. It should be insured that energy levels are still suitable for efficient exciton dissociation without electron back transfer, which yields efficient PC generation [59, 130]. Simultaneously, charge carrier recombination will have to be minimized in order extract the maximum possible V_{OC}.

1.5.7.1 Intensity dependent V_{OC}

Open circuit voltage dependence on the incident light intensity is found to be a useful parameter to quantify the recombination order in the polymer BHJ solar cells. Recent studies reveal that not only the energy level difference of D-A or photogenerated carrier concentration but also the available density of states (N_{DOS}) have a significant contribution to V_{OC}. Earlier, light intensity dependent V_{OC} in BHJ cells was mainly attributed to the 2nd term in the V_{OC} expression (equation 1.31) which is related to the quasi-Fermi level in the polymer and fullerene domains [60]. Bimolecular recombinations are found to be most dominant recombination mechanism for a large number of well optimized devices [125, 131]. But direct evaluation of trap-assist recombination on V_{OC} can be made by utilizing same equation. At solar cell operating condition (1.5 Sun) trap-assisted interfacial recombination also aggravates by the enhancement of trap occupied carriers. Devices made of different donor polymers in combination with fullerene acceptor reveal that intensity dependent V_{OC} is largely correlated to the disorder present in the donor polymer. The presence of hole trap levels above the HOMO of the disordered amorphous polymer depict more significant dependency of open circuit voltage on background light intensity compared to more crystalline donor polymer [121]. It is also observed, for fast grown polymer-fullerene device which accumulates large trap carrier density at interface, that trap-assist recombination dominates over Langevin recombination at 1.5 Sun [104]. However, the rate of trap-assist recombination should be quantified to determine its actual role in device performance.

1.5.8 Field dependence characteristics

In BHJ solar cells, the field dependent behavior of PC originates from the polaron pair dissociation and charge extraction process. *Michiletchi et al.* [132] first described the experimental PC of a BHJ cell as a combination of polaron pair dissociation (Braun-Onsager model) and polaron diffusion based on *Sokel-Hughes* model [133]. According to this model, neglecting trap states and recombination at the metal-organic interface and assuming a constant voltage drop across the device, PC for a simple BHJ structure is given as

$$J_{ph} = J_{ph,max}\left(\frac{exp(qV/kT)+1}{exp(qV/kT)-1} - \frac{2kT}{q}\right) \tag{1.33}$$

where $J_{ph,max} = qG(E,T)L$, denotes the maximum PC, G is field and temperature dependent carrier generation rate, L the device thickness and V the internal voltage. The exact shape as strong voltage dependent nature of PC in bulk heterojunction cells is reconstructed by considering the polaron pair dissociation and charge extraction as

$$J_{ph} = q\underbrace{\eta_{PPd}(E)G_{\overline{pp}}}_{G}L_{eff}\left(\frac{exp(qV/kT)+1}{exp(qV/kT)-1}-\frac{2kT}{q}\right) \qquad (1.34)$$

Here $\eta_{PPd}(E)$ is the polaron pair dissociation yield and $G_{\overline{pp}}$ is the polaron pair generation rate with effective device thickness L_{eff} as $E = V/L_{eff}$. [134] L_{eff} approximates the influence of the inhomogeneous voltage drop across the device, particularly close to the electrode. In a BHJ solar cell, irrespective of applied voltage, the work function difference of the two metal contacts yield another voltage V_0 in the device. At large forward bias, the liner dependence of J_{ph} is explained in *Sokel-Hughes* model by reducing equation 1.34 to $J_{ph} = q\eta_{PPd}(E)G_{\overline{pp}}L_{eff}$. Difference in electron and hole mobility develops an unbalanced carrier transport and subsequent space charge limited PC (SCL) at high intensity [135-137]. At moderate bias, recombination losses dominate and the extraction of photogenerated carriers are governed by the mean carrier drift width w, which is the mean distance that a carrier can travel before recombination to occurs. When w_n and w_h are large compared to the active layer thickness, charge carriers readily flow out without distorting the field in the device. However, in the case of w_p or $w_n < L_{eff}$, a space charge accumulates near the electrode as shown in the Figure 1.11d. Near the anode, the hole concentration dominates which results in a large space charge effect and ensuant a large voltage drop (Figure 1.11d, region 1). A neutral regime exists at intermitted position where electron and hole density are balanced (Figure 1.11d, region 2). Near the cathode, the electron density is much larger than the hole density (Figure 1.11d, region 3). At the space charge limited regime, PC is described by the relation -

$$J_{ph} \leq (qG)^{0.75}\left(\frac{9}{8}\varepsilon_r\epsilon_0\mu_h\right)^{0.25}\sqrt{V} \qquad (1.35)$$

Thus the space charge limited PC is characterized by a root square dependence on voltage and three quarter dependence on incident light intensity I ($I^{0.75}$). Since the space-charge limited PC is independent of device thickness, the transition from a non space-charge limited to a space-charge limited response can be experimentally verified by varying active layer thickness [135]. Considering a constant generation rate G throughout the active layer, two regimes in the J_{ph} - ($V_{OC} - V$) plot could be identified; one regime where drift and diffusion currents compete and PC varies linearly with voltage and the second regime where PC saturates (Figure 1.11a and c) [5].

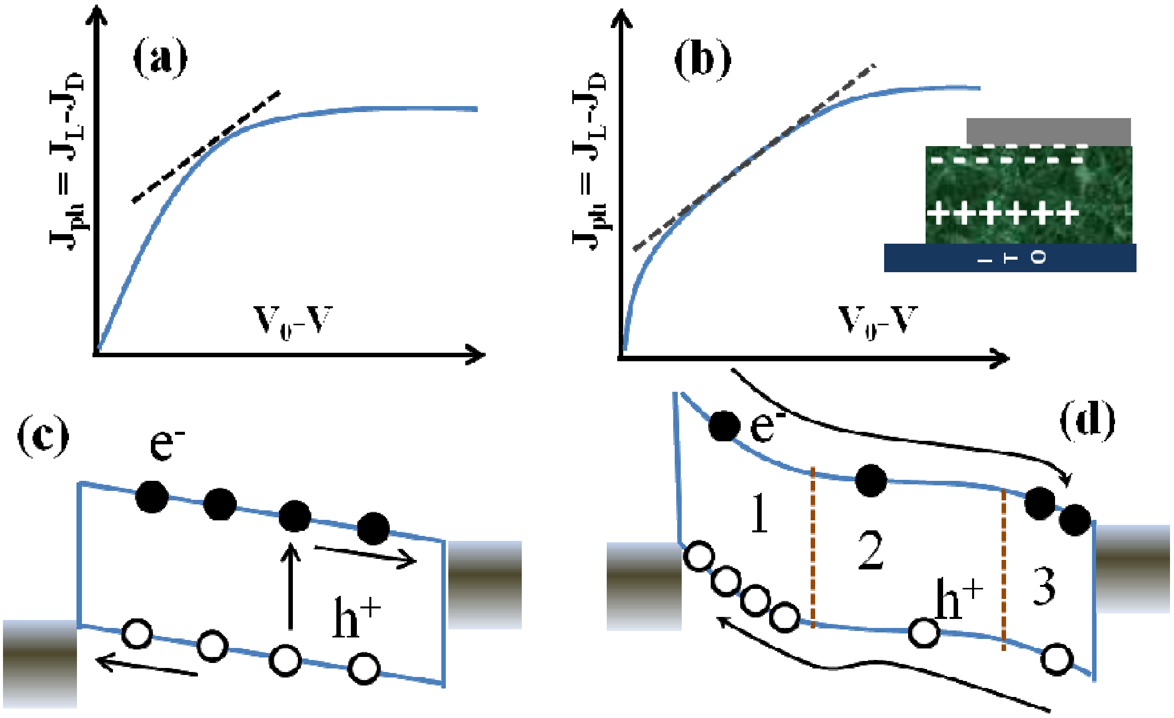

Figure 1.11: Schematic of PC versus voltage drop across the active layer for a device without (a) and with (b) space charge limitation. (c, d) Band diagram of BHJ solar cells for balances transport and space charge limited transport.

1.6 Materials and Architecture for BHJ-OPV

Polymer-polymer bulk heterojunction for organic photovoltaics were first described for poly[2-methoxy-5-(2-ethyl-hexyloxy)-1,4-phenylene-vinylene] (MEH-PPV) and cyano(poly-phenylene vinylene) (CN-PPV) as donor and acceptor respectively [138]. For farther improvement on device efficiency, significant developments are required in open circuit voltage, short circuit current as well as in fill factor, which can also be possible by improving active polymer semiconductor properties [55]. An ideal bulk heterojunction active layer should absorb majority of the light in the solar spectrum down to the around 950 nm or 1.3 eV. The maximum V_{OC} of the cell should be about 1.0 V with an assumption of 0.3-0.4 V driving force for charge separation. Donor material HOMO level should be lower than – 5.2 eV to avoid air oxidation and facilitate material handling and device assembly [5]. New potential materials, which have been used extensively in this work for BHJ device fabrication and device architecture utilized to optimize polymer BHJ performance are discussed in the following sections.

1.6.1 Donor materials

Structural optimization of the polymeric semiconductor like low-bandgap copolymers represent a promising way to increase the power conversion efficiency of organic bulk heterojunction solar cells (BHJ) [18, 139]. Alternate D-A units across the monomer results in an intrachain coupling between the electrons donating and accepting units and finally lower the band gap. This small bandgap is desired for increasing the conductivity and light absorption up to a near IR wavelength (~1200 nm) [140].

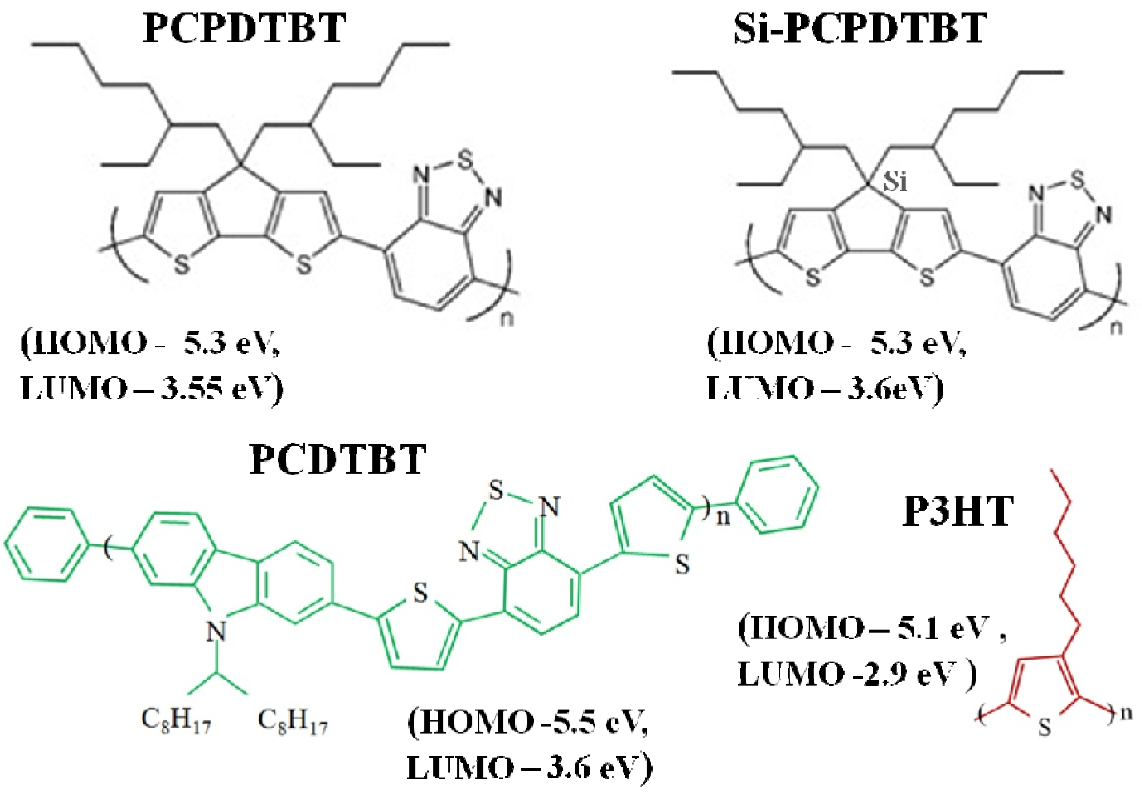

Figure 1.12: Chemical structure of different donor polymers and corresponding HOMO-LUMO levels.

For good power conversion efficiency, donor polymer absorption should have good coverage of the solar spectrum. One important class of such low band gap donor polymers consist of electron deficient heterocycles like benzothiadiazole (BT) or pyrazine (PQ) covalently attached to the electron rich moieties (thiophene) at both side [140]. The most well known class of alternative copolymer donors are based on the poly (2, 7-carbazole) such as poly [[9-(1-octylnonyl)-9H-carbazole-2,7-diyl]-2,5-thiophenediyl-2,1,3-benzothiadiazole-4,7-diyl-2,5-thiophenediyl] (PCDTBT) [141]. It exhibits almost 100% internal quantum yield when blended with $PC_{71}BM$ in bulk heterojunction geometry [142].

The other class of donor copolymer is based on the cyclopentadithiophene compound and used as a low band gap donor in tandem solar cells [143, 144]. Copolymer of this class Poly[2,1,3-benzothiadiazole-4,7-diyl[4,4-bis(2-ethylhexyl)-4H-cyclopenta[2,1-b:3,4-b']dithiophene-2,6-diyl]] (PCPDTBT) shows a promising improvement in terms of the device efficiency [145-147]. The upper limit of efficiency for these low bandgap polymers is, in principal, slightly higher due to their low refractive index and enhanced absorption in the red part of the spectrum as predicted after Shockley-Queisser limit [148]. The main drawback of these donor polymers is large exciton binding energy due to their low dielectric constant (~ 3). Replacing bridging carbon atom by silicon atom introduces a small distortion in the cyclopenta-di-thiophene unit and enhances the dielectric constant, backbone rigidity and overall crystallinity of the donor domain [147, 149]. Power conversion efficiency is improved to 5% following the influence of bridge atom in low band gap materials. The longer C-Si bond modifies the geometry of fused dithiophene which assists in better ordering of the polymer chains. The strong stacking of the Si-bridge materials leads to the limitation in solubility in common organic solvent and can be processed only at elevated temperatures. The high degree of π-delocalization in Si-bridge polymer yields large carrier mobility (2×10^{-2} cm^2/Vs). In this regards, a chain of Si-substituted low band gap materials were synthesized over last five years [150]. Poly[(4,4′-bis(2-ethylhexyl)dithieno[3,2-b:2′,3′-d]silole)-2,6-diyl-alt-(2,1,3-benzothiadiazole)-4,7-diyl] (PSBTBT)[151]; Poly[2,1,3-benzothiadiazole-4,7-diyl-2,5-thiophenediyl(9,9-dioctyl-9H-9-silafluorene-2,7-diyl)-2,5-thiophenediyl] (PSiFDTBT); poly[(4,40-bis(2-ethylhexyl)dithieno[3,2-b:20,30-d]silole)-2,6-diylalt-(2,1,3-benzothiadiazole)-4,7-diyl] (PSiPDTBT) [152] are some of the promising Si-substitutes low band gap materials for high efficient photovoltaic applications.

1.6.2 Acceptor materials

Fullerene and its derivatives have been adopted widely as n-type semiconductors in solution process bulk heterojunction organic photovoltaic [55]. The most well known fullerene derivative is phenyl-C_{61}-butyric acid methyl ester or $PC_{60}BM$ (Figure 1.13). The key parameters that determine device performance are solubility of n-type fullerene acceptor in organic solvent, electron mobility, LUMO levels and film morphology (reducing crystalline phase separation). Very recently, non-fullerene, air stable, electron accepting small molecule acceptor [2-({7-(9,9-di-n-propyl-9H-fluoren-2-ylbenzo}[c] [1,2,5] thiadiazol-4-yl) methylene]malononitrile (K12) and P(NDI2OD-T2)/(N2200) was synthesized with a power conversion efficiency about 1-2% with P3HT as donor [153-156].

Simple design, solution processable, possessing large electron mobility demonstrated the potentiality of whole class of non-fullerene electron acceptors.

Fullerene and most of its derivatives exhibit sub-picosecond forward photoinduced electron transfer in combination with various conjugated polymers [100]. The exciton diffusion length in pure C_{60} has been estimated to be of the order of 40 nm with electron mobility up to 6 $cm^2V^{-1}s^{-1}$ [157]. The isotropic (C_{60}) electron accepting nature of fullerene derivatives has a positive implication in D^+-A^- pair dissociation and charge transport across the grain boundaries. Fullerene derivatives have adequate LUMO (-3.7 eV) w.r.t most conjugated polymer (donor) LUMO levels for efficient photoinduced electron transfer. Further, the HOMO levels of C_{60} (- 6.1 eV) is low enough to avoid possible back energy transfer between donor and acceptor. Delocalization of π electrons in fullerene structure results in high polarizability and large dielectric constant (ε_r = 4.4), which allow the intimate D^+-A^- formation upon exciton dissociation and stabilizes it at the D-A interface [158], [159, 160]. Low optical absorption of C_{60} and its derivatives at visible range is one of the major drawbacks in increasing device efficiency.

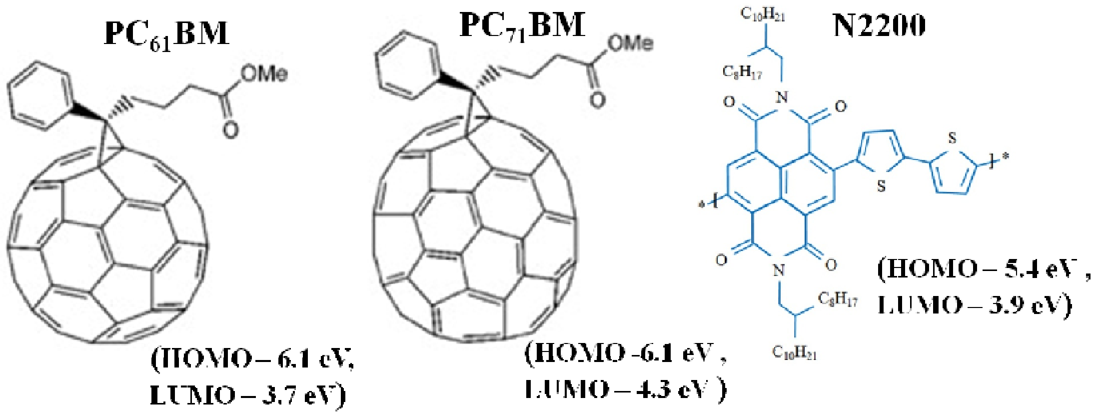

Figure 1.13: Chemical structure of different acceptor materials and relative position of their HOMO-LUMO levels.

The most effective development with respect to increasing optical absorption has been based on higher fullerene (C_{70} and C_{84}). $PC_{70}BM$ had shown substantial improvement in device performance when blended with MDMO:PPV and P3HT; but a extensive improvement was reported with low bandgap p-type polymer materials [19, 148]. With the increasing size of fullerene cage, the solubility of the big sized fullerene derivative becomes lower, and the miscibility of the methano-fullerenes with donor polymer clearly diminishes from polymer -$PC_{60}BM$ or $PC_{70}BM$ solution.

1.6.3 Additive materials

The device function of polymer BHJ solar cell arises from charge separation at discrete interfaces between phase-separated materials and subsequent charge transport [161]. Recently, improvement in device efficiency from 2.5% to 5.5% for P3HT and newly synthesized low band-gap polymers are observed in addition of alkane-dithiols into the solvent [162, 163]. Alkane-dithiols (boiling point~ 250°C) do not react with either the polymer or fullerene, and function as processing additives. In-situ measurements (FTIR, XPS and Raman Spectroscopy) demonstrate that alkane-dithiol is removed during thermal annealed process under high vacuum [139, 164]. Small acceptor molecules such as $PC_{60}BM$ and $PC_{71}BM$ readily dissolve in alkane-dithiols, but conjugated semiconducting polymers are not soluble in alkane-dithiols. This selective (differential) solubility of the fullerene components and higher boiling points than host solvent demonstrate the utility of this class of processing additives to control the morphology of the BHJ film used in solar cells. Various processing additives like 1, 8-di(R)octanes with various functional group (R = Cl, Br, I) have been investigated to improve the solar cell performances [162, 165]. Comparing these device performances, it was concluded that 1,8-di-iodooctane yield larger improvement in BHJ device efficiency. As fullerenes are selectively dissolved in 1,8-di-iodooctans, three distinct separated phases are formed during the process of liquid-liquid phase separation. A fullerene-alkanedithiols phase, a polymer segregated phase and polymer-fullerene phase are observed under high resolution TEM measurements [164]. Due to the higher boiling point of Alkane-dithiols as compared the host solvent, $PC_{60}BM$ tends to remain in solution (during thermal annealing process) longer than the donor polymer. This enables more control on phase separation and results in more optimized BHJ morphology for solar cells.

Efficiency of $P3HT:PC_{60}BM$ devices also improve when long alkyl chain surfactants such as poly(oxyethylene tridecal ether) (PET) are used as additive materials [166]. This improvement is mainly attributed to the increase in dissociation efficiency of *e-h* pairs, due to the orientated PET surfactant molecules at the interface between the phase-separated domains. These observations suggest that PET is a promising additive material for efficient polymer solar cells.

1.6.4 Metal contacts

To extract more photogenerated carriers from bulk active martial, low work function metals like Al (W_F=4.3 eV), or Ca (W_F=2.9 eV) are used as cathode (~ LUMO level of the acceptor) and high work function metals are used as anode (~ HOMO level of donor). A thin layer (5-10 nm) of titanium oxide (TiO_2) or LiF improves electron collection at the polymer/Al interface and works as hole blocking layer too [167], [168]. In case of inverted structure, a thin nano-structured oxide layer (ZnO, TiO_2) is introduced between bottom ITO electrode and polymer for efficient electron collection [169]. These oxides act as hole blocking and electron conducting layer and improve the efficiency of inverted organic solar cells. Similarly, thin layer of molybdenum oxide (MoO_3) or vanadium pentoxide (V_2O_5) improves hole collection and reduces recombination at gold/silver electrode [170].

1.6.5 Conducting materials

A thin buffer layer of conducting polymer poly(3,4- ethylenedioxythiophene) : poly(4-styrenesulfonic acid) [PEDOT:PSS] improves hole collection between ITO and active polymer. PEDOT:PSS is a water soluble dispersion of colloidal particles containing PEDOT and PSS-Sodium. PSS is utilized as charge balancing dopant during polymerization of PEDOT to produce water soluble PEDOT:PSS [171]. The conductivity of PEDOT:PSS can be improved by selective doping and proper annealing conditions. The Ohmic nature of ITO/PEDOT:PSS film with the polymer HOMO level has been demonstrated by Electro-absorption measurements [172].

1.7 Morphology Characterization Tools

Morphology of the bulk heterojunction governs the charge separation and charge transport, and therefore decisively determines the performance of the solar cell. So, proper investigation of BHJ morphology is required, which connects different processing condition to morphology and ultimately the device efficiency. A combination of transmission electron microscopy (TEM) and AFM [173] provides the identification of a two-phase system consisting of fullerene-rich domains embedded in polymer matrix. A high resolution scanning electron microscopy combining planar and cross-sectional views help to investigate the three dimensional structure of the bulk film [174].

1.7.1 Transmission electron microscopy

One of the most common techniques for examining bulk heterojunction morphology is transmission electron microscopy imaging at lower operating voltages [175]. Spin-coated polymer-$PC_{60}BM$ blend films are first floated onto the surface of deionized water and finally picked up by copper mesh grids for TEM measurement. For drop-cast films, TEM specimens are obtained by putting a droplet of the blend solution onto a carbon film supported copper grid. Energy dose was chosen properly such that morphological change or the crystalline structures of the samples remain undisturbed. The stability of $PC_{60}BM$ crystals under electron beam illumination is much better compared to most polymer samples. Polymer rich domains appear as bright regions, since the electron scattering density of $PC_{60}BM$ is higher as compared to P3HT [87, 176]. The TEM images as obtained by Yang *et al.* and co-authors clearly demonstrate a morphology in which $PC_{60}BM$-rich domains were dispersed in a polymer-rich matrix [87]. TEM images of film cast from different solvents reveal that the size of the $PC_{60}BM$-rich domain in the blend film changes drastically with the choice of solvent. The average $PC_{60}BM$-rich domain size appears to be 600 nm in film cast from the toluene, which is 80 nm when prepared from chlorobenzene solution. On the other hand, a dramatically different morphology was observed in TEM imaging with thermal annealed samples of different $PC_{60}BM$ concentrations [16]. $PC_{60}BM$ clusters, formed upon annealing, is identified in TEM images as dark areas in a grey polymer:$PC_{60}BM$ matrix. The brighter areas initially surrounding the $PC_{60}BM$ clusters reflect thinner regions of the film, being composed of almost pure polymer domains (depleted from $PC_{60}BM$). TEM images of drop-cast film provide different information such as the kinetics of phase separation process getting modified in presence grid and confines the volume available to the phase separation [177]. As TEM imaging is not possible to carry out in a working device, it is very difficult to rationalize the strongly different performance of photovoltaic devices fabricated using different solvents or annealing conditions merely based on the mages.

1.7.2 Photo-conducting atomic force microscopy

Photo-conducting AFM (pc-AFM) measurement on BHJ device provides opportunity to measure the generated PC at each pixel with laser illumination that has been focused onto a diffraction-limited beam spot on the sample and co-aligned with the tip [178]. A direct correlation between the PC generations with film morphology can be possible with this measurement. Photo-conducting AFM measurement on MDMO-PPV:$PC_{60}BM$ blend demonstrates that PC predominantly originated at the D-A boundary and the amplitude varies locally depending upon the $PC_{60}BM$ aggregation [179]. In-situ pc-AFM measurements of P3HT:$PC_{60}BM$ BHJ device depict the PC evolution and its spatial variation with thermal annealing [180, 181]. Spatial distribution of short-circuit PC reveals that the maximum, average, and standard deviation of the PC all increase with thermal annealing time. The effect of the 3D morphology on carrier transport and recombination can be identified from these PC maps. Measurements of local V_{OC} using AFM tip as an electrode suggest that the unusual light intensity dependent V_{OC} for BHJ devices is directly related to the morphological heterogeneity, present in the blend film.

1.7.3 3D electron tomography

3D Electron tomography somehow relates the morphology-performance relationship in polymer photovoltaic cells by providing volume information in nanometer resolution [61, 182]. This technique is used to reconstruct the 3D structure of the blend film from a series of two dimensional TEM projections. In this process, a series of 2D projections is taken from TEM at different angles by tilting the specimen with respect to the electron beam line. The tilt series thus obtained contains normally more than 100 images of the same specimen spot. These images are then carefully aligned to reconstruct a 3D image of the specimen with nanometer resolution by back projection algorithms [61]. The outcome of electron tomography ("volume pixel") provides the specimen's volume morphological organization in detail [183]. Volume data demonstrate the presence of 3D nanoscale networks of the P3HT nano-fibers and $PC_{60}BM$ domains, and indicates the inclination toward the crystalline P3HT nano-fibers. The reconstructed volume cross-section confirms the presence of genuine 3D rather than 2D networks in bulk film, which yields excellent hole transport from any place within the photoactive layer to the hole collecting electrode and vice versa [184, 185]. Imaging with different density values of P3HT and $PC_{60}BM$ demonstrate the modified 3D profile of photoactive layer. 3D topography analyses for the 100 nm thin film depict that 35% of the layer volume is actually made up of crystalline P3HT nanofibers. It indicates a high crystalline arrangement (60%) for the P3HT [186]. Upon annealing treatment, the formation of nano-scale interpenetrating networks of P3HT nanofibers and $PC_{60}BM$ nano-crystals with favorable gradients are observed within the thickness of the layer for thinner specimens [183, 185]. These changes in the 3D volume organization of the P3HT:$PC_{60}BM$ photoactive layer are paramount for obtaining high efficient PSCs. Recently Helium ion microscopy was utilized to image the nanostructure of P3HT:$PC_{60}BM$ in film following secondary quantum yield contrast [187].

1.7.4 Grazing incidence X-ray diffraction (GIXRD) analysis

Grazing Incident X-Ray Diffraction (GIXRD) provides detailed information about the crystallographic alignment of the individual domain in bulk heterojunction blend films [188, 189]. The technique utilizes x-ray incident on thin film below the critical angle such that only the evanescent component (which decays rapidly) gets diffracted from film surface (depth ~ 10-20 nm). The crystallization orientations (parallel or perpendicular to the substrate axis) of the model polymer (P3HT) is distinctly observed under this technique. These two orientations known as face-to and edge-to conformations as the π-π stacking direction is perpendicular and parallel to the substrate respectively [190]. While the edge-on stacking is desirable for the transistor geometry, the face-on orientation is preferable for OPV architecture where charge transport normal to the electrode is needed. In-situ GIXRD measurement of P3HT:$PC_{60}BM$ film depicts the role of $PC_{60}BM$ in P3HT crystallization and device optimization [131]. GIXRD data of annealed P3HT:$PC_{60}BM$ film cast from the higher boiling point solvent like dichlorobenzene have shown improved edge-on crystallinity in film [191]. The intercalation of $PC_{60}BM$ in thiophene-based polymer has been studied by GIXRD measurements following the lamellar spacing peaks in an edge-on crystal region. It has been shown that even at 1:1 blend ratio, devices could produce drastically different efficiencies depending on $PC_{60}BM$ intercalation in polymer matrix [192]. Therefore, the results obtained from GIXRD measurements are important for optimizing bulk heterojunction device.

1.8 Overview and Scope of Thesis

It is important to follow the heterogeneity of BHJ film at much smaller length scale (~ 40 – 100 nm). The challenges in experimentally probing these morphological and electronic structure of highly intermixed semiconducting polymer-small molecule blends, ultimately limit the fundamental understanding of the BHJ device performance. In this regard, near field scanning optical microscope (NSOM) is utilized to correlate local heterogeneity in morphology and local PC from microstructure with device performance for wide range of model BHJ systems.

In this thesis, Chapter 2 focuses on the fundamentals and selected applications of aperture NSOM to characterize BHJ morphology under different processing treatment and substrate modification. Near-field imaging was carried out by positioning a sub-micron optical probe over very short distances from the examined sample. The optical near-field is defined as the region above the surface of examined sample with dimensions less than a single wavelength of the light incident on it. Finite difference time domain analysis was employed to simulate the near field-BHJ film interactions which demonstrate the actual spatial resolution achieved in our measurements.

Chapter 3 involves with BHJ film morphological characterization technique to probe the phase separated polymer-fullerene domains in active solar cells devices. Spatial dependence of current-decay profiles vary with BHJ morphology and provide a nice route for optimization of constituent fraction ratio in BHJ films. Further, to study local short-circuit PC signal on a BHJ film layer, asymmetric device structure was fabricated with two cross type lateral electrode. The device structure was utilized to map out local PC and optical transmission variation following the carrier transport pathways. Advanced techniques such as 2-dimensional fast Fourier methods are demonstrated to determine the quasi-periodic distribution of domains. A simple circuit model employing spreading resistance analysis is developed to explain the peripheral PC decay in asymmetric device structure.

Evolution of Si-PCPDTBT:$PC_{71}BM$ blend morphology with different fraction ratio and post processing condition was established in Chapter 4 employing near field PC (NPC) and transmission contrast imaging (T-NSOM) method. The technique mainly relies on current-contrast-optical scanning microscopy on asymmetric device structures that provides a near-field access for the incident light beam. Correlations between the morphological changes with carrier generation and transport leadings to PC are clearly revealed from these images. Modifications in spatial power spectral density distribution as obtained from these images are used to quantify the evolution upon thermal annealing. The presence of local heterogeneity in PC is more informative as compared to the conventional measurement on bulk samples.

A combination of microscopic scanning method with trends in macroscopic spatially-dependent current decay profiles are discussed in Chapter 5. Variations in the spatial decay length and near field transmission contrast demonstrate nanoscale morphology dependent carrier transport for two different model blend systems with different underlying microstructures; crystalline network of Si-PCPDTBT and amorphous network of PCDTBT. The anisotropy in electron and hole decay length attributes the difference in the charge carrier mobilities in blend systems.

The contents in Chapter 6 constitute studies on systems which are not directly related to BHJ devices, but highlight the versatility of the instrumentation developed during the thesis period: single molecule spectroscopy, fluorescence nano-particle imaging and studies with biological protein system. Molecular based processes in variety of systems under near field illumination - far field collection mode operation are demonstrated and investigated. Fluorescence from single dye molecule encapsulated in host PMMA matrix and their time trace were monitored with ~ 60 nm spatial resolutions as obtained from NSOM. Intrachain energy transfer were studied by monitoring fluorescence form MEH-PPV polymer nano-particles. Nanoparticles prepared from the blend of high and low conjugated MEH-PPV were employed to study the energy transfer efficiency. The broad absorption of both the materials in visible range exhibits a new research field toward hybridized nanoparticle photovoltaic devices. Local temporal optical transmittance fluctuation through few layers bacteriorhodopsin film demonstrates the correlation effects between the trefoils in optically induced excitation and de-excitation processes (photo-cycle). Probability density functions analyses of transmission signal is obtained from different bacteriorhodopsin patch depict that for finite size ensemble a critical size regime exists which yields the characteristic stochastic feature. Local photoluminescence quenching of dye or conjugated polymer film coated on isolated few-layers graphene flakes was examined under near field scanning optical microscopy imaging methods. The decrease in emission intensity was accompanied by an increase in PC in the graphene-polymer bilayers. Spatial PC decay technique was employed to study potentiality of graphene as a transparent electrode.

Chapter 2

Near Field Scanning Optical Microscopy for Polymer Solar Cells

2.1 Introduction

Near Field Scanning Optical microscope (NSOM) has been developed to provide different optical contrast images with spatial resolution beyond the optical diffraction limit (~ 400 nm for visible light) [193, 194]. Resolution of any optical microscope is limited by the incident light wavelength and the numerical apertures of lens systems. Recent developments in scanning positioning microscopes and related techniques have enabled improvement in resolution, even to the level of visualizing individual atoms [195]. These super resolution capabilities are available with different contrast-enhancing mechanisms along with common optical microscope. But, the requirements of special specimen preparation for most of the high-resolution techniques limit their application in materials science and biological measurements.

The resolution of any optical microscope gets limited by the spatial frequencies leakage upon propagation from source to detector. This leaky nature imposed a boundary condition to spatial resolution (distinguish two-separate point like objects) for the entire optical microscopy technique. The central idea of near field scanning optical microscopy is to retain these spatial frequencies associated with the scattered near field light [196-199]. Near-field scanning optical microscopy is developed in combination with topographic resolution techniques with polarization characteristics in combination with local spectroscopic capabilities [197, 200, 201].

When incident light interacts with an object, it generates two different types of scatter light – near-field and far-field light components. The scattered far-field light propagates through space in an unconfined manner and is utilized in conventional microscopy. The near-field component consists of a non-propagating field that exists only very near the surface of an object at distances less than a single wavelength of light [202, 203]. Scattered near-field components contain high-spatial frequency information with maximum electric field amplitude in the region ≤ 20 nm [196]. As the near field amplitude decays sharply within a distance less than the wavelength of the light, in conventional optical microscope it usually goes undetected [197]. In NSOM technique, the higher spatial resolution was obtained by detecting and utilizing the near-field light before it undergoes diffraction [199]. Strong coupling between the NSOM probe and the sample yields a field enhancement in physical properties of the sample, which do not prevail in normal optical microscopy [204].

The most recent commercial NSOM instruments (MultiView4000 - Nanonics, alpha300S - Witec, XE-NSOM - Park Systems, etc) combine scanning force techniques with optical detection capabilities of conventional optical microscope [193, 205]. This combination provides near-field high-resolution in conjugation with various optical imaging modes [194]. The important advantage of NSOM technique is its ability to merge topographical data set with different optical data sets beyond the diffraction limited spatial resolution [206]. Imaging molecular and nanoscale features in photoactive conjugated polymer films is one of the great scientific challenges in recent years [207-209]. Recently direct PC mapping on organic solar cells was described utilizing near field scanning optical microscope where a NSOM probe of ~250 nm apertures was utilized to study 2D local PC amplitude variation in BHJ device. Topology and PC contrast was mapped by raster scanning of light output from NSOM probe through the semi-transparent electrode across the blend surface. The low device efficiency was then correlated to the presence of inhomogeneity and phase segregations in blend films [210-212]. These studies demonstrate the utility of the NSOM instrument to probe the BHJ bulk morphology at ~ 100 nm optical resolution. We improvise on the conventional NSOM scanning approach by introducing direct local PC mapping on BHJ-OPV films to optimize the BHJ device performance. The present chapter is focused on various studies, where conventional fluorescence NSOM scanning measurement was utilized, especially on the MEH-PPV copolymer films and P3HT-$PC_{60}BM$ blend films in preliminary manner.

2.2 Historical Background

Edward H. Synge, during early 1928, published a series of articles that first conceptualized the idea of an ultra-high resolution optical microscope. In a proposal, he suggested a new type of optical microscope to defeat diffraction limit that required fabrication of a 10-nm aperture (much smaller than the light wavelength) on an opaque screen [213, 214]. The proposal, although visionary and simple in concept, was far beyond the technical capabilities of that time.

E. A. Ash and G. Nicholls first demonstrated the near-field resolution from a sub-wavelength aperture scanning microscope utilizing microwave region of the electromagnetic spectrum [215]. In 1984, research groups from IBM Corporation's Zurich laboratory and Cornell University reported optical measurements at a sub-diffraction resolution level [216], [217-219]. With the development of shear-force feedback systems and employment of a multi-mode optical fiber as the NSOM probe, NSOM began to evolve as a scientifically useful instrument [205, 220].

2.3 The Aperture NSOM

Aperture NSOM, today is reaching a resolution of 50-100 nm on routine experiments and have a potential down to 10 - 30 nm [221]. It is at least a factor of 5 times better in spatial resolution than a standard scanning confocal optical microscope with oil immersed objectives (1.45 NA). The point-spread function (PSF) of a NSOM-aperture is defined as a Gaussian profile and optical output power through the aperture decays to *1/e* times of maximum power at the aperture end. The mode of field propagation is primarily evanescent and parallel to the specimen surface. In aperture NSOM technique, higher spatial resolution is achieved by positioning the probe tip on the examined surface within this near-field regime.

There are few fundamental differences between aperture-NSOM (Figure 2.1a) and conventional optical microscope (Figure 2.1b) – the size of the illuminated area, and the distance between the source of radiation and the specimen. In conventional far-field optical microscopy, the distance between the light source and the specimen is typically much greater than the wavelength of the incident light, whereas in aperture-NSOM, it is a necessary condition of the technique to place the nano-aperture very close to the specimen than the wavelength of the illuminating radiation.

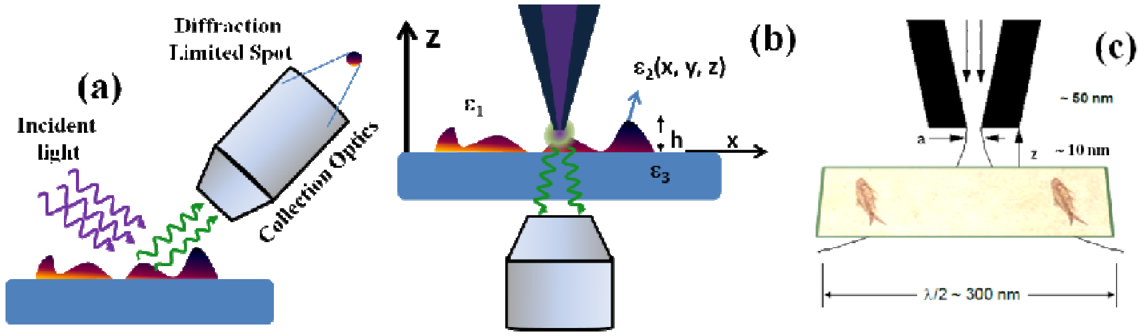

Figure 2.1: (a) Far field collection mode, (b) Near field illumination-far field collection mode, (c) Schematic aperture near field scanning optical microscope.

Imaging with NSOM is similar in procedure to the scanning confocal optical microscope except that the illumination spot is smaller. Scanning confocal microscope is successfully employed to the thick samples where optical sectioning is required, but NSOM is truly a surface sensitive technique. Nevertheless, all the optical contrast mechanisms such as absorption, fluorescence and phase, well-known in the standard optical imaging, are successfully transformed to the NSOM application.

2.3.1 X-Y-Z scanning and feedback methods

x-y-z piezo-scanning system is one of the most important components of all scanning probe microscope instrument. The design and functionality of scanning system primary depicts the attainable scan resolution from the instrument. Low noise (small position fluctuations) and precision positioning capability (typically less than 1 nm) are the prerequisite conditions for good scanning system [222].

The critical requirement of the near-field technique is that the probe tip must be positioned or held within ~ 10-20 nm vicinity of the surface in order to obtain high-resolution and artifact-free optical images. In most of the aperture NSOM instrument, tip-sample distance control is achieved by utilizing feedback mechanism. To date, the most commonly employed mechanisms of tip positioning are optical method that monitor the tip vibration amplitude. The method is usually followed laser reflection from tip to quartet position sensitive detector. In case of non-optical method feedback, share force amplitude is monitored utilizing quartz tuning fork.

In order to improve signal-to-noise ratios for the feedback signal, the NSOM tip is always oscillated at a fixed resonance frequency. This allows lock-in detection techniques (band pass filter with the central frequency set at the reference oscillation frequency) to be utilized, which eliminates positional detection problems associated with low-frequency noise and drift. As the oscillating tip approaches the specimen, forces between the tip and specimen dampen the tip oscillation amplitude.

In optical feedback method, a laser is tightly focused as close to the end of the NSOM probe. In the case of the bent probe method, the laser is reflected from the top surface of the probe to the split photodiode (similar to the optical feedback techniques employed in the AFM). The main problem associated with this type of feedback mechanism is that a light source (for example, a laser) is used to detect the tip vibration frequency, phase, and amplitude. This external light source becomes a potential source of stray photons that interferes with detection of the NSOM signal. In most cases, additional filter for feedback laser also block a small percentage of the near-field photons and reduces signal levels. A non-optical feedback such as tuning-fork technique reduces background noise issue in optical detection.

In tuning-fork feedback method, a single mode optical fiber is attached to one arm of a quartz crystal tuning fork, which is oscillated at the tuning fork's resonance frequency. The most common tuning fork resonance frequency is 32 kHz, but commercially, it varies with resonances ranging from 10 kilohertz to several tens of megahertz. The piezoelectric potential acquired from electrodes on the forks is amplified with a gain of approximately 100 (using an instrumentation amplifier) to produce a signal on the order of a few tens of mV. The signal is then fed into a lock-in amplifier and referenced to the drive signal of the oscillating tuning fork. Different output signals such as amplitude and phase are then compared to a user-specified reference to maintain the probe-specimen distance.

An example resonance curve produced by a *35.51*-kHz tuning fork with the attached NSOM fibre is illustrated in Figure 2.2. The fork response is measured by sweeping the frequency from 34 kHz to 40 kHz and simultaneously measuring the amplitude and phase of the signal. The advantages for the tuning-fork feedback are 1) improvement of spacial resolution without any optical background noise, 2) simultaneous topographic imaging, 3) presence of a rapidly varying evanescent electric field normal to the substrate surface. There are some limitations of aperture-NSOM microscope, like: (*i*) small working distance and an extremely low depth of field and (*ii*) long waiting time for high resolution images or large specimen areas.

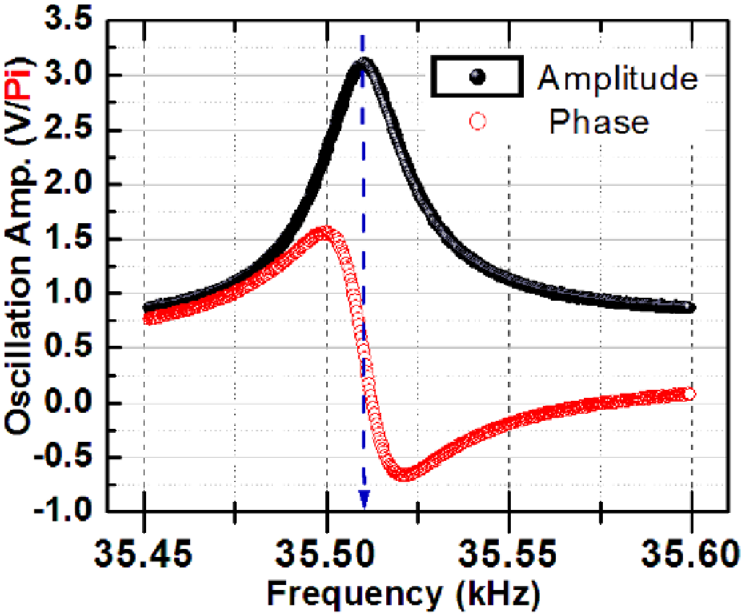

Figure 2.2: Amplitude and phase signal from the turning fork with the resonance oscillation frequency at 35.51 kHz.

2.4 Transmission Coefficient of NSOM Probes

The ultimate performance from aperture NSOM probe is achieved by combining two main properties: a) reducing illumination spot size (achieved by lowering aperture diameter) and b) increasing optical output power through the aperture. These are accomplished either by optimizing the overall light throughput or by improving the damage threshold of the metal coating, thus increasing the maximum input power [223].

2.4.1 The Taper region and aperture

Probes based on metal coated dielectrics with a transparent spot at the apex are referred to as aperture probes. The metal coating prevents the leakage of optical field through the side of the probes. Transmission coefficient of an aperture probe is defined as the ratio of the light power coupled at the tapered region to the light power emitted at the end of aperture. The power emitted by the aperture is generally measured by the far-field optical collection which does not reflect the near-field enhancement. The non-propagating electric field or evanescent waves at the apex of aperture-NSOM probe contribute to a time averaged *Poynting vector* and dominates the light-mater interaction. The transmission coefficient of any NSOM probes is characterized by its' structural components, a) wave-guiding in the vicinity of the aperture and b) the actual sub-wavelength aperture [224].

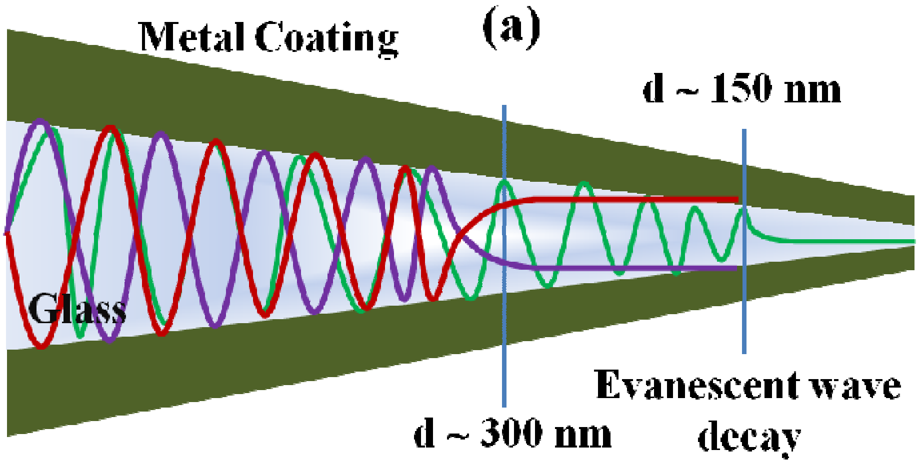

Figure 2.3: Cartoon of the successive cut-off of guided modes and exponential decay of field towards the aperture.

In a standard glass fibre NSOM probe, the guiding part corresponds to the tapered, conical shaped, metal coated dielectric wave guide. The efficiency of light guiding to the aperture is determined by the propagating modes distribution in the tapered region. This mode structure of metallic wave-guide at optical frequencies was first proposed by Novotny and Hafner as a function of dielectric core diameter [225]. In a tapered wave-guide with gradual decreasing of core diameter, different guiding modes disappear and finally only HE_{11} mode (fundamental mode of optical fibre) propagates through the wave guide. Aluminium-coated dielectric wave-guide supports the pure HE_{11} mode at a wavelength (λ = 488) nm for inner diameter between ≈ 250 nm and 160 nm [196]. Numerically, the transmission coefficient of the light up to this point was determined by the fraction of optical power contained in the cut-off modes as compared to the power in the still propagating HE_{11} mode [226]. The magnitude of this fraction depends on the geometry of the taper region (chemical etching or heating and pulling method). The leaky optical power is absorbed by the metal coating, leading to considerable heating of the NSOM probe.

Below the inner diameter of 150 nm, a HE_{11} mode runs into the cut-off mode with imaginary wave vector and thus mode field decays exponentially. Studies from Novotny et al. revealed that the optical power that is actually delivered to the aperture is depends on the distance between the HE_{11} cut-off diameter and the aperture plane [196]. Larger cone angle drastically reduces the distance between cut-off diameter and aperture plane (Chemically etched NSOM probe) and improves the overall transmission coefficient of the taper waveguide structure [221].

The transmission coefficient of a subwavelength hole in an infinitely thin conducting plate was first numerically calculated by Bethe, and the correction for the near field effect was mentioned by Bouwkamp. Bethe/Bouwkamp model of a subwavelength aperture yields an analytical expression for transmitted electric and magnetic field. According to the model, the transmission coefficient of subwavelength aperture is scaled as $(a/\lambda)^4$, where a represents the aperture diameter [227, 228]. More rigorous solution of Maxwell's equations employing multiple-multipoles method reveals that transmission coefficient of NSOM probes largely depends on the tapering cone angle. As the half-cone angle (δ) of taper part increases, the light spot size decreases and light leaks through the edge of the aperture. Light spot size remains almost constant for large range of δ but increases rapidly for $\delta >$ 50°. A strong variation on power transmission is observed in the range between the 10° and 30°. The analytical solution for the power transmission leads to

$$\frac{P_{out}}{P_{in}} \propto e^{-A\,cot\delta} \tag{2.1}$$

where parameter A depends on the dielectric core and metal coating on the NSOM probe. Optical power output enhances by nine orders of magnitude by changing the taper angle from 10° to 45°, as the light spot is maintained at constant size [196]. This behaviour defines the limitations of aperture probes fabrication method. With larger taper angle and refractive index of the dielectric core, the cutoff diameter approaches the probe apex and provides better light transmission through the probe. At the cutoff region, optical energy is partly reduces in the metal layer. This generates a significant heat at the metal coating which can destroy the glass tip. The distortion threshold of NSOM probe can be improved by larger heat dissipation rate from relevant region and higher thermal stability of the metal coating.

2.5 Electric Field Distribution

Electromagnetic field distribution close to the subwavelength size aperture assists in understanding light-mater interactions. Various methods are available for determining the electromagnetic field distribution near to the NSOM probe aperture. Most common method is the numerical solution of Maxwell's equations under selective boundary conditions; the rest are straight forward experimental methods by directly monitoring and examining the fluorescence from illuminated nanospheres or quantum dots.

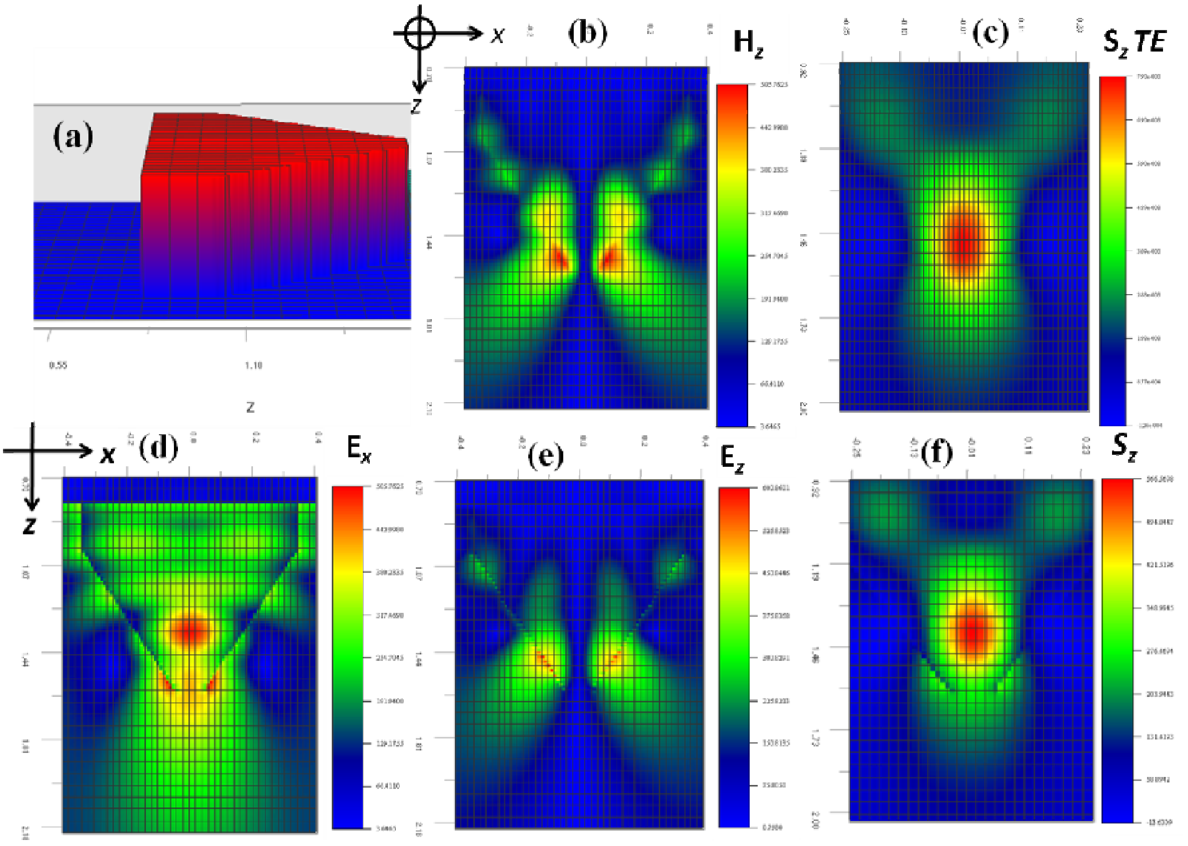

Figure 2.4: (a) Schematic of the simulated NSOM probe (b, c) electric field and power density distribution of s-polarized (TE) waves near NSOM aperture. (d, e, f) Propagating, evanescent, and evanescent wave power density distribution of p-polarized (TM) waves.

Multiple-multipole (MMP) technique and finite difference time domain (FDTD) are two well-established numerical methods for performing electrodynamics field calculation. Here, we have employed FDTD technique to simulate NSOM probe using commercially available OptiWave (Version 8.0) software. FDTD is a computational electrodynamics modeling technique based on the grid truncation method. The method is formulated on discretization of time-dependent Maxwell's equations (in partial differential form) employing central-difference approximations for numerical derivative in space and time with second order accuracy. The resulting finite-difference equations are solved using different boundary value calculations, and the process is repeated over and over again until the desired transient or steady-state electromagnetic field behavior is fully evolved. The schematic of NSOM probe utilized in the simulation is shown in Figure 2.4 (a). Simulated NSOM probes have a lateral dimension of 10 µm, aperture ~100 nm and surrounding metal coating of thickness ~ 150 nm with taper angle of 30^{o} (as received from Nanonics Supertips Ltd.) For simulation, dielectric constants for aluminium and glass were chosen to be *-34.5 + i8.5* and *2.25* respectively [196]. Both propagating (E_x and E_y) and evanescent waves (E_z) field distribution were monitored with different incident light polarization. Simulated field distributions reveal the local electric field energy density over the taper region and assist in determining the strength of the light-mater interaction. For a given incident polarization, *s-polarized* transmission power (transmitted electric field polarization is perpendicular to the incident polarization) decreases monotonically with the slit width, and electric field vanishes at the aperture boundary (Figure 2.4b and c). Transmitted electric field with *p-polarization* (transmitted electric field polarization is parallel to the incident polarization) remains finite at the metallic boundaries and induces charges at the aperture rim [229]. A considerable light flux moves downwards along the taper region following large light transmission through the aperture. It yields a strong near field at the aperture flange (Figure 2.4d, e and f). Field enhancement is observed for *p-polarized* light at the edge of the coating, which may be either due to the continuous field components perpendicular to the boundaries or large curved geometries (lightning-rod effects). At the edge of the aperture, electric field penetrates into the metal coating, thereby increasing the effective width of the aperture. The numerical mapping of electric field profile at the tip of the NSOM probe supports the Bethe-Bouwkamp approximation for the NSOM probe [230]. Generally, elaborate numerical simulation for tip-sample configuration depends on the choice of boundary conditions as well as discretization and iteration procedure used in simulation which, sometimes, is not appropriate with real measurements. So it appears to be important to develop a simple but realistic description of electric field to dominate the interaction with nano-object.

However, in resonance with the excitation light, fluorescence molecules and nanosphere are worked as selective detectors for incident light polarization since fluorescence intensity is proportional to the $(\mu \cdot E)^2$, where μ is the transition dipole moment and E the electric component of the incident field. For randomly oriented transition dipole moment of such ensemble of N, fluorescence intensity of incoherently emitted molecules is proportional to

$$I \propto \sum_{i=1}^{N} (\mu_i \cdot E_i)^2 \approx \frac{N}{3} \mu^2 \langle E^2 \rangle \tag{2.2}$$

Drezet et al. successfully used fluorescence-labelled nanosphere of diameter << probe aperture, as a scalar, isotropic volume detector, to characterize electric-field intensity distribution of triangular aperture NSOM probes [231]. FDTD simulated electric field distribution is similar to those obtained from fluorescence lobes with nanosphere diameter smaller than the probe aperture.

2.6 Spatial Resolution of NSOM

Spatial resolution of any instrument is defined as its' ability to distinguish two separated point-like objects from each other: spatial resolving power of any imaging system is measured by its Point Spread Function (PSF), which is defined as the spreading of a point source that has a direct consequence of spatial filtering [232, 233]. Physically PSF is proportional to the electric energy density which can be quantified utilizing optical detectors. Any point source in space is represented by the delta function with a finite spectrum of spatial frequencies (k_x and k_y). In process of image formation, high frequency components are filtered out. It leads to the further reduction in bandwidth and image of a point converts to an image of a finite size object. The total PSF of any optical instrument can be regarded as:

$$Total\ PSF = Excitation\ PSF \times Detection\ PSF \tag{2.3}$$

The loss of spatial frequencies associated to the evanescent waves upon propagation from source to detector leads to the diffraction limited image. The spatial resolution (inverse PSF) of aperture-NSOM is explained by the electric field distribution on the surface plane. Beyond the surface plane the confined near field spreads out rapidly. It is observed from our simulation that strength of evanescent electric field is apprenticed near to the surrounding of the metal coating of NSOM tip and extinct at the centre of the NSOM probe. In illumination mode, NSOM tip is used to illuminate the sample and related optical information is collected through the condenser of optical microscope. So a correction to collection PSF is required to reach the maximum spatial resolution of NSOM. In collection mode, optical signal is collected through the NSOM probe which comes with its maximum spatial resolution. We employed FDTD analyses (ϕ~ 100 nm) to identify variations of electric field distribution with incident light intensity on the surface plane which directly leads to the spatial resolution of our measurements (Figure 2.5).

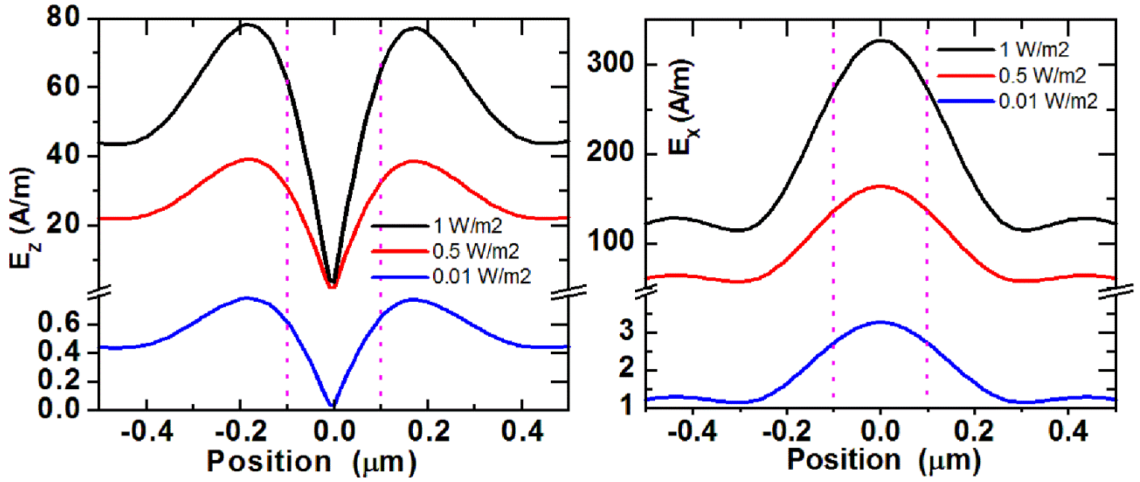

Figure 2.5: Intensity (W/m²) dependent electric field amplitude variation near the taper NSOM probes (a) evanescent wave and (b) propagating distribution. Dotted lines represent the NSOM probe aperture.

From the simulation, it can be concluded that the maximum resolution from NSOM probe is achieved for very small incident power. At high intensity, large scattering from the taper area diminishes the resolution of the instrument. Presence of evanescent wave (E_z) at the probe edge limits the spatial resolution of NSOM probe more than its opaque aperture.

2.7 Tip-Polymer Blend Interaction – Using FDTD Analysis

Commercially available finite difference time domain (FDTD) software package (OptiFDTD, Version 8.0) was employed to estimate the electromagnetic interaction between NSOM tip and polymer film at different excitation wavelengths. The electric field distribution of a NOSM probe of different aperture size (50 nm to 200 nm) and different taper angle (10° to 40°) was evaluated following this method. The extent of interaction strength between NSOM probe and polymer blend was assessed by accompanying the evanescent (E_z) and propagating wave (E_x, E_y) field distribution at different excitation wavelength.

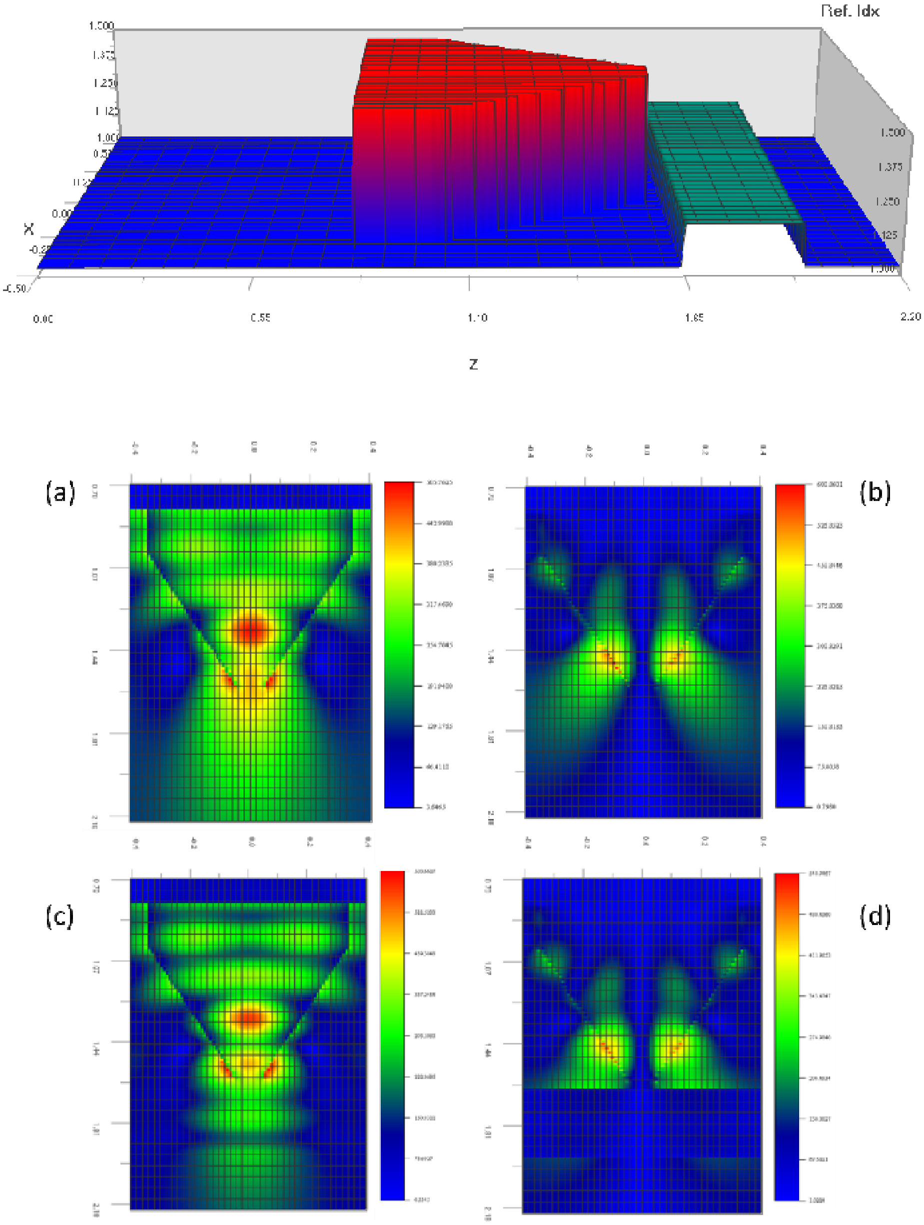

Figure 2.6: (Top) Schematic of NSOM probe–polymer simulation. (a and b) propagating and evanescent electric field distribution near NSOM probe without the presence of polymer film and (c and d) polymer film placed at a distance 10 nm form probe end.

For the simplicity of simulation, we assumed NSOM probe as a cone shape glass fiber, covered with Al metal. Both probe and polymer blend (P3HT:PC$_{60}$BM) were defined by their real and imaginary part of the dielectric constant with proper wavelength dispersion relation. Polarization dependent field was monitored with the reference of the incident polarization. A 5 µm × 5 µm wafer was used in this simulation with 1024×1024 grid point. Taper length of NSOM probe was fixed to ~ 1µm and tip-sample distance was varied between 10-50 nm. The scale down in the simulation was executed by the measured parameters of our experimental NSOM probes.

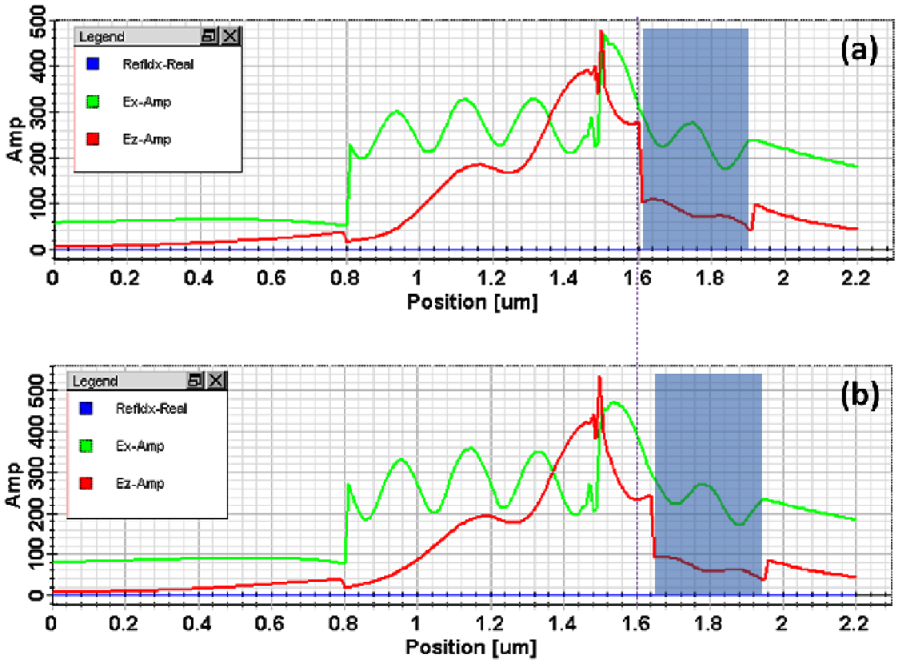

Figure 2.7: Propagating and evanescent electric field amplitude distribution with varying probe–sample distance (a) 10 nm and (b) 50 nm. A unit E_z/E_x *ratio changes to a value of 0.4 after tip–polymer interaction.*

Presence of polymer film near the NSOM tip yields a significant modification of the propagating electric field distribution (Figure 2.6). Presence of polymer film translates the continuous distribution of propagating field to a non-uniform oscillatory electric field. This behavior is directly attributed to the coupling of incident field with backwards external surface modes from polymer surface. Results from simulations demonstrate that evanescent field gets totally absorbed within polymer film (Figure 2.6d). Effects of ITO substrate were neglected in the simulation as evanescent field dies out within the blend film. A comparison between the evanescent and propagating field amplitude (E_z/E_x), depicts that near field interaction dominates over the propagating field interaction (Figure 2.7). Beside, the presence of a large transmitted propagating field yield a transmission contrast which carries the information about the bulk morphology. In this regard, the field amplitude comparison after tip-polymer interaction supports a larger contribution of evanescent component on the local PC compared to the propagating part. So, the spatial resolution of the near field PC mapping is limited by the NSOM probe aperture not by the propagating electric field distribution near taper region.

2.8 NSOM Probes

Normal transparent dielectric is used for NSOM probe fabrication. These probes are produced by tapering of optical fiber to give a conical shape [196]. Tapering of optical fiber is carried out in two different ways – (i) chemical etching and (ii) by local heating of a stripped glass fiber and subsequently pulling it. Chemical etching of glass fiber is very attractive because it has potential of large scale fabrication of identical tips. Glass fibers with their plastic coating stripped off are dipped into 40% HF solution.

A thin over layer of organic solvent is usually added to control height of the meniscus of the HF forming at glass fiber, and to prevent dangerous vapors escaping from the etching vessel. The taper angle is tuned by using different organic layers which change the opening angle because of surface tension. In another method, CO_2 laser at wavelength 10.6 μm, or alternatively a perforated heating foil or coil, is used to heat the glass fiber. Subsequently commercially available microprocessor controlled pipette pullers are used to pull the optical fiber. Finally the shape of the probe aperture (50-150 nm) is determined in scanning electron microscope. For advanced applications in nano optics, NSOM tip should exhibit a short and robust taper region with a large opening angle at the apex, which results in a high throughput optical probe. To reduce the optical leakage from the taper region, glass probes are coated with reflective metal (gold, chromium, Aluminum) coating.

Among all other metals, aluminum serves better with its smallest skin depth and easy processing. In the coating process, the tips are positioned and oriented in such a way that streams of metal vapor hit the tip at an angle slightly from behind. The deposition rate of metal at apex is much smaller than on the sides, which leads to self-aligned formation of an aperture at the apex. The small amount of light intensity (~ pW) from nano aperture sometimes limits its uses in experiments. But pronounced energy dissipation at metal coating and consequent heating limits the input optical power to the NSOM probe. NSOM probes prepared by Nanonics Supertips Ltd. (Figure 2.8) following local heating and pulling method were employed throughout our study.

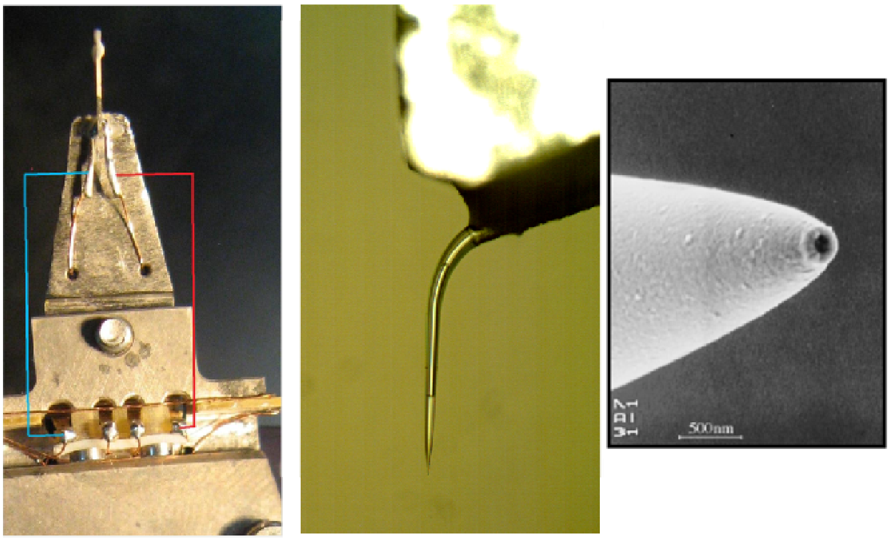

Figure 2.8: NSOM probe mount with electrical connection form turning fork arms. Mounted NSOM tip on the turning fork. SEM image of metal coated NSOM probes. (Nanonics Supertips Inc.)

2.9 Nanonics MultiView 4000^{TM}

MultiView 4000^{TM} instrument is an integrated scanning positioning microscope (SPM) with 2 NSOM probes in combination with dual optical microscopes (Figure 2.9a). The system consists of 3D FlatScan^{TM} scanner along with stepper motor mounted NSOM probe stage (Figure 2.9). The 3D Flatscan^{TM} has a novel planar, folded-piezo, flexure scan design and provides the ultimate in AFM resolution (e.g. atomic steps in highly oriented pyrolytic graphite). Normal force tuning fork technology with high Q factor (≈ 1500) and phase feedback delivers unprecedented control of the probe tip/sample separation. The instrument works on the share force feedback, not with the conventional beam bounce optical feedback. It delivers background noise free imaging when working with semiconductor devices or fluorescent materials. A computer with commercial Nanonics window software (NWS) simultaneously evaluates the probe position, incorporating data obtained from the feedback system, and controls scanning of the tip (or specimen) and the tip-specimen surface separation. NWS software processes pixel to pixel data into two-dimensional data sets (lines) following raster scanning of probe, subsequently compiles and displays as a three-dimensional reconstruction on a computer monitor. The typical size scale of features measured with this scanning probe microscope ranges from <5 nm to ~ 1µm.

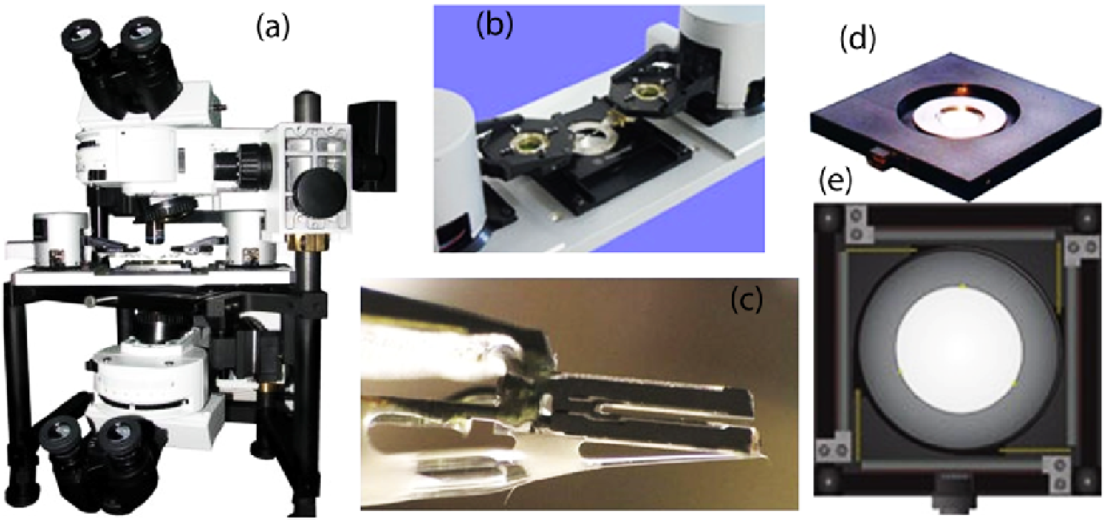

Figure 2.9: (a and b) Schematic of MultiView 4000TM. (c) Picture of a quartz turning fork sensor attached with tapered glass fiber. (d and e) 3D flat scanner for sample scan mode. (Nanonics Inc.)

2.10 Demonstration of NSOM Technique

2.10.1 Photophysics of MEH-PPV-x blended with different conjugation lengths

Phase-separation and energy transfer characteristic of segmented MEHPPV blend with two different distribution of conjugation lengths, namely MEHPPV-20 (LC, low conjugation length, high bandgap) and MEHPPV-100 (HC, high conjugation length, low bandgap) have already been demonstrated from our laboratory [234, 235]. Thin films containing different weight fractions of LC and HC were spin-cast from chloroform solutions on quartz substrate. A control phase separation in spin coated film was obtained following selective chain collapse of MEHPPV-100 in the presence of cyclohexane. Photoluminescence studies of these thin films suggested that complete energy transfer from LC to HC occurred even though complete phase-separation was not present in film.[235] Laser scanning microscopy images of the blends prepared by varying composition of cyclohexane demonstrated the formation of HC aggregates, which shows emission in the red region. The aggregate size increased from 1µm to 5 µm with increase in cyclohexane composition in blend solution. But this phase separation length scale, di-mixing did not happen properly at nanoscale, and a continuous phase of HC is observed which yield a solder peak in the local

PL spectrum. In order to get a nanoscale di-mixing of LC and HC, we utilized 5% of cyclohexene, and phase separation of ~ 200 nm has been achieved as observed in TEM imaging.

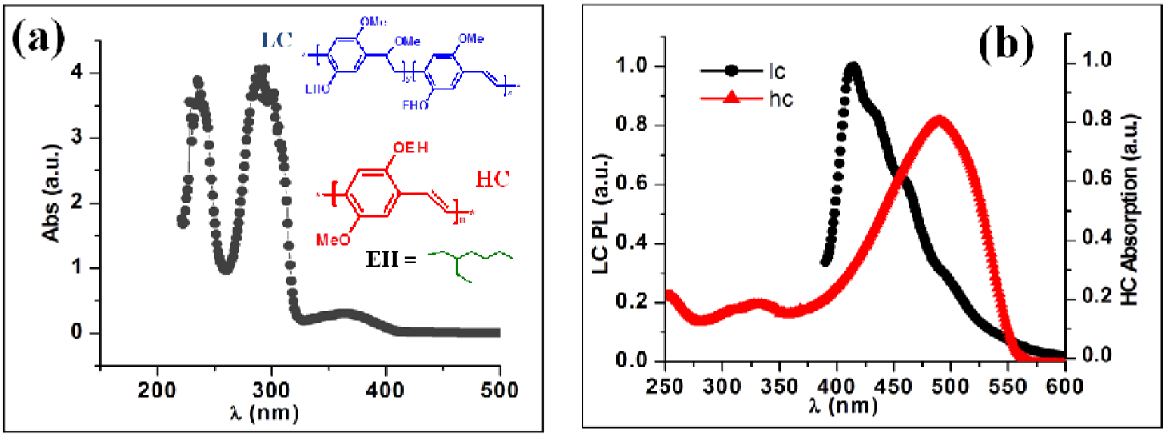

Figure 2.10: (a) Absorption spectrum of LC film (~ 50 nm) span on quartz substrate. Inset: Chemical structure of LC and HC polymers. (b) PL spectra of LC film with 365 nm excitation wavelength and optical absorption spectrum of HC films. A nice overlap is observed which renders the energy transfer from LC to HC.

A signature of energy transfer is observed by illuminating the local region with 365 nm LC excitation (~ 85 nm NSOM probe) and collecting the PL signal from HC part using 50× objective and 600 nm long pass filter. HC domains in the films are accurately identified by fluorescence mapping on the same region with 532 nm excitation. A spatial shift between topography and fluorescence images (~ 500) nm is observed both in x and y direction (Figure 2.11 a, c) due to finite size of NSOM probe aperture. This spatial shift is adjusted during the analysis following cross correlation method. Since 365 nm light excites only LC component, and there is no fluorescence signal from LC above 600 nm, the image (2.11b) is then directly represented in the region where the energy transfer occurs from LC to HC. Domains with large count rate in image 2.11b represent HC domains as obtained from 532 nm excitation. Comparing the line profiles of (b) and (d) with morphology image, it is reveals that significant amounts of energy transfer occur only at LC-HC interface. These results suggest that the finer phase separated LC-HC films yield nearly reddish emission, since bluish-yellow emission from LC would be suppressed by the energy transfer from LC to HC region. So, it is possible to realize a white emitting LED from LC-HC blend film with optimized phase separation where emission from film covers the whole visible spectral range.

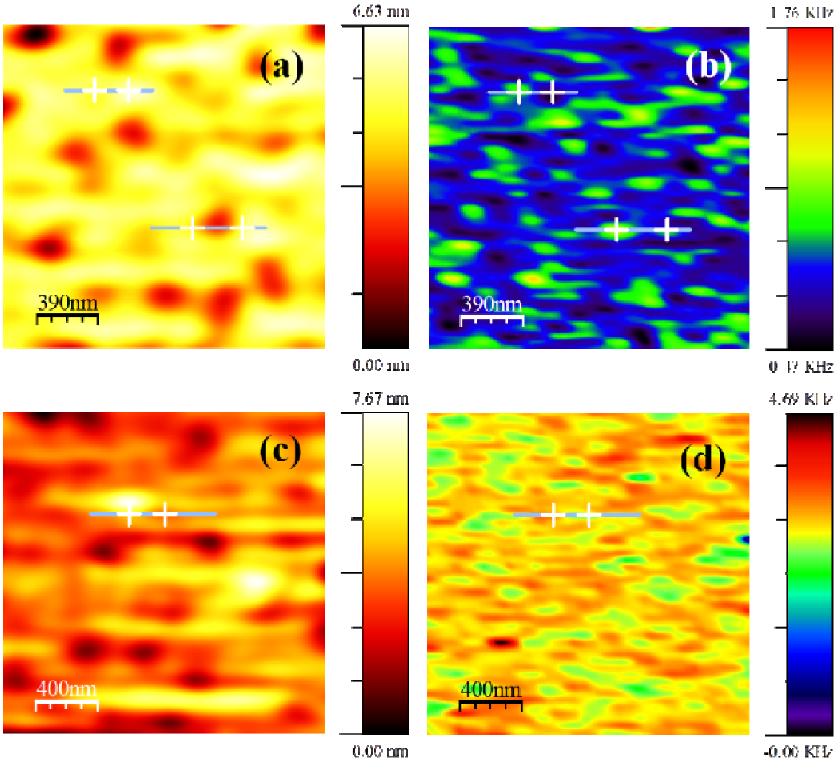

Figure 2.11: (a) and (c) show topography contrast morphology of LC-HC blend films. (b) and (d) represent local HC fluorescence map when illuminated with 365nm and 532 nm laser wavelength respectively.

2.10.2 Probing D-A domains in BHJ-OPVs

The understanding of electrical, optical and mechanical properties of semiconducting polymer-small molecule blends has been an important research field for growing efforts to adopt the use of blends in BHJ device fabrication. So there is an increasing need to characterize these properties at nanoscale resolution as organic optoelectronics devices are fabricated on an even smaller length scale. Near field scanning optical microscope technique provides optical and topographical characterization of thin blend films with lateral resolution significantly better than what can be achieved in ordinary microscope [236]. Along with transmission and fluorescence contrast imaging, topography images are simultaneously acquired as a result of feedback mechanism for maintaining constant tip-sample distance. This makes the NSOM a unique technique to map the dynamics of phase-separating polymer blends and energy transfer by correlating the changes in morphology with the local variation of fluorescence intensity in multi-component polymer films [237].

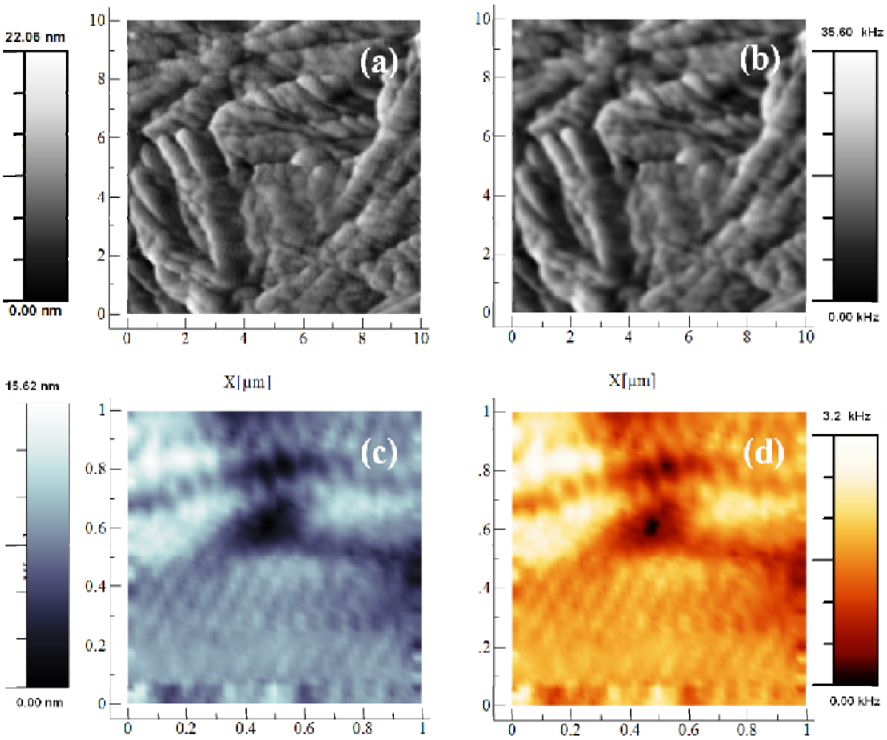

Figure 2.12: Morphology with phase contrast and corresponding fluorescence contrast image of MEH-PPV: $PC_{60}BM$ (a and b) and P3HT: $PC_{60}BM$ blend film (c and d).

Refection and transmission mode measurements were carried out with MEH-PPV: fullerene (1:4) and P3HT: fullerene (1:1) blend coated on ITO or on plane quartz substrates. The blend ratio was optimized in both systems by monitoring PL quenching of donor polymers blend film. Blend of P3HT has smoother surface compared to the MEH-PPV blend (average rms roughness~ 2.2 and 5.6 nm respectively). Topography images depict the phase separation on the surface of the blend film following interactions with two different chemical components (Figure 2.12a, c). The rod type domain formation in MEH-PPV: $PC_{60}BM$ blend is attributed to annealing induced phase separation at high temperatures. This large scale phase separation is ascribed to the diffusion of $PC_{60}BM$ molecules within the MEH-PPV matrix and subsequently large scale crystallization. A complete quenching of PL is barely observed for MEH-PPV blend films, even at nanoscale. The signature of energy transfer is observed only at the D-A interface where mixing D-A produces an amorphous region. The D-A interfaces on the film surface is determined following line profiles of the morphology and phase contrast images unambiguously. For a given illumination intensity, PL signal from the donor rich domains is higher for MEH-PPV compared to the P3HT films (35 kHz and 3.2 kHz respectively).

Self organized nano-crystalline structure of P3HT (~ 40 nm) is observed in the topographical images of P3HT:$PC_{60}BM$ blend film (Figure 2.12c, d). The one directional (~ 45° with image axis) growth of the P3HT crystal leads to highly elongated fiber-like structure with larger carrier mobility. This alignment also produces red shift in the optical absorption of P3HT and improves overlap with solar spectrum. $PC_{60}BM$ also establishes nanocrystal domains following P3HT crystals domains. As domain size is of order of the exciton diffusion length, an optimized carrier transport is facilitated in P3HT:$PC_{60}BM$ blend. Around 100% of local P3HT fluorescence quenching is observed in the blend film with ~ 80 nm spatial periodicity. The difference in absorption ($\alpha_{P3HT} > \alpha_{PCBM}$ at 532 nm) yields near field transmission contrast image where $PC_{60}BM$ nanocrystals appear as bright domains. 80 nm periodic structures are well visible in the T-NSOM image, which depict the spatial resolution potentiality of the NSOM measurements.

2.10.3 Probing substrate effect on morphology

Thermal annealing effects on blend morphology were investigated on P3HT:$PC_{60}BM$ blends with different composition ratios, starting from 1:1 to 1:4. Blend films were coated onto pre-cleaned and HMDS treated substrates (rms roughness <1 nm) from 12mg/ml chlorobenzene solvent at 1200 rpm. Thermal annealing was carried out at 120°C for 10 mins. Prior to thermal annealing treatment, AFM measurements depicted a homogeneous morphology within a relatively large area. The spin coated films are not in their equilibrium state and there is likely a strong thermodynamic driving force in the film to reorganize towards their stable equilibrium states. Upon annealing $PC_{60}BM$ crystals grow up gradually and with annealing time domains are stick out of the film plane. In case of annealed films, bright domains in AFM topography represent the $PC_{60}BM$ crystalline part. The dark area surrounded by the $PC_{60}BM$ crystals reflects the thinner region of the film, being composed of almost pure P3HT polymer. To accrue the substrate effects on kinetics of P3HT:$PC_{60}BM$ phase separation, a control experiment was applied on plain PEDOT:PSS coated ITO and HMDS treated PEDOT:PSS coated ITO substrate without altering thermal annealing and other preparation conditions.

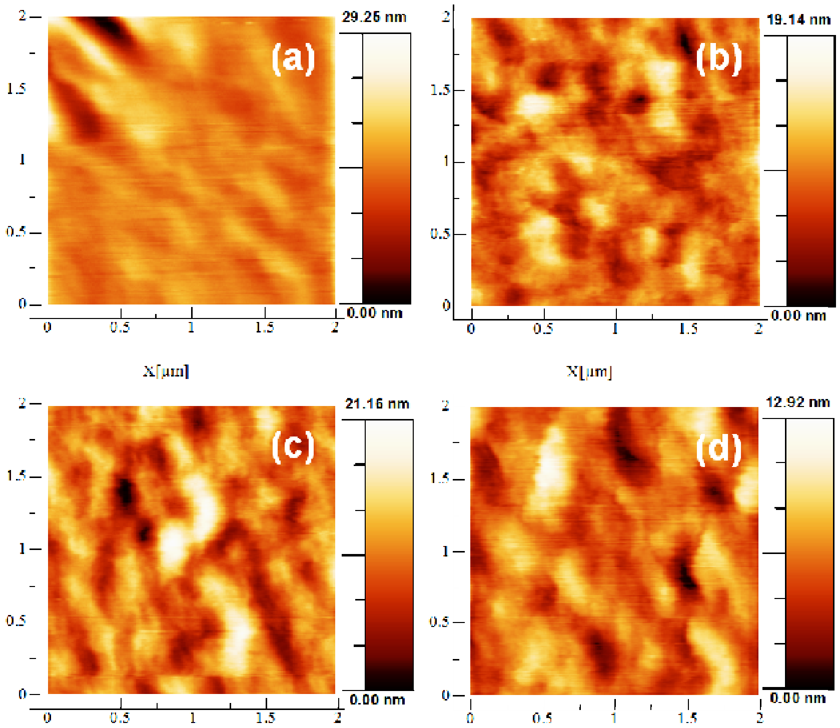

Figure 2.13: Surface morphology of P3HT:PC$_{60}$BM on quartz substrate before (a) and after thermal annealing (b). Morphology of same blend coated on HMDS treated quartz substrate (c) and (d).

Figures 2.13 (a) and (c) represent topographic images of blend films on ITO and HMDS-ITO respectively before annealing. During spin casting, HMDS treated surface helps P3HT polymer chains to self-organize into a microcrystalline structure which also enhances the interchain charge carrier transport [238-240]. This higher conformational dynamics of the P3HT chains benefit PC$_{60}$BM diffusion during solvent annealing process. As the P3HT apparently crystallizes faster than PC$_{60}$BM, P3HT forms small fibrillar crystals while the crystallization of PC$_{60}$BM is almost suppressed and only nanometer size crystal are produced. During this process the slowly grown fiber-like P3HT crystals build borders which directly hamper the extensive diffusion of PC$_{60}$BM molecules and their large area crystallization. So without any post-processing, blend films on HMDS treated ITO yields desire phase separated morphology for photovoltaic operation. The phase separation is experimentally realized following solar cells characterization of different solvent-assist devices (J_{SC} ~ 0.2 mA/cm^2 and 0.6 mA/cm^2 respectively).

During the annealing process at elevated temperatures, diffusion of PC$_{60}$BM through polymer matrix collapse the volume amount in depletion region and diffused PC$_{60}$BM get inserted in the crystals. As the annealing goes on, more and more PC$_{60}$BM diffuse into the crystals, which ultimately cause a sudden collapse of a large area in the remaining P3HT matrix. After reaching the equilibrium state the diffusion rate of the $PC_{60}BM$ reduces formation of large crystalline domains as observed in Figure 2.13b. However, for HMDS treated substrate, blend films already consist of large fiber-like P3HT crystals, so further annealing does not significantly reduces the volume amount in depleted region. But with annealing, $PC_{60}BM$ nanocrystals fill the space between the P3HT networks and reduce the film surface roughness along with continuous pathways for electron transport (Figure 2.13d). Results suggest that evolution of blend film with thermal annealing can be probed utilizing NSOM measurement, which is briefly discussed in Chapter 4.

2 .11 Conclusion

NSOM based approach is suited for examining bulk heterojunction film which consists of variety of length scale features. The combination of atomic force and near-field optical microscopy has proven to be an extremely powerful approach in certain areas of organic photovoltaic research, rendering new information about different specimen types that is simply not attainable with far-field microscopy. The best advantage of NSOM is its ability to generate optical and local spectroscopic mapping along with simultaneous topographic information.

Near field scanning optical microscopy was employed in studying photophysics and to obtain length scales present in phase separated polymer-polymer and polymer-small molecule blend film. Local fluorescence quenching at the D-A interface was demonstrated utilizing reflection and transmission mode near-field scanning optical mapping with 80 nm spatial resolution. Topological and optical phase contrast features are directly correlated to the phase segregation in two-component organic blend systems which develop local variation in device efficiency. Near-field scanning microscopy (NOSM) is a powerful technique which has potential to distinguish optical contrast of nanoscale phases in bulk heterojunction blend film and studies of solar cell morphology utilizing NSOM based approach will be considerably informative.

Chapter 3

Local Photocurrent Mapping on Asymmetric Electrode Devices

3.1 Introduction

An important prerequisite in obtaining high efficiency PSCs is met by achieving optimum nanomorphology [14, 178]. Achieving such a favorable nanomorphology using new materials possessing energy levels compatible with higher device efficiencies (e.g. lower optical band gap) is a key challenge for the development in solar cell performance [151, 152]. Optimal phase segregation must exist to minimize geminate and bimolecular recombination, and thus maximize internal quantum efficiency of a device. Moreover, both exciton dissociation and charge transport requirements need to be balanced for ideal BHJ-cells to achieve external quantum efficiency ~ 60% [241, 242]. For example, if a device consists of large D-A domains, due to the smaller diffusion length (~ 10 – 15 nm), excitons from different domains will not reach an interface within their lifetime. Conversely, fine phase separation (large interfacial area) may enhance geminate and bimolecular recombination at the D-A interface. Indeed, if the domain size is smaller than the Coulomb capture radius, then the charges will not be able to escape from one to another domain which results more geminate recombination [5, 243, 244]. In this case the charges may not be confined by the Coulomb attraction but rather by the physical size of the domains. As discussed in Introduction, it is possible to control BHJ morphology via different processing conditions (solvent, annealing), chemical composition of the donor and acceptor materials, and by adding selective solvent additives. Spatial domain sizes ranging from 5-10 nm to few μm was reported for phase separated morphology in MDMO-PPV/P3HT donor and fullerene acceptor based BHJ solar cells [74, 107, 173, 245]. The effect of external processing parameters on BHJ morphology can be well understood accompanying high resolution in-situ investigations which afford to follow the changes in nano-scopic BHJ morphology [16].

The evolution of local morphology with processing conditions is typically studied by transmission electron microscopy, atomic force microscopy (AFM) and GIXRD based methods which have already been discussed in Introduction. These measurements furnish structural data of the blend films but fail to provide the direct information of specific nano-scale optical or electrical variations with processing conditions. Probing of charge generation and transport in these mixed phase regions at nanoscale is expected to be informative compared to structural information, and improves the general understanding of the BHJ systems. In this line of pursuit, different techniques such as spatial photocurrent decay and near field scanning transmission imaging (T-NSOM) in combination with photocurrent mapping are proposed to examine functional solar cell devices, which directly provide information to correlate morphological features to the device performance parameters such as V_{OC}, J_{SC} and η.

Combinations of local optical and electrical measurements assist to ascertain more information about the morphology dependent charge generation and transport processes in BHJ. Transient electron force microscopy (trEFM) has been utilized to probe the charging rates in PFB/F8BT blends; it is reported that charging rates are maximum at the center of the topographically visible domains compared to the edges. Similarly, photoconducting-AFM (PC-AFM) has been utilized to map the microstructure in P3HT/$PC_{71}BM$ blends using an electrical tip with far-field as well as near-field illumination to probe local charge generation and percolation transport. These local measurements rely on the fact that only the active layer volume below the AFM tip participates in local electrical measurements. But in these measurements, photo-carriers are generated over the optical excitation volume in the film and average illuminated area is limited by the diffraction limited light spot (~ $\lambda/2$). Current studies show that substantial contribution to photo-response also arises from illuminated regions of the film outside of the patterned electrodes [246]. The length scale up to which photo generated carriers can diffuse to the electrode edge is of the order of few tens of μm. So local PC measured through AFM tips does not limit to the actual contribution from 20 nm regions, but it includes contribution from the illumination point resolution (~ 400 nm). It is natural to utilize high resolution (<100 nm) optical methods to examine the origin of PC in these binary mixture films and relate it to the macroscopic device performances. Earlier, near field scanning optical microscopy (NSOM) was utilized to map the monochromatic efficiency of OPVs in 2D directly, with ~ 300 nm optical resolutions [76, 212]. It is a powerful tool where tapered optical fiber tip scans across the sample and illuminates only the areas that lie directly under the tip aperture, which is typically 50 to 100 nm in diameter. These measurements demonstrated local variation in current generation accompanying micro-size pattern formation in PFB/F8BT blend devices [76, 210-212].

The cathode coating and sizable thickness of the substrate prevents near-field access to probe the active layer. We circumvent this practical constraint by noting the significant contribution to the device PC from the peripheral region of the films and utilize it for our studies [247-251]. The presence of this PC arising from the periphery enables high resolution PC contrast spatial imaging without the need for locally positioned electrodes. For light incident from the cathode side, PC decreases but persists over a distance of ~ 200 μm from the Al or ITO periphery. The access of near field optics to the active region yields topography, transmission, fluorescence, and PC contrast images simultaneously. PC decay near the electrode is relatively insignificant over scan areas of 10×10 μm, and the combination of these images from a given region in the binary-mixture film reveal spatial coordinates of the active spots for optical absorption and carrier generation along the carrier transport pathways.

3.2 Spatial Photocurrent Decay

The origin of PC outside the overlap electrode can be realized by spatial photocurrent decay measurement which also enables near field PC scan. Spatial photo current decay was developed and successfully implemented over the last few years in our laboratory to examine the degree of ambipolarity and correlation between the lateral to vertical transport process [247-250]. The method was well employed to estimate the efficiency of carrier (electron or hole) transport process by positioning a narrow-light beam outside the electrode periphery in asymmetric device structure (Figure 3.1a and b). Asymmetric device structure was fabricated by spin coating of active layer on pattern ITO substrate and subsequent aluminum (Al) evaporation such that electrodes form a cross-type structure. The distinctly measurable PC arising from the peripheral region of electrode is employed in the technique. PC decreases progressively as the light is scanned away from the overlap region of the electrodes. The origin of PC outside the overlapping electrode is attributed to three possible reasons (*i*) Optical effects – scattering at rough interfaces and wave-guiding in thin films, (*ii*) electric field fringing at electrode edges, and (*iii*) carrier diffusion from the generation point. The contribution of optical scattering for surface roughness was estimated by computing Haze parameter [246]. Haze parameter is defined as ratio of the diffused light to the total incident light. AFM studies on cover-slips and blend films reveal an average rms roughness of 10 nm and 3 nm respectively. In comparison at 532 nm illumination, the computed Haze parameter entails that only ~10% of incident light has diffusive nature. So incident light mostly gets absorbed at blend film or transmits through the film. Even at near normal incident, light guiding at polymer ITO interface is quite negligible. The monotonically decay nature of PC near the electrode edge rules out the optical scattering effects as an origin of peripheral PC. Peripheral PC is sustained over much larger length scale as compared to the extent of fringing field (field strength decays to 10-100 V cm^{-1} within a distance < 100 nm). So the existence of peripheral PC over the electrode edge can be treated as a diffusion process of the excess photogenerated carriers outside the overlap electrode.

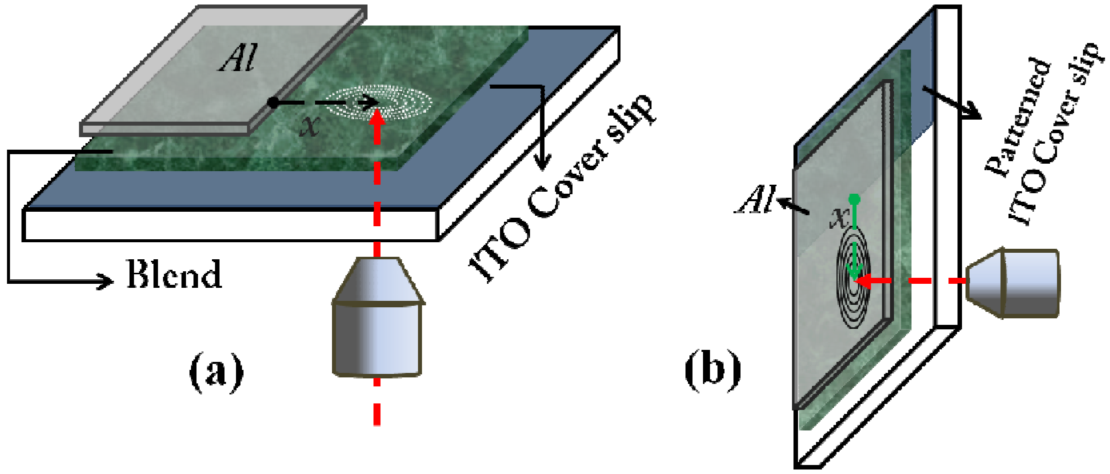

Figure 3.1: Schematic of spatial PC decay measurement in asymmetric devices structure for (a) electron and (b) hole transport. Reprinted with permission from Mukhopadhyay et al., Applied Physics Letters, 100, 163302. Copyright [2012], American Institute of Physics.

Considering steady state continuity equation, peripheral PC originated at illumination spot of any fixed distance x from electrode edge can be expressed as

$$D\frac{\partial^2 n}{\partial x^2} - k_r n^\gamma + g(x) = 0 \text{ where } g(x) = n(x) = \eta_{int}\alpha I_0 \int_0^t e^{-\alpha y} dy \qquad (3.1)$$

where γ is the non-linear recombination coefficient with rate constant k_r, α the average optical absorption coefficient, η_{int} the internal quantum efficiency, I_0 represents light intensity and 't' is the film thickness. Under small signal limit with a constant, intrinsic carriers concentration ($\Delta n/n_b \ll 1$) continuity equation reduces to

$$D\frac{\partial^2 \Delta n}{\partial x^2} - k_r \gamma n_b^{\gamma-1} \Delta n = 0 \qquad (3.2)$$

In steady state and in the absence of an external field at low level injection, the carrier transport equation yields an exponentially decaying solution form $\Delta n(x) = n_0 exp(-x/\Lambda_\gamma)$, where $\Lambda_\gamma^2 = D/k_r \gamma n_b^{\gamma-1}$. Assumption of linear recombination (γ =1) reduces Λ_γ to $\Lambda_\gamma = \sqrt{\frac{D}{k_r}} \cong \sqrt{D\tau}$ where τ represent recombination life-time at tail state of DOS and Λ_1 is interpreted as a decay length L_D (Appendix I). A simplistic analysis involves fitting the decreasing current tail with respect to the distance from electrode edge to the carrier generation point to an exponential-decay behavior, enables the extraction of L_D in these systems. The physical significance of spatial decay behavior of peripheral PC in pristine polymer and BHJ devices was inferred from the charge generation and transport mechanism. Upon laser illumination outside the Al electrode (electron current) photogenerated holes rapidly diffuse to the barrier-free ITO electrode over the short distance (order of thickness ~ 100 nm). It creates a local electron distribution in the polymer film and distorts the built-in potential which, in the steady state, sets up a non-local lateral electric field [248, 252]. It induces a unipolar lateral electron transport through polymer film (LPV effect) [252]. Illumination outside the ITO electrode similarly induces a hole current through the polymer film whereas electron goes to Al electrode (Schottky-field assisted process).

Spatial decay length measurements on polymer-small molecule blend is more informative compared to the pristine polymer. In bi-continuous BHJ film, the unipolar charges largely flow through the acceptor (electron current) or donor polymer (hole current) network. Spatial decay measurements on P3HT:PC$_{60}$BM and MEH-PPV:CN-PPV blend systems ascertained the direct correlation between PC decay profile and the efficiencies of the devices [247]. Decay lengths for the higher efficient (η~ 1%) P3HT:PC$_{60}$BM device

(L_D^e~ 16 μm and L_D^h~ 109 μm) are one order of magnitude higher as compared to the low efficient (η~ 0.2%) MEH-PPV/CN-PPV device (L_D^e~ 7 μm and L_D^h~ 13 μm) [246]. The functional behavior of the monotonically decaying PC profiles directly explicates the specific morphological properties of the photoactive films; *hence the method is particularly suited to estimate the degree of phase separation and percolation paths for the electrical transport in BHJ films.* Analyses of decay profiles ascertain a variation in electron and hole-decay lengths (L_D^e, L_D^h) with blend composition *i.e* D-A ratio. Enhancement of both *e* and *h*-decay length is observed for a certain acceptor fraction in blend and reduces with large acceptor concentration. It reveals that a certain acceptor concentration improves both *e* and *h* mobility following effective charge transport with less recombination.

Since PC decreases with the distance from electrode-edge, there must be different loss mechanism comprised in the process. These loss processes are attributed to either deep trap centre, recombination between free carriers or with existing trap carrier. To quantify different loss mechanism, we utilized different background intensity (n_b) and analyze the PC decay profile by spreading impedance approach [252]. Under DC optical bias, photogenerated carriers from background illumination occupy trap states and reduce local photo-current with enhanced recombination during the carrier transport to the electrode which simultaneously modifies decay profile.

3.2.1 Spatial photocurrent scanning technique

The experimental schematic of spatial PC decay measurement is shown in the Figure 3.2. The laser light spot was expanded using 10× optical expander to obtain a uniform intensity over light spot. Laser spot was focused on the device using a 60× objective, 0.95 NA (working distance ~ 250 μm with cover slip correction) with ~ 4 - 5 μm spot size. In order to maintain the normal incidence and tight focusing at Al electrode-polymer interface, 50/50 beam splitter was introduced in the optical path. Maximum back reflection from Al coating was maintained following this appropriate optical alignment.

PC was monitored at different distance from the electrode edge by precisely translating computer controlled stepper motor stage with 1μm resolution. PC and transmitted signal was simultaneously measured by standard Lock-in (SRS-830, Stanford Research Systems) technique utilizing optical chopper (ω ~ 300 – 700 Hz) and LabView software. Subtracting dark current contribution and normalization with transmittance power, constant PC at the overlap region reveals the most efficient charge transport between two electrodes. Since all the measurements were carried out at a steady state, RC time limitations that could be associated with current transient techniques close to open circuit, do not affect our measurements.

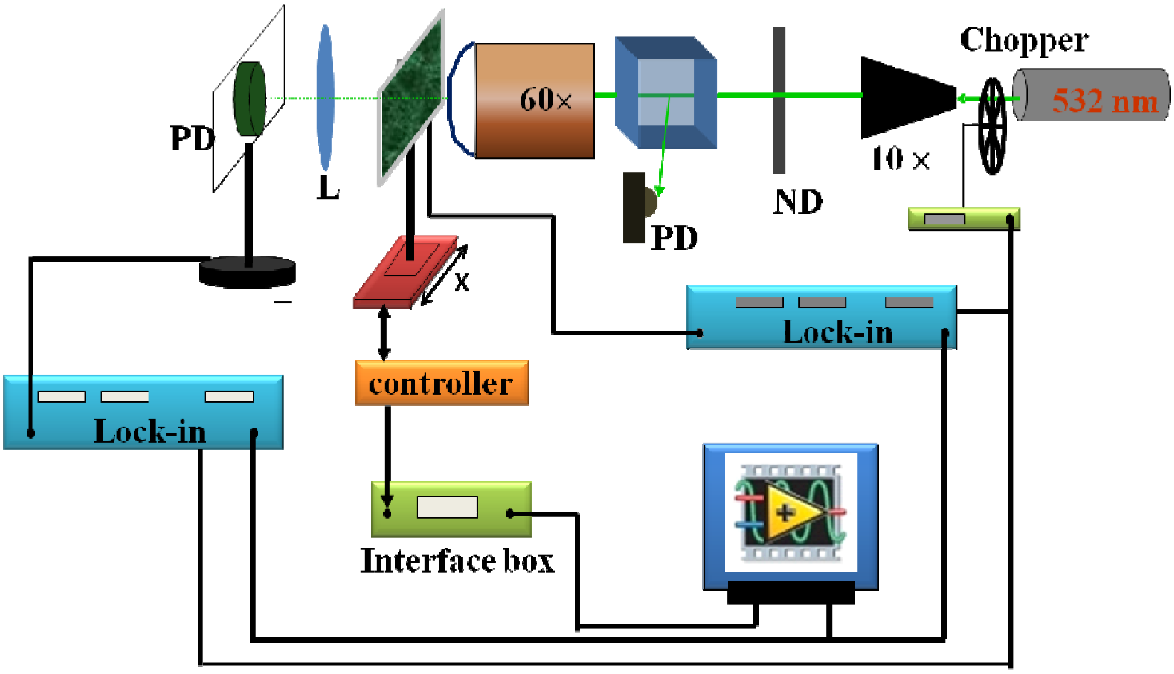

Figure 3.2: Schematic of the lateral decay length measurement setup.

A typical spatial PC decay profile is shown in the Figure 3.3. The green dot represents PC profile and red profile corresponds to optical transmission through device. Size and intensity of the illumination spot was controlled by neutral density optical filters. The sharp electrode edge (~ 1 – 4 µm) was accurately determined by monitoring transmission over the line profile and with the 1st derivative of the transmission profile.

The derivative of the transmission profile yields a Gaussian distribution over the electrode edge. It appears originally from the finite dimension of the optical spot (2 – 5µm), and scattering at the sharp electrode edge. PC persists over few hundred microns (80 – 120 µm) for low bandgap donor-fullerene blend devices and few microns (20 – 40 µm) for P3HT-fullerene blend. This affirms the efficient long lived trap assists carrier transport connectivity and less carrier loss in low band gap polymer blend as compared to the P3HT blend.

Spatial PC decay measurements under DC optical bias were performed under variable/continuous intensity illumination of 1W white LED incident from ITO side of the device. LED intensity was modulated by varying the current and was calibrated using reference silicon cell (0.01 to 0.6 Sun). Lock-in technique automatically subtracts the background current which is sometimes larger that of the probe PC. To avoid any damage of Lock-in instrument, photo-response under DC-illumination was measured as voltage signal across a 2 kΩ resistor-pot, connected in series with the device.

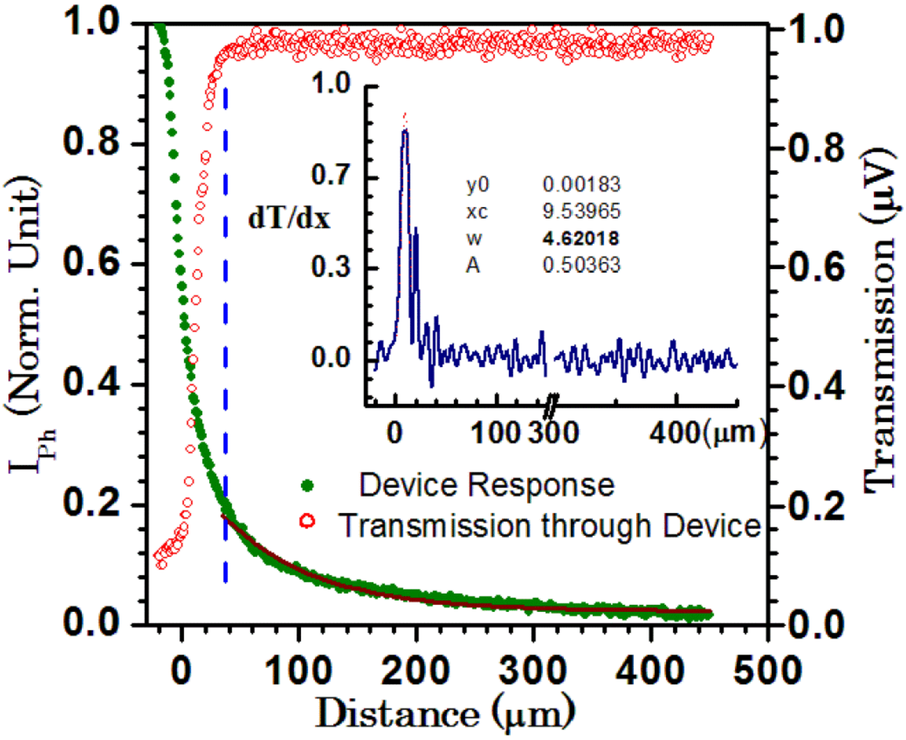

Figure 3.3: Typical PC decay behavior outside the overlap region and corresponding optical transmission. Inset: differentiated transmitted profile with Gaussian distribution at electrode edge, which yields accurate measurement of edge. Decay length is obtained by fitting single exponential to the decay profile (red line) from electrode edge (shown as dash blue line).

3.3 Circuit Model

The spatial PC decay profile outside the overlap region can be well represented by spreading impendence approach, which described the efficiency of charge carrier transport and loss mechanisms prevailing in the blend film. The asymmetric device structure is represented by an equivalent electrical circuit in combination with an ideal current source, rectifier diode, series resistor and a parallel resistor. Physically series resistor represents the carrier transport through percolation paths in bulk film, whereas parallel resistor represents the carrier loss due to mainly bimolecular recombination ($\gamma = 2$). Hopping transport process in disordered materials is effectively represented by a spreading resistance that varies with distance from electrode edge and the functional distance dependence is captured by a spreading function $g(r)$. In spreading impedance approach (SIA), lateral transport network between two points on the film is replaced by spatial morphology dependent resistor function $g(r) = exp((r/\xi)^{\alpha})$ [249]. $g(r)$ quantifies the blend morphology and electrical connectivity network in terms of a characteristic length scale ξ, and stretch exponent α. The relative magnitude of ξ obtained by comparison with experiments suggests that ξ represents persistence length that is order of the interconnected percolation path length [251]. Kinetics of two-component's phase separation in blend film support the existence of periodically distributed domains, which are directly correlated to the persistence transport length. The appearance of single length scale of ξ and stretch parameter α in phenomenological analysis is attributed to the maximum dominant persistence length of carrier transport present in the film. On the basis of the above analogy, the equivalent circuits of the asymmetric device (different for *e-decay* and *h-decay*) are derived (Figure 3.4 (b) and (c)). The model is exclusively resistive without any capacitive component which is valid in the present case of steady state operation in the low ω (~ 370 Hz) range.

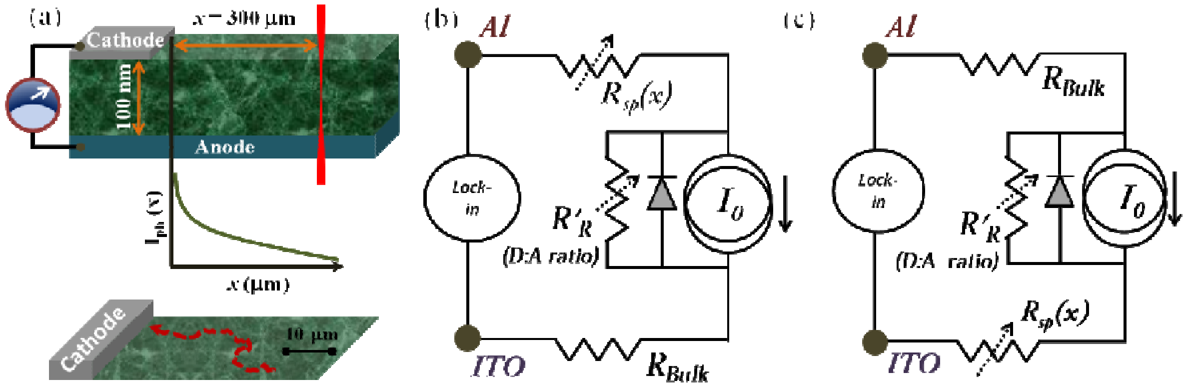

Figure 3.4: Schematic of probing efficient carrier transport using spatial PC decay. Equivalent circuit representation of asymmetric electrode device configurations (Figure 3.1) for (b) electron and (c) hole transport study respectively. Reprinted with permission from Mukhopadhyay et al., Applied Physics Letters, 100, 163302. Copyright [2012], American Institute of Physics.

The current source, I_0 represents the saturation current at the overlap region. In case of illumination outside Al electrode, the hole current is directly collected by the bottom ITO electrode, which can be represented as *fixed* electrode resistance R_{Bulk}. The predominantly lateral electron current flows through a spreading resistance $R_{sp}(x) = R_s g(x)$, where R_s is the sheet resistance of interconnected D/A network and R'_R represents recombination during transport. Here 'x' is the distance of the light beam from the Al-electrode edge along the scanning direction. The measured PC is represented by

$$I_{Ph}(x) = \frac{R'_R}{R'_R + R_{Bulk} + R_{sp}(x)} I_0 \tag{3.3}$$

Thus, the normalized PC as shown in Figure 3.4 (a), can be fitted to an expression of the form $I'_{ph}(x) = \{1 + a \exp[(x/\xi)^{\alpha}]\}^{-1}$ where $a = R_{sp}/R_R$ ($R_{bulk} << R_{sp}$).

Decay length (L_D^e, L_D^h) and ξ emphasize two different carrier transport quantities. The parameter ξ represents, in a sense, the microscopic charge carrier localization length [251]. In pristine polymer such as P3HT, ξ quantifies the spatial and energetic disordered present in the spin-coated film. The variation in ξ with acceptor concentration in BHJ film implies the modification of percolation network. The variance of the percolation length scale distribution in blend film is quantified by the strength of the stretch exponent α (α = 1 represents single length scale).

3.4 Topographical and Phase Contrast Measurements

Tapping mode AFM (JPK Instruments, hexagonal shape silicon-nitride tip ~ 15 nm; Nanonics, glass cantilever probes ~ 20 nm) imaging method was utilized to monitor the surface morphology of photo-active layers of BHJ solar cells. Evolution of film morphology with thermal annealing was closely examined with these measurements. Photo-conducting AFM at the same region was performed with Pt/Ir coated Si probes with +/- 2 bias ranges maintaining ITO as ground electrode.

3.5 Near Field Transmission and Photocurrent Measurements

AFM studies of D-A phase separation are limited to the BHJ film-surface. To get information about the overall heterojunction film morphology, a 3D overview of the bulk film is necessary. Fluorescence contrast from the blend film, in principle, yields information for donor and acceptor phase-domains. However, the efficient charge transfer in BHJ film, even at low acceptor ratio, results in a weak PL signal. In this regard, a near field transmission (T-NSOM) contrast imaging with subwavelength optical resolutions has been developed to address the overall film morphology along with the carrier transport network. T-NSOM measurement was performed in tapping mode configuration by raster scanning the NSOM probe outside the aluminum electrode edge (30-40 µm) and chopping laser beam (633 nm or 532 nm, 2 mW, excitation volume ~$10^{-3}\mu m^3$) at a frequency ~ 1 kHz. The transmitted light was collected through a 60×, 0.95 NA objective and a combination of optical filters before photo-multiplier tube (Parkin Elmer) detector (Figure 3.5a). Higher absorption at polymer domains (> 10^5 cm^{-1} in the entire spectral region of 500 nm < λ < 800 nm) as compared to $PC_{71}BM$ (~ 5 ×10^3 cm^{-1}, 532 nm and 2 × 10^3 cm^{-1}, 633 nm) renders near-field transmission contrast images [87]. This 2-dimensional local optical contrast provides the 3-dimensional D-A phase separated domains in BHJ film (Figure 3.5b). Brighter regions with higher photon count rates in the T-NSOM image represent the acceptor domains as compared to the absorbing donor domains (dark).

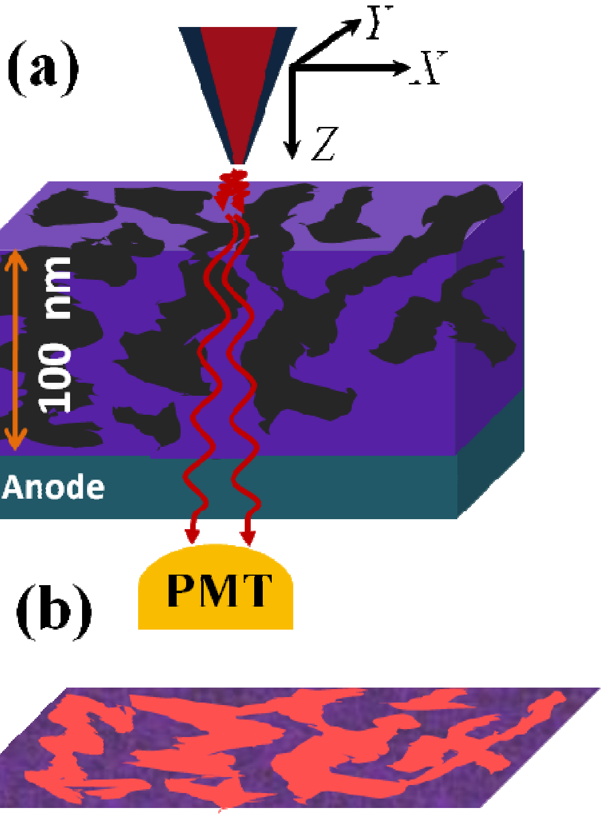

Figure 3.5 (a) Schematic of Transmission Near Field Scanning Optical Microscopy (T-NSOM) and (b) 2D projection of the phase-separated domains.

The evolution of local morphology as a function of processing conditions and its correlation to solar cell device performance were successfully explicated in recent studies [70, 75, 181, 253-255]. But probing of charge generation and carrier transport pathways in mixed phase region at nanoscale regime is expected to be more enlightening for general understanding of BHJ-PSC devices. So, along with the near field scanning transmission approach, different combinations of electrical measurements have been employed to track the effect of nanomorphology/phase segregation on photogenerated charge transport. The schematic of near field PC mapping is illustrated in Figure 3.6 where a NSOM tip is placed on the blend film very close to the Al electrode edge. In this local illumination, the photogenerated holes are directly collected at the extended ITO electrode and excess electron follow the interconnected acceptor domains and diffuse to the Al electrode through non-illuminated region. This current contrast mainly arises from the interaction between evanescent waves of NSOM probe with blend film. As the evanescent waves are mainly sustained near the tip aperture, high spatial resolution in current contrast image can be achieved as compared to transmission image. At any pixel, the local PC amplitude depends on the carrier generation efficiency and the acceptor connectivity to the electrode. So the evolution of carrier generation and D-A morphology with different processing conditions can be easily followed from near field PC contrast image. Local near field PC (NPC) image at different optical bias (background intensity) also depicts accumulation of trap carriers at the interface and its affect on device efficiency. It was observed that charge accumulation significantly reduces local current amplitude by enhancing both inter and intra-domain recombination. Thus background DC illumination modulates the current generation rate, hence charge density and trap states in the active layer. NPC measurement under steady background current takes into account the carrier transport under conditions similar to the solar illumination.

Near field scanning measurements were performed with Nanonics Multiview 4000^{TM} system and the experimental setup was shown in the Figure 3.6. To maintain large (10^2) signal to noise ratio in electrical measurements, we restricted our NSOM tip aperture to > 100 nm. The larger NSOM probe aperture limits the spatial resolution of near field transmission contrast to 120 nm. Spatial resolution of NSOM measurement was accurately estimated following the numerical simulation of beam propagation and evanescent wave interaction with blend film (see Section 2.7). The device current was always measured in short circuit conditions using a lock-in amplifier (SRS 830) with the output being fed into the auxiliary port of the Nanonics interface system. It converts analog short circuit current signal (TTL input) into a digital voltage signal (8 bit binary) for computer storage. Overlapping of PC line profiles in both trace and retrace scan direction indicate that the blend films do not exhibit any photo-degradation due to the incident light beam from NSOM probe.

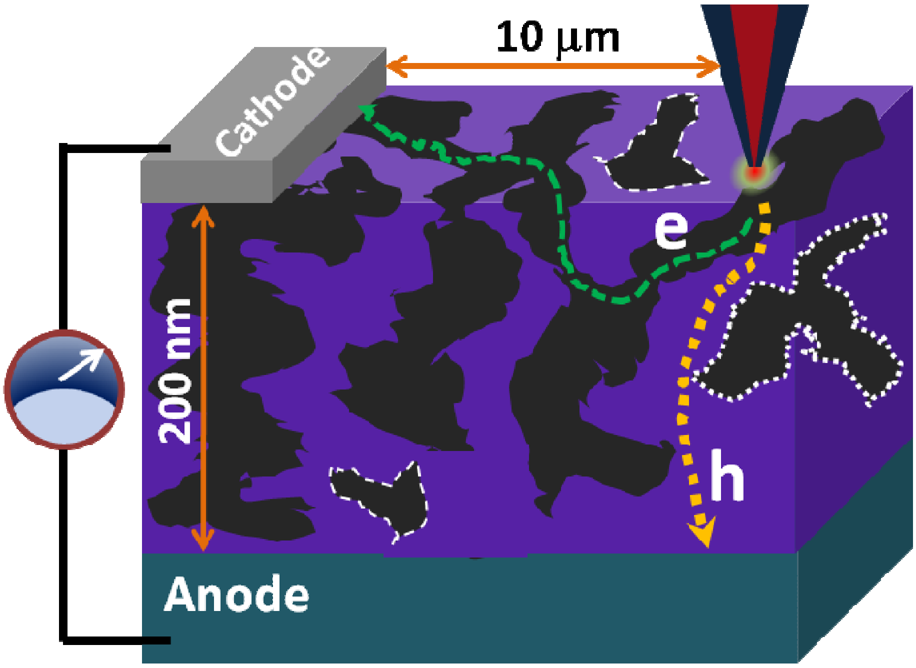

Figure 3.6: Schematic of 3D bulk heterojunction with asymmetric electrode geometry and carrier percolation pathways. Isolated acceptor domains which are not involved in carrier transport, are highlighted with white border. Reprinted with permission from Mukhopadhyay et al., J. Phys. Chem. C, 115, 17184. Copyright (2011) American Chemical Society.

Simultaneous mapping of topography, near field transmission contrast (T-NSOM) and PC (NPC) from different devices demonstrate the nanoscale phase separation and effective PC generation region. Phase separation scales which engender significant difference in device performance are extracted from these images utilizing fast Fourier transform (FT) and power spectral density (PSD) analyses.

Device Fabrication

The photovoltaic devices used for NPC study were fabricated as follows: a film of PEDOT:PPS (Baytron P) was spin coated onto a pre-cleaned Indium tin oxide (ITO) coated cover slip and dried at 110°C to get a thickness of about 30 nm. Then the active polymer blend of thickness of about 100 nm was deposited by spin coating from chlorobenzene solution at 1200 rpm on top of the PEDOT:PSS film under ambient condition. For electrical characterization, photovoltaic device fabrication was completed by vacuum evaporating (10^{-6} mbar) a 40 nm Al electrode using shadow metal mask. Lower evaporation rate (5Å/sec) was used to assure the uniform, good contact and less void spaces in top electrode coating [256]. I-V characterization was carried out in air tight chamber (10^{-3} mbar) using xenon lamp with UV cut-off filters.

3.6 Power Spectral Density Analysis

Power spectral density analyses of contrast images ascertain the 3-dimensional nano-scale D-A phase separation in bulk-heterojunction films. Methodically, like other thin films, polymer blends film can also be described by a spatial contrast profile. A rough surface is depicted as the surface height profile $h(x)$, where h denotes the height with respect to the substrate at a position x on the surface. Irrespective of topological contrast, thin film of active material in polymer solar cells can be characterized by local fluorescence contrast $I(x, y)$, transmission contrast $T(x, y)$ or local PC contrast $\mathrm{PC}(x, y)$ profiles. Various statistical parameters are defined in literature to characterize thin film, like average, mean contrast and rms roughness etc [257]. The average of any profile $f(x, y)$ on the surface is denoted as $\langle f(x, y)\rangle$, and defined as $\langle f(x,y) \rangle \equiv (\iint f(x,y) dx\, dy / (\iint dx\, dy)$. The mean contrast $\bar{f}$ of a surface profile is defined as $\bar{f} \equiv \langle f(x,y) \rangle$. Root mean standard deviation of thin film surface contrast profile or RMS roughness is defined as $\omega(t) \equiv \sqrt{(\langle [f(x,t)\,]^2 \,\rangle\,)}$. But statistical methods like mean or standard deviation of profiles are restricted to the surface, which does not reflect the correlations between the different lateral positions of the surface with 3D vertical contrast profile. To accomplish this, a new statistical quantity autocorrelation function $R(r)$ is introduced, which measures the correlation of the contrast profile separated laterally by the vector r. The autocorrelation function is defined as

$$R(r') \equiv \frac{1}{\omega^2} \langle f(r) f(r') \rangle \tag{3.4}$$

Following the definition of autocorrelation function, the lateral correlation length ξ' is defined as the value of r at which $R(r')$ decreases to the $1/e$ of its original value.

As defined, ξ' represents the spatial length behind which the profile information contrasts (I_{mn}) is not significantly correlated; the distance between the boundaries of drastic change in domain properties. Beyond the lateral correlation length, even though the profile is not significantly correlated, it exhibits a periodic behavior on a length scale large than the lateral correlation length. To determine the long range correlation behavior in bulk film, the power spectral density function (PSD) was utilized. The PSD is related to a d-dimensional Fourier or Hart-let transform of the profile, defined in the reciprocal space as

$$P(k,t) \equiv \frac{1}{(2\pi)^d} \left|\langle f(x,t) e^{-ik.x} \rangle\right|^2 \tag{3.5}$$

PSD analyses were employed on surface morphology, optical transmission and short circuit current contrast images of blend film to determine the strength of the periodic domain variations as a function of spatial frequencies. Autocorrelation analyses of the spatial spectral information yield the lateral correlation length *i.e.* individual periodicity of the phase separated donor/acceptor domains in BHJ film [258].

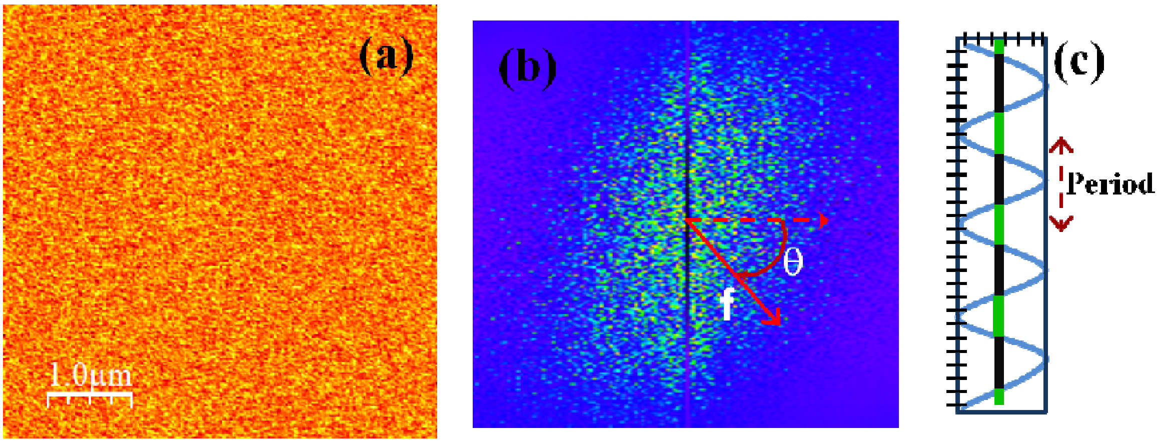

Figure 3.7: Typical T-NSOM image (a) and corresponding 2-dimentional fast Fourier analysis in spatial frequency domains (b). (c) The 'period' is defined as centre to centre distance between two specific components.

The spatial frequency distribution reveals relevant length scales which are exploited to quantify the changes with different composition ratio, and phase separation upon thermal annealing. All the images consist of 8 bit color contrast feature (0 to 256) with 512 ×512 pixels image resolution (Figure 3.7a). A taper window function was utilized to reduce the edge effects and to minimize the spectral leakage on all of the images before 2-dimension FFT calculation. Figure 3.7b represents the 2-dimensional FFT image of T-NSOM contrast, where the color contrast exemplifies the intensity of different spatial frequency which corresponds to the quasi-periodic length scales present in D-A phase-separated film. Then commercially available 2D fast Fourier transform program (WSxM 5.0, Nanotec Inc.) was applied to all the images [259]. Finally few of these obtained PSD data were cross-verified with MatLab simulation separately. In the present analyses, the computation for the 2D average discrete PSD function is express as

$$PSD_{2D}(k_x, k_x) = \frac{1}{L^2}\left\{\sum_{m=1}^{N}\sum_{n=1}^{N} I_{mn} e^{-2\pi i \Delta L (k_m x + k_n y)} (\Delta L)^2\right\}^2 \tag{3.6}$$

Here I_{mn} represents the profile information contrast (height, current or transmitted light intensity) for $(m, n)^{th}$ pixel with scan surface area (L^2) at sampling dimension ΔL (L/N) and k_i represents the spatial frequency along i direction. Finally average angular power spectral density was calculated which was represented as the radial frequencies k' ($= k/2\pi$) to generate radial 1D PSD as

$$PSD_{2D}(k') = \frac{1}{2\pi}\int_0^{2\pi} PSD(k', \theta)\, d\theta \tag{3.7}$$

Surface morphology, transmission and short circuit current contrast mapping of blend films with different acceptor concentration were evaluated by power spectrum analyses, which correspond to the strength of the periodic domain variations as a function of spatial frequencies. AFM and T-NSOM scans were carried out for different films at different region with 15μm × 15μm, 10μm × 10μm, 5μm × 5μm area at 512 × 512 data points which yields ~ 10 nm (5μm/512) sampling rate. The minimum spatial frequency corresponds to $k_{min} = 1/15\mu m = 0.066\ \mu m^{-1}$ and spatial frequency resolution is limited by the scan sampling size $k_{max} = 1/10nm = 100\ \mu m^{-1}$. These form the lower and upper bandwidths of limitation of our PSD plots. Further, PSD spectra obtained upon Fourier analyses of images recorded upon illuminating different areas away from the Al electrode result in similar PSD distributions, which indicate the consistency of phase separation over a large device area.

3.7 Conclusion

In conclusion, we have demonstrated different methods to probe and quantify the phase separated D-A morphology of active BHJ-OPV devices. Spatial PC decay and NSOM based imaging in the transmission mode were carried out on the OPV devices along with the AFM topology scans. In addition to these scans, local PC contrast image were obtained from film with different blend ratios at different excitation wavelengths and illumination intensities. PSD analyses of these images provide additional information where the correlation between device performances to the BHJ film morphology can be observed. The advanced near field scanning PC method is demonstrated to study morphological effects on the PC generation and carrier transport pathways. The utility of this approach for specific systems is demonstrated and discussed in Chapters 4 and 5.

Chapter 4

Direct Observation of Carrier Generation and Transport Pathways in BHJ Cells

4.1 Introduction

The performance of bulk heterojunction solar cells has been found to be strongly influenced by the thin film morphology [177]. Theoretical studies suggest that the best performance is obtained when the D-A phase separation length scale is of the order of the exciton diffusion length, in the presence of continuous percolation networks of phase separated ingredients extending from the bulk of the film to the corresponding collecting electrodes [260, 261].

We have utilized a combination of structural, optical and optoelectronic contrast mapping to study carrier generation and transport pathways in polymer-small molecule based BHJ solar cells. As discussed in the previous chapter, the technique mainly relies on current-contrast-optical scanning microscopy on asymmetric device structures that yield a near-field access for the incident light beam. The method is utilized to follow the morphological changes with annealing and different ratios of the Si-PCPDTBT:$PC_{71}BM$ blend devices, where correlations between the changes in morphology with carrier generation and transport leading to PC are clearly established. The viewpoint of increasing heterogeneity between the donor and acceptor components and continuous pathways in the entire photo-active layer upon thermal annealing are clearly evident from the optical and current contrast images. Fourier analysis of these images is used to extract relevant length scales which prevail in these binary mixtures and quantify the changes upon thermal annealing.

4.2 Near Field PC and T-NSOM Contrast Images

T-NSOM and NPC measurements of donor polymer-fullerene blend films were carried out outside of the Al electrode with a ~ 100 nm NSOM probe coupled with a He-Ne laser (633 nm, 2 mW, excitation volume ≈ 103 μm^3, Figure 4.1a). Measurements were carried out for devices based on both crystalline Si-PCPDTBT:PC$_{71}$BM and amorphous PCDTBT:PC$_{71}$BM blend.

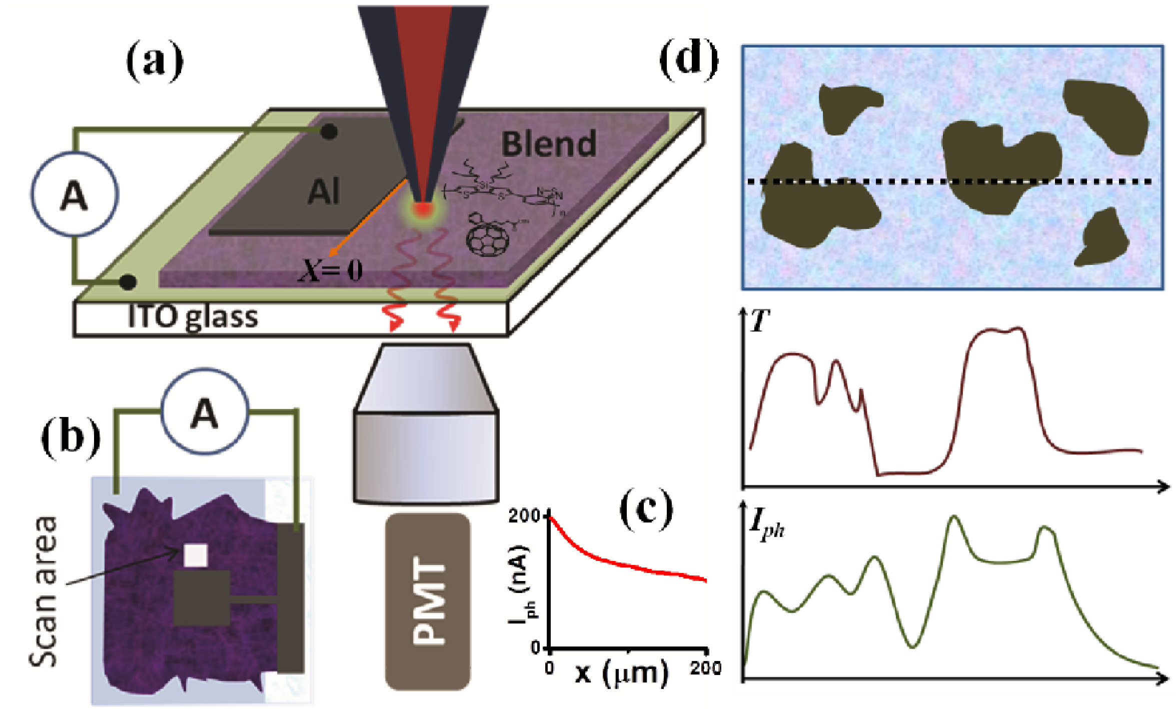

Figure 4.1: (a) and (b) are the schematic representations of the experimental set-up (c) PC decay profile outside the Al electrode. (d) Schematic representation of transmission and near field PC line profile. Reprinted with permission from Mukhopadhyay et al., J. Phys. Chem. C, 115, 17184. Copyright (2011) American Chemical Society.

The higher absorption of donor polymer relative to PC$_{71}$BM (at λ_{exc} = 633 nm) brings about the optical contrast in near-field transmission image (Figure 4.2). Simultaneously, the variation in local PC amplitude results in the NPC contrast. During device performance optimization process, it was observed that for a chosen set of processing steps, the device performance varies with D-A ratio. The differences in the device performances are mainly related to the D-A phase separation in heterojunction film. To study these morphological variations, devices consisting of different D-A ratios were examined with the NSOM microscope. However, due to the low light intensity and constrain in spatial resolution, near field measurements were carried out on blend films consisting of large domain sizes which were more suited to follow the morphological changes with the NSOM probe. In this line of pursuit, we examined devices fabricated by spin casting from solution containing larger weight fraction of acceptor (D-A - 1:2 and 1:3) rather than the optimized D:A ratio (~ 3:2) for crystalline blend. Finally, NSOM probe with smaller aperture (~ 80 nm) was utilized to probe the efficient devices which provide larger PC amplitude. During the measurement, scan area was restricted to 5 µm × 5 µm (Figure 4.1b) and the peripheral PC variation was found insignificant over the scan area (Figure 4.1c).

In the T-NSOM image (Figure 4.2a and 4.2c), the $PC_{71}BM$ network appears as brighter (red) regions with higher photon count rates as compared to the absorbing, large crystalline polymer domain (blue). Transmission contrast images reveal a dispersion of the blend components over the scan area with small aggregated acceptor domains (Figure 4.2a). During the spin-coating and solvent annealing process, crystalline donor and small molecule acceptor gets phase separated and forms interconnected D-A domains in the heterojunction film [253]. The higher acceptor concentration in blend (1:3) film drives $PC_{71}BM$ to aggregate more and reduces mixed amorphous (mixed D-A phase) fraction in blend film. This effectively enhances local transmission contrast and establishes acceptor domains more discernible in T-NSOM image (Figure 4.2c). T-NSOM image with lower acceptor concentration demonstrates a homogeneous D-A phase separation with < 200 nm length scale. With increasing acceptor ratio, a well separated D-A domain and sharp D-A interface were formed in the heterojunction film.

NPC images consist of a large number of PC-active domains with higher magnitude represented by red colored domains. PC-active domains in the NPC image correspond to the carrier generation regions, which are well connected to the electrode via. an electron transporting network (interconnected $PC_{71}BM$ domains). PC-active domains are quite inhomogenously distributed over the scan area for lower acceptor concentration, whereas overall coverage of photoactive domains increases with higher acceptor concentration in device. By comparing T-NSOM and NPC images obtained from different acceptor ratios, it can be clearly inferred that well connected acceptor networks are constituted in blends with higher acceptor concentrations.

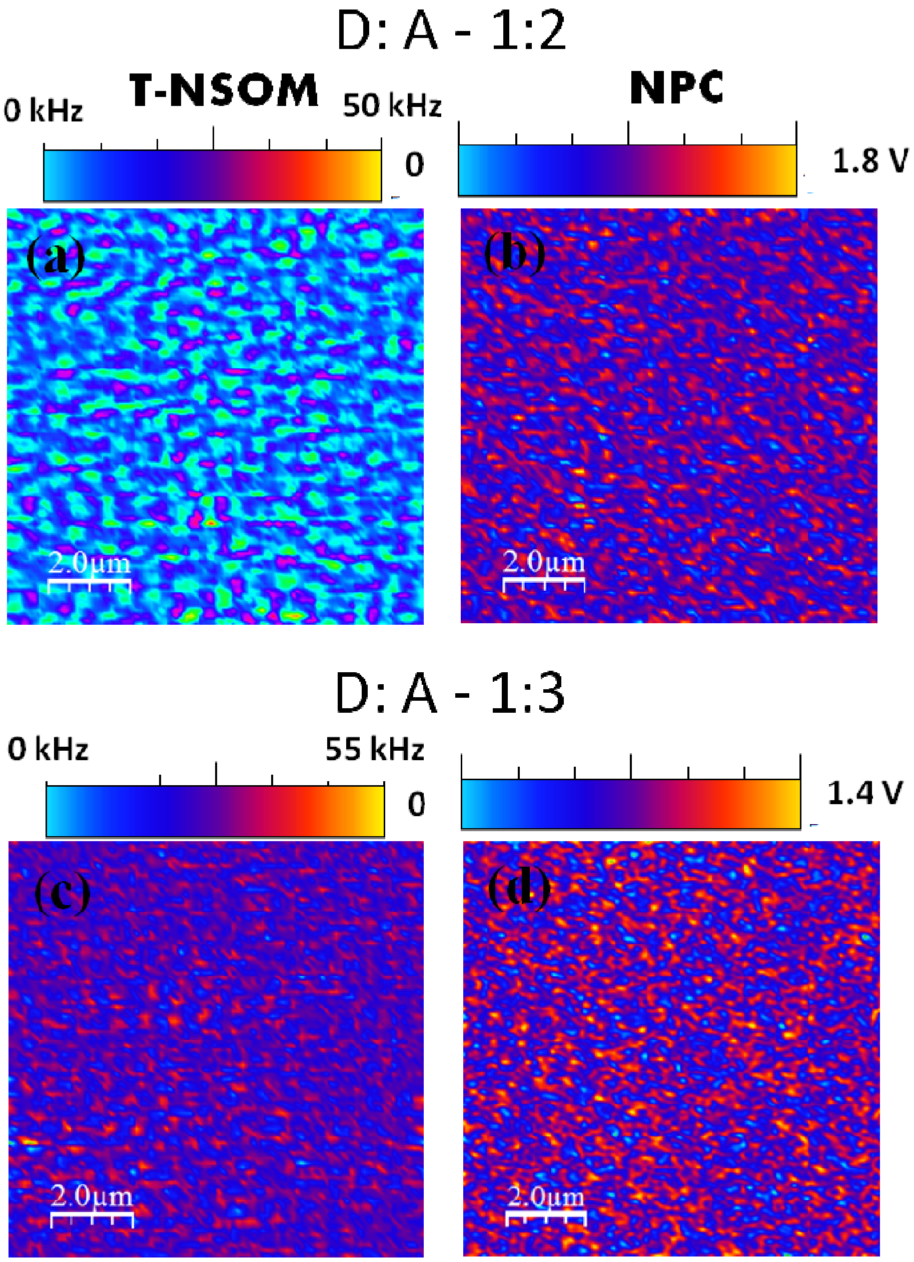

Figure 4.2: Transmission-NSOM and near field PC images of Si-PCPDTBT: PC$_{71}$*BM device with different blend ratios, 1:2 and 1:3. Reprinted with permission from Sabyasachi et al., J. Phys. Chem. C, 115, 17184. Copyright (2011) American Chemical Society.*

Current contrast in NPC measurements stems from a contributing factors, exciton generation under the excitation volume and their dissociation at D-A interface, followed by charge transport to the corresponding electrodes which is accompanied by recombination and trapping processes at different stages. Non-illuminated acceptor networks in BHJ film participate in electron transport from the point of generation to the Al electrode. So, the NPC contrast image profile represents not only active charge generation regions but also the continuous acceptor network which constitutes the current pathway (Figure 3.5). Adopting this analogy, acceptor network in BHJ film can be reconstructed from the 2D NPC contrast, and the T-NSOM image. This method of obtaining local information of PC-magnitude and connectivity can be taken as rational factors for arriving at an optimum D-A ratio for a given D-A combination.

The derivative of the T-NSOM image yields 2-dimensional contours which directly represent D-A interfacial regions in the heterojunction film. Further, it was observed that PC-active domains in a typical NPC image coincide (within ± 150 nm) with features in the derivative of the NSOM image (Figure 4.3) for scans around D-A interface. In contrast, for amorphous polymer (PCDTBT) and $PC_{71}BM$ blend devices, T-NSOM image typically is featureless and PC active domains are spread over the entire donor domain region. This can be directly attributed to the presence of amorphous regions in the polymer domains where small acceptor molecules are distributed in the microscopic length scale. Sharp D-A interface boundaries in T-NSOM image and corresponding PC amplitude for crystalline Si-PCPDTBT:$PC_{71}BM$ blend establishes the idea of efficient PC generation primarily in the vicinity of D-A interfaces.

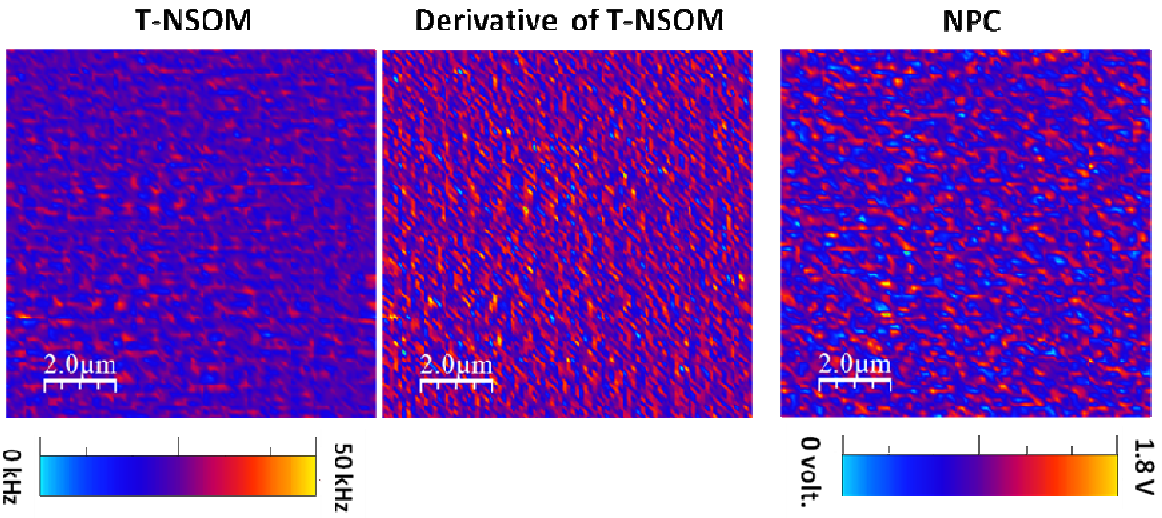

Figure 4.3: Correlations between the derivations of T-NSOM along with the NPC image form the same region for 1:2 blends.

4.3 Thermal Annealing Effects

The effects of thermal annealing process (120° C for 20 minutes) on BHJ performance were closely studied utilizing *current density-voltage* responses of pre-annealed and post-annealed devices. After thermal annealing process, improvements in both V_{OC} and J_{SC} for all devices were noticed for all different blend ratios (Figure 4.4 and Table -1). Pre-annealed and post-annealed device performance parameters for Si-PCPDTBT: $PC_{71}BM$ blend at 1:3 ratio, are summarized Table -1.

Table -1: Comparison of pre and post annealed device performances

D:A	Anneal	V_{OC} (V)	J_{SC} (mA/cm^2)	FF (%)	R_S (Ω/cm^2)	R_P (Ω/cm^2)	η (%)
1:3	Pre	0.4	10.5	33	37	118	1.17
	Post	0.63	18.2	42	43	156	3.6

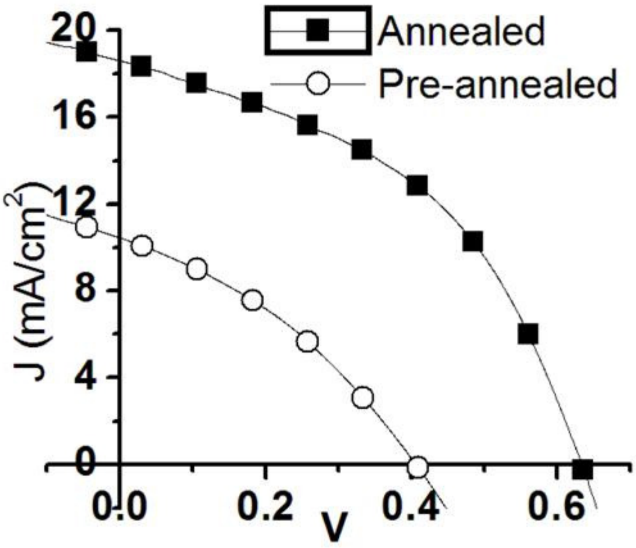

Figure 4.4: Pre and post annealed J-V characteristic for Si-PCPDTBT:$PC_{71}BM$ device with 1:3 ratio.

The enhancement in the device performance parameters, upon annealing, is directly attributed to the changes observed in the AFM/T-NSOM/NPC images. Comparison between the pre and post annealed topographic images revealed decrease in rms roughness of the blend surface with thermal annealing (~ 7 nm to ~ 3 nm). Fine nanostructures with domain size ~ 80 -110 nm (Figure 4.5a, b) were also developed upon thermal annealing.

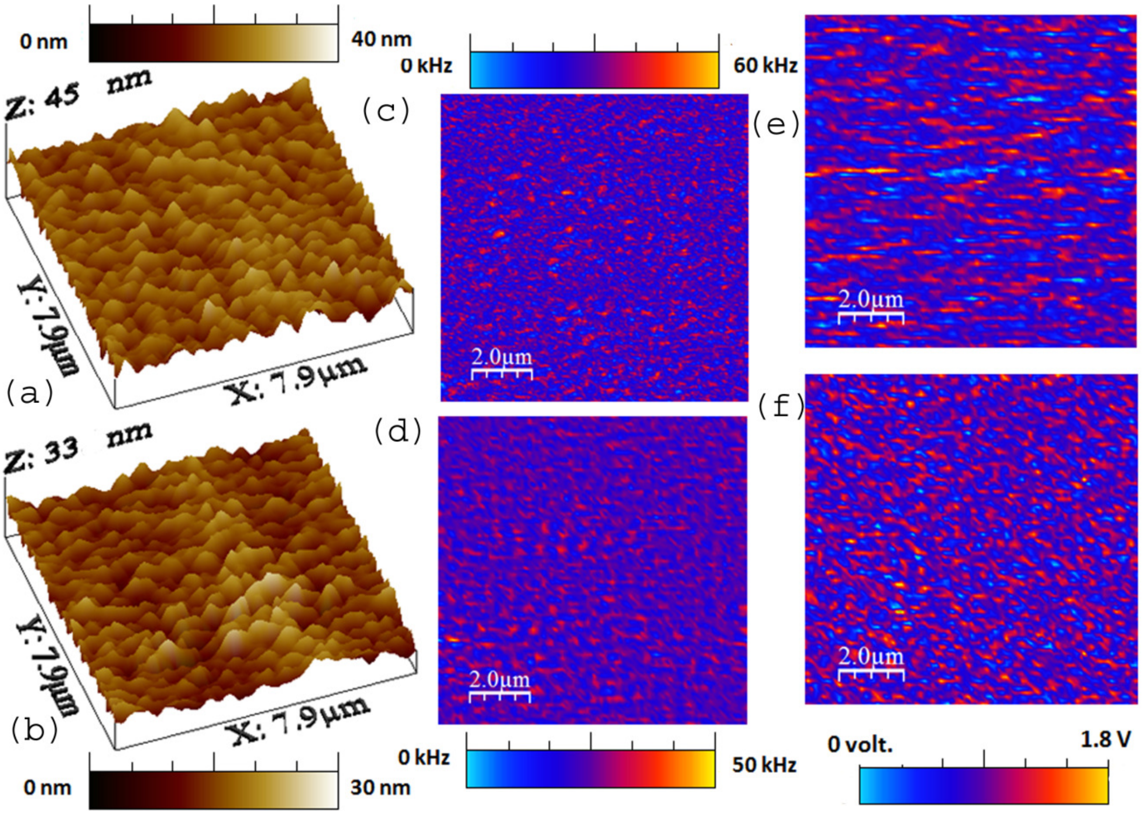

Figure 4.5: AFM and NSOM images of pre and post annealed 1:3 Si-PCPDTBT:$PC_{71}BM$ films. (a) Pre-annealed topography and (b) post-annealed topography. (c), and (d) represent transmission contrast map for pre and post annealed films respectively. Near field PC (NPC) contrasts from same region are shown in (e) and (f) respectively. Reprinted with permission from Mukhopadhyay et al., J. Phys. Chem. C, 115, 17184. Copyright (2011) American Chemical Society.

Phase contrast image of blend surface reveals that the $PC_{71}BM$ aggregation is responsible for this nano-structure formation. During annealing, polymer aggregates faster and forms larger donor domains as compared to the acceptor due to the inherent crystalline nature of the donor polymer. In this process, the $PC_{71}BM$ moieties come out from the amorphous regions and get aggregated on the top surface. The $PC_{71}BM$ aggregation on the surface improves device performance in two ways: (*i*) during thermal evaporation of counter electrode, the nanostructure surface provides less void space at the film-cathode interface, which directly improves cathode-blend film contact and (*ii*) LUMO (4.3 eV) of $PC_{71}BM$ directly matches with the workfunction (4.2 eV) of aluminum, which enhances the photogenerated carrier extraction efficiency by the aluminum electrode.

T-NSOM contrast image, before and after annealing the film are shown in Figure 4.5c and 4.5d respectively. Nearly random distributions with smaller acceptor domains are observed in pre-annealed heterojunction film (Figure 4.5c). So in a pre-annealed film, amorphous domains where small acceptor molecules are embedded in polymer matrix, dominate in the heterojunction film. These amorphous domains possess less inter-domain connectivity which is the origin of lower performance for pre-annealed devices. Moreover, an incomplete D-A phase separation during solvent annealing process is observed in T-NSOM images. After thermal annealing, significant changes in the $PC_{71}BM$ domains are observed, which is attributed to the larger diffusion range of $PC_{71}BM$ molecules that facilitates the aggregation to form sizable acceptor domains [262, 263]. Improved inter-domain connectivity for both donor and acceptor domains are clearly observable in the T-NSOM image of post-annealed films. Brighter patches with size of the order of 200 – 500 nm represent $PC_{71}BM$ domains, signifying its origin in the higher percentage of $PC_{71}BM$ in the blend. In fact, the optimum domain size for $PC_{71}BM$ for efficient device performance is expected to be of the order of 50 to 100 nm [175], and this optimum domain size is obtained in crystalline blend with a D:A ratio of 3:2. The presence of a sharper but finite number of D-A interfaces upon thermal annealing is also highlighted by noting the changes in the 2D derivative of these images.

PC-active domains in pre-annealed case are featureless and randomly distributed over the scan area. But, overall areal coverage of PC active domains increases in NPC image with thermal annealing. The enhancement in areal density of PC active domains in post-annealed devices is directly attributed to the improvement in inter-domain connectivity. This improved connectivity in the carrier transport network upon annealing also reduces carrier recombination during their transport through acceptor domains, which results in an increase of the local PC magnitude as obtained from NPC image [178, 181]. But a decrease in local PC amplitude is observed in devices containing larger weight faction of acceptor. Larger acceptor domain size in these devices reduces the donor-domain connectivity which develops an unbalanced transport in the heterojunction film. Small donor fraction in these devices reduces the light absorption in the heterojunction film and simultaneously reduces local exciton generation rate. This reduced photogeneration at large acceptor ratio results in poor device performance.

An elaborate analysis of the effects of thermal annealing on BHJ film morphology is carried out by utilizing power spectral density analysis, which is the main focus of the following section.

4.4. PSD Analysis for Pre-annealed and Post-Annealed Devices

Spatial Fourier transforms and PSD analysis of AFM/T-NSOM/NPC images yield detailed information about variations in spatial degree of BHJ films which arise from different choices of initial D-A ratios, solvent, additive factors and annealing conditions [175, 264]. The magnitude of dominant length scale along with the domain distribution is clearly identified from the PSD analyses. These length scales correspond to spatial frequencies of the features prevalent in the image (Figure 4.6). The reconstructed AFM images exhibit surface morphology features with spatial frequencies in 0.1 to 30 μm^{-1} range. The distribution of the quasi-periodic domains in reciprocal space (PSD) takes a skewed-Gaussian form signified by a dominant spatial frequency. The width and the central frequency shifts with different blend ratios and thermal annealing for AFM, NSOM and NPC images. Topography images of pre-annealed devices exhibit peak frequency distribution in the range of $0.95 \pm 0.3\ \mu m^{-1}$, representing a domain periodicity $\approx 1\ \mu m$. Upon thermal annealing, the smoothening of the surface translates to additional domain formation on the surface. The PSD frequency distribution shifts by a factor of two to $\sim 1.95 \pm 0.3\ \mu m^{-1}$ (Figure 4.6a). From PSD analyses, it is obtained that larger size of $PC_{71}BM$ domains and crystalline polymer rich domains appear at 200 – 500 nm lateral separation (the peak position corresponds to a k' value of $2\mu m^{-1}$, $k' = 1/\lambda$ and hence $\lambda = 500$ nm). This may be attributed to the donor polymer used here with a stronger tendency toward the aggregation and crystallization as compared to the processes for small molecule acceptor [149]. As shown in Figure 4.6a, the sharper profile of the PSD upon annealing indicates the larger quasi-periodic phase separation. Phase contrast image allows monitoring the changes in domains for different chemical compositions. Power spectral analyses yield insight into the domain reorganization accompanying thermal annealing. Increase in periodicity of the PSD frequency indicates diffusion of small acceptor molecules, which yield more ordered distribution of phase domains on the film surface.

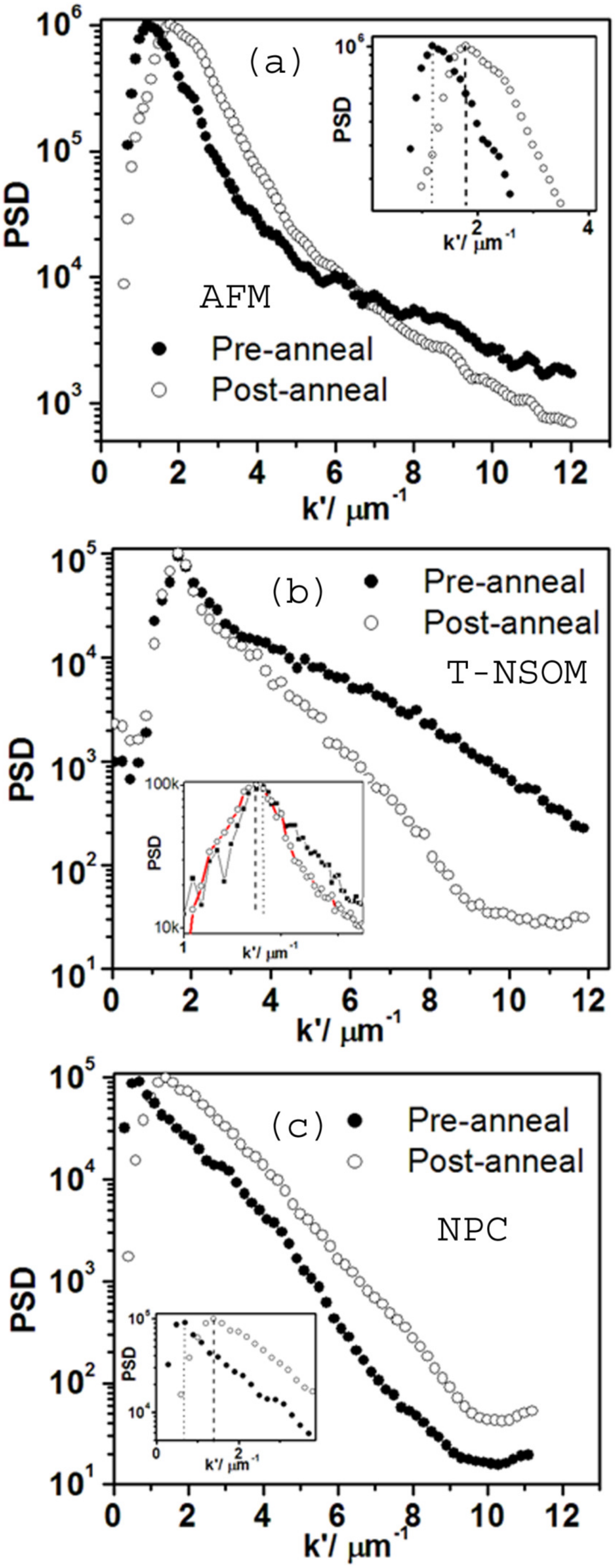(a)
AFM
Pre-anneal
Post-anneal
PSD
k'/ μm⁻¹
10⁶
10⁵
10⁴
10³
0
2
4
6
8
10
12
(b)
T-NSOM
Pre-anneal
Post-anneal
PSD
k'/ μm⁻¹
10⁵
10⁴
10³
10²
10¹
100k
10k
1
(c)
NPC
Pre-anneal
Post-anneal
PSD
k'/ μm⁻¹
10⁵
10⁴
10³
10²
10¹

Figure 4.6: Spatial power spectral distribution of pre and post-annealed images. (a) AFM-topography, (b) T-NSOM, and (c) near field PC. Insets are the zoomed part around dominant spatial frequencies. Dot and dash lines represent dominant spatial frequency for pre-annealed and post-annealed films respectively. Reprinted with permission from Mukhopadhyay et al., J. Phys. Chem. C, 115, 17184. Copyright (2011) American Chemical Society.

The PSD spectrum obtained for T-NSOM images for both pre-annealed (•) and post-annealed (o) devices are shown in Figure 4.6b. The general trend of domain size enlargement appears in form of a broad distribution with a shift of the k'_{max} to a lower value. Displacement of central spatial frequencies toward the smaller k' values (1.8 μm^{-1} to 1.6 μm^{-1}) is indicative of larger size domains and probably shorter inter-domain distances. PSD profile shifts to a lower frequency upon thermal annealing, indicating growth of both the donor polymer and the $PC_{71}BM$ domains. The shift to the lower frequency is accompanied by larger PSD intensity (9×10^4) and narrowing of the PSD distribution, and hence demonstrates a tendency towards uniform organization. However, in case of PSD analysis of NPC images, the PSD peak shifts to the higher frequency (0.65 μm^{-1} to 1.4 μm^{-1}) upon thermal annealing (Figure 4.5c). In addition, small intensity peaks are observed in PSD spectrum at spatial frequency range above 10 μm^{-1}, which corresponds to ≤ 100 nm phase separation. Upon thermal annealing, the shift to higher frequency indicates larger density of PC-active domains in the images which can be correlated with shorter inter-domain regions where the polymer matrix is dispersed. The effective dead-region or local PC-absent region is decreased upon annealing and this feature is also observed in length scales emerging from PSD analysis. The enhanced transport connectivity consequently results in higher utilization of the interfacial carrier generation and appears in form of higher areal coverage of the PC-active regions in the NPC image (Figure 4.6c).

PSD analysis correlates the annealing temperature/composition dependent phase morphology of the blend film with modified charge generation and transport properties as obtained from NSOM measurements of BHJ solar cells. The improvement in the percolation connectivity can be quantified from T-NSOM and NPC images. The components of the NPC image-matrix is analyzed by noting $[NPC(x, y)] \sim [CG] \times [\Gamma]$, where $[CG]$ is the co-ordinates for carrier generation and $[\Gamma]$ represents an electrical transport function. Connectivity matrix $[\Gamma]$ can be deduced from the NSOM and NPC images, with some basic assumptions. The PSD features are then taken as a measure for the observed trends. The decrease in the area of PSD (k') of the derivative of NSOM, accompanied by the increase in PSD (k') of NPC upon annealing is consistent with physical processes of the underlying microstructure. The 2-dimensional acceptor connectivity can be estimated by pixel to pixel comparison of T-NSOM and NPC image $\{[\Gamma] = [CG]^{-1} \times [NPC]\}$. The shift in the PSD (k') spectrum (2.5 $\mu m^{-1} \rightarrow 0.95\ \mu m^{-1}$) and increase in the area (40-60% depending on annealing condition) of the post annealed PSD (k') quantifies the improved connectivity upon annealing.

4.5 Wavelength Dependent Measurements

Optical absorption spectrum of pure Si-PCPDTBT polymer film reveals that absorption coefficient (α) is one order of magnitude higher for red region ($\alpha \sim 10^5$ cm^{-1}@ $\lambda \sim 633$ nm) as compared to green region ($\alpha \sim 10^4$ cm^{-1}@ $\lambda \sim 532$ nm) [87]. So, green light penetrates deeply in the blend film as opposed to the red light. In case of blend with $PC_{71}BM$, these trends also present. Hence, local PC images with low power red illumination primarily restricted to the absorption volume in the proximity of the film surface and can be considered as point spread light source (~ 70 nm below the surface); moreover, it does not yield the overall 3D bulk information of the blend film in optical transmission. Green light generates carrier in blend film as a line spread throughout the film and accompanies the bulk morphology of blend film (~300 nm). Near field PC measurements with different excitation sources confirm this hypothesis (Figure 4.7). Topography, phase and T-NSOM images show negligible changes with different excitation, but the NPC image is markedly different for the two types of laser excitations. The area coverage of PC-active domains is much smaller for red as compared to green, where a near uniform density is observed over the same region for green (Figure 4.7, last column). These results also support the vertical modulation of acceptor concentration in the blend film during spin coating, which is well studied for P3HT:$PC_{60}BM$ solar cells [254]. The combination of T-NSOM and NPC profiles can be utilized to arrive at a more realistic 3D interconnected acceptor network as shown in the schematic, which can additionally be verified using wavelength (λ) dependent imaging.

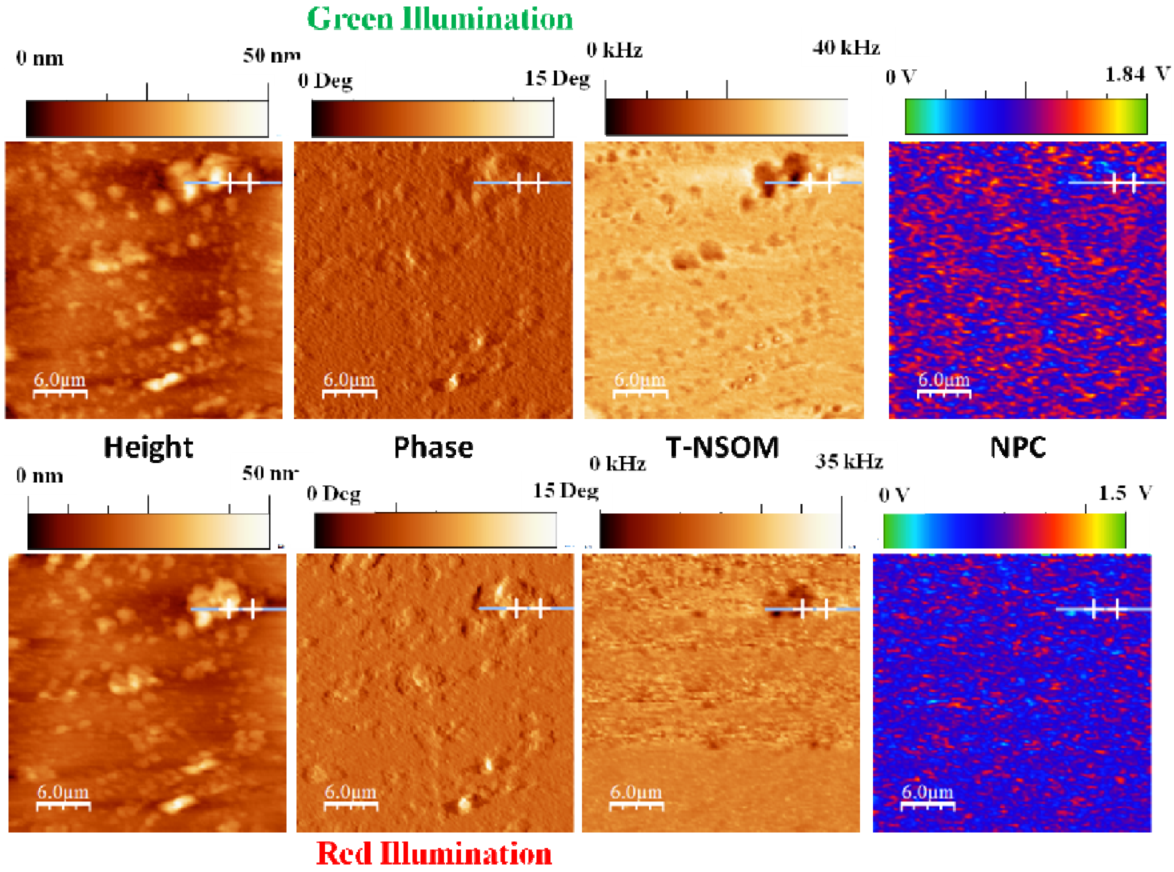

Figure 4.7: Height, Phase, T-NSOM and NPC contrast images of Si-PCPDTBT: $PC_{71}BM$ blend film (thickness ~ 200 nm) when probed with green and red laser.

4.6 Cross Correlation Analysis

In NSOM measurements, random height variations of film surface sometimes induce topographical artifacts in contrast image. This arises from the rapid variation of NSOM tip under the feedback mechanism of the raster scanner. Then, the distance between NSOM tip and sample surface drastically varies over a rough surface. Also, the thick metal coating surrounding the glass NSOM tip produces a spatial offset between the NSOM image and topographic contrast image obtained by AFM through feedback signal. Such artifact induced images are distinguished from the real images through cross correlation analysis [265]. As T-NSOM is a direct conjugate of the near-field absorption, we define cross correlation image analysis between the T-NSOM and NPC images in such a way that maximum correlation appears at larger PC amplitude and low transmission contrast. Cross correlation analyses were carried out using various devices with 3×3 µm scan area, at

256×256 pixel resolution. Each pixel in the correlation mapping corresponds to the scalar product between two images– $a \otimes b = \sum_{x,y} a_{x,y} b_{x,y}$.

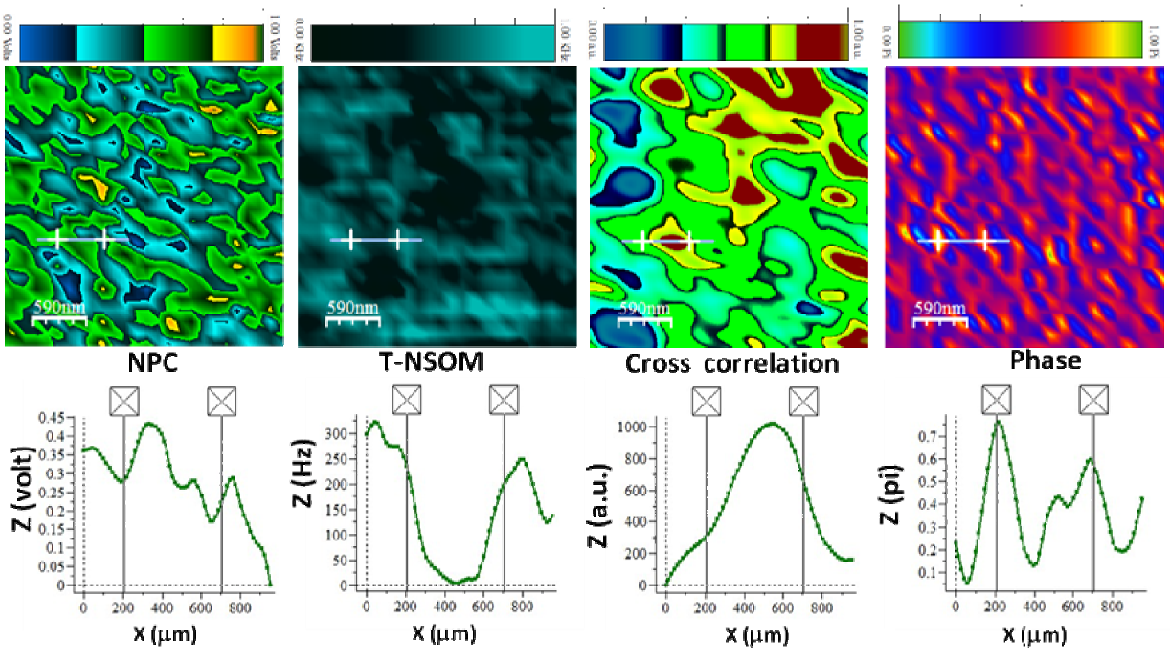

Figure 4.8: Cross correlation of T-NSOM and NPC images. Oscillatory phase variations are also observed at the maximum NPC region.

The dark and bright regions in correlation image signify the high and low correlation between light transmission and NPC images respectively (Figure 4.8). The presence of peak in the line profiles of correlation image indicate the mismatch between the NSOM transmission and NPC images (higher PC amplitude corresponds to lower transmission i.e. larger absorption, donor domains). Correlation analyses between the topography (phase) and NSOM transmission images depict a spatial off-set of ≈ 250 nm with respect to the optical image because of the large contribution of shear force from the edge of the NSOM probes. The spatial offset (≈ 100 nm) between the T-NSOM and NPC can be extrapolated by exciton diffusion from donor domains to the D-A interface. *Cross correlation analysis at the interface concludes that maximum PC generation regions are slightly toward the polymer phase where excitons are generated upon light absorption.* Given the expected quantitative correlation between the NSOM transmission/phase contrast and local PC contribution, it appears that local PC sometimes is totally anti-correlated to the phase and correlated with light transmission. But, at some regions on the film surface, phase contrast image is more informative than T-NSOM image and supports the basic hypothesis about charge separation at the D-A interfaces (Figure 4.8). Indeed, when the images are overlaid, it appears that the largest PC does not associate with large domains, but rather correlate to the interfacial regions (with ~ 100 nm offset). Substantial differences in optical transmission signals were observed for spin-cast and annealed films where darker regions in the NSOM images always correlated to the areas of donor polymer aggregation in the film.

4.7 NPC Measurements in a DC light Background

In a BHJ network, carriers are mostly trapped both energetically and spatially, either at the D-A interface and in isolated polymer, or fullerene domains, due to the lack of percolation path [266]. Solar cells working under operating condition (AM 1.5) has enhanced intrinsic carrier concentration compared to dark condition and it affects the overall charge generation and trap state distribution throughout bulk film, and finally IPCE of the devices [267]. It is well understood that geminate losses are primarily responsible for limiting J_{SC}, but the device fill factor is mostly determined by the nongeminate recombination due to the enhanced carrier concentration at the device operating conditions [268]. Charge accumulation at the interface directly modifies internal electric field distribution with enhanced bimolecular recombination [111, 269]. Near field PC mapping with optical perturbation (DC illumination) is appropriate for studying the carrier transport and recombination in organic solar cells by monitoring local response over a given scan area (Figure 4.9).

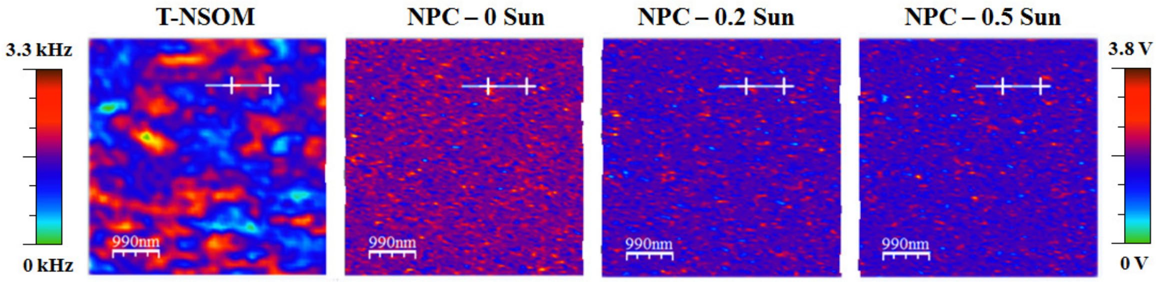

Figure 4.9: T-NSOM and corresponding near field PC (NPC) images for same region with different background intensities (labeled at the top of each images).

With optical bias, the areal contribution to the PC-active domains decreases gradually such that at intensity of 0.5 Sun, only 10% of the scanned area is PC active. These images reveal the important meso-scale effects of background light on charge generation and recombination process. Si-PCPDTBT:$PC_{71}BM$ blends have an intrinsic tendency for hole trapping with a broad trap distribution in energy (~ 400 meV) [113]. Hole mobility in

Si-PCPDTBT:$PC_{71}BM$ blend films is found to be ten times lower than the pristine one (pristine μ_h~ 1 ×10^{-2} cm^2 V^{-1} s^{-1}, blend μ_h~ 1×10^{-3} cm^2 V^{-1} s^{-1})[149]. NPC mapping with constant DC light illumination demonstrates electron transport through the uniformly illuminated acceptor networks. Images not only yield active recombination centre for the electron but also account recombination in the continuous transport network. At dark condition or low DC light intensity, trap states present at D-A domain significantly contribute in the trap-assisted lateral transport by preventing recombination with trap holes at the D-A interfaces. Hole trap states above the HOMO level of donor and defect states in $PC_{71}BM$ get occupied with optical bias which increases bimolecular recombination rate at the D-A interface. Filled trap states under DC background blocks the various transport pathways and free carriers during their transit to corresponding electrodes that experience an enhanced bimolecular recombination. It can be concluded that under the operating condition (~ 1.5 Sun), not only the exciton generation or bimolecular recombination (because of large carrier density) at the interface occurs, but occupied trap states also enhance recombination rate during carrier transport, which plays the most significant role in limiting device fill factor and EQE.

4.8 Conclusion

In conclusion, we have demonstrated a versatile technique to examine the D-A based bulk heterojunction morphology using a combination of current-contrast-optical scanning microscopy on asymmetric photovoltaic device structures. The technique is used to follow the changes in charge carrier generation and transport with thermal annealing and different ratios of Si-PCPDTBT:$PC_{71}BM$ blend system. Fast Fourier analysis and power spectral density methods are utilized on optical and PC contrast images to extract the relevant length scales which prevail in blend films. This approach is widely applicable to other D-A systems, and can be used to monitor the evolution of morphology and charge generation with different processing conditions and their optimization for achieving efficient solar cells.

Chapter 5

Rationalization of Donor-Acceptor Ratio Complying Spatial Photocurrent Studies and T-NSOM Mapping

5.1 Introduction

In the previous chapter we introduced the scanning approach to image the BHJ devices with the active layer consisting of crystalline Si-PCPDTBT donor polymer and $PC_{71}BM$ acceptor molecule. Distinct phases of the individual components were imaged. The effects of thermal treatment were observed and analyzed. In the present chapter we have emphasized the power of this approach in determining and rationalized the D-A ratio for a BHJ structure. The optimum D-A ratio is expected to be vary with the crystalline nature and aggregation characteristics of the donor polymer. Phase separated D-A film morphology in photoactive layer plays a crucial role in polymer/fullerene BHJ-PSC performance [5, 270]. The most common picture of bulk heterojunction cells (BHJ) is that photogenerated exciton at the donor phase diffuses to the interface with the nearby acceptor phase where weakly bound exciton dissociates and charge (electron) transfer from donor to acceptor occurs. These free polaronic type carriers are then transported to the electrodes through corresponding percolating pathways that exist in different phases [5, 89, 270]. All the above mentioned sequential processes are directly or indirectly affected by the active blend morphology [184, 271, 272]. The existence of distinct phases corresponding to the donor and acceptor components has been questioned recently, especially in the context of amorphous donor polymers [273]. Morphological studies on these systems have indicated a mixed phase representing the polymer network with entrapped acceptor molecules and a distinct acceptor phase [243]. In case of well annealed BHJ blend film of crystalline polymer such as P3HT, donor and acceptor phases appear to emerge at 20 – 40 nm length scales (Figure 2.14) [5, 191, 274, 275]. Recent studies demonstrated that for small molecule fullerene derivative such as $PC_{61}BM$ or $PC_{71}BM$, phase separated morphology is primarily governed by the crystalline or amorphous nature of the donor polymer [276, 277]. Optimum device performance is obtained at 1:3 (D-A) blend ratio with a model amorphous polymer PCDTBT (Poly [N-9'-heptadecanyl-2,7-carbazole-alt-5,5-(4',7'-di-2-thienyl 2',1',3' benzothiadiazole)]), whereas for crystalline polymer like Si-PCPDTBT (Poly [(4, 4-bis(2-ethylhexyl)dithieno[3,2-b:20,30-d]silole)-2,6-diyl-alt-(4,7-bis(2-thienyl)-2,1,3-benzothiadiazole)-5,50-diyl]), 3:2 is the optimum. Beside the charge transport factor, carrier generation and charge separation (charge transfer complex) processes in BHJ are also affected by the fine or coarse nanoscale D-A phase separation. The charge-transfer complexes associated with the fine dispersion of $PC_{71}BM$ in the amorphous PCDTBT matrix are not observed in the Si-PCPDTBT blend, where polymer and $PC_{71}BM$ form distinct crystalline domains [276]. From the microstructure perspective, these different families of BHJs are expected to have their highest device efficiency for entirely different D-A ratio.

A direct measure of local short circuit PC from the mixed phase region reveals considerable insight into the microstructure [278, 279]. Different types of D-A network have been explored utilizing this method [247]. A key process in PC mapping is imaging of the local optical and PC contrast over a large number of D-A domains in a given scan area (5×5 μm^2). D-A domains in Si-PCPDTBT:$PC_{71}BM$ blend are sizable and can exceed 200 nm in lateral dimension for (> 50% $PC_{71}BM$) and is within the scan-resolution of PC mapping.

Different model systems for broad class of polymer-small molecule BHJ with relatively higher efficiencies have been utilized for further studies [5, 276]. Devices studied consisted of different fractions of $PC_{71}BM$, blended with crystalline Si-PCPDTBT and amorphous PCDTBT as donor polymers. PCDTBT form distinct microstructure in blend film whereas bridging atom (silicon) leads to higher chain packing and high degree of π-delocalization in pristine as well as blended Si-PCPDTBT films [276].

5.2. Fabrication and Electrical Measurements

Photovoltaic devices are fabricated on ITO coated cover slip (thickness ~ 170 μm) to minimize wave-guiding and scattering effects upon local illumination. Blend films are prepared with varying $PC_{71}BM$ concentration from 20% to 80% with respect to the composite film by spin-casting the appropriate concentration from cholorobenzene/Dicholorobenzene solutions (15 mg/ml). Optimized solar cell device structure with appropriate solvent and annealing conditions along with asymmetric electrodes (ITO electrode orthogonal to Al electrode strip) were fabricated to study the spatially varying PC measured using standard lock-in technique (ω ~ 270 Hz) [278]. The optical absorption of both individual as well as Si-PCPDTBT/$PC_{71}BM$ blend film (1:1) was measured in the range of 450 – 1000 nm (Figure 5.1a). Strong absorption of $PC_{71}BM$ in green region yielded a nearly constant absorption of the blend in the visible range.

The optimum solvent evaporation techniques differ generally on chemical composition of donor polymers and solvents used. The process-optimized devices typically showed the following characteristics: PCE ~ 1.5 %, J_{SC} ~ 6 mAcm^{-2}, FF ~ 0.42 and V_{OC} = 0.63 V at AM 1.3 illumination. *J-V* characteristics of PCDTBT:$PC_{71}BM$ devices with different blend ratios are shown in the Figure 5.1(b). The trend of increasing V_{OC} and J_{SC}, at specific D-A ratio, indicates optimal range for interfacial area. Figure 5.1(c) demonstrates the change in the calculated series and parallel resistances with blend composition. For all devices, parallel resistance is 10^3 times higher compared to series resistance. Variations in blend morphology have less effect on the series resistance and reveals that a certain fraction of continuous percolation path for carrier transport is always present in blend morphology. But blend morphology significantly modifies the carrier recombination kinetics as observed in parallel resistance variation. Origin of low parallel resistance for 1:3 blend ratio can be explained by the efficient extraction of free charges and lower carriers loss due to the optimized domain size and interconnected transport path. The large scale phase separation and effects of interfacial defect states (amorphous region) can be correlated to the lower V_{OC} for 1:1 and 1:2 blend devices. With increasing $PC_{71}BM$ fraction in blend, more pure D-A phase separated domains are formed, which reduce carrier loss, and balanced electron and hole transport ($\mu_e \approx \mu_h$) in blend film.

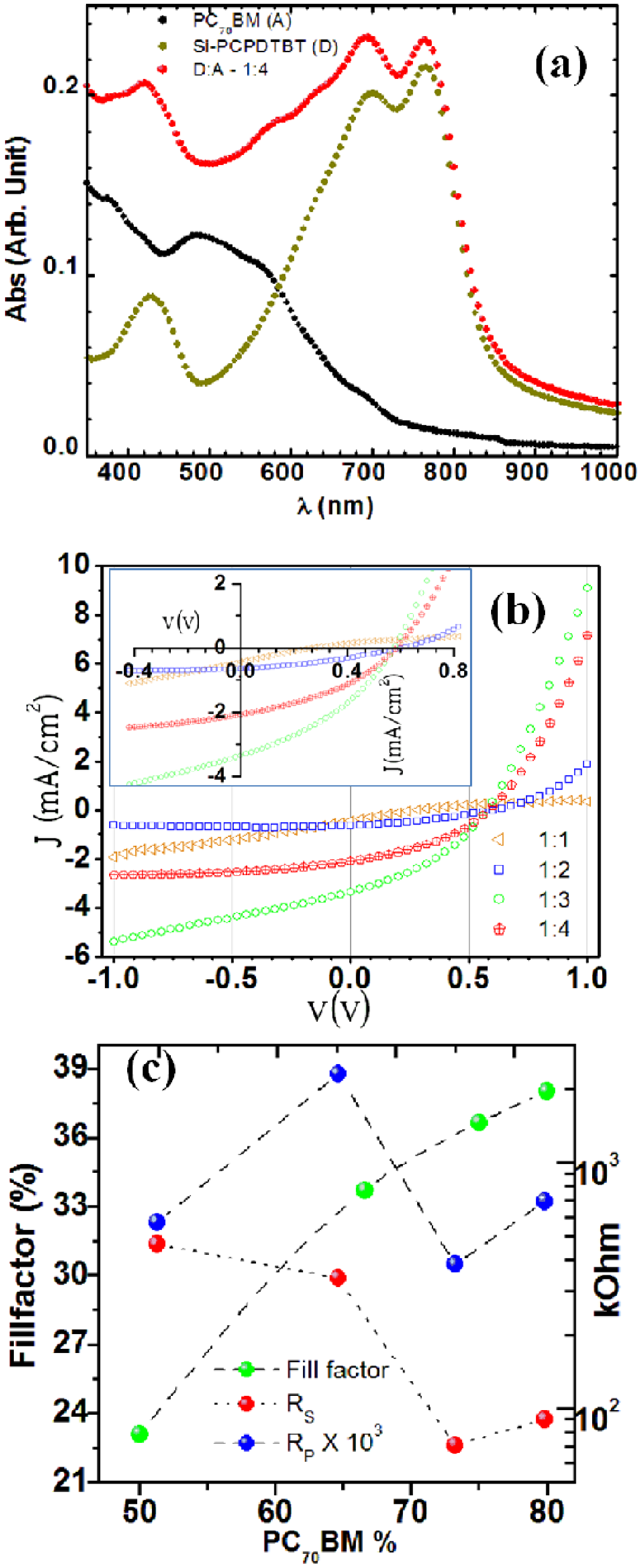
(a)
PC70BM (A)
SI-PCPDTBT (D)
D:A - 1:4
Abs (Arb. Unit)
0.0
0.1
0.2
λ (nm)
400
500
600
700
800
900
1000
(b)
J (mA/cm2)
V(V)
-6
-4
-2
0
2
4
6
8
10
-1.0
-0.5
0.0
0.5
1.0
1:1
1:2
1:3
1:4
v(v)
J(mA/cm2)
-0.4
0.0
0.4
0.8
2
0
-2
-4
(c)
Fillfactor (%)
kOhm
PC70BM %
21
24
27
30
33
36
39
50
60
70
80
10^3
10^2
Fill factor
RS
RP X 10^3

Figure 5.1(a) Optical absorption coefficient of $PC_{71}BM$, Si-PCDTBT and blend film spun on quartz substrate. (b) BHJ characterization of PCDTBT:$PC_{71}BM$ with different blend ratios and inset shows the variation of V_{OC} and J_{SC} with blend ratio. (c) FF, series resistance (R_S) and parallel resistance (R_P) variation.

Device fabrication process can be optimized by varying blend ratio with the best combinations of all the above mentioned parameters. Balanced transport serves better fill factor for any blend in bulk heterojunction structure as observed in 1:3 ratio for PCDTBT: $PC_{71}BM$ blend. Bulky active layer (large film thickness) reduces the fill factor in different ways – strong exciton dissociation rates at the interface, unbalanced transport and consequence space charge effects. The device thickness was optimized by comparing dark and light *J*-V, which in other ways help avoid Space Charge Limited Current (SCLC) regime (Figure 5.2a). From the slope values, it is (> ~ 0.8) evident that none of the device performance is limited by SCLC. At 1.5 Sun intensity, fill factor and extracted PC ($J_{Ph} = J_L - J_D$) at reverse bias are maximum for 1:3 blend ratio as compared to other ratios.

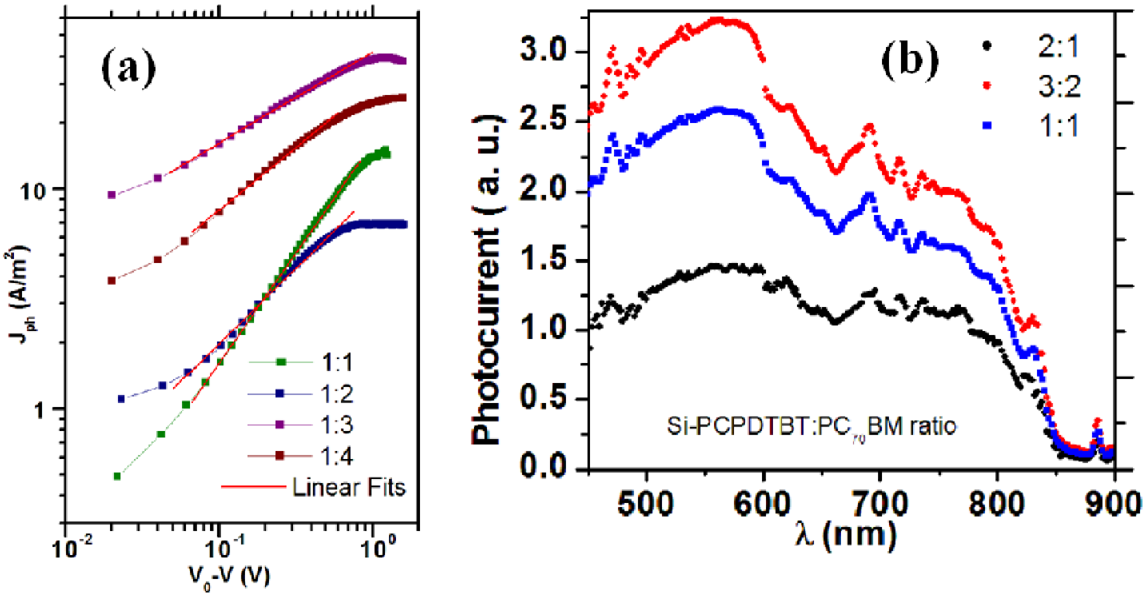

Figure 5.2: (a) Logarithmic plot of extracted PC (J_{Ph}) vs. applied internal electric field for PCDTBT:$PC_{71}BM$ devices with different acceptor ratio. (b) PC response of Si-PCPDTBT:$PC_{71}BM$ BHJ solar cells with different blend composition.

PC action spectrum of Si-PCPDTBT:$PC_{71}BM$ devices with different acceptor ratios demonstrate that 3:2 (D-A ratio) is optimum for obtaining height performances from this blend (Figure 5.2 b). It can be also confirmed from the *J-V* characteristic of these devices (Figure 5.3).

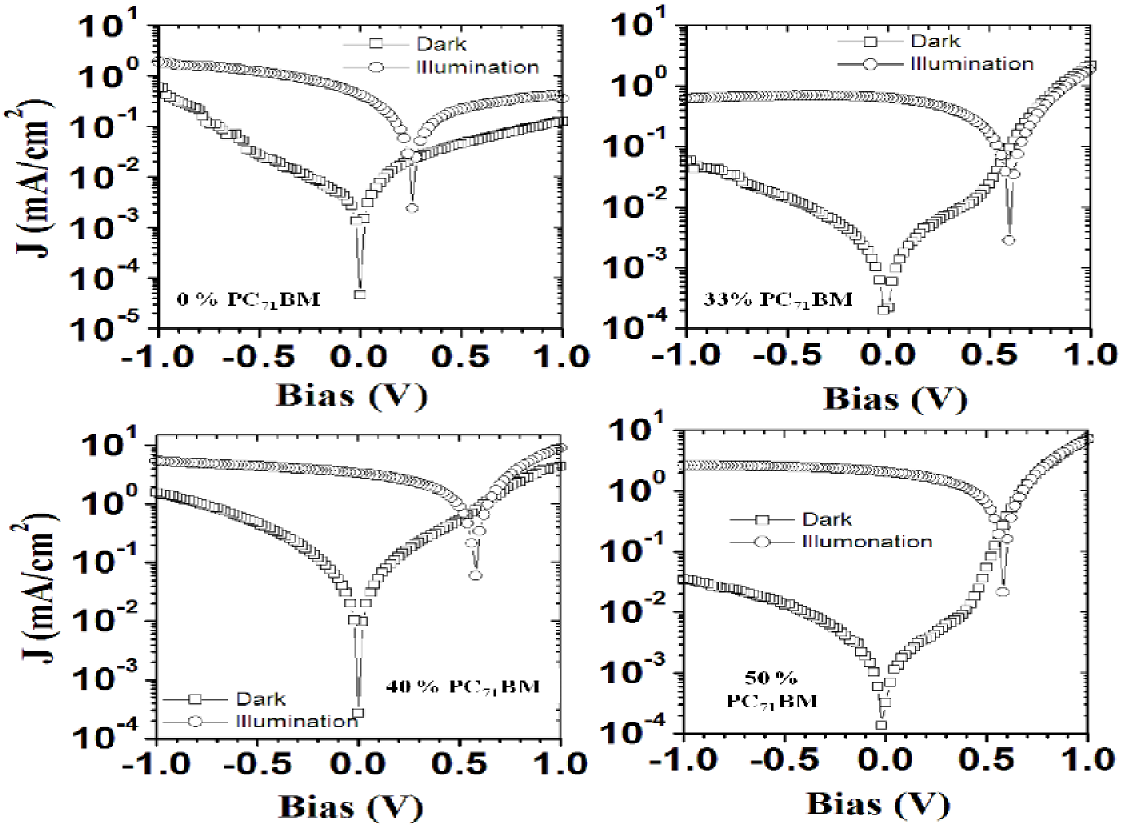

Figure 5.3: Semi-logarithmic Current density-Voltage characteristic of Si-PCPDTBT:PC$_{71}$BM devices with different blend ratio.

5.3. Morphological Study: AFM Imaging

AFM topography images of Si-PCPDTBT:PC$_{71}$BM films depict the existence of morphological length scale of ~ 40 nm (Figure 5.4a and b). The approximate rms roughness of the films is ≈ 6 ± 2.5 nm. Phase contrast images depict the pure phase segregation of donor and acceptor materials in BHJ films and their interconnected networks (Figure 5.4c). Other than BHJ morphology, active polymer-cathode interface properties have critical influences on the solar cell efficiency [246]. This practical constraint was defeated by controlling thermal evaporation rate (3-5 Å/s) of cathode metal contact. High resolution AFM studies of blend films with different acceptor concentrations reveal the distribution of D-A component on film surface. In the absence of any additional blocking layer, aggregation of acceptor material at cathode-blend film interface directly improves the solar cell performance. So along with bulk morphology of the spin coated films, enrichment of acceptor material on film surface has a crucial role in charge extraction. Photo-conducting AFM at the same region was performed with Pt/Ir coated Si probes with +/- 2 bias range, keeping ITO electrode as ground. Local current variations at different tip bias can be correlated to $PC_{71}BM$ aggregation on the film surface.

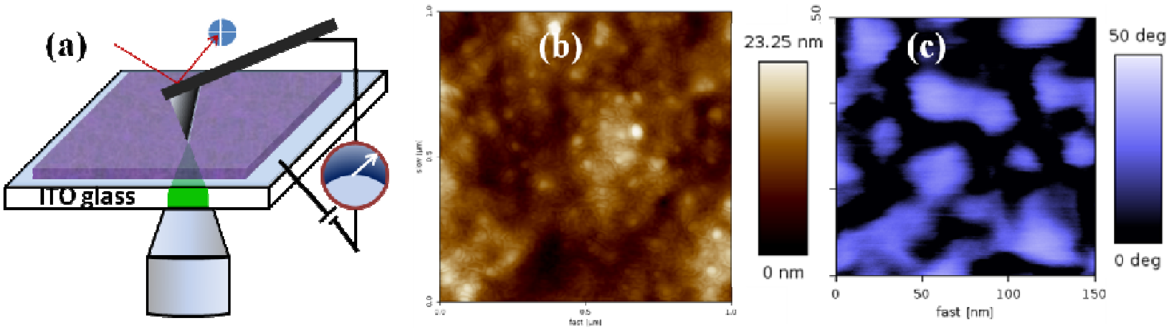

Figure 5.4: (a) Schematic of photo conducting AFM measurement, (b and c) topographical and phase contrast measurements of blend film (~ 70 nm) with 1:3 ratio.

Phase contrast AFM image of PCDTBT:$PC_{71}BM$ blend helps in distinguishing individual islands of different chemical constituent in the film (Figure 5.5). The height of the domains is in between 10-15 nm, and not much of a variation was observed in rms roughness (~ 2 nm) for varying $PC_{71}BM$ ratios. A homogeneous phase distribution was observed for low $PC_{71}BM$ containing films (≤ 50%). As $PC_{71}BM$ fraction increases, the phase distribution becomes inhomogeneous and distinct phase separation between the two components is discerned. The lateral phase distribution is attributed to the diffusion of $PC_{71}BM$ molecules within the polymer matrix under thermal annealing process and substituent crystallization to large lateral dimensions. Lateral periodicity is approximately 10-30 nm for 1:1 ratio and is increased to the order of 40-60 nm for 1:3 blend ratio. This large-scale phase separation (1:3) enormously reduces the overall interfacial area, causing a significant decrease in recombination process with an improved device performance. A larger D-A phase distribution (>100 nm) is observed in blend films with > 80% $PC_{71}BM$ concentration and simultaneously less interconnected donor domains yield low device efficiency.

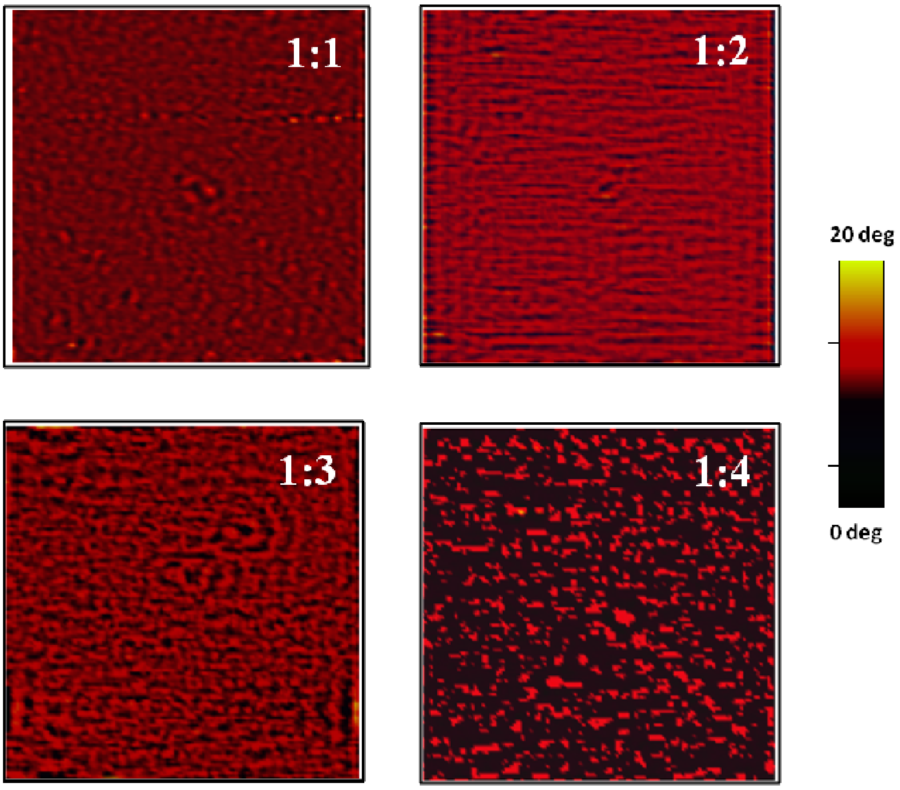

Figure 5.5: Phase contrast image (500 × 500 μm) of blend films with different D-A ratio. Domains with larger phase contrast reflect the distribution of donor chemical composition.

5.4 Spatial Decay Measurements

The local illumination induced spatial PC profile was obtained using a tightly-focused laser spot which was scanned across the electrode boundary in an asymmetric device structure (Figure 5.6 and 5.7) [278, 280]. Results from decay measurements with Si-PCPDTBT and PCDTBT blends with different PC$_{71}$BM concentrations demonstrate that initially both *e* and *h*-decay lengths (L_D^e and L_D^h) improve with increasing PC$_{71}$BM fraction.

This trend has been utilized to obtain an optimum value for the (carrier generation) × (charge-separation) × (charge-transport) product which is accessed for a critical acceptor-concentration. Beyond the critical acceptor concentration, well connected acceptor network enhances electron mobility, which creates an unbalanced transport with modified bimolecular recombination kinetics in bulk film [281]. A simplistic first order exponential decay fit for all PC profiles yield the decay length as obtained from the expression $\Delta n(x) = \Delta n_0 exp\left(-x/\Lambda_\gamma\right)$ where $\Lambda_\gamma^2 = D/k_r \gamma n_b^{\gamma-1}$.

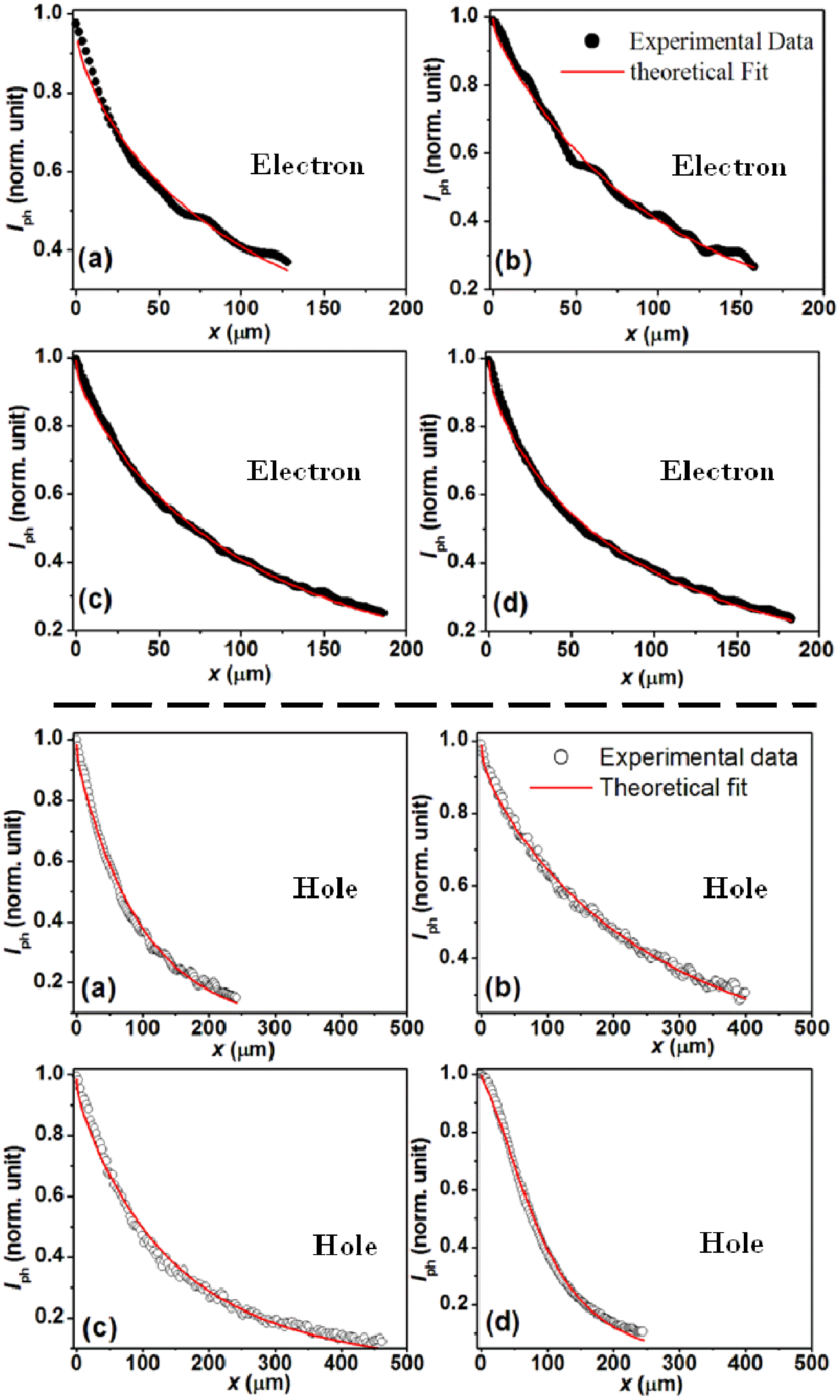

Figure 5.6: Spatial PC decay profile for electron (filled circle) and hole (open circle) current and corresponding theoretical fits for PCDTBT:PC$_{71}$BM devices. Decay profile is obtained by varying PC$_{71}$BM composition in blend ratio from (a) 50%, (b) 66%, (c) 75% and (d) 80%.

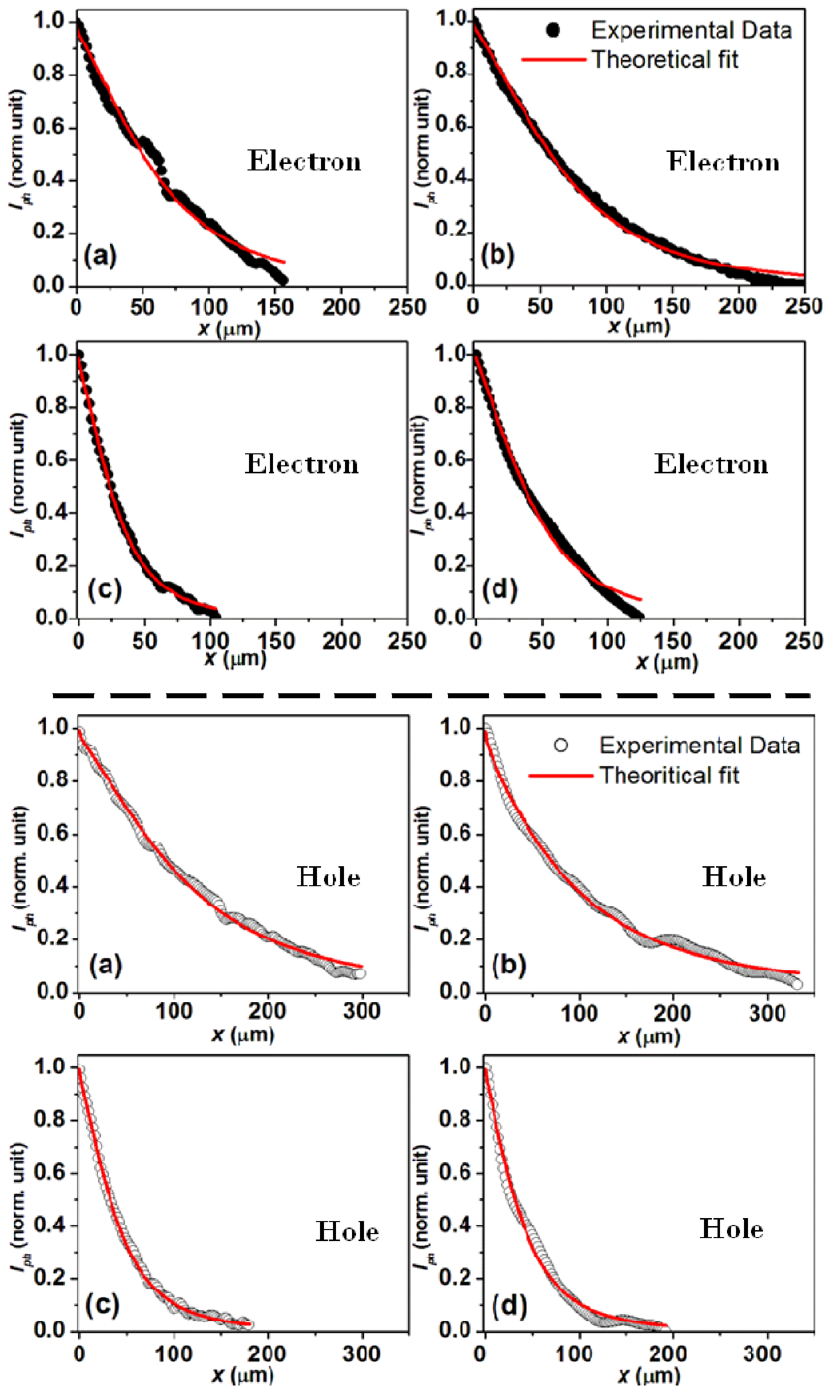

Figure 5.7: Spatial PC decay profile for electron (filled circle) and hole (open circle) current and corresponding theoretical fits for Si-PCPDTBT:PC$_{71}$BM devices. Decay profile is obtained by varying PC$_{71}$BM composition in blend ratio from (a) 33%, (b) 40%, (c) 50% and (d) 66%.

Large anisotropy in decay length ratio (L_D^h/L_D^e) for amorphous system were observed as compared to crystalline system even at the optimum acceptor concentration. Electron decay (L_D^e) magnitude varies gradually in the amorphous system and comparatively sharper changes are observed in the crystalline system with respect to the acceptor-concentration (Figure 5.8a and b). The anisotropy in decay length can be directly attributed to the microstructure properties of the donor polymer. Si-PCPDTBT:PC$_{71}$BM blend film attests a strong aggregation feature in an absorption spectra range of 600-850 nm. It indicates that polymer chain tends to stack even in presence of PC$_{71}$BM. This highly crystalline nature of the silicon bridged polymer improves the charge carrier transport; reduces probability of charge transfer complex formation and bimolecular recombination rate (k_r). Presence of long-lived charge transfer states in amorphous PCDTBT:PC$_{71}$BM blends are evident from transient measurements, but are absent in Si-PCPDTBT:PC$_{71}$BM blends [276]. In pristine polymer films, carrier mobilities (μ_h) were found to differ by a factor of 5, with Si-PCPDTBT polymers having higher mobilities [149].

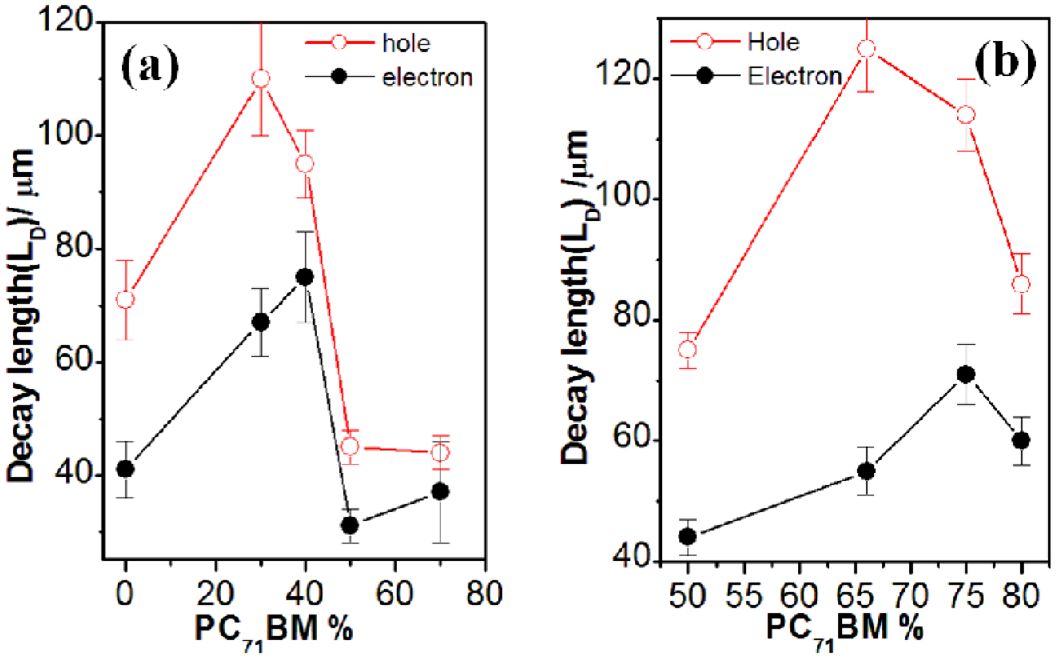

Figure 5.8: Electron and hole decay length from single exponential fit to the decay profiles for (a) Si-PCPDTBT:PC$_{71}$BM and (b) PCDTBT:PC$_{71}$BM blend with varying PC$_{71}$BM concentration. Error bar shows device to device variation in measured decay length (L_D). Reprinted with permission from Mukhopadhyay et al., Applied Physics Letters, 100, 163302. Copyright [2012], American Institute of Physics.

Balanced electron and hole mobilities could be obtained by introducing acceptor molecule (PC$_{71}$BM) with the polymer. Anisotropy in mobilities (μ_h/μ_e) was found to be about a factor 3-5 lower in the PCDTBT blend as compared to the blend with Si-PCPDTBT

[149]. Si-bridge device exhibits a non-Langevin type recombination with coefficient (~ k_r) ~ 1.2 × 10^{-12}cm^{3}s^{-1} whereas PCDTBT solar cells exhibit Langevin type recombination with rate ~ 10^{-10} cm^{3}s^{-1} [149]. Transient photo-voltage spectroscopy measurements with different D-A morphology support that bimolecular recombination gets suppressed at critical morphology of polymer-fullerene blend [149]. The difference in carrier mobilities ((μ_h/μ_e) and recombination rates mainly direct the anisotropy in the first order decay lengths (L^h_D/L^e_D) for amorphous and crystalline donor polymer blend.

5.5 Circuit Model Analysis

The morphology dependent decay profile is analyzed by spreading impedance analysis incorporating the percolation network parameters [251, 282]. The interconnected D-A networks in BHJ films are represented by the series resistor ($R_{sp}(x)$), whereas parallel resistor R'_R represents the recombination during the carrier transport [282]. A morphology dependent spreading resistance function $g(x) = exp((x/\xi)^{\alpha})$ quantifies the blend morphology and electrical connectivity of networks in terms of a characteristic length scale ξ and a stretch exponent α [282]. The change in the percolation path length with different D-A ratios for *e*/*h* transport accounts for the variation of the meso-scopic correlation length ξ (Table-2). ξ_e and ξ_h increases initially with PC$_{71}$BM concentration, reflecting the trend towards balanced carrier transport ($\mu_e\tau_e \sim \mu_h\tau_h$) in BHJ film. The decrease in ξ at higher PC$_{71}$BM concentrations can be attributed to larger domain sizes as well as interfacial recombination. A sizable difference in ξ with $\xi_e \approx 110$ nm and $\xi_h \approx 510$ nm is observed for the amorphous PCDTBT blends, even at optimized morphology (D-A - 1:3), as compared to crystalline Si-PCPDTBT (D-A - 3:2) blend (ξ_e – 570 nm and ξ_h - 420 nm). A consistent lower magnitude of the exponent α associated with ξ_e was observed for the PCDTBT devices compared to Si-PCPDTBT devices, indicative of a smaller extent of acceptor percolation-path (less connectivity) for the amorphous network.

The change in the percolation paths with different donor/acceptor ratios for *e*/*h* transport is accountable for the variation of the meso-scopic correlation length ξ. The parameter value obtained by fitting the experimental decay profile is quite consistent with the single exponential fit decay length (L_D). A balanced transport condition entails a large ξ (low spreading resistance R_{sp} and large R'_R as less recombination). An optimized D-A blend ratio can be determined following inferior value of “a” parameter (R_{sp}/ R'_R). The consequence of spatial decay length measurement are further pursued more carefully employing 3D phase variation mapping of each blend film utilizing near field scanning optical microscopy with ~ 80 nm optical resolution.

Table 2: Comparison of theoretically fitted parameters

PCDTBT:PC$_{71}$BM blend

PC$_{71}$BM%	**Electron**			**Hole**		
	a	**ξ (μm)**	**α**	**a**	**ξ (μm)**	**α**
50	**0.0132**	**0.082**	**0.22**	**0.015**	**0.48**	**0.29**
66	**0.0091**	**0.09**	**0.23**	**0.015**	**0.73**	**0.23**
75	**0.0073**	**0.11**	**0.25**	**0.015**	**0.51**	**0.27**
80	**0.0083**	**0.03**	**0.21**	**0.003**	**0.31**	**0.31**

Si-PCPDTBT:PC$_{71}$BM blend

PC$_{71}$BM%	**Electron**			**Hole**		
	a	**ξ (μm)**	**α**	**a**	**ξ (μm)**	**α**
0	**0.0096**	**0.38**	**0.35**	**0.0102**	**0.13**	**0.26**
33	**0.0084**	**0.5**	**0.34**	**0.0072**	**0.53**	**0.31**
40	**0.0075**	**0.57**	**0.35**	**0.0123**	**0.42**	**0.29**
50	**0.0111**	**0.35**	**0.36**	**0.0067**	**0.19**	**0.31**
66	**0.0089**	**0.42**	**0.35**	**0.0076**	**0.2**	**0.31**

5.6. Near Field Optical Transmission Images (T-NSOM)

The interpretation from decay profile studies are further substantiated in the near field scanning optical microscope based transmission (T-NSOM) and local PC measurements. The asymmetric geometry of the device permits NSOM probe to access the active layer with the light incident through the NSOM tip from the Al side of the device (Figure 5.9a). The $PC_{71}BM$ domains in a BHJ blend is identified by comparing the transmission images obtained at the wavelengths – 532 and 633 nm [279]. Films with 10 – 30% $PC_{71}BM$ concentration demonstrated a very homogeneous morphology in PCDTBT:$PC_{71}BM$ bulk films.

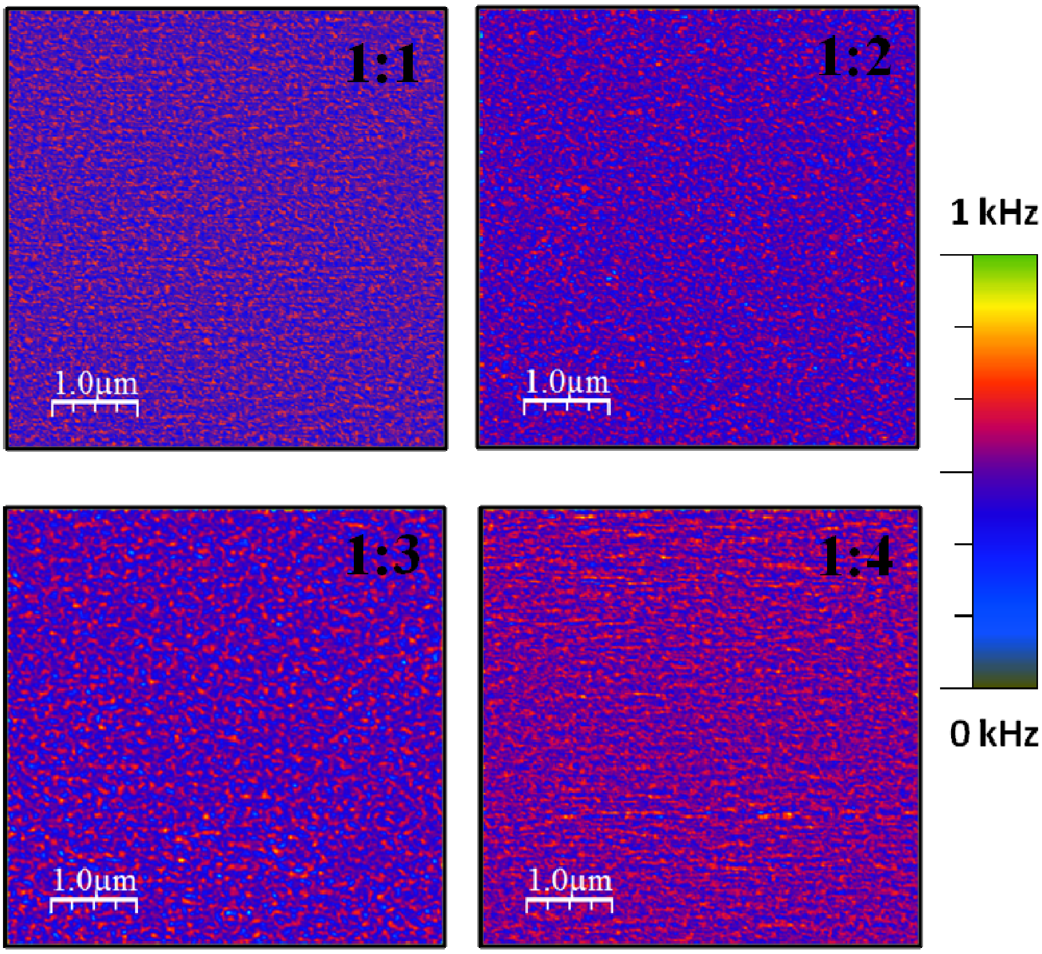

Figure 5.9: (c) T-NSOM images of BHJ films with different blend ratios. Reprinted with permission from Mukhopadhyay et al., Applied Physics Letters, 100, 163302. Copyright [2012], American Institute of Physics.

Phase separated $PC_{71}BM$ regions corresponding to 20 – 40 nm length scales and the amorphous-polymer matrix regions spanning over > 70 nm were resolved in T-NSOM images obtained from 1:1 D-A ratio films (Figure 5.9c). Presence of amorphous regions in PCDTBT-$PC_{71}BM$ blend is evident from homogeneously distributed PC active region in near field PC contrast (NPC) image [279]. The local-PC magnitude and variations indicate that mixed phases are more prevalent rather than pure polymer domains in the amorphous regions. In contrast, PC active regions are quite distinct for crystalline Si-PCPDTBT:$PC_{71}BM$ blend and takes on the profile of the 2D derivative of T-NSOM image at the domain boundaries [279].

However, beyond 80% $PC_{71}BM$ concentration, phase separation between the components is clearly observable in PCDTBT:$PC_{71}BM$ bulk films. The interconnected $PC_{71}BM$-rich domains have large lateral dimensions ~ 100 – 200 nm, which render the blend film more transparent to the probe light (Figure 5.9c). The critical D-A concentration drives $PC_{71}BM$ to aggregate, and reduces the fraction of the mixed amorphous region in the T-NSOM images.

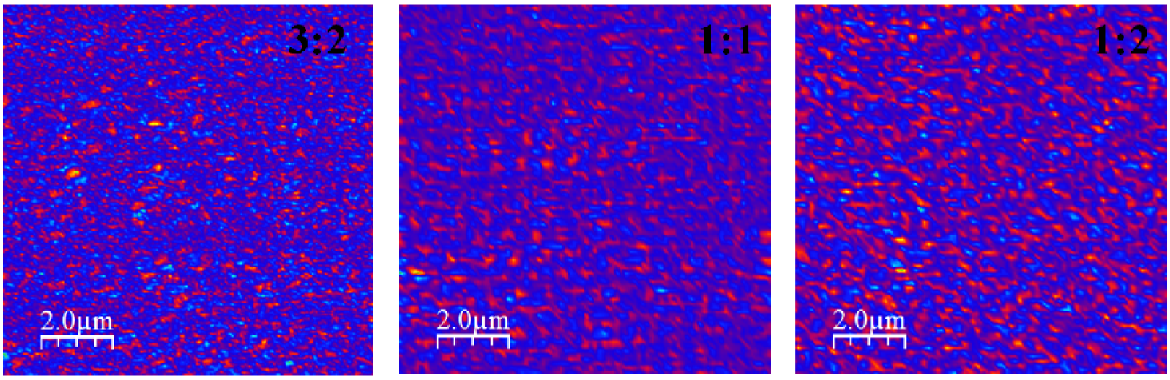

Figure 5.10: T-NSOM images of Si-PCPDTBT:$PC_{71}BM$ films with different acceptor ratios.

Measurements with Si-PCPDTBT blend depict domains of lateral dimensions of 30 – 60 nm for < 40% $PC_{71}BM$ compositions (Figure 5.10) [279]. Higher concentration of $PC_{71}BM$ leads to larger domains (~ 250 nm) which can be attributed to the aggregation of the small molecules facilitated by the crystalline polymer matrix [279]. Quantitative information from the T-NSOM images are extracted using fast Fourier transform (FFT) and power spectral density analysis (PSD) to understand the effects of phase separated length scales on device performance.

5.7. PSD Analysis of T-NSOM Images

The PSD analyses of these T-NSOM images bring out the spatial frequency distribution of domains, which range from 2 to 50 μm^{-1} (Figure 5.11a) and reveal the quasi-periodic pattern of the D-A domains in bulk film. Multiple Gaussian fits to the peak spatial frequencies indicate the contribution from different D-A domain sizes (Figure 5.11b).

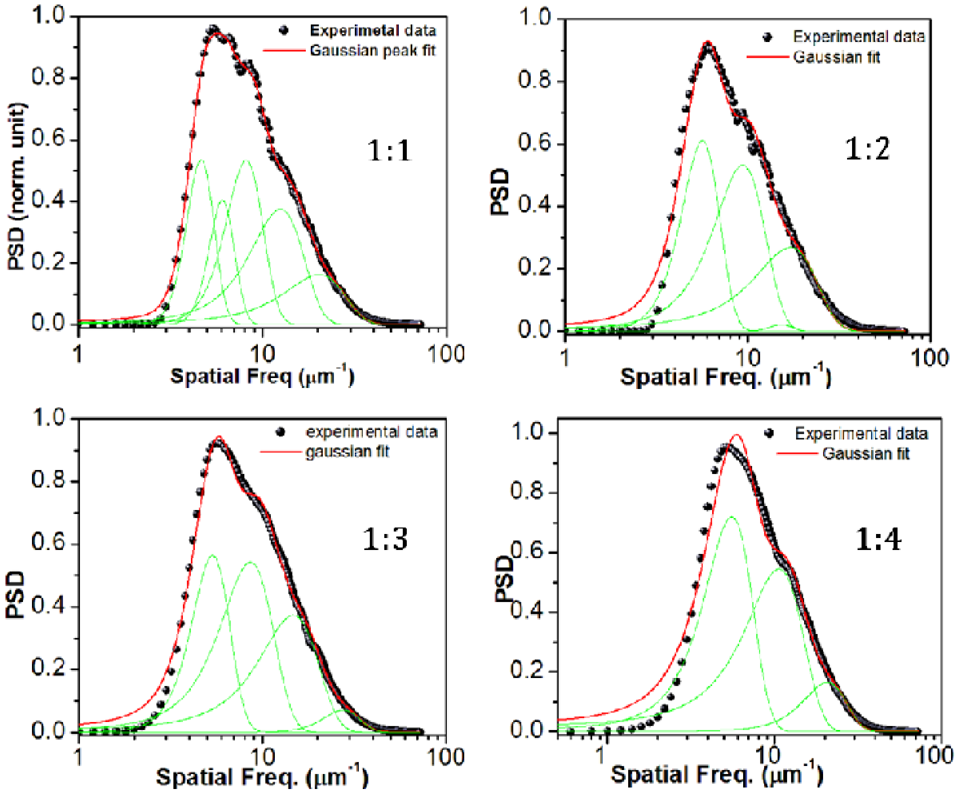

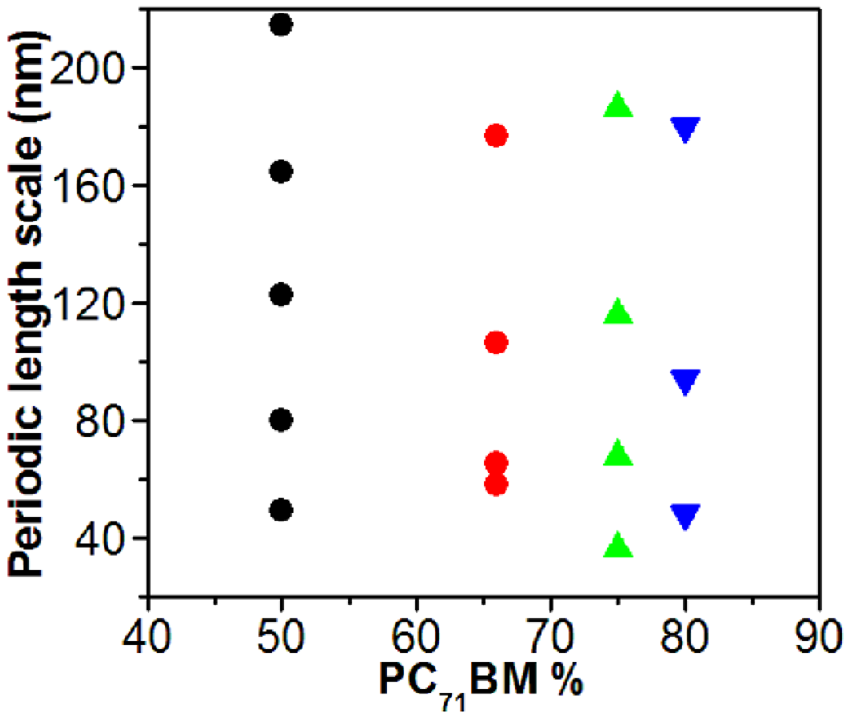

Figure 5.11: (Top) Power spectral density analysis of T-NSOM images with different D-A ratio. (Bottom) demonstrates corresponding periodic length scales present in the BHJ film. Reprinted with permission from Mukhopadhyay et al. Applied Physics Letters, 100, 163302. Copyright [2012], American Institute of Physics.

PSD spectrum of 1:1 PCDTBT:$PC_{71}BM$ film reveals the presence of five distinct periodic distributions ranging from 50 nm to 250 nm. The largest periodic-distribution in 1:1 film is centered around 20 μm^{-1} corresponding to the small lateral dimensions (~ 60 nm) of the $PC_{71}BM$ domain size. The minimum periodicity of ~ 4.6 μm^{-1} (220 nm) is ascribed to the average dimensions of the enclosed amorphous regions. The heterogeneity in domain size develops an unbalanced carrier transport and space charge effect that lower the device (1:1) performance. Periodicity smaller than 10 μm^{-1} (~ >100 nm) was achieved at low $PC_{71}BM$ concentration in blend where hole percolation to the ITO electrode dominates over the electron transport.

The most probable occurrences of individual domains in film are obtained by comparing the area contribution of individual Gaussian peak to the whole PSD spectrum. A uniform lateral dimension for both polymer and $PC_{71}BM$ phase separated domains (~ 14 μm^{-1} - 27 $\mu m^{-1} \rightarrow$ 60 - 40 nm) are observed in T-NSOM image at 1:3 ratio (Figure 5.11a). This effectively improves the percolation for both hole and electron by reducing recombination between trapped carriers with mobile ones during carrier transport. The smallest possible periodic domain (< 40 nm) is possibly achieved in BHJ films with ~ 1:3 compositions for PCDTBT: $PC_{71}BM$ blend.

As the acceptor-content increases, the coverage from $PC_{71}BM$ phase (10.6 $\mu m^{-1} \rightarrow$ 90 nm) dominates over the polymer domains, as indicated in the T-NSOM image of 1:4 film (Figure 5.9c). It improves the percolation for the electron, but reduces hole mobility and the effective interface-area. The reduced donor-polymer content consequently results in reduced J_{SC} as compared to the 1:3 devices which exhibited V_{OC} ~ 0.63 and J_{SC} = 6 mA/cm^2. PSD analyses of Si-PCPDTBT:$PC_{71}BM$ blend images with different acceptor ratios, indicate 3:2 ratio as the optimum D-A ratio for better device performance. Lateral periodicity ~ 30 μm^{-1} (< 40 nm) is achieved at 40% $PC_{71}BM$ concentration. Distribution around 35 nm and 50 nm lateral sizes are the most dominant domains representing $PC_{71}BM$ and Si-PCPDTBT domain respectively. Due to crystallization tendency of the Si-PCPDTBT, $PC_{71}BM$ moieties emerge out to form the mixed phase, thereby resulting in optimum phase separation without any additional processing conditions, even at lower $PC_{71}BM$ concentrations. The analyses from PC mapping and T-NSOM image also correlate with the spatial decay profile measurements (Figure 5.8).

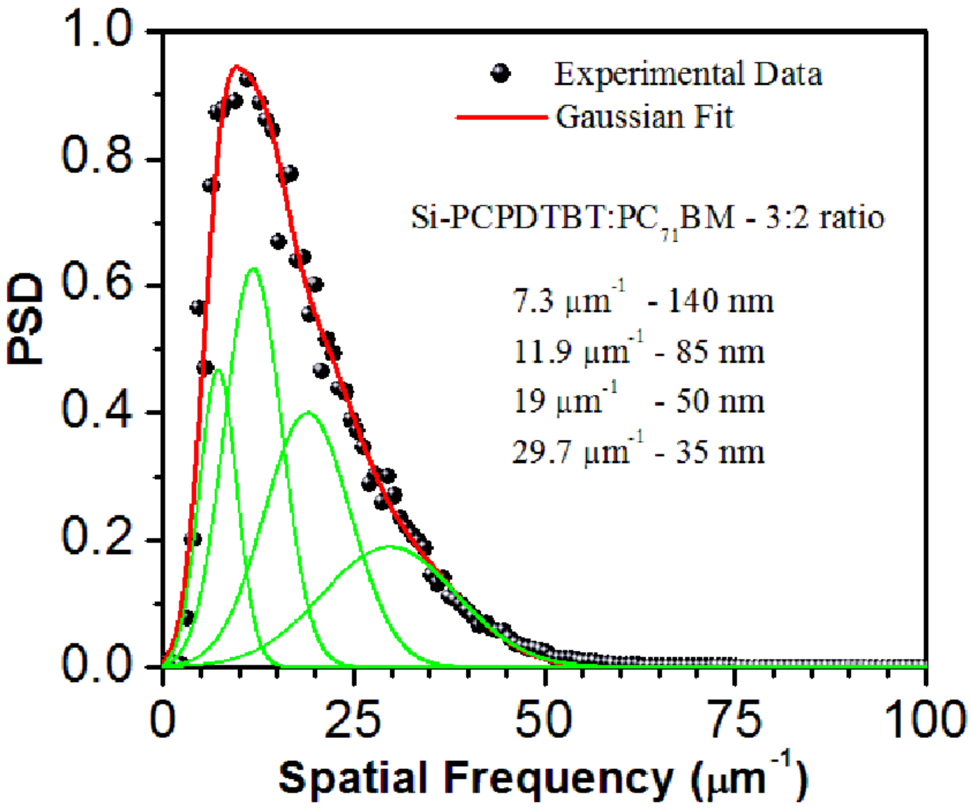

Figure 5.12: Power spectral analysis of Si-PCPDTBT:$PC_{71}BM$ blend film with 3:2 ratio and corresponding periodic length scale.

5.8. Conclusion

In conclusion, the requirement of the different D-A compositions, to achieve optimum morphology with different donor blend is clearly revealed from the PSD analysis of T-NSOM images. The analyses of various morphologies obtained from different D-A ratios are consistent with the trend obtained in the spatial PC decay profiles. The decay length assumes a large value for the D-A range of 1:3 for PCDTBT: $PC_{71}BM$, which incidentally corresponds to the small-optimum domain size observed in the PSD analysis. T-NSOM measurements revealed vertical as well as nanoscale lateral phase separation information in BHJ films with varying D-A composition. Results from PSD analyses of T-

NSOM along with the combination of lateral decay establish that the blend film with different D-A ratios have different characteristic length scales and appear as frequency maxima in the PSD spectra.

The series resistance, which influences the FF of the device can be correlated to the percolative pathways for a particular composition. Smaller size, marginally-interconnected domains results in inefficient carrier transport and corresponds to large series resistance. Upon increasing the $PC_{71}BM$ fractions, connection between the domains improve, and thereby reduces the series resistance resulting in improved FF. Results also suggest that the optimum ratio of D-A blend varies with the chemical structure of the donor polymer and with post annealing conditions. Spatial decay length measurements yield direct relation between the mesoscale (> 1 μm) morphology and nanoscale phase segregation (< 500 nm) in the BHJ films, and can be followed as a generalized method to optimize the BHJ morphology for different blend systems.

Chapter 6

Some Applications of NSOM to probe Molecular and Surface Processes

6.1 Introduction

In earlier chapters, we have demonstrated the utility of near field scanning optical microscope (NSOM) to optimize bulk heterojunction based device performance. In the present chapter the use of NSOM technique to investigate single molecular processes, excitonic processes in conjugated polymer nanoparticle, and photoreceptors in membrane proteins are demonstrated. Beside these topics, the effects of graphene coated substrates on the charge transfer processes in BHJs are also discussed.

The studies on each of these systems are quite challenging and exhaustive. The highlights of the microscopic-photophysical properties are emphasized and the salient features of each of these measurements are briefly discussed in this chapter. (i) Near field image of single dye molecule demonstrates the high spatial resolution possible in the NSOM apparatus and set-up. (ii) The conjugated polymer nanoparticle based films were studied to obtain local spectral information which can assist in quantifying intra-chain and inter-chain interactions. (iii) Transmission contrast and pump-probe measurement of bacteriorhodopsin demonstrate the photocycle and coherence effects from an assembly of bacteriorhodopsin trimers present in the monolayer films. (iv) The utility of near field scanning optical microscopy imaging methods to study few-layers graphene coating on substrates is demonstrated by making use of its interaction with electron donor and acceptor molecules. The strength of the charge-transfer absorption band resulting from graphene-donor/acceptor molecule interaction depends on the number of graphene layers. It was observed that in the case of conjugated polymer-coated graphene substrates, the decrease in photoluminescence emission intensity of the polymer is dependent on the number of underlying graphene layers. The decrease in emission intensity is accompanied by an increase in photocurrent in the composite system.

6.2 Single molecule Imaging of Rhodamine 6G Dye

Conventional optical spectroscopy techniques which are utilized to examine macroscopic samples yield average bulk value of the optical parameters. The spectral properties of the dye based condensed films are mainly dictated by the spectral properties of the dye molecules. Spectral properties of individual molecule are not only defined by their structure, but also by their *local environment*. The heterogeneity at microscopic level modifies local environment of a molecule to its neighbor. Therefore, spectral information of a macroscopic sample, as obtained from conventional optical spectroscopy technique, is a result of statistical averaging over an ensemble of molecules and results in inhomogeneous broadening [283-286]. The drawbacks of studying such macro-processes are the loss of spectral structure and the consequent loss of information of individual molecules.

The most natural way to overcome this issue is to study a single molecule as a sample. However, there are some experimental challenges that could not be met until 1989, when the first paper on optical detection of single molecules was published by *Moerner and Kador* [287]. This work is followed by a contribution from M. Orrit et. al., who introduced single-molecule spectroscopy of dye molecules by means of fluorescence excitation in 1990 [288]. One of the most spectacular effects observed with single-molecule spectroscopy is the so-called fluorescence intermittency (or blinking effect) [289]. The phenomenon consists of interrupted fluorescence from a single molecule excited with a continuous light source. The reason for fluorescence interruption are the quantum jumps of the molecule from the first singlet excited state to the first triplet excited state, which is lower in energy. As radiative transition from the triplet state is forbidden, molecule stays at triplet state for a long time (up to milliseconds or even more depending on the system) without absorption and emission of photons. Then the molecule relaxes back into the ground state non-radiatively, and the process repeats itself. Another well-known intrinsically single-molecule effect discovered with the new technique is so-called spectral diffusion [290, 291]. This is a phenomenon of absorption frequency change in a single molecule, resulting from a change in its photophysical parameters or a change in local environment. Utilizing near field scanning optical microscopy, we have demonstrated room temperature detection of single, fluorescence Rhodamine-6G (R-6G) on silicon substrate.

6.2.1 Sample preparation and experiment

To study spectroscopic properties of single molecules, individual molecule should be isolated from others and distance between two molecules should be greater than the optical resolution of experimental setup. It requires different environmental conditions for different molecules which create inhomogeneous broadening in spectral response [283, 292-294]. To minimize the broadening effect, we have enclosed the dye-molecules (Rhodamine 6G dye, as procured from Sigma-Aldrich, fluorescence quantum yield ≈ 98%) into a relatively homogeneous chemically inert polymer host matrix (Poly (methyl methacrylate) (PMMA)).

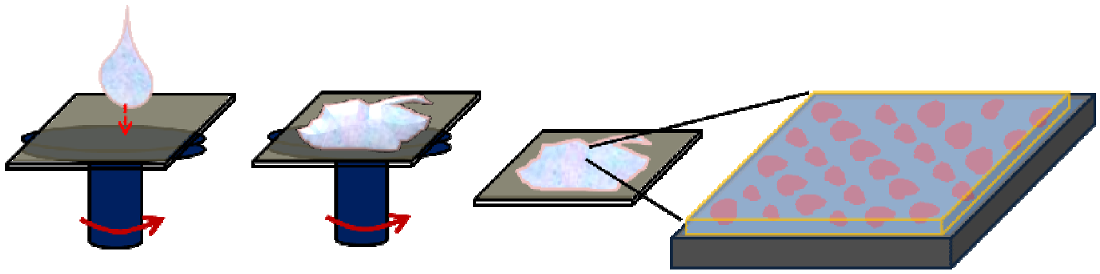

Figure 6.1: Schematic of single molecule sample preparation on Si-substrate.

PMMA also works as a cap-matrix rather than a host-matrix and protects the molecules against atmospheric oxygen. The typical sample structure used in this study is shown in Figure 6.1. Pre-cleaned oxidized silicon wafers (≈ 50 nm) were used as substrates. PMMA (number-average molecular weight M_N in the range 150,000–250,000 and polydispersity P_M = 1.06) was purchased from Sigma-Aldrich and used as received. To prepare the substrates for polymer deposition, a special cleaning routine was applied. First, the wafers were cleaned mechanically with a standard detergent used for washing glassware. Then they were rinsed in acetone/iso-propyl alcohol, dried, and then rinsed with deionized water. Finally, substrates were kept in "*piranha*" mixture (1:2 – H_2O_2:H_2SO_4) under ≈ 80° C water bath for ~ 20 minutes in order to remove organic impurities. To neutralize the acidity, the wafers were rinsed thoroughly with ultra-pure Milli-Q water. Substrates were left to be stored in Milli-Q water and to prevent subsequent precipitation of impurities from air.

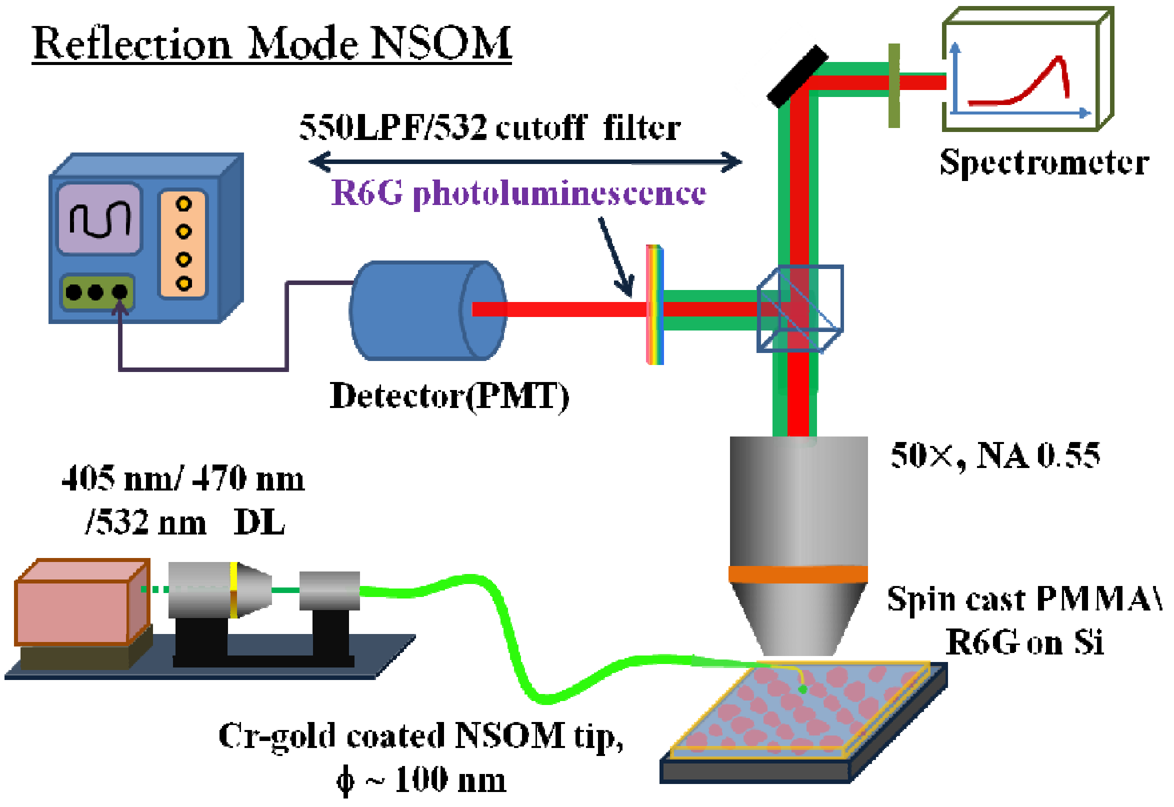

Figure 6.2: Schematic of reflection mode NSOM

All of the above steps, apart from the "piranha" treatment, were performed in an ultra-sonic bath. Finally, just before polymer layers casting, substrates were taken out from Milli-Q water, rinsed once again, dried with a jet of nitrogen and kept under UV-lamp for half an hour to photobleach the remaining fluorescent impurities. The concentration of Rhodamine 6G in solution was maintained at ~ 10^{-9} g/L. The dye solution was then added into a 0.5% weight PMMA in toluene to get final concentration of 10^{-10} g/L. Standard spin-coating technique was employed for film preparation. Spin-coating implies either putting a droplet of a solution (30–50 µL) onto the center of a rotating substrate or first putting the solution onto the substrate and then spinning it at angular velocity is 3500 rpm (Figure 6.1). The resulting layer thickness was within the 5-10 nm range with a surface coverage of typically a few dye molecules per square micrometer. Films of pure PMMA without R-6G molecule was also deposited on clean Si wafer for reference. A near-field optical light source consisting of a tapered, Au/Cr-coated single-mode optical fiber with an aperture of less than 100 nm was used to illuminate the sample. Different laser lines were used as the excitation wavelengths (405/470/532 nm) and were coupled into the coated fiber while the excitation power was adjusted to give about 3 nW at the end of the tip (as measured in the far field with Si-detector). The sample was scanned underneath the fiber and the fluorescence emission from the sample plane was collected with a 50×, 0.45 NA objective and directed to the detectors. The fluorescence signal was filtered from the excitation light using a long-pass optical filter ($\lambda > 600$ nm). A broad-band beam splitter cube (Olympus, 400-800 nm) was used to separate the fluorescence signal into two components and then directed to the detection channels. Fluorescence intensity was collected by solid state photomultiplier tube from Parkin-Elmer (dark count ~ 100 Hz), and high resolution spectrometer was used to digitalize spectral response. In the near-field operation, fiber aperture was *confocally* aligned onto the detectors. Shear-force feedback based on a tuning fork system was used to maintain a constant tip-sample separation and to generate high-resolution topographical images (Figure 6.2). Background fluorescence from the fiber tip itself was minimized by keeping its length as short as possible (< 500μm). The detection efficiency of the optical path was optimized for maximum signal collection (collection efficiency was approximately 40%, including quantum efficiency of the detectors). Count rates between 500-1k counts/s were obtained in detector compared to background ~ 300 counts/s. Area of few square micron was imaged approximately once in every 30 min. and dye molecules were traced over more than an hour before its photo degradation.

6.2.2 Results

R-6G on silicon was chosen for demonstrating optical single molecule detection in fluorescence and reflection NSOM mode, since many photo physical properties of this system are well known. Figure 6.3a and c show different sequences of fluorescence images taken at different $1\times1\mu m^2$ area. Each image corresponds to the 256 × 256 pixel resolution at scanning rate 50 ms per pixel. In order to overcome the lateral resolution issues of the microscope, different pixel combinations were utilized with different scan areas. The optical resolution is obtained from the line profile of the small fluorescence features and is estimated to be ~ 40 nm full width at half maximum. This length scale of single molecule fluorescence features is comparable to the bright-field single molecule imaging value of R-6G (≤ 90 nm) [288, 295]. A monotonically decaying fluorescence signal was observed with number of scans and enlarged the coverage of dark, bleached spots in the sample. A consistent fluorescence signal was observed from few R-6G molecule within the near field zone. Different brightness and step size of fluorescence signal in Figure 6.3b could be attributed to the random orientation of transition dipole moments of dye molecules in the polymer matrix, which yield different rates of excitation by the illuminated electric field.

The quantitative features (mean bleaching time, distributed intensity) are consistent with the previously reported results of R-6G and other laser dyes on the Si-surface [296-298].

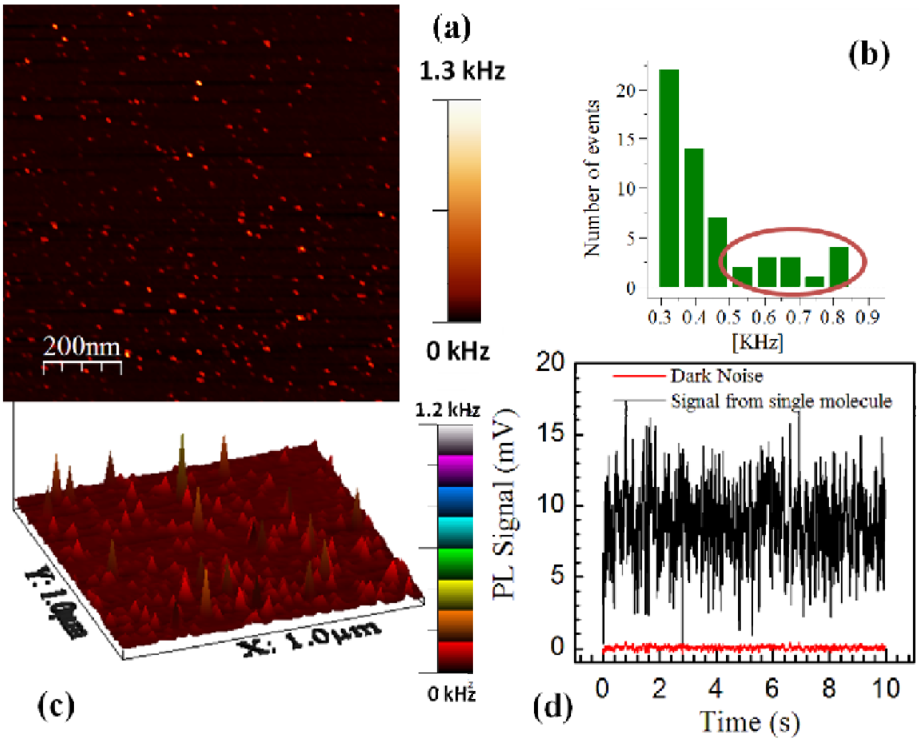

Figure 6.3: (a) NSOM fluorescence image of Single R6-G molecules in PMMA host (b) Emission intensity histogram from a single molecule (c) 3-dimentional image of the R6-G single molecule over $1\mu m^2$ *(d) Typical florescence response from individual molecule.*

For fixed point illumination with NSOM tip, an almost constant fluorescence signal is observed with a rapid fluctuation, larger than noise signal. This feature reveals the photo-blinking properties of single R-6G molecule as shown in the Figure 6.3d. We assert that the transient fluorescence response in Figure 6.3d is an evidence of achieving optical single molecule detection sensitivity on Si-surface. Measurements demonstrate the potentiality of our instrument for examining photophysical properties at single molecule level.

6.3 Polymer Nano-particle Imaging

Fluorescence polymers like Poly ((4,4′-hexafluoroisopropylidene)diphthalic anhydride-alt-thionin), Poly(2-vinylnaphthalene), Poly(2-naphthyl methacrylate), Poly(p-phenylene vinylene) have already been demonstrated to possess a wide range of optical and electrical application like LEDs, OPVs, and leasing material [14, 299-301]. There is a considerable interest in controlling the nanoscale variation in conjugated polymer films to improve the efficiency of polymer LEDs and photovoltaic cells [302-306]. Submicron size conjugated polymer nanoparticles showed an improved control over the composition of the film and device performance [307]. These fluorescent polymer nanoparticles are also of interest for biomolecule labeling and sensing owing to their enhanced brightness, photostability and bio-compatibility as nanoparticle compared to conventional fluorescent dyes [308].

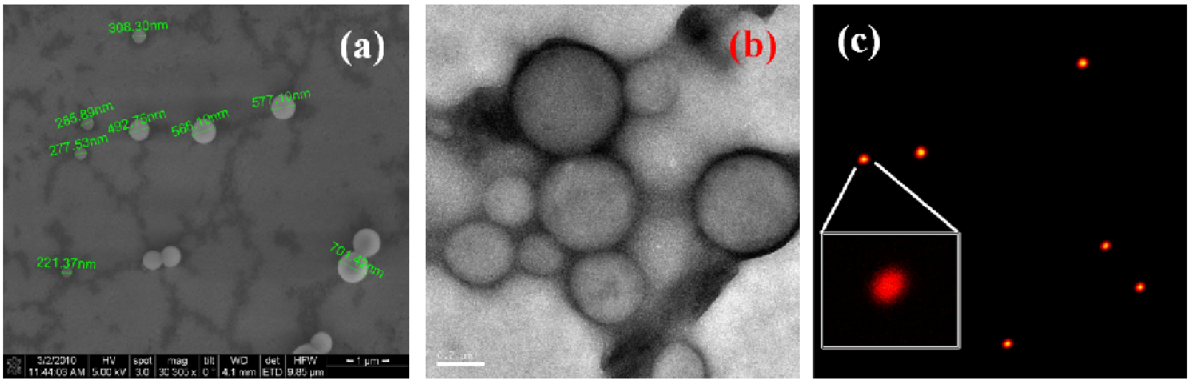

Figure 6.4: (a) SEM, (b) TEM and (c) high resolution confocal (STED) images of MEH-PPV nanoparticles. Inset- zoom image of a single nanoparticle of diameter ~ 100 nm.

The conjugated polymer poly[2-methoxy-5-(2'-ethyl-hexyloxy)-1,4-phenylene vinylene] (MEH-PPV) is of particular interest for fluorescence-based sensing due to its large absorption cross-section per particle and short excited life times (400 ns) with high fluorescence quantum yield (~ 1) [239, 309, 310]. Nanoparticles of low (10%) and high (100%) conjugated MEH-PPV polymer were prepared under *reprecipitation method* [311], a simple solution processing technique, where a solution of organic material in a good solvent was injected into a very poor solvent for organic materials. In our case, MEH-PPV polymer first dissolved in the good solvent tetrahydrofuran (THF) that is immiscible in water. Then 500 µL of organic solution was rapidly injected into 4mL of Milli-Q water leading to a quick aggregation of polymer chains. Nanoparticles of 50 – 200 nm in diameter range were prepared by varying MEH-PPV concentration in THF.

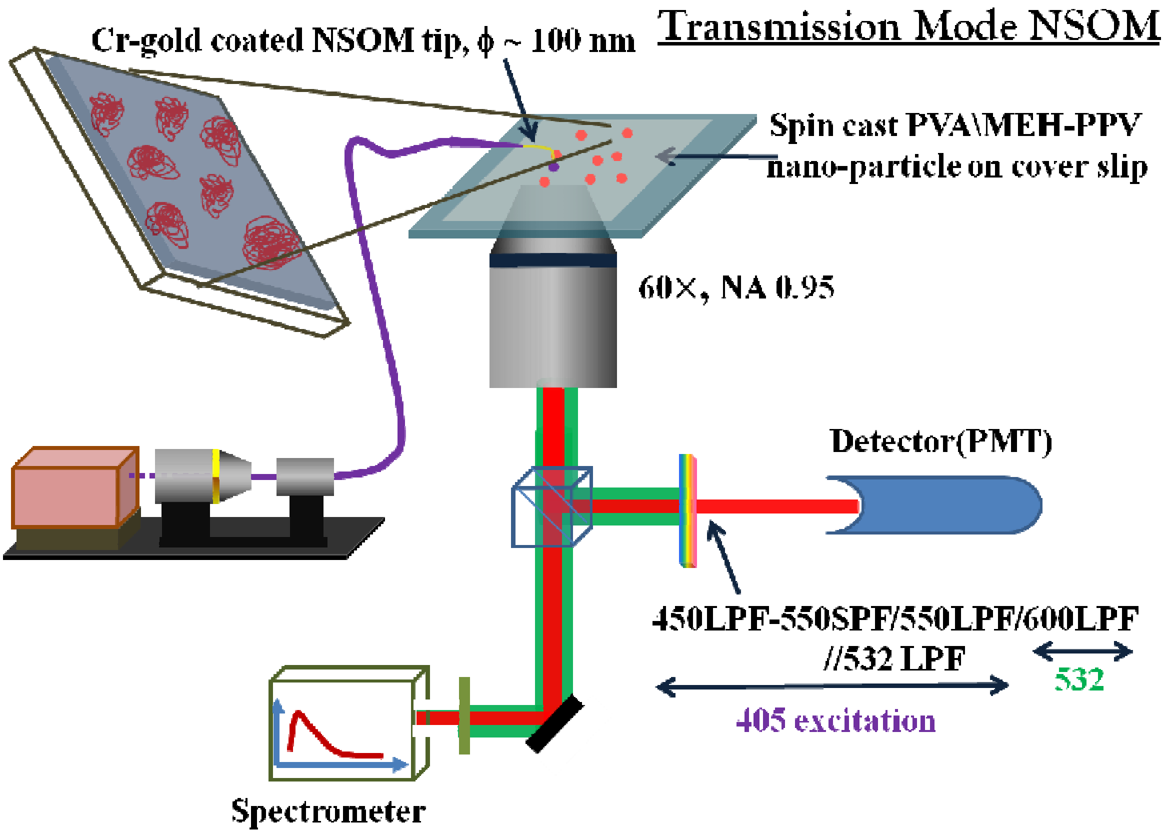

Figure 6.5: Transmission mode NSOM imaging of MEH-PPV nanoparticles in PVA matrix. 60 nm spatial resolutions are achieved with NSOM probe of aperture ~ 45 nm.

Finally organic solvent was separated out by solid freezing method. These nanoparticles were characterized in SEM, TEM, Stimulated Emission Depletion fluorescence confocal microscopy (STED), and NSOM for size, morphology and photophysical properties respectively (Figure 6.4). TEM images of drop-cast film on metal grid revealed that nanoparticles form large islands of roughly spherical particles of diameters ranging from 60-300 nm (Figure 6.4b). For NSOM measurements, < 50 nm thick films were prepared by spin casting (3500 rpm) of aqueous nanoparticles suspension mixed with 0.1% weight ratio of PVA (in water) solution with optimum volume ratio [312, 313]. Lateral dimension of the nanoparticle in host matrix was cross-verified by SEM and TEM measurements. Nanoparticles appeared much larger in lateral dimension in confocal images compared to its original size because of point spread function (PSF) of collection objective. After digital filtering and STED technique, the dimension of the nanoparticles reduced to ~ 100 – 300 nm which reveals that it's an aggregation of 2 - 3 individual nano particles of size ~ 50 - 100 nm (Figure 6.4c). Florescence from conjugated polymers depend on chain conformation and the interaction between the segments of polymer chains [28]. This intrachain interaction is directly discernible in the UV-Vis spectrum following the red shifted absorption and fluorescence of nanoparticles (Figure 6.6a).

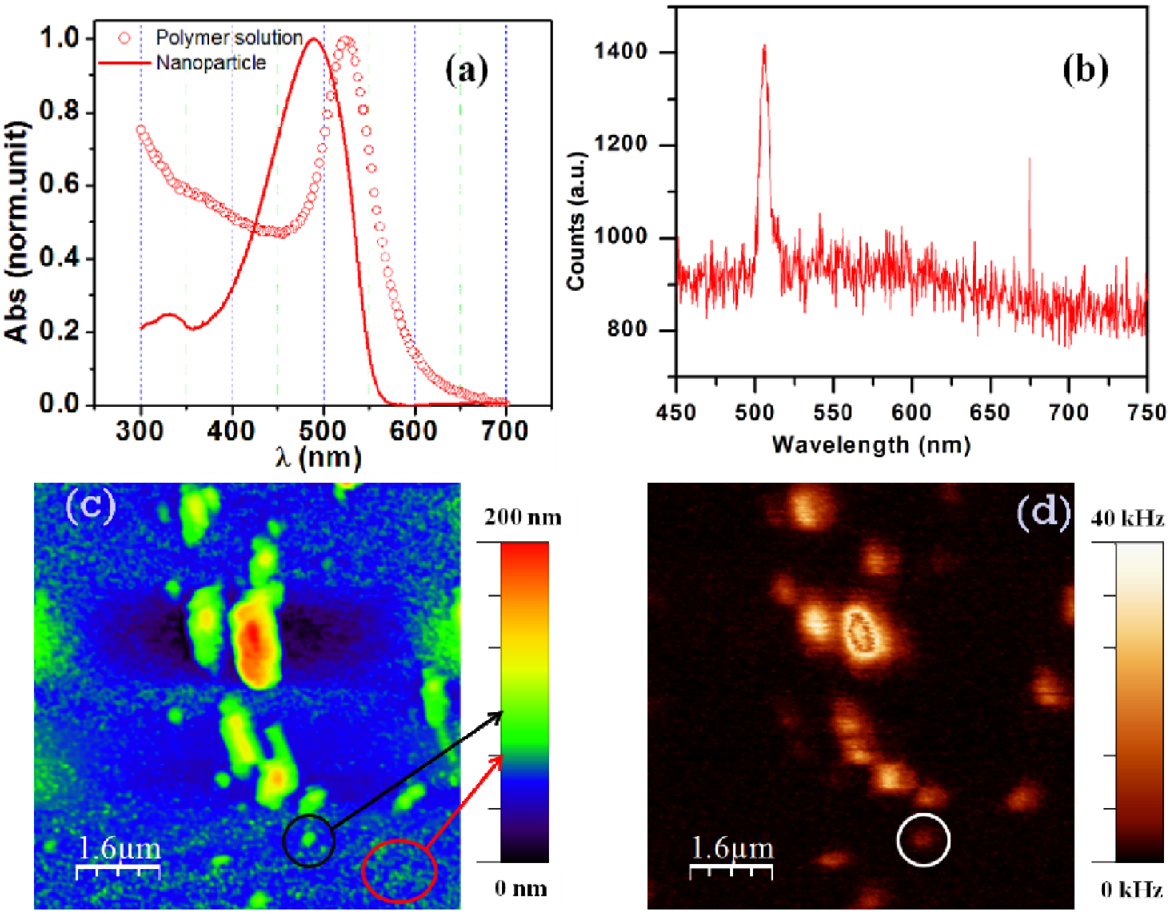

Figure 6.6: (a) Comparison of absorption spectra from polymer solution and aqueous nanoparticle suspension, (b) emission spectra of LC nanoparticles with 365 nm optical excitation. Below are the morphologies and corresponding NSOM images with 356 excitation and HC fluorescence collection.

This unique observation can be explained by the conformation of polymer chains in the nanoparticle, which are formed when the MEH-PPV in THF solution is rapidly injected in the water. The polymer chains collapse upon rapid injection in water and *freeze* into different conformations of the polymer chains with kinking and bending of conjugated backbone. These stiff conjugated polymer chains bend at a small number of locations in the polymer backbone into coil structure, while mostly maintaining straight segments that fold back into each other to form a large number of intrachain π-stacking. Ignoring the solvent effects, the red shift absorption for nanoparticles represents more intrachain interaction as compared to the solution. For a dilute aqueous suspension of hydrophobic polymer nanoparticles, the interaction between molecules is miniscule, but the interactions between different segments of a given polymer chain increases. The aqueous suspension thus yields a way to eliminate interchain effects and determine the optical properties associated with intrachain interactions in individual collapsed polymer chains. These effects of conjugated polymer conformation and intrachain interactions on its electrical or optical properties have been probed using high resolution spectrometer coupled with the NSOM [314, 315].

Polymer nanoparticle in PVA matrix was measured under NSOM microscope with high resolution objective and by digital filtering (Figure 6.5). The size distribution of polymer nanoparticles is clearly evident from NSOM images. Larger particles with count rate > 30 kHz demonstrate aggregation nature of polymer nanoparticle even in inert polymer matrix (black circle). In contrast, particle with height of ~ 100 nm and count rate of ~ 10 kHz represent individual polymer nanoparticle (white circle). Utilizing NSOM probe, individual nanoparticles were illuminated by controlling tip position on the film. Emissions from individual domains depict a sharp PL signal near to the emission band of the LC-MEH-PPV nanoparticle (Figure 6.6b). In order to probe energy transfer from low conjugated MEH-PPV (LC) to high conjugated (HC) one, nanoparticles were prepared by 50% weight mixing of different composition. Individual nanoparticles were illuminated by LC excitation wavelength (~ 365 nm), and PL from the HC (480 – 600 nm) was collected using razor sharp optical filters. Considerably stronger PL from the HC and suppressed emission of LC demonstrate the efficient energy transfer from LC to HC chain (Figure 6.6c - AFM and 6.6d - NSOM image). This efficient energy transfer process by keeping donor and acceptor polymer within a close proximity, exhibits a method toward the hybridize polymer nanoparticle photovoltaic device.

6.4 Optical Transmittance through Bacteriorhodopsin Film

Studies of functional proteins at single molecular level yield results that can be different from the measurement of the ensemble or bulk where the individual characteristic cannot be distinguished and only an average behavior is measured [291]. Structural properties at the single molecular level are studies by single molecule force technique (AFM) whereas in single molecule spectroscopic method, the functionality is studied but morphological properties are ignored [316, 317]. In this context near field scanning optical microcopy (NSOM) has emerged as a tool in which both the structural as well as the functionality at the single molecular level can be studied [290]. This new technique has a potential to examine fluctuation phenomena that are common in conventional measurement techniques such as fluorescence blinking, fluctuation in optical counts [292, 318, 319]. Analyses of these fluctuations at single molecular level reveal important information on the dynamic processes of correlated systems as well as important information on the statistical distribution [297].

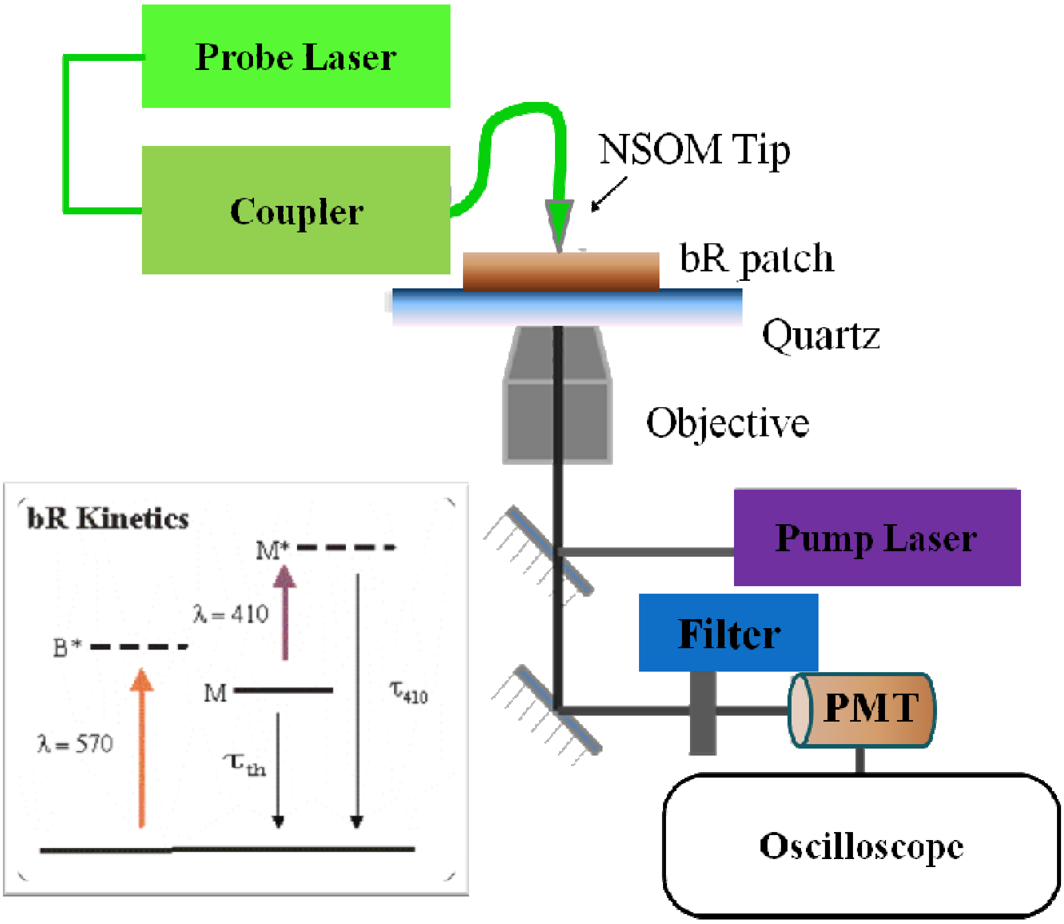

Figure 6.7: (Right) Schematic of pump-probe measurement and inset represents bR photocycle.

Thin films of wild-type bacteriorhodopsin (bR) protein from halophilic bacteria have been employed as a model system for temporal fluctuation studies utilizing its photo induced absorption change characteristic [320]. The distinct spectroscopic signatures of the intermediate states in the bR photocycle render a platform to study its optical properties at different molecular states [321]. bR film was grown on the quartz substrate following electrostatic layer by layer assembly method (LBL technique) [322, 323]. The microscopic patch heights are representative of single layer bR film (~ 7 nm) to the multi layer film (~ 30 - 40 nm) [321]. The changes in the photophysical parameter or local environments (*e. g.*

pH, humidity) modify the absorption coefficient of bR film [324]. This shifting of the absorption coefficient generates amplitude fluctuation in the detected transmission signal. A pump-probe near field scanning microscopy in transmission mode was utilized to monitor the intensity fluctuation time series through the bR assembly [321]. The method involves analysis of transmittance fluctuation Tr(t) from single layer to finite size of bR assembly that yields the kinetics associated to biochemical reaction and the internal molecular changes. The photon pump mechanism in bR is initiated by the photo-isomerization of the retinal chromophore from all-*trans* to 13-*cis* configuration, followed by the formation of secondary intermediate states (J, K, L, M, N, and O) [320].

External parameters such as pH, humidity, temperature and additional light pump (λ - 405 nm) corresponding to M-state excitation modify photocycle kinetics and M-state lifetime [320]. These external parameters yield a good control over transmittance intensity fluctuation. bR patches grown in the preclean quartz substrate were characterized by AFM and transmission NSOM measurement with 532 nm probe laser. Typically bR patchs have lateral dimensions ranging from 500 nm – 4 μm with height of 8 nm (monolayer) – 200 nm (several layers). For local transmission measurement, NSOM probe ~ 100 nm aperture was placed on the bR patch using computer control stepper motor software. The NSOM tip illuminates only little fraction of region of the bR patch. The photoexcitation volume is governed by the coverage area of the NSOM probe and thickness of the bR patch. For a monolayer bR patch, calculation yield for an ensemble of ~ 400 molecules is studies with pump-probe combination [321]. Transmission signal through bR patch was measured using micro-objective (60×, 0.95 NA) and photomultiplier tube. Additional pump laser was introduced in the setup through inverted eye-piece and measurements with appropriate cut-off filter were carried out (Figure 6.7). Tr(t) was captured using a digital oscilloscope (Wave Runner 6100A) at 250 kHz sampling rate. Transformation of Tr(t) to the frequency domains yielded consistent picture of the different photo-induced processed. About 100 conjugative data set of 1s (for WT-bR) and 10s (for D96N mutant) were captured as separate window. The frequency corresponding to the maximum amplitude in the FFT signal was captured for each separate Tr(t) window employing Matlab code. A histogram of frequency and their occurrences was constructed leaving out the DC contribution.

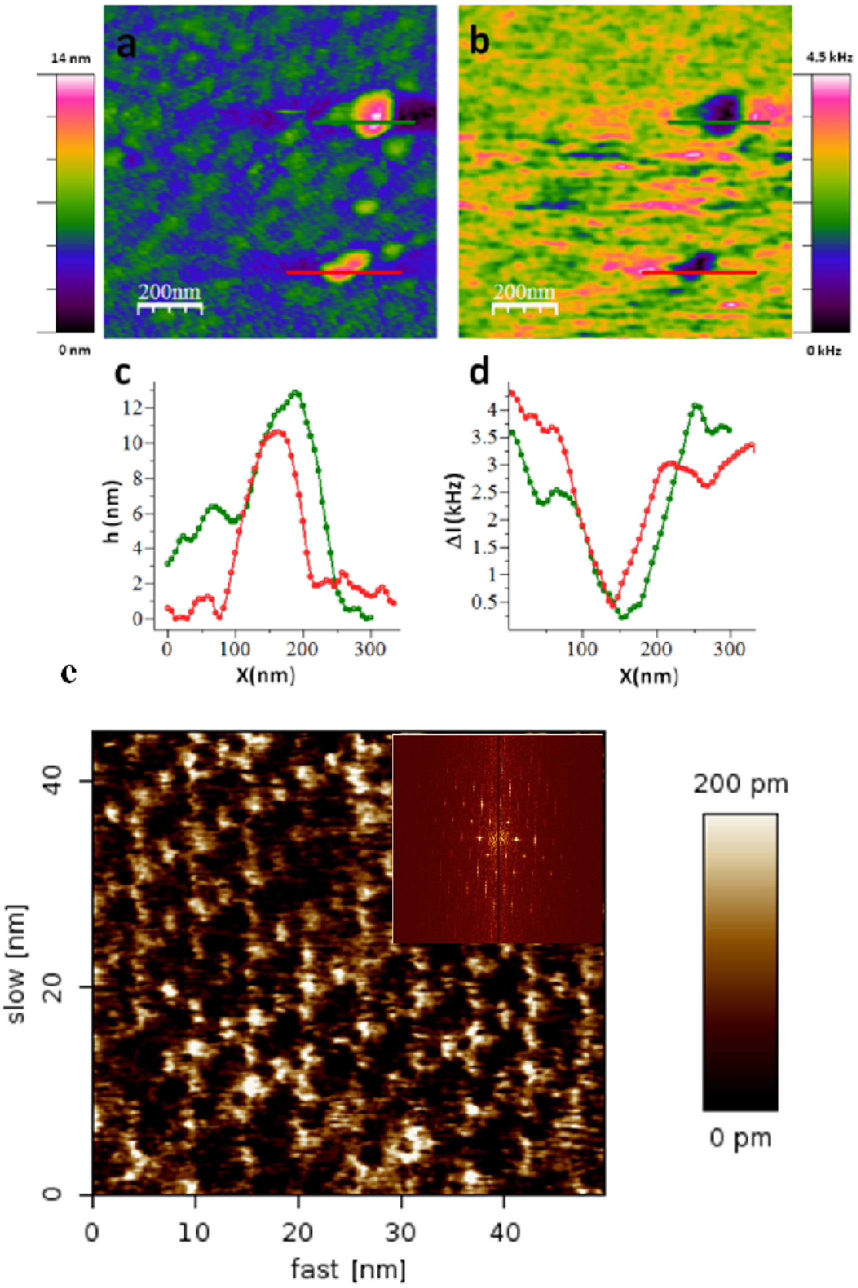

Figure 6.8: (a and c) AFM image of sample containing bR patches and corresponding height profiles of the bR patches. (b and d) T-NSOM image from the same region and corresponding absorption profile of the bR patches. (e) High resolution AFM image of D96N mutant with hexagonal ordering. Inset shows the hexagonal pattern in Fourier transformed image. Reprinted with permission from Das et al., J. Chem. Phys., 134, 075101. Copyright [2011], American Institute of Physics.

The functional change of the bacteriorhodopsin protein is closely associated to its ability to undergo structural change [320]. Hexagonally arranged trimers are known to reveal the effects arising from correlation in optically induced excitation and de-excitation process (Figure 6.8e). High resolution visualization of bR film explains the positive and negative cooperative effects elicited by bR-bR interaction within neighboring trimers [325]. Due to heterogeneity, external stimulus is not able to excite all the trimers in bR simultaneously. The kinetics associated with this biochemical process can be formulated as modified Langevin equations with the rate constant $k_i^f = \alpha\,(\lambda)I$, where $\alpha\ (\lambda)$ is the absorption coefficient and I represents incident light intensity, whereas k_i^r is the inverse of the M-state life time (Figure 6.7). The model system with the time dependent term-

$$\frac{\partial N_B}{\partial t} = -k_i^f N_B + k_i^r N_M + \varphi_B(t)\ and\ \frac{\partial N_M}{\partial t} = k_i^f N_B - k_i^r N_N + \varphi_M(t) \qquad (6.1)$$

Fluctuations in the optical transmission through finite size bR film yield a lognormal distribution type probability density function (PDF) about a characteristic frequency (ω_{max}) [318, 319]. This non-normal probability density function reveals statistically correlated nature of these fluctuations. Correlation between transiently assemble trimers, e.g. “trefoil”, plays a crucial role in developing the non-Gaussian PDF which defines bacteriorhodopsin system [325]. The fluctuation arising from the cooperative effects get further modified by random optical excitation, nature of substrate, local environment, reversibility in photocycle and thermally driven transitions [325].

Autocorrelation function obtained from time traces, Tr(t) for plane quartz and bR-grown quartz, depict the absence of correlation for the bare quartz and a sizable correlation for the bR film. Maximum correlation between different photophysical processes is observed for bR tri-layer and correlation diminishes with number of bR layers [320].

PSD analysis of Tr(t)s yield characteristic maxima in occurrence amplitude corresponding to a frequency, ω_{max} prevails in the distribution. Typically $\omega_{max} \sim 500 - 700$ Hz, is the range of the M-state lifetime (~ ms) which endures over the entire molecular photocycle [320]. This interpretation of the dominant frequency associated with the intensity fluctuation to bR photocycle is cross verified with different sets of measurements where M-state lifetime was intentionally modified by varying external factor. These results reveal that profile of the noise spectrum is dictated by the distribution arising from the heterogeneity at the molecular level in the ensemble and the photocycle kinetics.

6.5 Studies of BHJ Devices on Graphene Modified Electrode

Organic optoelectronic devices such as organic light emitting diodes (OLED) [326], photovoltaic cells [327, 328] and organic photodetectors[329] have been proven to be attractive from fundamental research and commercial viewpoints. This interest stems from the fact that they can be fabricated on flexible, lighter substrates by low-cost printing methods. One important aspect that is primarily under focus in these thin film polymer optoelectronic devices is the replacement of transparent conducting electrode indium tin oxide (ITO) [330, 331]. Graphene, which is a two dimensional (2D) semi-metal, is a promising candidate for transparent electrodes because of its optical and electrical properties [332]. Thin films obtained from graphene dispersion have been used as transparent electrodes in device applications owing to their high conductivity, excellent transparency and higher chemical and thermal stability [333-335]. The proximity of graphene work function ($\varphi \sim 4.2 - 4.5$ eV) to that of commonly used transparent indium tin oxide (ITO) electrodes (4.8 eV), suggests its potential as an electrode or a suitable gradient medium for hole extraction[336]. Chemical, optical, and opto-electronic properties of 2-D graphene surface can also be modified by introducing different chemicals on graphene surface [337].

Apart from the electrode option, the other feature with graphene is its ability to quench photoluminescence (PL) of suitable dye molecules and fluorescence polymers [338]. The PL quenching in donor and acceptor polymer systems have been explained both on the basis of energy transfer and charge transfer processes [339-342]. Effects of molecular charge-transfer (CT) interactions between donor (D) or acceptor (A) molecules with few-layer graphenes have been reported recently, and these effects are monitored effectively by Raman Spectroscopy [343, 344]. Further insight into these processes at a macroscopic level is obtained by using spatially resolved methods at lateral length scales of < 100 nm. Near Field Scanning Optical Microscopy (NSOM) methods are useful in identifying optically active regions at sub – 100 nm levels and yield information on the nature of CT interaction. A transmission based NSOM technique is employed to identify and study the interface between few-layer graphene and the D/A molecular layers. In conjunction with topography scans, graphene thickness (number of layers) dependent interfacial CT absorption band was obtained simultaneously from optical-profile data. This method can, in principle, be used to quantify the magnitude of CT interaction of graphene with molecules. Graphenes obtained from different preparative routes show different strength in CT interactions [337]. Graphene composites with dye molecules or conjugated polymers demonstrate acceptor-type characteristic of graphene.

This combination of properties has led to a renamed interest in incorporating graphene in bulk heterojunction polymer solar cell (BHJ-PSC). Graphene layers have been inserted in a BHJ-PSC along with a poly (3,4-ethylenedioxythiophene):poly (styrenesulfonate) layer as an electron blocking layer [338]. In principle, graphene oxide can be used as a hole transporter which can function additionally as an electron-blocking layer. In this study, solution deposited graphene on ITO electrode was utilized as an interface for charge separation as well as hole-carrier collection layer and also in blend form with light absorbing active polymer. Introduction of active organic layer on graphene coated patterned ITO electrodes modify the organic-semiconductor bulk transport. A lateral scanning PC approach has been implemented to study the affect of graphene substrate on ambipolar transport. Finally, the spatial PC decay profile in these asymmetric devices was explained by steady state equivalent circuit model within a spreading impedance approach.

Graphene samples were prepared from graphitic oxide by reacting graphite with a mixture of concentrated nitric acid (2 ml), sulfuric acid (2 ml) with potassium chlorate at room temperature for 5 days. Then, thermal exfoliation of graphitic oxide was carried out in a long quartz tube at 1050°C under an argon atmosphere to yield exfoliated graphene (EG). Similarly, hydrogenated graphene (HG) was prepared following arc-discharge of graphite in H_2 + He mixture. Diamond graphene (DG) was prepared by the transformation of commercial nanodiamond [337].

Topological and optical feature of chemically synthesized few layer graphene was examined by conventional AFM, Raman spectroscopy along with local near field transmission contrast. Graphene flakes were deposited from THF solution on the Silicon/300nm SiO_2 substrate. 2-dimentaional height variation of graphene flakes were mapped by conventional contact mode AFM imaging (Figure 6.9). Intensity ratios of G to D band (micro Raman measurements) confirm the number of layers and doping level of the local graphene flakes. These measurements demonstrate that EG graphene has less number of layers (3-5) compared to HG and DG graphene (8-10 layers). TGA measurements depict that surface volume area is large in DG graphene as compared to others [344].

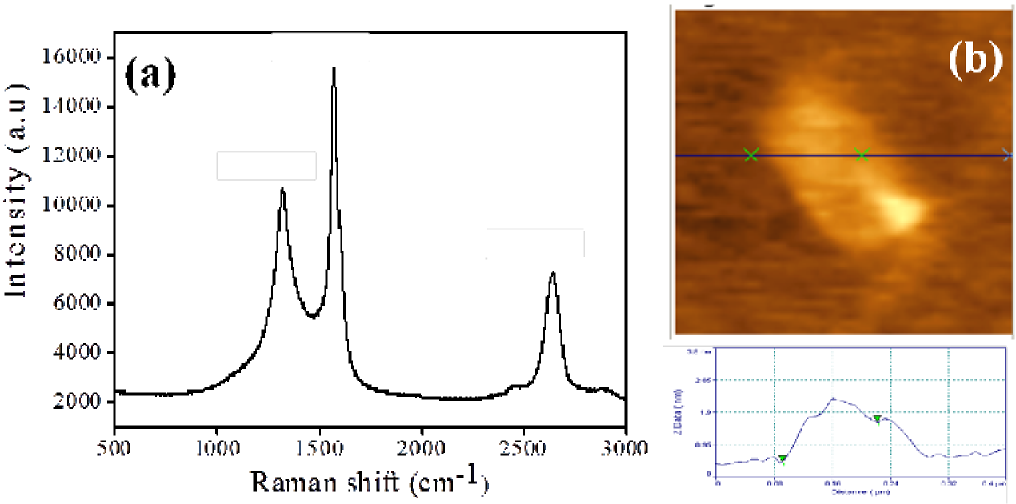

Figure 6.9: Raman spectra of as prepared graphene prepared by exfoliation of graphite oxide. (b) AFM image and corresponding height profile.

Local optical contrast of few layer graphene was explored by the reflection/transmission NSOM contrast imaging. The set-up used for near-field optical microscopy (Multiview 4000, Nanonics Inc.) is based on a duel channel optical microscope (normal with inverted). In a typical experiment, 532 nm laser (≈ 10 mW) was coupled to the NSOM tip (aperture ≈ 100 nm, Nanonics Supertips Inc.). The transmission optical signal was measured using a solid state Photomultiplier tube (MP 692 PerkinElmer, Dark count rate 100 Hz) through the objective (50X, N.A = 0.45). Optical and topographical information are simultaneously obtained from the near-field optical microscope by raster scanning the sample using the piezo-scanner in such a way that the tip and the objective lens maintained at the same position with respect to each other. The accuracy of the feedback electronics and z-axis calibration were additionally verified by examining molecular monolayer film grown by electrostatic self-assembly method [321]. A near-perfect molecular layer over reasonably large areas is observed with the characteristic absorption in the visible region [321]. Single graphene layer on a quartz substrate is reported to be largely transparent with transmission (T) of 97% at 532 nm [333, 345]. Transmission loss increases with the number of graphene layers. Pristine (few-layer) graphene films were observed to have T > 96%. The transmission was found to monotonically decrease as the scattering increases with the increasing number of layers. This observation is consistent with the general trend of linear increase in opacity with the number of stacked graphene layers with the low value (~ 0.3 eV) of the interlayer hopping term in few-layered graphene [346].

6.5.1 Layer dependent charge transfer interaction

Recent report infers the presence of charge-transfer states when few-layer graphene interact with electron donating tetracyanoethylene (TCNE) or electron removal tetrathiafulvalene (TTF) molecule [344, 347]. The CT induced absorption features is evident in the UV-Vis spectra [344, 347]. This collective response in far-field CT-absorption in principle is spatially deconvoluted by local transmission scans using near-field microscopy. The CT feature of the graphene-molecule complex was indicated by a distinct decrease in transmission on a local well characterized region, along with a characteristic dependence on the graphene-layer number. Typical solution-deposited graphene films on quartz substrate consist of many layers of graphene. The transmission NSOM images of graphene films were relatively uniform and featureless. Upon introducing the charge transfer molecule such as TCNE or TTF on graphene, the film assumes morphology which was clearly followed by AFM imaging. Corresponding NSOM image reveals transmission-contrasting features of higher magnitude which provides a clear indication of the interface charge-transfer induced absorption band (Figure 6.10).

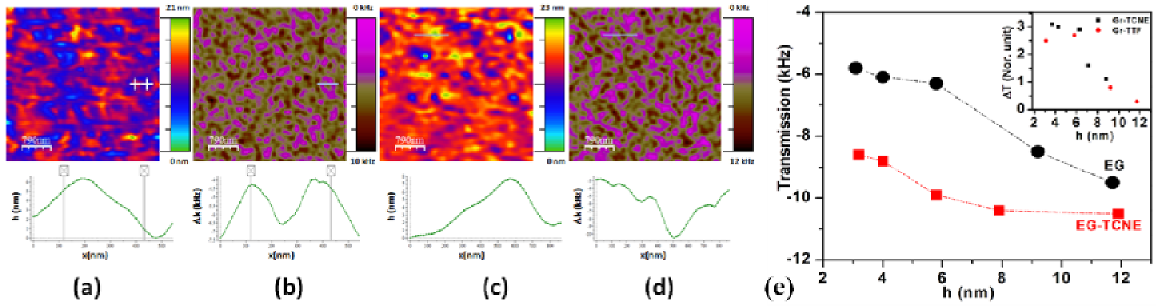

Figure 6.10: (a) and (b) AFM and NSOM images of spin-cast EG graphene on a quartz substrate respectively. (c) and (d) AFM and NSOM images of TCNE deposited EG graphene on quartz substrate. Line scan corresponding to the region depicted in the images are shown below. (e) Variation of transmission (in units of PMT counts) as a function of the underlying EG graphene layer thickness with adsorbed TCNE. Inset shows the graphene-donor/acceptor interaction strength following the difference in transmission for EG-TCNE/TTF as a function of the underlying EG thickness.

NSOM studies were carried out on different graphene samples prepared from three separate methods. All the necessary background measurements such as that of plain quartz substrates, TCNE and TTF deposited films on quartz substrates were carried out to ascertain the specificity of the interaction of these molecules on graphene coated substrates. The limitation in z-resolution (~ 1 nm) restricts NSOM method to carry out studies of the CT molecules for mono or bilayer graphene. However, the graphene deposited from solution with thickness > 3 nm were conducive for our technique. To ensure the molecular film thickness < 10 nm on graphene film, appropriate concentrations of TCNE and TTF were utilized.

The images obtained from a large number of scans over different areas reveal the following trends: (a) Graphene prepared by exfoliation of graphite oxide (EG) showed the largest changes in the local absorption upon introducing TCNE or TTF (b) Relative changes in the absorption introduced by the molecular species decreases as the number of underlying layer (EG) graphene layer increases. (c) Introducing TCNE (acceptor) on graphene showed a marginal enhancement in absorption as compared to the introduction of TTF (donor) on graphene. (d) Graphene prepared by Arc-evaporation of graphite in Hydrogen Atmosphere (HG) or by conversion of nano-diamond (DG), the large scattering-losses appeared to be more sizable compared to the absorption from the CT band. This feature is attributed to the significant increase in scattering related loss in thickness as compared to the changes introduced by the CT processes. In the near field regime, the scattering contribution from graphene is primarily controlled by topographical features of the surface [348]. The results are indicative of the dominant modification in optical activity at the TCNE/TTF-graphene interface. The interface encountered within the volume of the beam is nearly constant and is independent of the underlying thickness of the graphene layer (from monolayer to multilayer). A relative decrease in the transmitted intensity with graphene thickness then represents the interaction strength. Change in transmission as a function of graphene flake thickness was obtained from a line scan over a region where a smooth thickness variation is present (Figure 6.10). Analyses over several such regions clearly indicate that the larger absorption occurs for thinner layer graphene-TCNE/TTF complex. This measure of interaction strength follows near linear response with slope of ≈ 0.4 kHz/layer, indicating a sizable dependence with thickness.

6.5.2 Polymer photoluminescence quenching

Fluorescence quenching properties of graphene was examined by monitoring local photoluminescence intensity from polymer film coated on graphene (Figure 6.11d). Poly [2-

methoxy-5-(2-ethyl-hexyloxy)-1, 4-phenylene-vinylene (MEH-PPV) polymer with large fluorescence quantum yield was utilized as the donor. MEHPPV [λ_{max} (absorption) ~ 490 nm, photoluminescence (PL) emission range 550 – 750 nm] in its pristine form in solution upon photo-excitation, radiatively decays efficiently through the intra-chain $1B_u$ singlet exciton state where the lifetime of the excited state has been observed to be ~ 320 ps [83]. In the dried film state, the PL quantum yield gets lowered with a radiative lifetime of 1 ns – 5 ns range [83]. The exciton diffusion length in these systems is estimated to be ~10 nm [83, 326, 349]. The PL emission quenching of MEHPPV, upon introducing acceptor systems such as C_{60} and its derivatives, has been extensively studied. Similarly PL quenching ability of carbon nano-tube and 2D graphene sheet were demonstrated through transfer of photo-generated charge carriers from optically excited ZnO nanoparticle [350]. The effect of EG graphene in the MEHPPV solution was similar and a discernable PL emission weakening was clearly observed (Figure 6.11a).

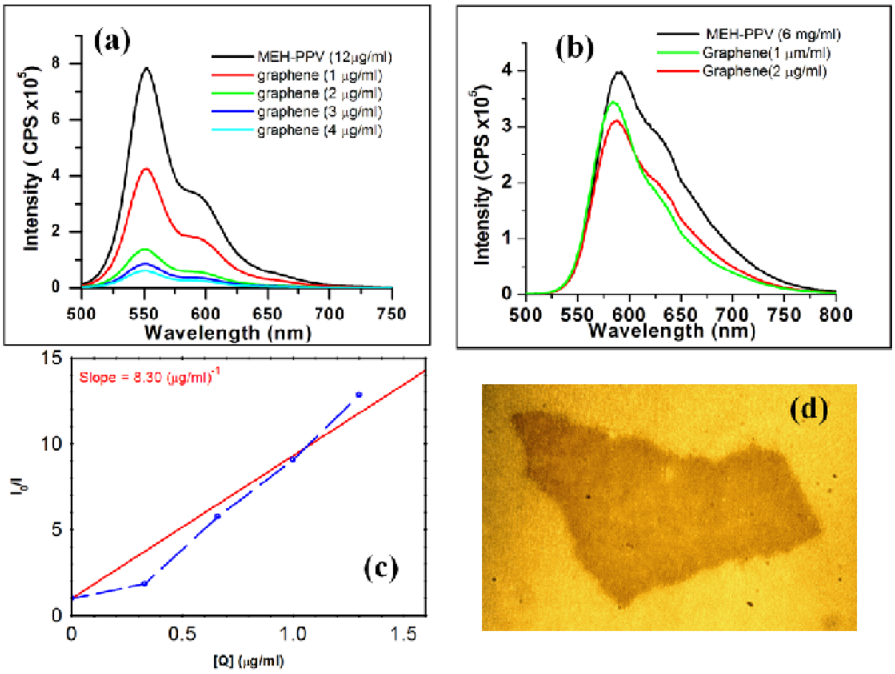

Figure 6.11: MEH-PPV fluorescence quenching with different concentration of EG graphene in solutions (a) and in dried thin films (b). (c) Stern-Volmer type plot (I_0/I) as a function of graphene concentration in solution. (d) Polymer PL quenching when coated on graphene flake exploited from HOPG substrate.

Fluorescence quenching of graphene MEH-PPV composites were studied using spin casting films on quartz from 6mg/ml MEH-PPV solution in xylene with different graphene concentration (Figure 6.11b). Homogenous films consisting of MEHPPV blended with EG was formed using EG content < 10%. The decreasing PL trend with EG content was also observed in these films. The bulk features were examined more closely using NSOM fluorescence scans. For NSOM measurement, few-layer-graphene was spin coated from xylene solution on oxidized (300 nm) silicon substrate. AFM scans prior to MEH-PPV deposition were carried out to identify the graphene regions and used for a systematic analysis of the PL intensity variations with respect to the interface formation (Figure 6.12a). Then MEH-PPV was dropped cast on it from chloroform solution (weight ratio ~ 7x10^{-3} %).

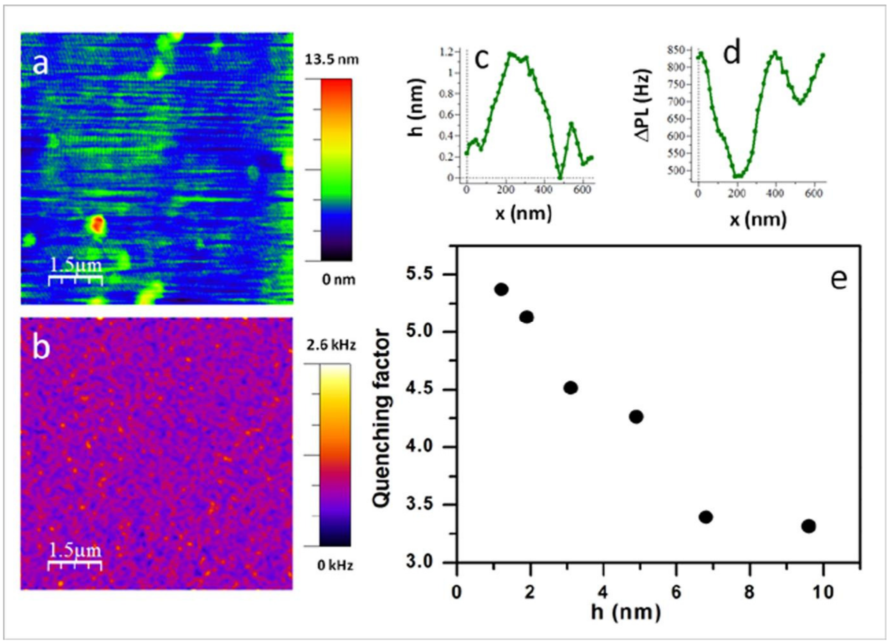

Figure 6.12: (a) AFM image of spin cast graphene on silicon substrate prior to polymer deposition. (b) 2D map of PL intensity variation on graphene/polymer film. (c, d) are the Line profiles of (c) AFM and (d) NSOM image respectively. (e) Polymer PL quenching factor as a function of local graphene flake height. Copyright 2011, The Japan Society of Applied Physics.

The films were then examined with 100 nm NSOM tip as a near field light source coupled with 532 nm laser and raster scanning of sample using phase feedback mode (Figure 6.12b). PL signal was collected in reflection mode microscopy with 532 sharp cut-off filter (Ocean optics) and long working distance objective (50X, N.A = 0.45). The data was analyzed using WSXM software [259], with standard normalization procedure and color scales were used to portray the NSOM images (Transmission $_{max}$ = 0). The MEH-PPV fluorescence quenching at graphene layer is attributed to the energy transfer or charge transfer processes analogous to the extensively studied polymer hetero-structures with C_{60} type acceptor systems [331, 351]. The mechanism of quenching can probably be inferred by introducing a spacer layer and observing the distance dependence, and comparing it with theoretical predictions [338]. The graphene-polymer systems exhibit features where the extent of the interaction appears to depend on the number of graphene layers (Figure 6.12e). A larger fraction of photoluminescence quenching was observed on thinner graphene regions. These direct observations clearly indicate the presence of charge transfer from the photo-excited polymer chains to underlying graphene flakes, with the degree of charge transfer appearing to be a function of number of graphene layers. The local quenching factor was estimated as ($\rho = I_0/I_G$), where I_0 and I_G are PL intensity of the polymer on silicon substrate (or ITO substrates) and in the presence of the underlying graphene layer (Figure 6.12e). An inversely proportional relation was obtained between ρ and the number of graphene layers.

6.5.3 Sandwich device characterization

The important consequence of photoluminescence quenching is a charge separated state which opens up the possibility of incorporating graphene-polymer combination in a photovoltaic device structure. Homogenous films consisting of MEH-PPV blended with EG (< 10% weight ratio) were explored for these studies. Graphene-MEH-PPV devices were fabricated by spin casting MEH-PPV (6 mg/ml) solution with different graphene concentration on clean ITO substrate, and then aluminum (Al) was thermally deposited on it to use as a counter electrode. Standard Lock-in measurements of these photovoltaic structures were carried out with calibrated white light source and monochromator at chopper frequency 17 Hz. A large number of devices fabricated with different ratios of MEH-PPV (D) and graphene (A) clearly indicate the trend where device response (short-circuit current/incident power) increased with increasing graphene content (≈ 1 pA/µW to 10 pA/µW for similar dimensions and thickness of the active layer).

Enhancement in short circuit PC with increasing graphene content up to a certain concentration is attributed to more excitons dissociation at the graphene-polymer interface. However, at larger proportions of graphene, the non-uniformity of the film leads to large leakage (dark) current. (Figure 6.13) A uniformly blended film of appropriate thickness improves both V_{OC} (~ 0.4 V) and power conversion efficiencies (~ 0.3%) of these devices. The presence of enhanced PC from composite film indicates efficient carrier separation at polymer-graphene interface. The 2D graphene surface interfacing with the polymer chains can be expected to be conducive for a 2D planar charge delocalization upon photoexcitation. A controlled and optimized intercalated stack of such constituents can possibly lead to efficient charge transport and solar cell structures.

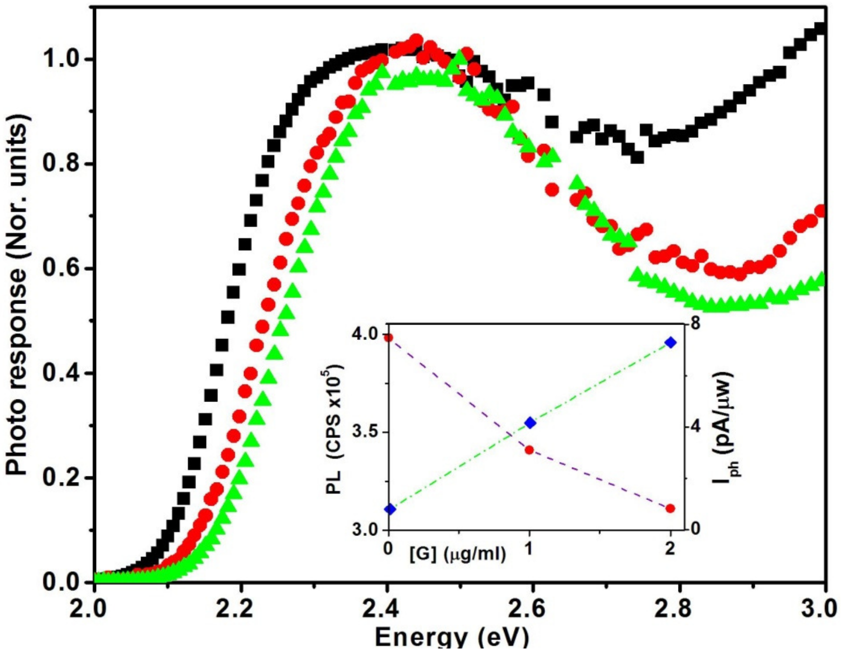

Figure 6.13: Spectral response of PC in a sandwich configuration (ITO/MEH-PPV, EG graphene/Al) based devices with different graphene concentration, [0 (▶), 1 μg/ml (•) and 2 μg/ml (▪)]. Inset (b) is the PL emission intensity using excitation (λ = 490 nm) along with the short-circuit PC response (λ = 490 nm) as function of graphene concentration in dried films.

6.5.4 Variation in spatial decay length on graphene coated substrate

Spatial PC decay measurement was utilized to contemplate the applicability of graphene electrode in BHJ solar cells. The modification of PC decay profile outside the overlapping electrode was employed on p-type poly(3-hexylthiophene) (P3HT) and n-type napthalene-dicarboximide (N2200) polymers upon introducing graphene layer on ITO electrode [352, 353]. The device fabrication involved patterning of ITO coated thin cover slips (to enable a tight focus of the beam with 60X objective) on top of which, the graphene was deposited from xylene solution. P3HT and N2200 procured from Sigma Aldrich and Polyera ActivInk respectively were spin coated from chlorobenzene solution. Subsequently, counter aluminum electrode (40 nm) was thermally evaporated using physical mask such that the distinct overlapping and non-overlapping regions were present between the electrodes. The choice of P3HT and N2200 yielded a nice complementary pair to demonstrate the validity of graphene as electrode, since $\mu_e^{N2200} > \mu_e^{P3HT}$ and $\mu_h^{N2200} < \mu_h^{P3HT}$. [339, 352, 353]

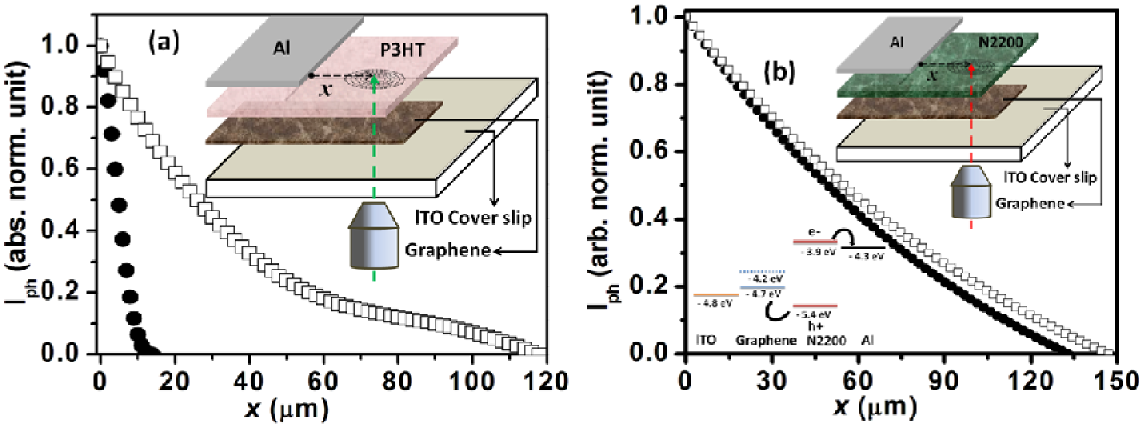

Figure 6.14: (a) Spatial PC decay (PC) profiles outside the Al electrode for ITO|P3HT|Al (filled circle) and ITO|Graphene|P3HT|Al (square). (b) PC decay profiles for ITO|N2200|Al (filled circle) and ITO|Graphene|N2200|Al (square). Copyright 2011, The Japan Society of Applied Physics.

This feature was reflected in the L^e_D obtained from decay profiles of the pristine system on ITO substrate (Figure 6.14a). Graphene coating on ITO was found to modify the decay for P3HT considerably with $L^e_D \sim 35$ μm as compared to L^e_D of 5 μm in pristine P3HT. In spite of lower magnitude ($PC^{ITO|graphene|P3HT|Al}/PC^{ITO|P3HT|Al} \sim 0.3$) of PC in the overlapping region in ITO|graphene|P3HT|Al device, the decay current persisted outside the Al edge over a larger length scale. This feature was unlike the situation we observed, where an increase in both the bulk transport features as well as decay lengths upon subjecting the films to appropriate thermal and surface treatment was seen [248]. The introduction of graphene layer significantly alters the decay profile in systems with smaller μ_e. In case of electron transporting polymer N2200, profiles with higher L^e_D were observed as the light beam position was scanned over the ITO region and extended beyond the Al electrode boundary (Figure 6.14b). PC scans of n-transport in N2200|ITO ($L^e_D \sim 80$ μm) and N2200|graphene|ITO device demonstrated a marginal increase in L^e_D (~ 100 μm), with an estimated mobility–lifetime product ≈ 3.6×10^{-7} cm^2 V^{-1}.

The observed decay profiles do not reflect three-dimensional transport of the photogenerated holes for light incident on the extended Al electrode region (where $x = 0$, ⇒ ITO edge) in the graphene coated substrates compared to the graphene-absent devices.

Graphene layer was not patterned and was extended to the entire region of the active polymer coating. The light beam focused on this non-overlapping region resulted in PC initiated by the photo induced electron transfer at the Al-P3HT Schottky type interface. The excess holes then spread from the generation zone towards the graphene layer, which yielded the sink, akin to an extended electrode for the holes and restricted the hole-spreading in the dark region of the polymer layer (Figure 6.15). PC(x) magnitude, and the decay reflected the graphene conductance rather than the bulk property of the polymer especially at large x. PC(x) persisted beyond x = 250 μm, indicating the hole transport-efficiency of the graphene layer. The distance over which PC decreases depends on graphene flake organization, and the PC profile is governed by dimensions describing the 2D fractal type network of the graphene patches. Solution-dispersed graphene yielded a slowly varying exponential decaying PC(x) and was expected to take up a linear response for a continuous extended graphene films. Direct applications of graphene modified electrode, from these observations, points towards the utility of graphene in position sensitive detectors and hole collecting electrodes in flexible BHJ cells.

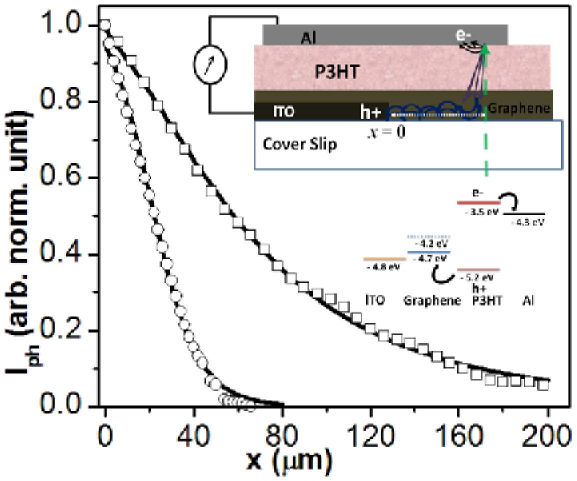

Figure 6.15: Normalized PC decay outside the ITO electrode for ITO|P3HT|Al and ITO|Graphene|P3HT|Al devices. Inset: Schematic of fabricated device and details of energy diagram. Copyright 2011, The Japan Society of Applied Physics.

Contributions from the finite beam size, light scattering and local heating effects, which are accounted for the imaging method, were well examined by FDTD simulation (Figure 6.16). Simulated optical scattering (OptiFDTD, Ver. 8.0) from graphene flakes on

ITO coated (50 nm) cover slips (thickness ~ 170 μm) demonstrated that optical scattering decays within a μm from the flake edge (<< L_D).

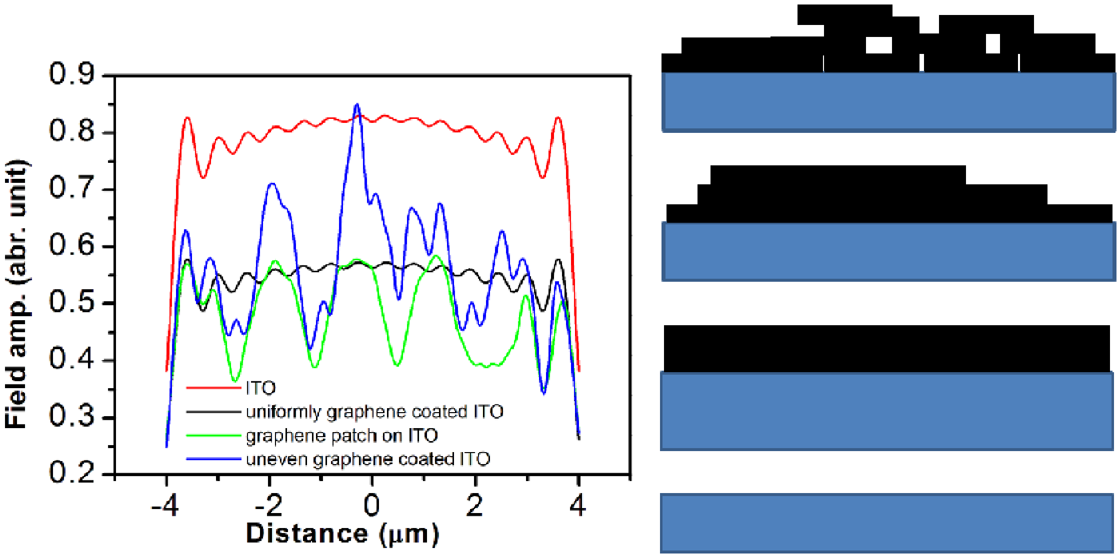

Figure 6.16: Optical field scattering from films consisting of graphene flakes (500 μm to 2 μm). The schematic of simulated structure is shown in right. Graphene films (black block) where blue represents ITO coating on glass (20-30 nm).

Assuming that the bulk structure and morphology is not considerably altered by graphene coating, the explanation for these differences should arise from the interfacial properties. The graphene layer essentially minimizes the interfacial recombination and increases the barrier for re-injection of the holes (in the dark region). In order to correlate the spatial dependency of PC with microscopic transport processes in polymer systems, we employed a spreading impedance model which was previously developed for similar device structures [251]. The electrical properties and heterogeneity of the extended graphene electrode was quantified by analyzing spatial-decay profile employing spreading impedance approach (SIA) [249, 251]. The PC in equivalent circuit is represented by

$$I_{ph}(x)=\frac{R_R}{R_R+R_E+R_{sp}(x)}I_0 \qquad (6.2)$$

Normalized PC profile was fitted to the expression $I'_{ph}(x) = \{1 + a \exp[(x/\xi)^{\alpha}]\}^{-1}$, where $a = R_s/R_R$ (ignoring the electrode resistance R_E). The presence of graphene, as argued above, would increase R_R substantially, thus the parameter a decreases upon introducing graphene.

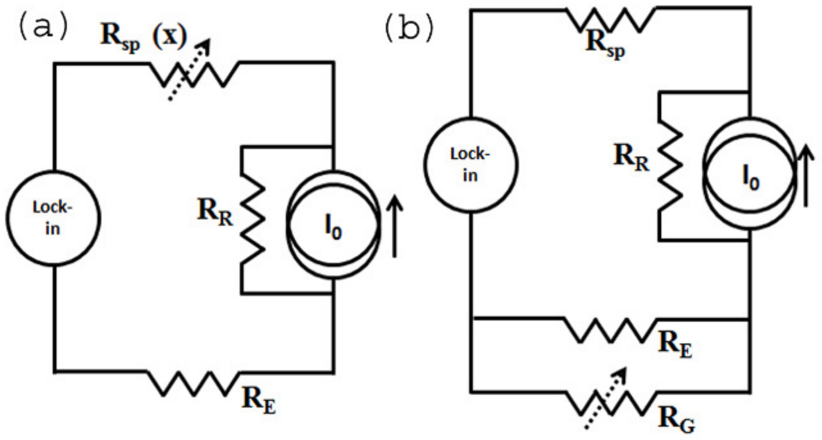

Figure 6.17: Equivalent circuit representation of spatial PC decay measurement for (a) electron and (b) hole current. Copyright 2011, The Japan Society of Applied Physics.

Upon photoexcitation, the electrons transfer across the Schottky-type Al-electrode, while the holes directly drift to the graphene layer. Physically, to reach the collecting ITO-electrode, the holes must travel through the patchy graphene network. Thus, the length scales extracted here reflect hole transporting characteristics of graphene layer. The spreading function ξ represents the graphene morphological characteristics (Table 3, rows 3 and 4). In the absence of graphene, the holes travel through the P3HT to reach ITO, and the spreading function parameters reflect the P3HT morphology. In pristine P3HT, $\mu_h \sim 10\ \mu_e$ and it reflects on ξ and α values in the absence of graphene. Lower α values are rationalized by significant influence of granularity of the graphene layer on spin-coated P3HT network. Although graphene is known to have a very high mobility, the patchy network here is responsible for such high sheet resistance.

Table 3: Comparison or theoretically fitted parameter

	a	ξ	α
P3HT electron decay	0.0365	1.01	0.766
Graphene P3HT electron decay	0.0114	0.302	0.335
P3HT hole decay	0.0541	5.61	0.780
Graphene P3HT hole decay	0.005	0.337	0.324
N2200 Electron decay	0.0543	9.98	0.665
Graphene N220 electron decay	0.0543	11	0.665

For n-type polymer while graphene has no effect on hole current decay profile, electron decay profile is affected to a very little extent and is attributed to the charge shielding properties of graphene. Presence of graphene at ITO-N2200 interface attracts the excess hole from the generation spot, and finally the hole spreads over through the fractal graphene network.

6.6 Conclusion

The uses of NSOM based approach to examine molecular processes are demonstrated in variety of systems. High spatial resolution (~ 50 nm) utilizing near field microscope is demonstrated by the single dye molecule imaging. NSOM microscopy was also successful in establishing the differences in optical behavior of different types of polymer nanoparticles. The hybrid nanoparticle consists of conjugated polymers with varying bandgap, exhibited considerably stronger emission for the acceptor with the suppressed donor emission. The images obtained from the NSOM and AFM analysis confirm and provide information on the interactions in the nanoscale. It is expected that this NSOM-based nanoscopic observation technique offers the potential for studying bio-molecular interactions at the single molecular level. In this pursuit, a NSOM-based approach was introduced that provides information in terms of the orientation and the efficiency of the bacteriorhodopsin photocycle on different substrates. The local transmission variations are directly correlated to the electronic processes occurring within bacteriorhodopsin film. Absorption changes provide quantitative assessment of the photocycle, including the distribution of the population densities in different intermediate states. Spatial and temporal features of the bacteriorhodopsin photophysical processes are directly studied upon introduction of a blue light as a pump source corresponding to the specific intermediate state. Introduction of graphene coating in asymmetric device structures modifies the photocarrier generation and transport features considerably upon localized photoexcitation. Local fluorescence contrast from conjugated polymer film coated on graphene substrate reveals the energy/charge transfer interaction of graphene film and conjugated polymer. This charge extraction and transport properties can be utilized to design functional electrodes for optoelectronic devices.

Chapter 7

Summary and Future Directions

The two new techniques, namely the spatial PC decay and near field current contrast optical imaging method and their application to organic photovoltaics form the main focus of the thesis. These techniques are mainly utilized to study the phase separated morphology of the bulk heterojunction film and the electrical transport efficacies of the active media. To understand critical parameters determining heterojunction morphology, and to correlate BHJ morphology with the performance of bulk-heterojunction solar cell, it is essential to have microscopic information of photoactive layer and its interfaces with electrodes. The developed techniques are successfully utilized to follow the evolution of heterojunction film morphology with different processing conditions. The overall results and relevant remarks of these studies on BHJ morphology have been summarized in the thesis.

Spatial PC decay technique is based on the PC decay profile outside the overlap electrode in an asymmetric device structure. Morphology dependent spatial current-decay profile and extent of unipolar lateral decay length rationalize donor-acceptor ratio for efficient bulk-heterojunction solar cell. Heterogeneity between donor-acceptor components, ambipolar transport, and continuous percolation pathways in active layer are followed in combination with the lateral PC decay profile in asymmetric electrode device and high resolution near field transmission contrast measurement.

Near field current contrast mapping is realized utilizing near field scanning optical microscopy on asymmetric device structure. Photocurrent from the peripheral region of the electrode provides near field access of the blend film, optical contrast image, and spatially resolved photocurrent contrast. These studies demonstrate near field scanning optical microscope, as a powerful tool to follow the in-situ evolution of nanoscale phase separation of donor-acceptor domains in bulk heterojunction film. The topological, transmission and PC contrast images are obtained from near field scan on bulk heterojunction film and renders local structural, optical and optoelectronic contrast at ~ 80 nm spatial resolution. The quasi-periodic length scales present in the contrast images are obtained from the 2-dimensional fast Fourier transform and power spectral density analysis of these images. This method has been employed to follow changes in bulk heterojunction morphology with the variation in donor-acceptor ratio in blend and thermal annealing conditions. The near field transmission and PC measurements (fluorescence, transmission) can be further used to predict the 3-dimensional phase distribution in BHJ film. The attempt can be made by the reconstruction of 2-dimensional transmission and PC contrast images to a 3-domensioal image. The wavelength dependent absorption coefficient of donor polymer provides information about the vertical cross-section of heterojunction film. Following this procedure, by modulating the probe light intensity, a *z*-stack view or vertical cross-section image of the bulk film can be possible to obtain. Then the 3-diemnsional acceptor distribution can be estimated from the transmission contrast image whereas PC contrast will provide the vertical connectivity present in the bulk film.

These newly developed techniques are further utilized to understand and quantify the dissimilarity present in the D-A ratio between crystalline and amorphous blend for optimized device performance. The effects of acceptor concentration to initiate D-A phase separation in amorphous blend have been investigated. The requirement of lower acceptor ratio for crystalline blend is investigated following the optical transmission through phase separated microstructure, present in BHJ film. Results from these methods demonstrate that nature of the donor polymer determines the D-A ratio to develop an optimized BHJ morphology. Combination of these two methods can be farther employed for various D-A systems to probe, evaluate and arrive at an optimized network for efficient BHJ solar cell.

The approach designed to examine BHJ based solar cells can be utilized to optimize the processing parameters for recently reported materials, which demonstrate high efficiency. Further optimization of these devices may possibly lead to efficiencies exceeding the 10% range.

Appendix I

Interpretation of the Decay Length

Considering nonlinear recombination process, continuity equation for carrier transport can be expressed as

$$\frac{\partial n}{\partial t} = D'\frac{\partial^2 n}{\partial x^2} - k_r' n^\gamma + G' \tag{A1.1}$$

Where n represents total collection of carriers ($n = n_f + n_t$), D' and k_r' are the carrier diffusion and recombination rate constant with exponent γ where G' is the carrier generation rate. Utilizing a partial differentiation, $\left(\frac{\partial n_t}{\partial t} = \frac{\partial n_t}{\partial n_f}\frac{\partial n_f}{\partial t}\right)$ equation reduces to

$$\frac{\partial n_f}{\partial t}\left(1 + \frac{\partial n_t}{\partial n_f}\right) = D'\frac{\partial^2}{\partial x^2}\left(n_f + n_t\right) - k_r'\left(n_f + n_t\right)^\gamma + G' \tag{A1.2}$$

The equation can be expressed in terms of the free carrier density as

$$\frac{\partial n_f}{\partial t} = D\frac{\partial^2 n_f}{\partial x^2} - k_r n_f^\gamma + G \tag{A1.3}$$

Here D and k_r are the modified diffusion constant and recombination rate in present of considerable trap state. At steady state and under small signal approximation $n_f = n_i + \Delta n$ and $\Delta n/n_i \ll 1$, continuity equation can further reduced to

$$D\frac{\partial^2 \Delta n}{\partial x^2} - k_r \gamma n_i^{\gamma-1}\Delta n = 0 \Rightarrow \frac{\partial^2 \Delta n}{\partial x^2} - \frac{\Delta n}{\Lambda_\gamma^2} = 0 \text{ where } \Lambda_\gamma^2 = \left(\mathrm{D}/k_r \gamma n_i^{\gamma-1}\right) \tag{A1.4}$$

Equation A1.4 provides an exponential solution $\Delta n = \Delta n_0 exp(-x/\Lambda)$. Assuming generalized Einstein relation (equation 1.7), decay constant Λ_γ (*i.e.* decay length for γ = 1; $\Lambda_1 \approx L_D$) has an inverse proportional relation with D, k_r and n_i.

Appendix II

Numerical Calculation of Decay under DC Optical Bias

PC decay profile outside the overlap region at different background illumination demonstrates carrier recombination with the trapped carriers throughout their transit following different percolation paths to the electrode (Figure A-2.1). With increasing DC background, trap states near the demarcation energy get occupied with carriers which directly take part in the recombination and modify PC decay profile. The carrier recombination effect on lateral and vertical transport was estimated by comparing normalized PC response at different positions outside the electrode with different light bias.

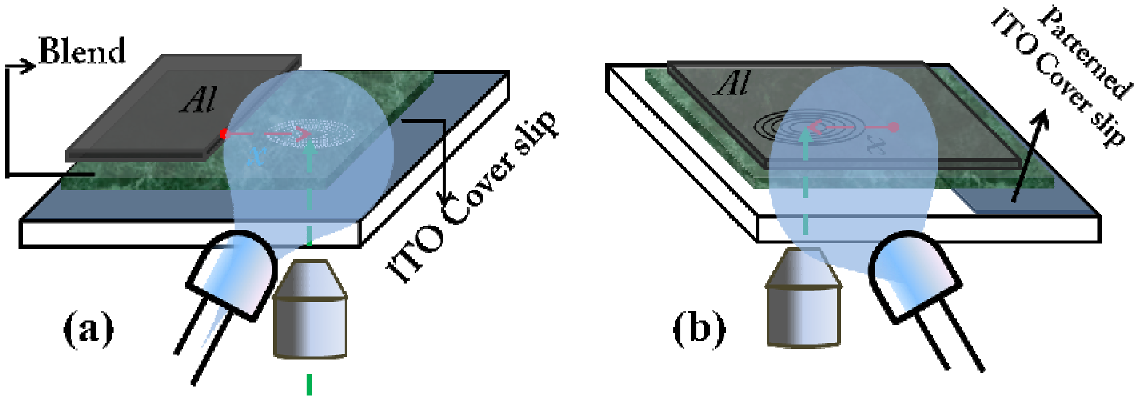

Figure A-2.1: Schematic of electron (a) and hole (b) decay length measurement under constant DC optical bias.

In absence of background intensity, photo response amplitude at 100 µm away from the electrode edge decreases to ~ 30 % of photo response at overlap region. Photo responsivity depletes nearly 70% as compared to overlap region in presence of 0.2 Sun background illumination. It reveals that bimolecular recombination between trap carriers and photogenerated carriers dominate during lateral transport and it enhances under DC light bias correlating lower device efficiency at operating condition.

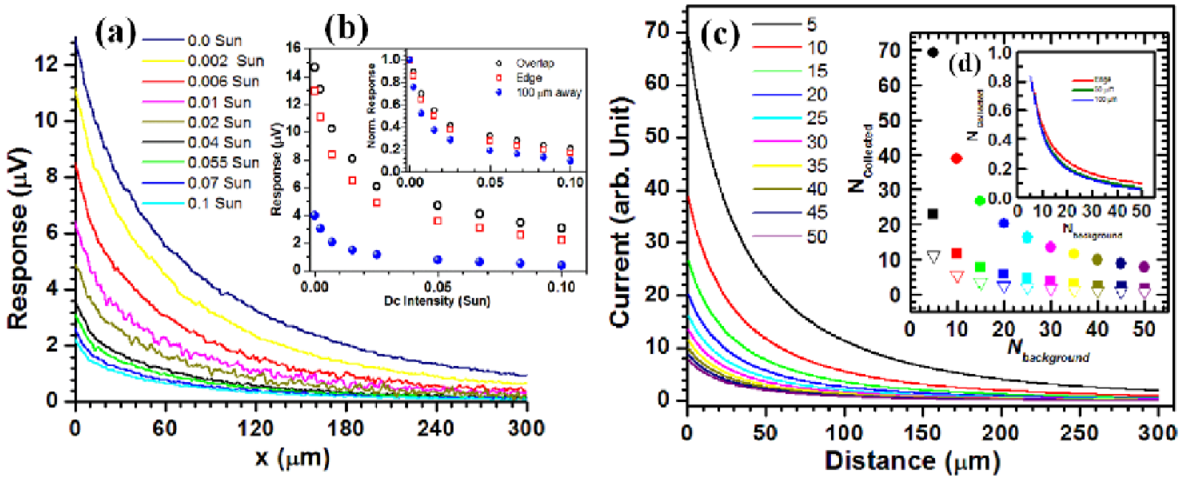

Figure A-2.2: (a) Spatial PC decay measurement under different background illumination. (b) Variation of relative photo response at different distance from electrode edge with different background intensity. (c) Numerical simulation of number of carriers reached to the electrode under different background carrier concentration as presented on the legend (for 500 probe carriers). (d) Relative variation of carriers collected from different distance from edge at different background carrier concentration as experimentally observed in (b).

DC illumination provides a uniform background current which serves to replete these trap states with uniform charge generation all over the bulk. Thus in presence of steady state current, carrier transport can be explained by a combined process of relaxation and transport within a broad and continuous density of state. This idea has been utilized to model spatial PC profiles in asymmetric devices. The number of carrier generated at the distance x from the electrode edge assumed to be $n^0(x) = PG$, where P is the internal quantum efficiency, G the number of photon incident on the device. Interfacial geminate pair recombination also incorporated in the term P here. $R_R(x)$ denote as recombination resistance incorporating total recombination process during carrier transport to the electrode and follows inversely proportional relation with recombination rate. Considering trapping and bimolecular recombination process, the rate of carrier recombination during the travel to reach to the electrode from generation point is [269]

$$R(x) = (1 - P)\gamma(np - n_i^2) \tag{A2.1}$$

where γ is the Langevin recombination factor ($q(\mu_n+\mu_p)/\epsilon$), n_i the intrinsic carrier concentration. Background illumination modifies the recombination rate of optically and electrically created excess carriers along with occupied trap carriers. These effects are incorporated in simulation by modifying intrinsic carrier concentration of device accompanying incident photon rate and external quantum yield. At small signal limit ($I_{\text{DC}} >> I_{\text{probe}}$), these carriers alters the overall recombination rate significantly and can be expressed in the mathematical formalism as

$$R'(x) = (1 - P')\gamma(n_{DC}p_{DC} - \Delta n p_{DC}) \tag{A2.2}$$

Where P' is the position dependent internal quantum efficiency, n_{DC} and p_{DC} are photo-generated carriers under DC illumination, Δn is the carrier generated by probe intensity. As the current, following through the circuit is directly proportional to the number of carriers, the expression for the carrier extracted by the electrode from the generating point at distance x can be given as

$$n(x) = n^0(x)/\{1 + R'(x)exp(x/\xi)^\alpha\} \tag{A2.3}$$

For a given morphology, ξ and α were evaluated from the PC decay measurement in absence of background illumination, which in simulation are assumed to be 40 µm and 0.6 respectively. In general, large intrinsic carrier density in devices significantly enhances Langevin recombination over trap-assisted recombination. Devices consists of low band gap donor and acceptor material (fullerene derivatives), bimolecular recombination at interfacial trap/localized states limits the FF and EQE of the device which finally inflicts solar cell performance under operating condition.

MATLAB code for numerical calculation:

```
gama=input('enter internal quantum efficiency');
g=input('enter number of probe photon');
% dn = no of carriers, nph = no of photon, b = decay length scale,
DCG = no of DC photon, G = total carrier generation, Dp = DC carrier,
nR = total recombination rate, ng = no of carriers after recombination,
nx = no of carrier reaching to electrode from illumination point at distance x %
dn = g;
```

```
nph=zeros(300,30);
P=input('enter internal dissociation probability');
b = 2000;
count=1;
for DCG=10:10:300;
 G=g+DCG;
 Dp=DCG;
i=linspace(1,300,300);
 gama1 = gama*exp(-i/b);
 nR =(1-P)*gama1*(((Dp)^2)+(dn*(Dp)));
ng=P*g;
nx=ng./(1+((nR.*exp((i/40).^.65))));
nph(:,count)=nx;
plot(i,nph(:,count));hold on
count=count+1;
end
```

Appendix III

Transient Measurement at Low Temperature under Background Illumination

To evaluate the impact of occupied trap state in bulk transport and its influence on recombination process on device performance transient PC measurements (TPC) were carried out under constant DC illumination at various intensity levels. In low mobility photo-conducting material, transient PC measurements at different temperature provide direct information about the DOS following the dynamics of charge and their recombination process as they relax toward the tails of the density of states. Normalized transient profiles were found to be consistence with increasing probe pulse energy and background light over the range of intensity used. It indicates that our measurements are free from space charge limitation. Optical bias (DC illumination) itself causes exaction at traps which leads to saturation transient current with incomplete occupancy. To defeat this issue, transient measurement at different background intensity was utilized that provide trap dependent recombination carrier dynamics. Fast rise part of TPC is attributed to the transport of highly mobile carriers and slow decay components can be explained by the slower carriers transport complying trapping de-trapping process. Furthermore, change in TPC profiles and magnitude at different optical bias and temperature provide strong evidence that TPC profiles reflect tail states of DOS along with trap carrier dynamics.

At high temperature (350K – 300K), a direct influence of background light intensity on photo-response amplitude signifies that TPC dynamics follows the trapping process of charge rather than charge extraction. It also depicts that charge collection dynamics are much faster compare to the charge carrier loss through different process. Large time-scale thermal energy assisted de-trapping processes are evident from long tail in transient decay (375 K) profile.

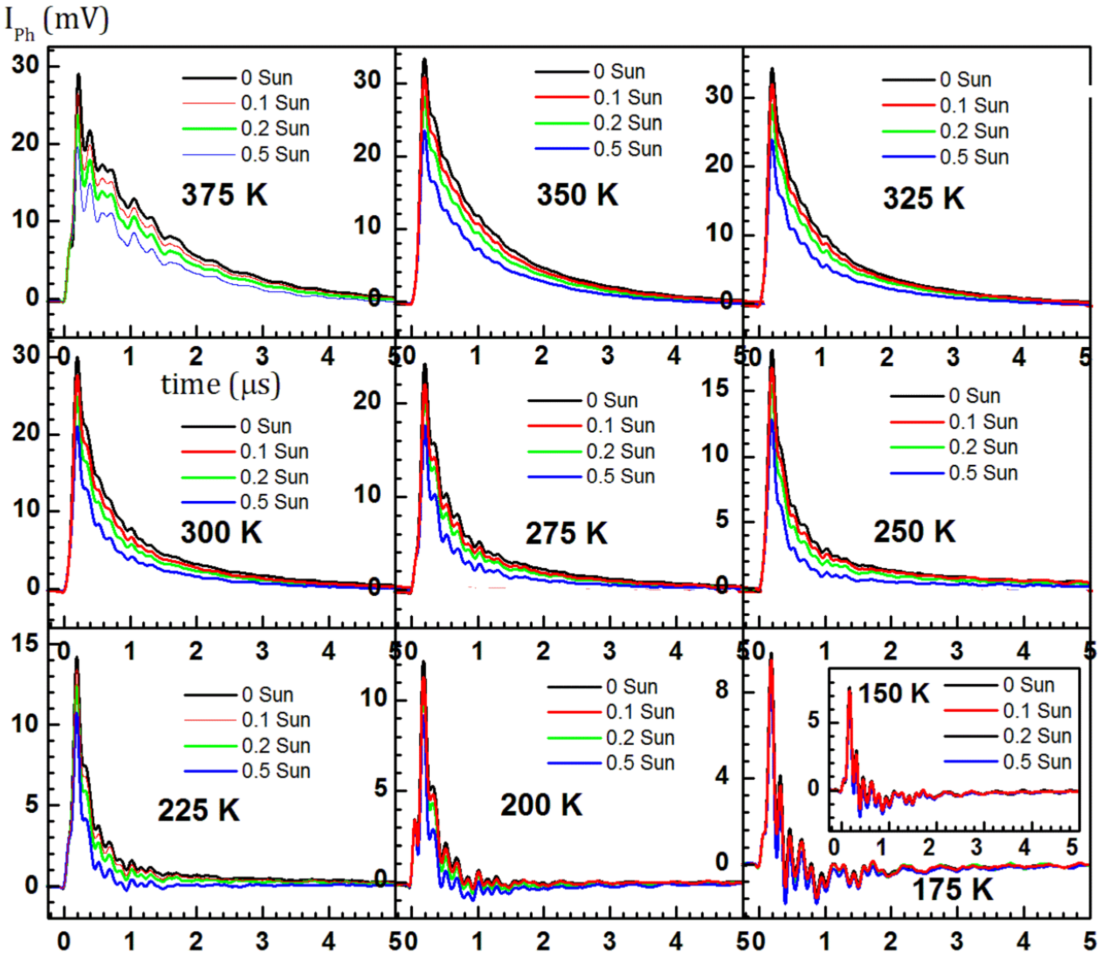

Figure A-3: Temperature dependent transient PC measurements of BHJ film with 10 ns, 532 nm laser pulse (pulse energy~ 80 nJ/sec) in presence of different background intensities (0 Sun to 0.5 Sun).

At high temperatures (375 – 275 K), background light intensity diminishes photo-signal amplitude while consistent features are observed for normalized TPC profiles. Trap-assisted recombination process is insignificant at this temperature range and carrier transport mainly governs by the temperature induced transport and demarcation energy in DOS system. At low background intensity, majority of the trap states are empty and photogenerated carriers from laser pulse descend into these traps state. Utilizing single exponential fit to TPC, trapping time scale is estimated – fraction of μs, while detrapping occurs at 2 – 10 μs time scale. In a given temperature, fast decay with increasing background intensity can be explained by inaccessibility of trap states (trap states are occupied with carriers generated from background illumination) for the photogenerated carriers from probe pulse. Transport energy and demarcation energy in the DOS gets modified at low temperature and only energetically sallow trap states contribute to the electrical transport. Photogenerated carriers from the front of laser pulse, populate available traps and take a long transit time. In absence of sufficient trap occupation, a significant portion of the probe pulse generated carriers populate the lower part of HOMO DOS and upper part of LUMO DOS levels (> E_t) and engender a 'trap free' transport. Following trap-free transport, generated carriers from the next portion of probe pulse, transit rapidly. Simultaneously recombination probability gets enhanced at lower temperature with lower carrier mobility and de-trapping rates (low thermal energy). At 150K, large proportion of trap states get frozen (low detrapping rate) and trap-free carries are departed with fast transient decay (~ 700 ns). A reversed transient PC was observed at low temperature range (175, 150 K) between 1 – 4 μs. During free carrier transport, the discrepancy between electron and hole mobilities is the origin for this behavior. At short circuit condition, and considering enhanced generation near cathode electrode, electron diffused much faster to the electrode in comparison to hole. This slowly diffused hole has negative current signature compared the hole drift current. So reverse response in the PC transient results from the hole diffusion rather than the electron.

The amount of charge extracted (ΔQ) from device subsequent to each laser pulse was estimated by integrating these TPC profiles. Total charge extraction reduces with temperature due to unavailable of accessible DOS. In conclusion, this analysis helps to examine the role of the localized trap states which influence both the total charge present in the device and the decay dynamics at any instant. It is also an extensive evidence for carrier trapping and associated energetic disorder, which strongly influenced the transport dynamics of the organic solar cell under solar illumination.

Biography

Sabyasachi Mukhopadhyay was born in West Bengal, INDIA, in 1983. He received his Bachelor of Science (Physics as a major) from University of Calcutta (Ramakrishna Mission Vidyamandira, Belur Math, Howrah) and Master of Science (Physics) from Indian Institute of Technology, Kharagpur, India in 2004 and 2006 respectively.

Since August, 2006 he has been with the Molecular Electronics Laboratory in Chemistry and Physics of Materials Unit at Jawaharlal Nehru Centre for Advanced Scientific Research, Bangalore, INDIA, working towards his PhD in the area of Near Field Optics and Organic Solar Cell. His current research interests include Scanning Probe Microscopy, Polymer Solar cells, Nano-optics and Plasmonics.

References

[1] A. Goetzberger, C. Hebling, and H. W. Schock, "Photovoltaic materials, history, status and outlook," *Mater. Sci. Engg: R: Reports,* vol. 40, pp. 1, 2003.

[2] D. Chapin, C. Fuller, and G. Pearson, "A New Silicon p-n Junction Photocell for Converting Solar Radiation into Electrical Power," *J. Appl. Phys.,* vol. 25, pp. 2, 1954.

[3] H. Hoppe and N. S. Sariciftci, "Organic solar cells: An overview," *J. Mater. Res.,* vol. 19, pp. 1924, 2004.

[4] H. Spanggaard and F. C. Krebs, "A brief history of the development of organic and polymeric photovoltaics," *Sol. Energy Mater. Sol. Cells,* vol. 83, pp. 125, 2004.

[5] J. B. Christoph, D. Vladimir, and S. E. Ullrich, *Organic photovoltaics: Materials, Device Physics and Manufacturing Technologies* vol. 1 edn. Weinheim: Wiley VCH, 2008.

[6] H. Akamatsu, and H. Inokuchi, "Electrical conductivity of the perylene–bromine complex," *Nature,* vol. 173, pp. 168, 1954.

[7] M. Pope and C. E. Swenberg, *Electronic Processes in Organic Crystals and Polymers* vol. 2nd edn., 1999.

[8] H. Shirakawa, E. J. Louis, A. G. MacDiarmid, C. K. Chiang, and A. J. Heeger, "Synthesis of electrically conducting organic polymers: halogen derivatives of polyacetylene, (CH)x," *J. Chem. Soc. Chem. Commun.,* pp. 579, 1977.

[9] G. A. Chamberlain, "Organic solar cells: a review," *Solar. Cells,* vol. 8, pp. 47, 1983.

[10] D. Hertel and H. Baessler, "Photoconduction in amorphous organic solids," *Chem Phys Chem,* vol. 9, pp. 666, 2008.

[11] G. Lanzani, *Photophysics of Molecular Materials: From Single molecules to Single Crystals* vol. 1 edn, 2006.

[12] W. E. Brutting, *Physics of Organic Semiconductor* vol. 1 edn, 2005.

[13] C. W. Tang, "Two-layer organic photovoltaic cell," *Appl. Phys. Lett.,* vol. 48, pp. 183, 1986.

[14] G. Yu, J. Gao, J. C. Hummelen, F. Wudl, and A. J. Heeger, "Polymer Photovoltaic Cells: Enhanced Efficiencies via a Network of Internal Donor-Acceptor Heterojunctions," *Science,* vol. 270, pp. 1789, 1995.

[15] S. E. Shaheen, C. J. Brabec, N. S. Sariciftci, F. Padinger, T. Fromherz, and J. C. Hummelen, "2.5% efficient organic plastic solar cells," *Appl. Phys. Lett.,* vol. 78, pp. 841, 2001.

[16] F. Padinger, R. S. Rittberger, and N. S. Sariciftci, "Effects of Postproduction Treatment on Plastic Solar Cells," *Adv. Funct. Mater.,* vol. 13, pp. 85, 2003.

[17] J. Xue, B. P. Rand, S. Uchida, and S. R. Forrest, "Mixed donor-acceptor molecular heterojunctions for photovoltaic applications. II. Device performance," *J. Appl. Phys.,* vol. 98, pp. 124903, 2005.

[18] S. H. Park, A. Roy, S. Beaupre, S. Cho, N. Coates, J. S. Moon, D. Moses, M. Leclerc, K. Lee, and A. J. Heeger, "Bulk heterojunction solar cells with internal quantum efficiency approaching 100%," *Nature Photon.,* vol. 3, pp. 297, 2009.

[19] J. Peet, J. Y. Kim, N. E. Coates, W. L. Ma, D. Moses, A. J. Heeger, and G. C. Bazan, "Efficiency enhancement in low-bandgap polymer solar cells by processing with alkane dithiols," *Nature Mater.,* vol. 6, pp. 497, 2007.

[20] V. I. Arkhipov, I. I. Fishchuk, A. Kadashchuk, and H. Bassler, *Charge transport in disordered organic semiconductors - Photophysics of Molecular Materials* vol. 1 edn: Wiley-VCH Verlag GmbH & Co. KGaA, 2006.

[21] W. Schnabel, *Polymers and Light - Fundamentals and Technical Applications.* vol. 1 edn. Weinheim: WILEY-VCH Verlag GmbH & Co. KGaA, 2007.

[22] W. P. Su, J. R. Schrieffer, and A. J. Heeger, "Solitons in Polyacetylene," *Phys. Rev. Lett.,* vol. 42, pp. 1698, 1979.

[23] A. J. Heeger, S. Kivelson, J. R. Schrieffer, and W. P. Su, "Solitons in conducting polymers," *Rev. Mod. Phys.,* vol. 60, pp. 781, 1988.

[24] Y. Lu, *Solitons and Polarons in Conducting Polymers*, 1988.

[25] D. Beljonne, G. Pourtois, C. Silva, E. Hennebicq, L. M. Herz, R. H. Friend, G. D. Scholes, S. Setayesh, K. Mallen, and J. L. Bradas, "Interchain vs. intrachain energy transfer in acceptor-capped conjugated polymers," *Proc. Natl. Acad. Sci.,* vol. 99, pp. 10982, 2002.

[26] T. Q. Nguyen, J. Wu, S. H. Tolbert, and B. J. Schwartz, "Control of Energy Transport in Conjugated Polymers Using an Ordered Mesoporous Silica Matrix," *Adv. Mater.,* vol. 13, pp. 609, 2001.

[27] J. Yu, D. Hu, and P. F. Barbara, "Unmasking Electronic Energy Transfer of Conjugated Polymers by Suppression of O2 Quenching," *Science,* vol. 289, pp. 1327, 2000.

[28] E. Collini and G. D. Scholes, "Coherent Intrachain Energy Migration in a Conjugated Polymer at Room Temperature," *Science,* vol. 323, pp. 369, 2009.

[29] S. V. Novikov, D. H. Dunlap, V. M. Kenkre, P. E. Parris, and A. V. Vannikov, "Essential Role of Correlations in Governing Charge Transport in Disordered Organic Materials," *Phys. Rev. Lett.,* vol. 81, pp. 4472, 1998.

[30] M. Van der Auweraer, F. C. De Schryver, P. M. Borsenberger, and H. Bässler, "Disorder in Charge Transport in doped polymers," *Adv. Mater.,* vol. 6, pp. 199, 1994.

[31] M. Gailberger and H. Bassler, "dc and transient photoconductivity of poly(2-phenyl-1,4-phenylenevinylene)," *Phys. Rev. B,* vol. 44, pp. 8643, 1991.

[32] S. Shaked, S. Tal, Y. Roichman, A. Razin, S. Xiao, Y. Eichen, and N. Tessler, "Charge Density and Film Morphology Dependence of Charge Mobility in Polymer Field-Effect Transistors," *Adv. Mater.,* vol. 15, pp. 913, 2003.

[33] Y. Roichman and N. Tessler, "Charge transport in conjugated polymers -- The influence of charge concentration," *Synth. Met.,* vol. 135-136, pp. 443, 2003.

[34] D. Monroe, "Hopping in Exponential Band Tails," *Phys. Rev. Lett.,* vol. 54, pp. 146, 1985.

[35] J. Orenstein and M. Kastner, "Photocurrent Transient Spectroscopy: Measurement of the Density of Localized States in a-As_2Se_3," *Phys. Rev. Lett.,* vol. 46, pp. 1421, 1981.

[36] T. Tiedje and A. Rose, "A physical interpretation of dispersive transport in disordered semiconductors," *Solid State Commun.,* vol. 37, pp. 49, 1981.

[37] M. S. Iovu, I. A. Vasiliev, E. P. Colomeico, E. V. Emelianova, V. I. Arkhipov, and G. J. Adriaenssens, "Photocurrent relaxation in pure and Pr-doped a-As_2S_3 films," *J. Phys. Condens. Matter,* vol. 16, pp. 2949, 2004.

[38] V. I. Arkhipov, P. Heremans, E. V. Emelianova, G. J. Adriaenssens, and H. BÃ¤ssler, "Weak-field carrier hopping in disordered organic semiconductors: the

effects of deep traps and partly filled density-of-states distribution," *J. Phys. Condens. Matter,* vol. 14, pp. 9899, 2002.

[39] D. Y. Kim, J. K. Grey, and P. F. Barbara, "A detailed single molecule spectroscopy study of the vibronic states and energy transfer pathways of the conjugated polymer MEH-PPV," *Synth. Metal.,* vol. 156, pp. 336, 2006.

[40] V. I. Arkhipov, E. V. Emelianova, and G. J. Adriaenssens, "The effect of jumps into distant sites on carrier energy relaxation in a disordered hopping system," *J. Phys. Condens. Matter,* vol. 11, pp. 2531, 1999.

[41] V. I. Arkhipov, E. V. Emelianova, and G. J. Adriaenssens, "Variable-range hopping within a fluctuating potential landscape," *J. Phys. Condens. Matter,* vol. 12, p. 2021, 2000.

[42] H. Bässler, "Charge Transport in Disordered Organic Photoconductors a Monte Carlo Simulation Study," *Phys. Status Solidi B,* vol. 175, pp. 15, 1993.

[43] R. A. Marcus, "On the Theory of Oxidation-Reduction Reactions Involving Electron Transfer. I," *J. Chem. Phys.,* vol. 24, pp. 966, 1956.

[44] R. A. Marcus, "Electron transfer reactions in chemistry. Theory and experiment," *Rev. Mod. Phys.,* vol. 65, pp. 599, 1993.

[45] A. Miller and E. Abrahams, "Impurity Conduction at Low Concentrations," *Phys. Rev.,* vol. 120, pp. 745, 1960.

[46] F. Laquai, G. Wegner, and H. Bassler, "What determines the mobility of charge carriers in conjugated polymers?," *Phil. Trans. R. Soc. A,* 1993.

[47] W. D. Gill, "Drift mobilities in amorphous charge-transfer complexes of trinitrofluorenone and poly-n-vinylcarbazole," *J. Appl. Phys.,* vol. 43, pp. 5033, 1972.

[48] A. J. Mozer and N. S. Sariciftci, "Negative electric field dependence of charge carrier drift mobility in conjugated, semiconducting polymers," *Chem. Phys. Lett.,* vol. 389, pp. 438, 2004.

[49] S. M. Tuladhar, M. Sims, J. Kirkpatrick, R. C. Maher, A. J. Chatten, D. D. C. Bradley, J. Nelson, P. G. Etchegoin, C. B. Nielsen, P. Massiot, W. N. George, and J. H. G. Steinke, "Influence of alkyl chain length on charge transport in symmetrically substituted poly(2,5-dialkoxy-p-phenylenevinylene) polymers," *Phys. Rev. B,* vol. 79, pp. 035201, 2009.

[50] W. F. Pasveer, J. Cottaar, C. Tanase, R. Coehoorn, P. A. Bobbert, P. W. M. Blom, D. M. deaLeeuw, and M. A. J. Michels, "Unified Description of Charge-Carrier

Mobilities in Disordered Semiconducting Polymers," *Phys. Rev. Lett.,* vol. 94, pp. 206601, 2005.

[51] Y. Roichman and N. Tessler, "Generalized Einstein relation for disordered semiconductors---implications for device performance," *Appl. Phys. Lett.,* vol. 80, pp. 1948, 2002.

[52] C. H. Lei, A. Das, M. Elliott, J. E. Macdonald, and M. L. Turner, "Au-poly(3-hexylthiophene) contact behaviour at high resolution," *Synth. Metal.,* vol. 145, pp. 217, 2004.

[53] J. Bisquert, G. Garcia-Belmonte, A. Munar, M. Sessolo, A. Soriano, and H. J. Bolink, "Band unpinning and photovoltaic model for P3HT:PCBM organic bulk heterojunctions under illumination," *Chem. Phys. Lett.,* vol. 465, pp. 57, 2008.

[54] G. A. Chamberlain, "Organic solar cells: A review," *Solar Cells,* vol. 8, pp. 47, 1983.

[55] C. J. Brabec, V. Dyakonov, J. Parisi, and N. S. Sariciftci, *Organic Photovoltaics: Concepts and Realization* 1ed.: Springer 2003.

[56] S. Gunes, H. Neugebauer, and N. S. Sariciftci, "Conjugated Polymer-Based Organic Solar Cells," *Chem. Rev.,* vol. 107, pp. 1329, 2007.

[57] L. Liming and L. Guangyong, "Modeling and simulation of organic solar cells," in *Nanotechnology Materials and Devices Conference (NMDC), 2010 IEEE*, 2010, pp. 334.

[58] Y. Shang, Q. Li, L. Meng, D. Wang, and Z. Shuai, "Device simulation of low-band gap polymer solar cells: Influence of electron-hole pair dissociation and decay rates on open-circuit voltage," *Appl. Phys. Lett.,* vol. 97, pp. 143511, 2010.

[59] I. Riedel, E. von Hauff, J. Parisi, N. Martín, F. Giacalone, and V. Dyakonov, "Diphenylmethanofullerenes: New and Efficient Acceptors in Bulk-Heterojunction Solar Cells," *Adv. Funct. Mater,* vol. 15, pp. 1979, 2005.

[60] P. Schilinsky, C. Waldauf, J. Hauch, and C. J. Brabec, "Simulation of light intensity dependent current characteristics of polymer solar cells," *J. Appl. Phys.,* vol. 95, pp. 2816, 2004.

[61] J. Nelson, "Polymer:fullerene bulk heterojunction solar cells - Review article," *Materialstoday,* vol. 14, pp. 463, 2011.

[62] C. M. Bjorstrom, K. O. Magnusson, and E. Moons, "Control of phase separation in blends of polyfluorene (co)polymers and the C60-derivative PCBM," *Synth. Metal,* vol. 152, pp. 109, 2005.

[63] J.-H. Huang, Z.-Y. Ho, D. Kekuda, C.-W. Chu, and K.-C. Ho, "Controlled Growth of Nanofiber Network Hole Collection Layers with Pore Structure for Polymer-Fullerene Solar Cells," *J. Phys. Chem. C,* vol. 112, pp. 19125, 2008.

[64] W. J. Grzegorczyk, T. J. Savenije, M. Heeney, S. Tierney, I. McCulloch, S. v. Bavel, and L. D. A. Siebbeles, "Relationship between Film Morphology, Optical, and Conductive Properties of Poly(thienothiophene): [6,6]-Phenyl C-61-Butyric Acid Methyl Ester Bulk Heterojunctions," *J. Phys. Chem. C,* vol. 112, pp. 15973, 2008.

[65] B. A. Collins, J. R. Tumbleston, and H. Ade, "Miscibility, Crystallinity, and Phase Development in P3HT/PCBM Solar Cells: Toward an Enlightened Understanding of Device Morphology and Stability," *J. Phys. Chem. Lett.,* vol. 2, pp. 3135, 2011.

[66] J. Y. Kim and C. D. Frisbie, "Correlation of Phase Behavior and Charge Transport in Conjugated Polymer/Fullerene Blends," *J. Phys. Chem. C,* vol. 112, pp. 17726, 2008.

[67] M. G. Bawendi and K. F. Freed, "Systematic corrections to Flory--Huggins theory: Polymer--solvent--void systems and binary blend--void systems," *J. Chem. Phys.,* vol. 88, pp. 2741, 1988.

[68] P. J. Flory, "Thermodynamics of High Polymer Solutions," *J. Chem. Phys.,* vol. 9, p. 660, 1941.

[69] M. L. Huggins, "Solutions of Long Chain Compounds," *J. Phys. Chem.,* vol. 9, pp. 440, 1941.

[70] B. Ray, M. S. Lundstrom, and M. A. Alam, "Can morphology tailoring improve the open circuit voltage of organic solar cells?," *Appl. Phys. Lett.,* vol. 100, pp. 013307, 2012.

[71] S. Nilsson, A. Bernasik, A. Budkowski, and E. Moons, "Morphology and Phase Segregation of Spin-Casted Films of Polyfluorene/PCBM Blends," *Macromolecules,* vol. 40, pp. 8291, 2007.

[72] R. Meier, M. A. Ruderer, A. Diethert, G. Kaune, V. Koirstgens, S. V. Roth, and P. MuÌˆller-Buschbaum, "Influence of Film Thickness on the Phase Separation Mechanism in Ultrathin Conducting Polymer Blend Films," *J. Phys. Chem. B,* vol. 115, pp. 2899, 2011.

[73] Y. Vaynzof, D. Kabra, L. Zhao, L. L. Chua, U. Steiner, and R. H. Friend, "Surface-Directed Spinodal Decomposition in Poly[3-hexylthiophene] and C61-Butyric Acid Methyl Ester Blends," *ACS Nano,* vol. 5, pp. 329, 2011.

[74] A. J. Parnell, A. J. Cadby, O. O. Mykhaylyk, A. D. F. Dunbar, P. E. Hopkinson, A. M. Donald, and R. A. L. Jones, "Nanoscale Phase Separation of P3HT:PCBM Thick Films As Measured by Small-Angle X-ray Scattering," *Macromolecules,* vol. 44, pp. 6503, 2011.

[75] B. Watts, W. J. Belcher, L. Thomsen, H. Ade, and P. C. Dastoor, "A Quantitative Study of PCBM Diffusion during Annealing of P3HT:PCBM Blend Films," *Macromolecules,* vol. 42, pp. 8392, 2009.

[76] C. R. McNeill and P. C. Dastoor, "Photocurrent pattern formation in polymer/methanofullerene blends imaged by near-field scanning photocurrent microscopy," *J. Appl. Phys.,* vol. 99, pp. 033502, 2006.

[77] B. Tuck, *Introduction to Diffusion in Semiconductors*: Peregrinus, Salisbury,, 1974.

[78] T. J. Savenije, J. E. Kroeze, M. M. Wienk, J. M. Kroon, and J. M. Warman, "Mobility and decay kinetics of charge carriers in photoexcited PCBM/PPV blends," *Phys. Rev. B,* vol. 69, pp. 155205, 2004.

[79] N. S. Sariciftci, L. Smilowitz, A. J. Heeger, and F. Wudl, "Photoinduced Electron Transfer from a Conducting Polymer to Buckminsterfullerene," *Science,* vol. 258, pp. 1474, 1992.

[80] S. A. Jenekhe and J. A. Osaheni, "Excimers and Exciplexes of Conjugated Polymers," *Science,* vol. 265, pp. 765, 1994.

[81] M. Mehringi, *Electronic Properties of Conjugated Polymers*, 1 ed. vol. 91. Berlin: Springer, 1989.

[82] K. F. Voss, C. M. Foster, L. Smilowitz, D. MihailoviÄ, S. Askari, G. Srdanov, Z. Ni, S. Shi, A. J. Heeger, and F. Wudl, "Substitution effects on bipolarons in alkoxy derivatives of poly(1,4-phenylene-vinylene)," *Phys. Rev. B,* vol. 43, pp. 5109, 1991.

[83] I. D. W. Samuel, G. Rumbles, C. J. Collison, R. H. Friend, S. C. Moratti, and A. B. Holmes, "Picosecond Time-Resolved Photoluminescence of PPV Derivatives," *Synth. Metal,* vol. 84, pp. 497, 1997.

[84] M. Hallermann, S. Haneder, and E. Da Como, "Charge-transfer states in conjugated polymer/fullerene blends: Below-gap weakly bound excitons for polymer photovoltaics," *Appl. Phys. Lett.,* vol. 93, pp. 053307, 2008.

[85] Y. Zhou, K. Tvingstedt, F. Zhang, C. Du, W.-X. Ni, M. R. Andersson, and O. Inganäs, "Observation of a Charge Transfer State in Low-Bandgap Polymer/Fullerene Blend Systems by Photoluminescence and Electroluminescence Studies," *Adv. Func. Mater.,* vol. 19, pp. 3293, 2009.

[86] J. Lee, K. Vandewal, S. R. Yost, M. E. Bahlke, L. Goris, M. A. Baldo, J. V. Manca, and T. V. Voorhis, "Charge Transfer State Versus Hot Exciton Dissociation in Polymer-'Fullerene Blended Solar Cells," *J. Am. Chem. Soc.,* vol. 132, pp. 11878, 2012.

[87] X. Yang, J. K. J. van Duren, R. A. J. Janssen, M. A. J. Michels, and J. Loos, "Morphology and Thermal Stability of the Active Layer in Poly(p-phenylenevinylene)/Methanofullerene Plastic Photovoltaic Devices," *Macromolecules,* vol. 37, pp. 2151, 2004.

[88] H. Zhou, L. Yang, and W. You, "Rational Design of High Performance Conjugated Polymers for Organic Solar Cells," *Macromolecules,* vol. 45, pp. 607, 2012.

[89] T. M. Clarke and J. R. Durrant, "Charge Photogeneration in Organic Solar Cells," *Chem. Rev.,* vol. 110, pp. 6736, 2010.

[90] C. Deibel, T. Strobel, and V. Dyakonov, "Role of the Charge Transfer State in Organic Donor–Acceptor Solar Cells," *Adv. Mater.,* vol. 22, pp. 4097, 2010.

[91] C. L. Braun, "Electric field assisted dissociation of charge transfer states as a mechanism of photocarrier production," *J. Chem. Phys.,* vol. 80, pp. 4157, 1984.

[92] L. Onsager, "Initial Recombination of Ions," *Phys. Rev.,* vol. 54, pp. 554, 1938.

[93] P. Langevin, "Recombinaison et mobilites des ions dans les gaz," vol. 28, pp. 433, 1903.

[94] C. Deibel, A. Wagenpfahl, and V. Dyakonov, "Influence of charge carrier mobility on the performance of organic solar cells," *phys. status solidi (RRL) – Rapid Research Letters,* vol. 2, pp. 175, 2008.

[95] K. Vandewal, A. Gadisa, W. D. Oosterbaan, S. Bertho, F. Banishoeib, I. Van Severen, L. Lutsen, T. J. Cleij, D. Vanderzande, and J. V. Manca, "The Relation Between Open-Circuit Voltage and the Onset of Photocurrent Generation by Charge-Transfer Absorption in Polymer : Fullerene Bulk Heterojunction Solar Cells," *Adv. Func. Mater.,* vol. 18, pp. 2064, 2008.

[96] D. Veldman, S. C. J. Meskers, and R. A. J. Janssen, "The Energy of Charge-Transfer States in Electron Donor–Acceptor Blends: Insight into the Energy Losses in Organic Solar Cells," *Adv. Funct. Mater.,* vol. 19, pp. 1939, 2009.

[97] C. Deibel, A. Baumann, and V. Dyakonov, "Polaron recombination in pristine and annealed bulk heterojunction solar cells," *Appl. Phys. Lett.,* vol. 93, pp. 163303, 2008.

[98] A. Pivrikas, G. Juaika, R. Asterbacka, M. Westerling, M. Vilianas, K. Arlauskas, and H. Stubb, "Langevin recombination and space-charge-perturbed current transients in regiorandom poly(3-hexylthiophene)," *Phys. Rev. B,* vol. 71, pp. 125205, 2005.

[99] J. Bisquert, "Interpretation of electron diffusion coefficient in organic and inorganic semiconductors with broad distributions of states," *Phys. Chem. Chem. Phys.,* vol. 10, pp. 3019, 2008.

[100] C. J. Brabec, G. Zerza, G. Cerullo, S. De Silvestri, S. Luzzati, J. C. Hummelen, and S. Sariciftci, "Tracing photoinduced electron transfer process in conjugated polymer/fullerene bulk heterojunctions in real time," *Chem. Phys. Lett.,* vol. 340, pp. 232, 2001.

[101] N. Tessler and N. Rappaport, "Loss of photocurrent efficiency in low mobility semiconductors: Analytic approach to space charge effects," *Appl. Phys. Lett.,* vol. 89, pp. 013504, 2006.

[102] N. F. Mott and E. A. Davis, *Electronic Processes in Noncrystalline Materials*. New York: Oxford University Press, 1979.

[103] I. Hwang, C. R. McNeill, and N. C. Greenham, "Drift-diffusion modeling of photocurrent transients in bulk heterojunction solar cells," *J. Appl. Phys.,* vol. 106, pp. 094506, 2009.

[104] K. S. Nalwa, H. K. Kodali, B. Ganapathysubramanian, and S. Chaudhary, "Dependence of recombination mechanisms and strength on processing conditions in polymer solar cells," *Appl. Phys. Lett.,* vol. 99, pp. 263301, 2011.

[105] L. J. A. Koster, E. C. P. Smits, V. D. Mihailetchi, and P. W. M. Blom, "Device model for the operation of polymer/fullerene bulk heterojunction solar cells," *Phys. Rev. B,* vol. 72, pp. 085205, 2005.

[106] M. M. Mandoc, F. B. Kooistra, J. C. Hummelen, B. de Boer, and P. W. M. Blom, "Effect of traps on the performance of bulk heterojunction organic solar cells," *Appl. Phys. Lett.,* vol. 91, pp. 263505, 2007.

[107] M. M. Mandoc, W. Veurman, L. J. A. Koster, B. de Boer, and P. W. M. Blom, "Origin of the Reduced Fill Factor and Photocurrent in MDMO-PPV:PCNEPV All-Polymer Solar Cells," *Adv. Funct. Mater.,* vol. 17, pp. 2167, 2007.

[108] L. Tzabari and N. Tessler, "Shockley--Read--Hall recombination in P3HT:PCBM solar cells as observed under ultralow light intensities," *J. Appl. Phys.,* vol. 109, pp. 064501, 2011.

[109] W. L. Leong, S. R. Cowan, and A. J. Heeger, "Differential Resistance Analysis of Charge Carrier Losses in Organic Bulk Heterojunction Solar Cells: Observing the Transition from Bimolecular to Trap-Assisted Recombination and Quantifying the Order of Recombination," *Adv. Energy Mater.,* vol. 1, pp. 517, 2011.

[110] L. J. A. Koster, M. Kemerink, M. M. Wienk, K. Maturová, and R. A. J. Janssen, "Quantifying Bimolecular Recombination Losses in Organic Bulk Heterojunction Solar Cells," *Adv. Mater.,* vol. 23, pp. 1670, 2011.

[111] C. G. Shuttle, B. Oregan, A. M. Ballantyne, J. Nelson, D. D. C. Bradley, and J. R. Durrant, "Bimolecular recombination losses in polythiophene: Fullerene solar cells," *Phys. Rev. B,* vol. 78, pp. 113201, 2008.

[112] C. G. Shuttle, B. O'Regan, A. M. Ballantyne, J. Nelson, D. D. C. Bradley, J. de Mello, and J. R. Durrant, "Experimental determination of the rate law for charge carrier decay in a polythiophene: Fullerene solar cell," *Appl. Phys. Lett.,* vol. 92, pp. 093311, 2008.

[113] R. A. Street, "Localized state distribution and its effect on recombination in organic solar cells," *Phys. Rev. B,* vol. 84, pp. 075208, 2011.

[114] R. A. Street, M. Schoendorf, A. Roy, and J. H. Lee, "Interface state recombination in organic solar cells," *Phys. Rev. B,* vol. 81, pp. 205307, 2010.

[115] T. Kirchartz, B. E. Pieters, J. Kirkpatrick, U. Rau, and J. Nelson, "Recombination via tail states in polythiophene:fullerene solar cells," *Phys. Rev. B,* vol. 83, pp. 115209, 2011.

[116] A. Baumann, T. J. Savenije, D. H. K. Murthy, M. Heeney, V. Dyakonov, and C. Deibel, "Influence of Phase Segregation on Recombination Dynamics in Organic Bulk-Heterojunction Solar Cells," *Adv. Funct. Mater., (Early View)* 2012.

[117] X. Zhu and A. Kahn, "Electronics structure and dynamics at organic donor/acceptor intraface," *MRS Bull.,* vol. 35, pp. 443, 2010.

[118] H. Bottger and V. V. Bryskin, *Hopping Conduction in Solids* vol. 1: Akademie Verlag, Berlin,, 1985.

[119] B. Maennig, M. Pfeiffer, A. Nollau, X. Zhou, K. Leo, and P. Simon, "Controlled p-type doping of polycrystalline and amorphous organic layers: Self-consistent description of conductivity and field-effect mobility by a microscopic percolation model," *Phys. Rev. B,* vol. 64, pp. 195208, 2001.

[120] D. Gupta, M. Bag, and K. S. Narayan, "Correlating reduced fill factor in polymer solar cells to contact effects," *Appl. Phys. Lett.,* vol. 92, pp. 093301, 2008.

[121] D. Credgington, R. Hamilton, P. Atienzar, J. Nelson, and J. R. Durrant, "Non-Geminate Recombination as the Primary Determinant of Open-Circuit Voltage in Polythiophene:Fullerene Blend Solar Cells: an Analysis of the Influence of Device Processing Conditions," *Adv. Funct. Mater.,* vol. 21, pp. 2744, 2011.

[122] D. Carsten and D. Vladimir, "Polymer-fullerene bulk heterojunction solar cells," *Rep. Prog. Phys.,* vol. 73, pp. 096401, 2010.

[123] D. Cheyns, J. Poortmans, P. Heremans, C. Deibel, S. Verlaak, B. P. Rand, and J. Genoe, "Analytical model for the open-circuit voltage and its associated resistance in organic planar heterojunction solar cells," *Phys. Rev. B,* vol. 77, pp. 165332, 2008.

[124] C. M. Ramsdale, J. A. Barker, A. C. Arias, J. D. MacKenzie, R. H. Friend, and N. C. Greenham, "The origin of the open-circuit voltage in polyfluorene-based photovoltaic devices," *J. Appl. Phys.,* vol. 92, pp. 4266, 2002.

[125] C. J. Brabec, A. Cravino, D. Meissner, N. S. Sariciftci, T. Fromherz, M. T. Rispens, L. Sanchez, and J. C. Hummelen, "Origin of the Open Circuit Voltage of Plastic Solar Cells," *Adv. Funct. Mater.,* vol. 11, pp. 374, 2001.

[126] A. Gadisa, M. Svensson, M. R. Andersson, and O. Inganas, "Correlation between oxidation potential and open-circuit voltage of composite solar cells based on blends of polythiophenes/ fullerene derivative," *Appl. Phys. Lett.,* vol. 84, pp. 1609, 2004.

[127] L. J. A. Koster, V. D. Mihailetchi, R. Ramaker, and P. W. M. Blom, "Light intensity dependence of open-circuit voltage of polymer:fullerene solar cells," *Appl. Phys. Lett.,* vol. 86, pp. 123509, 2005.

[128] K. Vandewal, A. Gadisa, W. D. Oosterbaan, S. Bertho, F. Banishoeib, I. Van Severen, L. Lutsen, T. J. Cleij, D. Vanderzande, and J. V. Manca, "The Relation Between Open-Circuit Voltage and the Onset of Photocurrent Generation by Charge-Transfer Absorption in Polymer : Fullerene Bulk Heterojunction Solar Cells," *Adv. Funct. Mater.,* vol. 18, pp. 2064, 2008.

[129] K. Vandewal, W. D. Oosterbaan, S. Bertho, V. Vrindts, A. Gadisa, L. Lutsen, D. Vanderzande, and J. V. Manca, "Varying polymer crystallinity in nanofiber poly(3-alkylthiophene) :PBCM solar cells: influence on charge-transfer state energy and open-circuit voltage," *Appl. Phys. Lett.,* vol. 95, pp. 123303, 2009.

[130] R. B. Ross, C. M. Cardona, D. M. Guldi, S. G. Sankaranarayanan, M. O. Reese, N. Kopidakis, J. Peet, B. Walker, G. C. Bazan, E. Van Keuren, B. C. Holloway, and M.

Drees, "Endohedral fullerenes for organic photovoltaic devices," *Nat Mater,* vol. 8, pp. 208, 2009.

[131] T. Erb, U. Zhokhavets, G. Gobsch, S. Raleva, B. Stühn, P. Schilinsky, C. Waldauf, and C. J. Brabec, "Correlation Between Structural and Optical Properties of Composite Polymer/Fullerene Films for Organic Solar Cells," *Adv. Funct. Mater.,* vol. 15, pp. 1193, 2005.

[132] S. Cook, R. Katoh, and A. Furube, "Ultrafast Studies of Charge Generation in PCBM:P3HT Blend Films following Excitation of the Fullerene PCBM," *J. Phys. Chem. C,* vol. 113, pp. 2547, 2009.

[133] R. Sokel and R. C. Hughes, "Numerical analysis of transient photoconductivity in insulators," *J. Appl. Phys.,* vol. 53, pp. 7414, 1982.

[134] M. Limpinsel, A. Wagenpfahl, M. Mingebach, C. Deibel, and V. Dyakonov, "Photocurrent in bulk heterojunction solar cells," *Phys. Rev. B,* vol. 81, pp. 085203, 2010.

[135] M. Lenes, L. J. A. Koster, V. D. Mihailetchi, and P. W. M. Blom, "Thickness dependence of the efficiency of polymer:fullerene bulk heterojunction solar cells," *Appl. Phys. Lett.,* vol. 88, pp. 243502, 2006.

[136] A. M. Goodman and A. Rose, "Double Extraction of Uniformly Generated Electron-Hole Pairs from Insulators with Noninjecting Contacts," *J. Appl. Phys.,* vol. 42, pp. 2823, 1971.

[137] V. D. Mihailetchi, L. J. A. Koster, J. C. Hummelen, and P. W. M. Blom, "Photocurrent Generation in Polymer-Fullerene Bulk Heterojunctions," *Phys. Rev. Lett.,* vol. 93, pp. 216601, 2004.

[138] D. Gupta, D. Kabra, N. Kolishetti, S. Ramakrishnan, and K. S. Narayan, "An Efficient Bulk-Heterojunction Photovoltaic Cell Based on Energy Transfer in Graded-Bandgap Polymers," *Adv. Funct. Mater.,* vol. 17, pp. 226, 2007.

[139] J. Peet, J. Y. Kim, N. E. Coates, W. L. Ma, D. Moses, A. J. Heeger, and G. C. Bazan, "Efficiency enhancement in low-bandgap polymer solar cells by processing with alkane dithiols," *Nat Mater,* vol. 6, pp. 497, 2007.

[140] J. Y. Kim, Y. Qin, D. M. Stevens, V. Kalihari, M. A. Hillmyer, and C. D. Frisbie, "High Open-Circuit Voltage Photovoltaic Cells with a Low Bandgap Copolymer of Isothianaphthene, Thiophene, and Benzothiadiazole Units," *J. Phys. Chem. C,* vol. 113, pp. 21928, 2009.

[141] N. Blouin, A. Michaud, D. Gendron, S. Wakim, E. Blair, R. Neagu-Plesu, M. Belletate, G. Durocher, Y. Tao, and M. Leclerc, "Toward a Rational Design of Poly(2,7-Carbazole) Derivatives for Solar Cells," *J. Am. Chem. Soc.,* vol. 130, pp. 732, 2007.

[142] S. H. Park, A. Roy, S. Beaupre, S. Cho, N. Coates, J. S. Moon, D. Moses, M. Leclerc, K. Lee, and A. J. Heeger, "Bulk heterojunction solar cells with internal quantum efficiency approaching 100%," *Nat Photon,* vol. 3, pp. 297, 2009.

[143] M. Morana, M. Wegscheider, A. Bonanni, N. Kopidakis, S. Shaheen, M. Scharber, Z. Zhu, D. Waller, R. Gaudiana, and C. Brabec, "Bipolar Charge Transport in PCPDTBT-PCBM Bulk-Heterojunctions for Photovoltaic Applications," *Adv. Funct. Mater.,* vol. 18, pp. 1757, 2008.

[144] C. Soci, I. W. Hwang, D. Moses, Z. Zhu, D. Waller, R. Gaudiana, C. J. Brabec, and A. J. Heeger, "Photoconductivity of a Low-Bandgap Conjugated Polymer," *Adv. Funct. Mater.,* vol. 17, pp. 632, 2007.

[145] P. Boland, K. Lee, and G. Namkoong, "Device optimization in PCPDTBT:PCBM plastic solar cells," *Sol. Energy Mater. Sol. Cells,* vol. 94, pp. 915, 2010.

[146] F. C. Jamieson, T. Agostinelli, H. Azimi, J. Nelson, and J. R. Durrant, "Field-Independent Charge Photogeneration in PCPDTBT/$PC_{70}BM$ Solar Cells," *J. Phys. Chem. Lett.,* vol. 1, pp. 3306, 2010.

[147] M. Koppe, H.-J. Egelhaaf, G. Dennler, M. C. Scharber, C. J. Brabec, P. Schilinsky, and C. N. Hoth, "Near IR Sensitization of Organic Bulk Heterojunction Solar Cells: Towards Optimization of the Spectral Response of Organic Solar Cells," *Adv. Funct. Mater.,* vol. 20, pp. 338, 2010.

[148] J. Y. Kim, K. Lee, N. E. Coates, D. Moses, T.-Q. Nguyen, M. Dante, and A. J. Heeger, "Efficient Tandem Polymer Solar Cells Fabricated by All-Solution Processing," *Science,* vol. 317, pp. 222, 2007.

[149] M. C. Scharber, M. Koppe, J. Gao, F. Cordella, M. A. Loi, P. Denk, M. Morana, H.-J. Egelhaaf, K. Forberich, G. Dennler, R. Gaudiana, D. Waller, Z. Zhu, X. Shi, and C. J. Brabec, "Influence of the Bridging Atom on the Performance of a Low-Bandgap Bulk Heterojunction Solar Cell," *Adv. Mater.,* vol. 22, pp. 367, 2010.

[150] G. Lu, H. Usta, C. Risko, L. Wang, A. Facchetti, M. A. Ratner, and T. J. Marks, "Synthesis, Characterization, and Transistor Response of Semiconducting Silole Polymers with Substantial Hole Mobility and Air Stability. Experiment and Theory," *J. Am. Chem. Soc.,* vol. 130, pp. 7670, 2008.

[151] J. Hou, H.-Y. Chen, S. Zhang, G. Li, and Y. Yang, "Synthesis, Characterization, and Photovoltaic Properties of a Low Band Gap Polymer Based on Silole-Containing Polythiophenes and 2,1,3-Benzothiadiazole," *J. Am. Chem. Soc.,* vol. 130, pp. 16144, 2008.

[152] E. Wang, L. Wang, L. Lan, C. Luo, W. Zhuang, J. Peng, and Y. Cao, "High-performance polymer heterojunction solar cells of a polysilafluorene derivative," *Appl. Phys. Lett.,* vol. 92, pp. 033307, 2008.

[153] K. B. Krueger, P. E. Schwenn, K. Gui, A. Pivrikas, P. Meredith, and P. L. Burn, "Morphology dependent electron transport in an n-type electron accepting small molecule for solar cell applications," *Appl. Phys. Lett.,* vol. 98, pp. 083301, 2011.

[154] K. Mutkins, K. Gui, M. Aljada, P. E. Schwenn, E. B. Namdas, P. L. Burn, and P. Meredith, "A solution processable fluorene-benzothiadiazole small molecule for n-type organic field-effect transistors," *Appl. Phys. Lett.,* vol. 98, pp. 153301, 2011.

[155] P. E. Schwenn, K. Gui, A. M. Nardes, K. B. Krueger, K. H. Lee, K. Mutkins, H. Rubinstein-Dunlop, P. E. Shaw, N. Kopidakis, P. L. Burn, and P. Meredith, "A Small Molecule Non-fullerene Electron Acceptor for Organic Solar Cells," *Adv. Energy Mater.,* vol. 1, pp. 73, 2011.

[156] J. R. Moore, S. Albert-Seifried, A. Rao, S. Massip, B. Watts, D. J. Morgan, R. H. Friend, C. R. McNeill, and H. Sirringhaus, "Polymer Blend Solar Cells Based on a High-Mobility Naphthalenediimide-Based Polymer Acceptor: Device Physics, Photophysics and Morphology," *Adv. Energy Mater.,* vol. 1, pp. 230, 2011.

[157] P. Peumans, A. Yakimov, and S. R. Forrest, "Small molecular weight organic thin-film photodetectors and solar cells," *J. Appl. Phys.,* vol. 93, pp. 3693, 2003.

[158] A. F. Hebard, R. C. Haddon, R. M. Fleming, and A. R. Kortan, "Deposition and characterization of fullerene films," *Appl. Phys. Lett.,* vol. 59, pp. 2109, 1991.

[159] V. D. Mihailetchi, L. J. A. Koster, P. W. M. Blom, C. Melzer, B. de Boer, J. K. J. van Duren, and R. A. J. Janssen, "Compositional Dependence of the Performance of Poly(p-phenylene vinylene):Methanofullerene Bulk-Heterojunction Solar Cells," *Adv. Funct. Mater.,* vol. 15, pp. 795, 2005.

[160] V. D. Mihailetchi, J. K. J. van Duren, P. W. M. Blom, J. C. Hummelen, R. A. J. Janssen, J. M. Kroon, M. T. Rispens, W. J. H. Verhees, and M. M. Wienk, "Electron Transport in a Methanofullerene," *Adv. Funct. Mater.,* vol. 13, pp. 43, 2003.

[161] B. A. Collins, E. Gann, L. Guignard, X. He, C. R. McNeill, and H. Ade, "Molecular Miscibility of Polymer-Fullerene Blends," *J. Phys. Chem. Lett.,* vol. 1, pp. 3160, 2010.

[162] J. K. Lee, W. L. Ma, C. J. Brabec, J. Yuen, J. S. Moon, J. Y. Kim, K. Lee, G. C. Bazan, and A. J. Heeger, "Processing Additives for Improved Efficiency from Bulk Heterojunction Solar Cells," *J. Am. Chem. Soc.,* vol. 130, pp. 3619, 2008.

[163] J. Peet, C. Soci, R. C. Coffin, T. Q. Nguyen, A. Mikhailovsky, D. Moses, and G. C. Bazan, "Method for increasing the photoconductive response in conjugated polymer/fullerene composites," *Appl. Phys. Lett.,* vol. 89, pp. 252105, 2006.

[164] J. T. Rogers, K. Schmidt, M. F. Toney, G. C. Bazan, and E. J. Kramer, "Time-Resolved Structural Evolution of Additive-Processed Bulk Heterojunction Solar Cells," *J. Am. Chem. Soc.,* vol. 134, pp. 2884, 2010.

[165] S. J. Lou, J. M. Szarko, T. Xu, L. Yu, T. J. Marks, and L. X. Chen, "Effects of Additives on the Morphology of Solution Phase Aggregates Formed by Active Layer Components of High-Efficiency Organic Solar Cells," *J. Am. Chem. Soc.,* vol. 133, pp. 20661, 2010.

[166] B. Park, Y. H. Huh, and M. Kim, "Surfactant additives for improved photovoltaic effect of polymer solar cells," *J. Mater. Chem.,* vol. 20, 2010.

[167] M. Reyes-Reyes, K. Kim, and D. L. Carroll, "High-efficiency photovoltaic devices based on annealed poly(3-hexylthiophene) and 1-(3-methoxycarbonyl)-propyl-1-phenyl-(6,6)C[sub 61] blends," *Appl. Phys. Lett.,* vol. 87, pp. 083506, 2005.

[168] J.-H. Kim, S.-Y. Huh, T.-i. Kim, and H. H. Lee, "Thin pentacene interlayer for polymer bulk-heterojunction solar cell," *Appl. Phys. Lett.,* vol. 93, pp. 143305, 2008.

[169] M. Reinhard, J. Hanisch, Z. Zhang, E. Ahlswede, A. Colsmann, and U. Lemmer, "Inverted organic solar cells comprising a solution-processed cesium fluoride interlayer," *Appl. Phys. Lett.,* vol. 98, pp. 053303, 2011.

[170] S. K. Hau, H.-L. Yip, and A. K. Y. Jen, "A Review on the Development of the Inverted Polymer Solar Cell Architecture," *Polym. Rev.,* vol. 50, pp. 474, 2010.

[171] J. Huang, P. F. Miller, J. S. Wilson, A. J. de Mello, J. C. de Mello, and D. D. C. Bradley, "Investigation of the Effects of Doping and Post-Deposition Treatments on the Conductivity, Morphology, and Work Function of Poly(3,4-ethylenedioxythiophene)/Poly(styrene sulfonate) Films," *Adv. Funct. Mater.,* vol. 15, pp. 290, 2005.

[172] F. Louwet, L. Groenendaal, J. Dhaen, J. Manca, J. Van Luppen, E. Ver-donck, and L. Leenders, "PEDOT/PSS: Synthesis, characterization, properties and applications," *Synth. Metal.,* vol. 135, pp. 115, 2003.

[173] T. Martens, J. DaHaen, T. Munters, Z. Beelen, L. Goris, J. Manca, M. DaOlieslaeger, D. Vanderzande, L. De Schepper, and R. Andriessen, "Disclosure of the nanostructure of MDMO-PPV:PCBM bulk hetero-junction organic solar cells by a combination of SPM and TEM," *Synth. Metal.,* vol. 138, pp. 243, 2003.

[174] H. Hoppe, M. Niggemann, C. Winder, J. Kraut, R. Hiesgen, A. Hinsch, D. Meissner, and N. S. Sariciftci, "Nanoscale Morphology of Conjugated Polymer/Fullerene-Based Bulk- Heterojunction Solar Cells," *Adv. Funct. Mater.,* vol. 14, pp. 1005, 2004.

[175] W. Ma, C. Yang, and A. J. Heeger, "Spatial Fourier-Transform Analysis of the Morphology of Bulk Heterojunction Materials Used in “Plastic” Solar Cells," *Adv. Mater.,* vol. 19, pp. 1387, 2007.

[176] C. W. T. Bulle-Lieuwma, W. J. H. van Gennip, J. K. J. van Duren, P. Jonkheijm, R. A. J. Janssen, and J. W. Niemantsverdriet, "Characterization of polymer solar cells by TOF-SIMS depth profiling," *Appl. Surf. Sci.,* vol. 203-204, pp. 547, 2003.

[177] H. Hoppe and N. S. Sariciftci, "Morphology of polymer/fullerene bulk heterojunction solar cells," *J. Mater. Chem.,* vol. 16, pp. 45, 2006.

[178] C. Groves, O. G. Reid, and D. S. Ginger, "Heterogeneity in Polymer Solar Cells: Local Morphology and Performance in Organic Photovoltaics Studied with Scanning Probe Microscopy," *Acc. Chem. Res.,* vol. 43, pp. 612, 2010.

[179] R. Giridharagopal and D. S. Ginger, "Characterizing Morphology in Bulk Heterojunction Organic Photovoltaic Systems," *J. Phys. Chem. Lett.,* vol. 1, pp. 1160, 2010.

[180] O. G. Reid, G. E. Rayermann, D. C. Coffey, and D. S. Ginger, "Imaging Local Trap Formation in Conjugated Polymer Solar Cells: A Comparison of Time-Resolved Electrostatic Force Microscopy and Scanning Kelvin Probe Imaging" *J. Phys. Chem. C,* vol. 114, pp. 20672, 2010.

[181] L. S. C. Pingree, O. G. Reid, and D. S. Ginger, "Imaging the Evolution of Nanoscale Photocurrent Collection and Transport Networks during Annealing of Polythiophene/Fullerene Solar Cells," *Nano Lett.,* vol. 9, pp. 2946, 2009.

[182] S. S. van Bavel and J. Loos, "Volume Organization of Polymer and Hybrid Solar Cells as Revealed by Electron Tomography," *Adv. Funct. Mater.,* vol. 20, pp. 3217, 2010.

[183] S. S. van Bavel, M. Bärenklau, G. de With, H. Hoppe, and J. Loos, "P3HT/PCBM Bulk Heterojunction Solar Cells: Impact of Blend Composition and 3D Morphology on Device Performance," *Adv. Funct. Mater.,* vol. 20, pp. 1458, 2010.

[184] S. S. v. Bavel, E. Sourty, G. d. With, and J. Loos, "Three-Dimensional Nanoscale Organization of Bulk Heterojunction Polymer Solar Cells," *Nano Lett.,* vol. 9, pp. 507, 2008.

[185] T. J. Savenije, J. E. Kroeze, X. Yang, and J. Loos, "The formation of crystalline P3HT fibrils upon annealing of a PCBM:P3HT bulk heterojunction," *Thin Solid Films,* vol. 511-512, pp. 2, 2006.

[186] J. Loos, "Volume morphology of printable solar cells," *Materials Today,* vol. 13, pp. 14 2010.

[187] A. J. Pearson, S. A. Boden, D. M. Bagnall, D. G. Lidzey, and C. Rodenburg, "Imaging the Bulk Nanoscale Morphology of Organic Solar Cell Blends Using Helium Ion Microscopy," *Nano Letters,* vol. 11, pp. 4275, 2011.

[188] P. M. Beaujuge and J. M. J. Frachet, "Molecular Design and Ordering Effects in Functional Materials for Transistor and Solar Cell Applications," *J. Am. Chem. Soc.,* vol. 133, pp. 20009, 2011.

[189] C. H. Woo, B. C. Thompson, B. J. Kim, M. F. Toney, and J. M. J. Freichet, "The Influence of Poly(3-hexylthiophene) Regioregularity on Fullerene-Composite Solar Cell Performance," *J. Am. Chem. Soc.,* vol. 130, pp. 16324, 2008.

[190] H. Sirringhaus, P. J. Brown, R. H. Friend, M. M. Nielsen, K. Bechgaard, B. M. W. Langeveld-Voss, A. J. H. Spiering, R. A. J. Janssen, E. W. Meijer, P. Herwig, and D. M. de Leeuw, "Two-dimensional charge transport in self-organized, high-mobility conjugated polymers," *Nature,* vol. 401, pp. 685, 1999.

[191] C.-W. Chu, H. Yang, W.-J. Hou, J. Huang, G. Li, and Y. Yang, "Control of the nanoscale crystallinity and phase separation in polymer solar cells," *Appl. Phys. Lett.,* vol. 92, pp. 103306, 2008.

[192] N. C. Cates, R. Gysel, Z. Beiley, C. E. Miller, M. F. Toney, M. Heeney, I. McCulloch, and M. D. McGehee, "Tuning the Properties of Polymer Bulk Heterojunction Solar Cells by Adjusting Fullerene Size to Control Intercalation," *Nano Lett.,* vol. 9, pp. 4153, 2009.

[193] M. e. Ohtsu, "Near-Field Nano/Atom Optics and Technology," *Springer, Tokyo, Japan,* 1998.

[194] A. Lewis, K. Lieberman, N. Ben-Ami, G. Fish, E. Khachatryan, U. Ben-Ami, and S. Shalom, "Design and imaging concepts in NSOM," *Ultramicroscopy,* vol. 61, 1995.

[195] G. Binnig and H. Rohrer, "In touch with atoms," *Rev. Mod. Phys.,* vol. 71, pp. S324, 1999.

[196] L. Novotny and B. Hecht, *Principles of Nano-Optics*, 2006.

[197] R. Dunn, "Near-field scanning optical microscopy," *Chem. Rev.,* vol. 99, pp. 2891, 1999.

[198] J. Fillard, "Near Field Optics and Nanoscopy," *World Scientific Publishing, Singapore,* 1998.

[199] X. Zhu, M. Ohtsu, and (eds.), "Near-Field Optics: Principles and Applications," *World Scientific Publishing, Singapore,* 1999.

[200] T. Dokland, D. W. Hutmacher, M. M. Lee Ng, and J. Schantz, "Techniques in Microscopy for Biomedical Applications," *Manuals in Biomedical Research* vol. 2, 2006.

[201] A. Lewis, A. Radko, N. Ben-Ami, D. Palanker, and K. Lieberman, "Near-field scanning optical microscopy in cell biology," *Trends Cell Bio.,* vol. 70-72, 1999.

[202] D. Pohl, "Scanning near-field optical microscopy (SNOM)," *Adv. Optical and Electron Microscopy,* vol. 12, pp. 243, 1991.

[203] A. Zayats and D. Richards, "Nano-optics and near-field optical microscopy," *Artech House, cop., Boston, ,* vol. Nanoscale science and engineering Series, 2009.

[204] A. V. Bragas and O. E. Martínez, "Field-enhanced scanning optical microscope," *Opt. Lett.,* vol. 25, pp. 631, 2000.

[205] E. Betzig and J. Trautman, "Near-field optics: Microscopy, spectroscopy, and surface modification beyond the diffraction limit," *Science,* vol. 257, pp. 189, 1992.

[206] K. Vijaya Sarathy, K. S. Narayan, J. Kim, and J. O. White, "Novel fluorescence and morphological structures in gold nanoparticle-polyoctylthiophene based thin films," *Chem. Phys. Lett.,* vol. 318, pp. 543, 2000.

[207] J. A. Teetsov and D. A. Vanden Bout, "Imaging Molecular and Nanoscale Order in Conjugated Polymer Thin Films with Near-field Scanning Optical Microscopy," *J. Am. Chem. Soc.,* vol. 123, pp. 3605, 2001.

[208] E.-S. Kwak and D. A. Vanden Bout, "Fully time-resolved near-field scanning optical microscopy fluorescence imaging," *Anal. Chim. Acta,* vol. 496, pp. 259, 2003.

[209] P. F. Barbara, D. M. Adams, and D. B. O'Connor, "Characterization of organic thin film materials with near-field scanning optical microscopy (NSOM)," *Annu. Rev. Mater. Sci.,* vol. 29, pp. 433, 1999.

[210] C. R. McNeill, C. J. R. Fell, J. L. Holdsworth, and P. C. Dastoor, "Screening for artifacts in near-field scanning photocurrent microscopy images of polymer solar cells," *Synth. Metal.,* vol. 153, pp. 85, 2005.

[211] C. R. McNeill, H. Frohne, J. L. Holdsworth, and P. C. Dastoor, "Near-Field Scanning Photocurrent Measurements of Polyfluorene Blend Devices: Directly Correlating Morphology with Current Generation," *Nano Lett.,* vol. 4, pp. 2503, 2004.

[212] C. R. McNeill, H. Frohne, J. L. Holdsworth, J. E. Furst, B. V. King, and P. C. Dastoor, "Direct Photocurrent Mapping of Organic Solar Cells Using a Near-Field Scanning Optical Microscope," *Nano Lett.,* vol. 4, pp. 219, 2004.

[213] E. Synge, "A suggested method for extending microscopic resolution into the ultra-microscopic region," *Philos. Mag.,* vol. 6, pp. 356, 2928.

[214] E. H. Synge, "An application of piezoelectricity to microscopy," *Philos. Mag.,* vol. 13, 1932.

[215] E. A. Ash and G. Nichols, "Super-resolution aperture scanning microscope," *Nature,* vol. 237, p. 510, 1972.

[216] D. W. Pohl, W. Denk, and M. Lanz, "Optical stethoscopy: Image recording with resolution lambda/20," *Appl. Phys. Lett.,* vol. 44, pp. 651, 1984.

[217] E. Betzig, A. Lewis, A. Harootunian, M. Isaacson, and E. Kratschmer, "Near-field Scanning Optical Microscopy (NSOM) - Development and Biophysical Applications," *Biophys. J.,* vol. 49, pp. 269, 1986.

[218] A. Lewis, M. Isaacson, A. Harootunian, and A. Muray, "Development of a 500 Ã… spatial resolution light microscope: I. light is efficiently transmitted through Î»/16 diameter apertures," *Ultramicroscopy,* vol. 13, pp. 227, 1984.

[219] A. Lewis, M. Isaacson, A. Harootunian, and A. Muray, "Super-resolution aperture optical scanning microscope," *Biophys. J.,* vol. 41, p. 405a, 1984.

[220] C. L. Jahncke and H. D. Hallen, "A versatile, stable scanning proximal probe microscope," *Rev. Sci. Instrum.,* vol. 68, p. 1759, 1997.

[221] L. Novotny, D. W. Pohl, and P. Regli, "Light propagation through nanometer-sized structures: the two-dimensional-aperture scanning near-field optical microscope," *J. Opt. Soc. Am. A,* vol. 11, pp. 1768, 1994.

[222] C. Girard and D. Courjon, "The role of scanning mode in near-field optical microscopy," *Surf. Sci.,* vol. 382, pp. 9, 1997.

[223] B. Hecht, B. Sick, U. P. Wild, V. Deckert, R. Zenobi, O. J. F. Martin, and D. W. Pohl, "Scanning near-field optical microscopy with aperture probes: Fundamentals and applications," *J. Chem. Phys.,* vol. 112, pp. 7761, 2000.

[224] B. Hecht, H. Bielefeldt, D. W. Pohl, L. Novotny, and H. Heinzelmann, "Influence of detection conditions on near-field optical imaging," *J. Appl. Phys.,* vol. 84, pp. 5873, 1998.

[225] L. Novotny and C. Hafner, "Light propagation in a cylindrical waveguide with a complex, metallic, dielectric function," *Phys. Rev. E,* vol. 50, pp. 4094, 1994.

[226] L. Novotny, D. W. Pohl, and B. Hecht, "Scanning near-field optical probe with ultrasmall spot size," *Opt. Lett.,* vol. 20, pp. 970, 1995.

[227] H. A. Bethe, "Theory of Diffraction by Small Holes," *Phys. Rev.,* vol. 66, pp. 163, 1944.

[228] C. J. Bouwkamp, "On Bethe's theory of diffraction by small holes," *Philips. Res. Rep.,* vol. 5, pp. 321 1950.

[229] J. Kim, S. Na, and W. Changm, "Effect of Polarization Direction on the Electric Field Distribution at the Near-Field of a Tip-on-Aperture Near-Field Scanning Optical Microscope Probe," *Jpn. J. Appl. Phys.,* vol. 46, p. 5577, 2007.

[230] R. S. Decca, H. D. Drew, and K. L. Empson, "Investigation of the electric-field distribution at the subwavelength aperture of a near-field scanning optical microscope," *Appl. Phys. Lett.,* vol. 70, pp. 1932, 1997.

[231] A. Drezet, S. Huant, and J. Woehl, "In situ characterization of optical tips using single fluorescent nanobeads," *J. Lumin.,* vol. 107, pp. 176, 2004.

[232] J. Enderlein, "Theoretical study of detection of a dipole emitter through an objective with high numerical aperture," *Opt. Lett.,* vol. 25, pp. 634, 2000.

[233] C. J. R. Sheppard and T. Wilson, "The Image of a Single Point in Microscopes of Large Numerical Aperture," *Proceedings of the Royal Society of London. A. Mathematical and Physical Sciences,* vol. 379, pp. 145, 1982.

[234] K. Nagesh, D. Kabra, K. S. Narayan, and S. Ramakrishnan, "Modulating phase-separation in blends of MEHPPV-x with different conjugation lengths," *Synth. Metal.,* vol. 155, pp. 295 2005.

[235] K. Nagesh, D. Gupta, D. Kabra, K. S. Narayan, and S. Ramakrishnan, "Tunable two-colour patterning of MEHPPV from a single precursor," *J. Mater. Chem.,* vol. 17, pp. 1682, 2007.

[236] J. Chappell, D. G. Lidzey, P. C. Jukes, A. M. Higgins, R. L. Thompson, S. O. Connor, I. Grizzi, R. Fletcher, J. O'Brien, M. Geoghegan, and R. A. L. Jones, "Correlating structure with fluorescence emission in phase-separated conjugated-polymer blends," *Nat Mater,* vol. 2, pp. 616, 2003.

[237] T. Rader, H. S. Kitzerow, and J. C. Hummelen, "Morphology and fluorescence quenching in photovoltaic samples containing fullerene and poly(p-phenylene-vinylene) derivatives," *Synth. Metal.,* vol. 141, pp. 271, 2004.

[238] Z. Bao, A. Dodabalapur, and A. J. Lovinger, "Soluble and processable regioregular poly(3-hexylthiophene) for thin film field-effect transistor applications with high mobility," *Appl. Phys. Lett.,* vol. 69, pp. 4108, 1996.

[239] J. Pecher and S. Mecking, "Nanoparticles of Conjugated Polymers," *Chem. Rev.,* vol. 110, pp. 6260, 2010.

[240] T. J. Prosa, M. J. Winokur, J. Moulton, P. Smith, and A. J. Heeger, "X-ray structural studies of poly(3-alkylthiophenes): an example of an inverse comb," *Macromolecules,* vol. 25, pp. 4364, 1992.

[241] Z. M. Beiley, E. T. Hoke, R. Noriega, J. Dacuña, G. F. Burkhard, J. A. Bartelt, A. Salleo, M. F. Toney, and M. D. McGehee, "Morphology-Dependent Trap Formation in High Performance Polymer Bulk Heterojunction Solar Cells," *Adv. Energy Mater.,* vol. 1, pp. 954, 2011.

[242] K. Maturová, S. S. van Bavel, M. M. Wienk, R. A. J. Janssen, and M. Kemerink, "Description of the Morphology Dependent Charge Transport and Performance of Polymer:Fullerene Bulk Heterojunction Solar Cells," *Adv. Funct. Mater.,* vol. 21, pp. 261, 2011.

[243] P. A. Staniec, A. J. Parnell, A. D. F. Dunbar, H. Yi, A. J. Pearson, T. Wang, P. E. Hopkinson, C. Kinane, R. M. Dalgliesh, A. M. Donald, A. J. Ryan, A. Iraqi, R. A. L. Jones, and D. G. Lidzey, "The Nanoscale Morphology of a PCDTBT:PCBM Photovoltaic Blend," *Adv. Energy Mater.,* vol. 1, pp. 499, 2011.

[244] A. Pivrikas, N. S. Sariciftci, G. Juska, and R. Österbacka, "A review of charge transport and recombination in polymer/fullerene organic solar cells," *Prog. Photovoltaics Res. Appl.,* vol. 15, pp. 677, 2007.

[245] D. J. D. Moet, L. J. A. Koster, B. de Boer, and P. W. M. Blom, "Hybrid Polymer Solar Cells from Highly Reactive Diethylzinc: MDMO-PPV versus P3HT," *Chemistry of Materials,* vol. 19, pp. 5856, 2007.

[246] D. Gupta, "Studies of Polymer based Solar Cells and Performance Limiting Factors," in *Chemistry and Physics of Materials Unit*. vol. PhD. Thesis, Bangalore: Jawaharlal Nehru Centre for Advanced Scientific Research, 2008.

[247] D. Gupta, N. S. Vidhyadhiraja, and K. S. Narayan, "Transport of Photogenerated Charge Carriers in Polymer Semiconductors," *Proc. IEEE,* vol. 97, pp. 1558, 2009.

[248] D. Kabra and K. Narayan, "Direct Estimate of Transport Length Scales in Semiconducting Polymers," *Adv. Mater.,* vol. 19, pp. 1465, 2007.

[249] D. Kabra, S. Shriram, N. S. Vidhyadhiraja, and K. S. Narayan, "Charge carrier dynamics in organic semiconductors by position dependent optical probing," *J. Appl. Phys.,* vol. 101, pp. 064510, 2007.

[250] D. Kabra, T. B. Singh, and K. S. Narayan, "Semiconducting-polymer-based position-sensitive detectors," *Appl. Phys. Lett.,* vol. 85, pp. 5073, 2004.

[251] D. Kabra, J. Verma, N. S. Vidhyadhiraja, and K. S. Narayan, "Model for Studies of Lateral Photovoltaic Effect in Polymeric Semiconductors," *IEEE Sensor. J.,* vol. 8, p. 1663, 2008.

[252] D. Kabra, "Studies of Length Scales in Semiconducting Polymers using Scanning Photocurrent Contrast Microscopy," in *Chemistray and physics of Materials Unit*. PhD Thesis, Bangalore: Jawaharlal Nehru Centre for Advanced Scientific Research, 2007.

[253] R. Riehn, R. Stevenson, D. Richards, D. J. Kang, M. Blamire, A. Downes, and F. Cacialli, "Local Probing of Photocurrent and Photoluminescence in a Phase-Separated Conjugated-Polymer Blend by Means of Near-Field Excitation," *Adv. Funct. Mater.,* vol. 16, pp. 469, 2006.

[254] B. Xue, B. Vaughan, C.-H. Poh, K. B. Burke, L. Thomsen, A. Stapleton, X. Zhou, G. W. Bryant, W. Belcher, and P. C. Dastoor, "Vertical Stratification and Interfacial Structure in P3HT:PCBM Organic Solar Cells," *J. Phys. Chem. C,* vol. 114, pp. 15797, 2010.

[255] X. Yang, J. Loos, S. C. Veenstra, W. J. H. Verhees, M. M. Wienk, J. M. Kroon, M. A. J. Michels, and R. A. J. Janssen, "Nanoscale Morphology of High-Performance Polymer Solar Cells," *Nano Lett.,* vol. 5, pp. 579, 2005.

[256] D. Gupta, S. Mukhopadhyay, and K. S. Narayan, "Fill factor in organic solar cells," *Solar Energy Mater. Solar Cells,* vol. 94, pp. 1309, 2010.

[257] S. J. Fang, S. Haplepete, W. Chen, C. R. Helms, and H. Edwards, "Analyzing atomic force microscopy images using spectral methods," *J. Appl. Phys.,* vol. 82, pp. 5891, 1997.

[258] M. Pelliccione and T. Lu, "Evolution of Thin Film Morphology; Modeling and Simulations," in *Springer Series in materials science*. vol. 108, R. Hull, R. M. Osgood, J. J. Parisi, and H. Warlimont, Eds. Springer-Verlag Berlin Heidelberg: Springer, 2008.

[259] I. Horcas, R. Fernandez, J. M. Gomez-Rodriguez, J. Colchero, J. Gomez-Herrero, and A. M. Baro, "WSXM: A software for scanning probe microscopy and a tool for nanotechnology," *Rev. of Scient. Instrum.,* vol. 78, pp. 013705, 2007.

[260] K. MaturovaÌ, S. S. van Bavel, M. M. Wienk, R. A. J. Janssen, and M. Kemerink, "Morphological Device Model for Organic Bulk Heterojunction Solar Cells," *Nano Lett.,* vol. 9, pp. 3032, 2009.

[261] B. Ray, P. R. Nair, R. E. Garcia, and M. A. Alam, "Modeling and optimization of polymer based bulk heterojunction (BHJ) solar cell," in *Electron Devices Meeting (IEDM), 2009 IEEE International*, pp. 1, 2009.

[262] M. Campoy-Quiles, T. Ferenczi, T. Agostinelli, P. G. Etchegoin, Y. Kim, T. D. Anthopoulos, P. N. Stavrinou, D. D. C. Bradley, and J. Nelson, "Morphology evolution via self-organization and lateral and vertical diffusion in polymer:fullerene solar cell blends," *Nat. Mater.,* vol. 7, pp. 158, 2008.

[263] N. D. Treat, M. A. Brady, G. Smith, M. F. Toney, E. J. Kramer, C. J. Hawker, and M. L. Chabinyc, "Interdiffusion of PCBM and P3HT Reveals Miscibility in a Photovoltaically Active Blend," *Adv. Energy Mater.,* vol. 1, pp. 82, 2011.

[264] E. Marken, G. Maurstad, and B. T. Stokke, "Quantitative analysis of atomic force microscopy topographs of biopolymer multilayers: Surface structure and polymer assembly modes," *Thin Solid Films,* vol. 516, pp. 7770, 2008.

[265] X. Wang, D. Zhang, K. Braun, H.-J. Egelhaaf, C. J. Brabec, and A. J. Meixner, "High-Resolution Spectroscopic Mapping of the Chemical Contrast from Nanometer Domains in P3HT:PCBM Organic Blend Films for Solar-Cell Applications," *Adv. Funct. Mater.,* vol. 20, pp. 492, 2010.

[266] X. Zhu and A. Kahn, "Electronic Structure and Dynamics at Organic Donor/Acceptor Interfaces," *MRS Bull.,* vol. 35, pp. 443, 2011.

[267] L. J. A. Koster, V. D. Mihailetchi, R. Ramaker, and P. W. M. Blom, "Light intensity dependence of open-circuit voltage of polymer:fullerene solar cells," *Appl. Phys. Lett.,* vol. 86, pp. 123509, 2005.

[268] L. J. A. Koster, V. D. Mihailetchi, H. Xie, and P. W. M. Blom, "Origin of the light intensity dependence of the short-circuit current of polymer/fullerene solar cells," *Appl. Phys. Lett.,* vol. 87, pp. 203502, 2005.

[269] L. J. A. Koster, V. D. Mihailetchi, and P. W. M. Blom, "Bimolecular recombination in polymer/fullerene bulk heterojunction solar cells," *appl. Phys. Lett.,* vol. 88, p. 052104, 2006.

[270] C. J. Brabec, N. S. Sariciftci, and J. C. Hummelen, "Plastic Solar Cells," *Adv. Funct. Mater. ,* vol. 11, p. 15, 2001.

[271] J. M. Frost, F. Cheynis, S. M. Tuladhar, and J. Nelson, "Influence of Polymer-Blend Morphology on Charge Transport and Photocurrent Generation in Donor-Acceptor Polymer Blends," *Nano Lett.,* vol. 6, pp. 1674, 2006.

[272] B. H. Hamadani, S. Jung, P. M. Haney, L. J. Richter, and N. B. Zhitenev, "Origin of Nanoscale Variations in Photoresponse of an Organic Solar Cell," *Nano Lett.,* vol. 10, pp. 1611, 2010.

[273] T.-Y. Chu, S. Alem, S.-W. Tsang, S.-C. Tse, S. Wakim, J. Lu, G. Dennler, D. Waller, R. Gaudiana, and Y. Tao, "Morphology control in polycarbazole based bulk heterojunction solar cells and its impact on device performance," *Appl. Phys. Lett.,* vol. 98, pp. 253301, 2011.

[274] D. Chen, A. Nakahara, D. Wei, D. Nordlund, and T. P. Russell, "P3HT/PCBM Bulk Heterojunction Organic Photovoltaics: Correlating Efficiency and Morphology," *Nano Lett.,* vol. 11, pp. 561, 2011.

[275] K. Vandewal, W. D. Oosterbaan, S. Bertho, V. Vrindts, A. Gadisa, L. Lutsen, D. Vanderzande, and J. V. Manca, "Varying polymer crystallinity in nanofiber poly(3-alkylthiophene):PCBM solar cells: Influence on charge-transfer state energy and open-circuit voltage," *Appl. Phys. Lett.,* vol. 95, pp. 123303, 2009.

[276] M. Morana, H. Azimi, G. Dennler, H.-J. Egelhaaf, M. Scharber, K. Forberich, J. Hauch, R. Gaudiana, D. Waller, Z. Zhu, K. Hingerl, S. S. van Bavel, J. Loos, and C. J. Brabec, "Nanomorphology and Charge Generation in Bulk Heterojunctions Based on Low-Bandgap Dithiophene Polymers with Different Bridging Atoms," *Adv. Funct. Mater.,* vol. 20, pp. 1180, 2010.

[277] G. Dennler, M. C. Scharber, and C. J. Brabec, "Polymer-Fulleren Bulk-Heterojunction Solar Cells," *Adv. Mater.,* vol. 21, p. 1323, 2009.

[278] D. Kabra and K. Narayan, *Adv. Mater.,* vol. 19, p. 1465, 2007.

[279] S. Mukhopadhyay, S. Ramachandra, and K. S. Narayan, "Direct Observation of Charge Generating Regions and Transport Pathways in Bulk Heterojunction Solar Cells with Asymmetric Electrodes Using near Field Photocurrent Microscopy," *J. Phys. Chem. C,* vol. 115, pp. 17184, 2011.

[280] D. Gupta, N. S. Vidhyadhiraja, and K. S. Narayan, *Proc. IEEE,* vol. 97, p. 1558, 2009.

[281] K. S. Nalwa, H. K. Kodali, B. Ganapathysubramanian, and S. Chaudhary, "Dependence of recombination mechanisms and strength on processing conditions in polymer solar cells," *Appl. Phys. Lett.,* vol. 99, pp. 263301, 2011.

[282] S. Mukhopadhyay, R. Voggu, C. N. R. Rao, N. S. Vidhyadhiraja, and K. S. Narayan, "Lateral Photocurrent Scanning of Donor and Acceptor Polymers on Graphene Coated Substrates," *Jpn. J. Appl. Phys.,* vol. 50, p. 061602, 2011.

[283] W. P. Ambrose, P. M. Goodwin, J. H. Jett, A. Van Orden, J. H. Werner, and R. A. Keller, "Single Molecule Fluorescence Spectroscopy at Ambient Temperature," *Chem. Rev.,* vol. 99, pp. 2929, 1999.

[284] H. Gersen, M. F. Garca-Paraja, L. Novotny, J. A. Veerman, L. Kuipers, and N. F. van Hulst, "Influencing the Angular Emission of a Single Molecule," *Phys. Rev. Lett.,* vol. 85, pp. 5312, 2000.

[285] F. Kulzer and M. Orrit, "Single molecule optics," *Annu. Rev. Phys. Chem.,* vol. 55, pp. 585, 2011/04/21 2004.

[286] W. E. Moerner, "Persistent Spectral Hole-Burning: Photon-Gating and Fundamental Statistical Limits," *Polymers for Microelectronics, Science, and Technology, Kodansha Scientific: Tokyo, Japan,* vol. 1 edn, 1990.

[287] L. Kador, D. E. Horne, and W. E. Moerner, "Optical detection and probing of single dopant molecules of pentacene in a p-terphenyl host crystal by means of absorption spectroscopy," *J. Phys. Chem.,* vol. 94, pp. 1237, 1990.

[288] T. Basche, W. E. Moerner, M. Orrit, and H. Talon, "Photon antibunching in the fluorescence of a single dye molecule trapped in a solid," *Phys. Rev. Lett.,* vol. 69, pp. 1516, 1992.

[289] T. Basche´, W. E. Moerner, M. Orrit, and U. P. E. Wild, "Single Molecule Optical Detection, Imaging, and Spectroscopy," *Verlag-Chemie: Munich,,* vol. 1 edn, 1997.

[290] W. P. Ambrose, P. M. Goodwin, R. A. Keller, and J. C. Martin, "Alterations of Single Molecule Fluorescence Lifetimes in Near-Field Optical Microscopy," *Science,* vol. 265, pp. 364, 1994.

[291] E. Barkai, Y. Jung, and R. Silbey, "THEORY OF SINGLE-MOLECULE SPECTROSCOPY: Beyond the Ensemble Average," *Annu. Rev. Phys. Chem.,* vol. 55, pp. 457, 2004.

[292] S. Fore, "Introduction to Single Molecule Fluorescence Detection and Spectroscopy," *NSF Center for Biophotonics Science and Technology, University of California, Davis,* 2008.

[293] A. J. Meixner, *Optical Single-Molecule Detection at Room Temperature* vol. 2 edn: John Wiley & Sons, Inc., 2007.

[294] V. Vukojevic, M. Heidkamp, Y. Ming, B. r. Johansson, L. Terenius, and R. Rigler, "Quantitative single-molecule imaging by confocal laser scanning microscopy," *Proc. Natl. Acad. Sci. U.S.A.,* vol. 105, pp. 18176, 2008.

[295] O. Mirzov and I. G. Scheblykin, "Polydispersity of the photoluminescence quantum yield in single conjugated polymer chains," *Chem. Phys.,* vol. 318, pp. 217, 2005.

[296] W. P. Ambrose, P. M. Goodwin, J. C. Martin, and R. A. Keller, "Single molecule detection and photochemistry on a surface using near-field optical excitation," *Phys. Rev. Lett.,* vol. 72, p. 160, 1994.

[297] M. F. Garcia-Parajo, J. A. Veerman, A. G. T. Ruiter, and N. F. van Hulst, "Near-field optical and shear-force microscopy of single fluorophores and DNA molecules," *Ultramicroscopy,* vol. 71, pp. 311, 1998.

[298] A. Lewis, Y. Y. Kuttner, R. Dekhter, and M. Polhan, "Fluorescence correlation spectroscopy at 100 nM concentrations using near-field scanning optical microscopic (NSOM) geometries and highly diffracting force sensing fiber probes," *Isr. J. Chem.,* vol. 47, pp. 171, 2007.

[299] C. S. Lin, R. H. Yeh, F. J. Pai, and J. W. Hong, "Optoelectronic characteristics of MEH-PPV polymer LEDs with n-a-SiCGe:H and p-a-Si:H carrier injection layers," *Optoelect, IEE Proc.,* vol. 149, pp. 193, 2002.

[300] P. S. Heeger and A. J. Heeger, "Making sense of polymer-based biosensors," *Proc. Natl. Acad. Sci. USA.,* vol. 96, pp. 12219, 1999.

[301] F. Hide, M. a. A. DÃ-az-Garca, B. J. Schwartz, M. R. Andersson, Q. Pei, and A. J. Heeger, "Semiconducting Polymers: A New Class of Solid-State Laser Materials," *Science,* vol. 273, pp. 1833, 1996.

[302] D. Tenery and A. J. Gesquiere, "Effect of PCBM Concentration on Photoluminescence Properties of Composite MEH-PPV/PCBM Nanoparticles Investigated by a Franck–Condon Analysis of Single-Particle Emission Spectra," *Chem. Phys. Chem,* vol. 10, pp. 2449, 2009.

[303] D. Tenery and A. J. Gesquiere, "Interplay between fluorescence and morphology in composite MEH-PPV/PCBM nanoparticles studied at the single particle level," *Chemical Physics,* vol. 365, pp. 138, 2009.

[304] M. S. Kim, D. H. Park, E. H. Cho, K. H. Kim, Q. H. Park, H. Song, D.-C. Kim, J. Kim, and J. Joo, "Complex Nanoparticle of Light-Emitting MEH-PPV with Au: Enhanced Luminescence," *ACS Nano,* vol. 3, pp. 1329, 2009.

[305] D. Tenery and A. J. Gesquiere, "Interplay between fluorescence and morphology in composite MEH-PPV/PCBM nanoparticles studied at the single particle level," *Chem. Phys.,* vol. 365, pp. 138, 2009.

[306] D. Tenery, J. G. Worden, Z. Hu, and A. J. Gesquiere, "Single particle spectroscopy on composite MEH-PPV/PCBM nanoparticles," *J. Lumin.,* vol. 129, pp. 423, 2009.

[307] D. Tenery and A. J. Gesquiere, "Effect of PCBM Concentration on Photoluminescence Properties of Composite MEH-PPV/PCBM Nanoparticles Investigated by a Franck–Condon Analysis of Single-Particle Emission Spectra," *Chem. Phys. Chem.,* vol. 10, pp. 2449, 2009.

[308] S. Kim, C.-K. Lim, J. Na, Y.-D. Lee, K. Kim, K. Choi, J. F. Leary, and I. C. Kwon, "Conjugated polymer nanoparticles for biomedical in vivo imaging," *Chem. Commun.,* vol. 46, pp. 1617, 2010.

[309] H. Lin, Y. Tian, K. Zapadka, G. Persson, D. Thomsson, O. Mirzov, P.-O. Larsson, J. Widengren, and I. G. Scheblykin, "Fate of Excitations in Conjugated Polymers: Single-Molecule Spectroscopy Reveals Nonemissive Dark Regions in MEH-PPV Individual Chains," *Nano Letters,* vol. 9, pp. 4456, 2009.

[310] O. Mirzov, R. Bloem, P. R. Hania, D. Thomsson, H. Lin, and I. G. Scheblykin, "Polarization Portraits of Single Multichromophoric Systems: Visualizing Conformation and Energy Transfer," *Small,* vol. 5, pp. 1877, 2009.

[311] C. Szymanski, C. Wu, J. Hooper, M. A. Salazar, A. Perdomo, A. Dukes, and J. McNeill, "Single Molecule Nanoparticles of the Conjugated Polymer MEH-PPV, Preparation and Characterization by Near-Field Scanning Optical Microscopy," *J. Phys. Chem. B,* vol. 109, pp. 8543, 2005.

[312] M. Fujihira, H. Monobe, N. Yamamoto, H. Muramatsu, N. Chiba, K. Nakajima, and T. Ataka, "Scanning near-field optical microscopy of fluorescent polystyrene spheres with a combined SNOM and AFM," *Ultramicroscopy,* vol. 61, pp. 271, 1995.

[313] H. K. Park, Y. T. Lim, J. K. Kim, H. G. Park, and B. H. Chung, "Nanoscopic observation of a gold nanoparticle-conjugated protein using near-field scanning optical microscopy," *Ultramicroscopy,* vol. 108, pp. 1115, 2008.

[314] W. Trabesinger, A. Kramer, M. Kreiter, B. Hecht, and U. P. Wild, "Single-molecule near-field optical energy transfer microscopy," *Appl. Phys. Lett.,* vol. 81, pp. 2118, 2002.

[315] Y. J. Lee, D. Y. Kim, and P. F. Barbara, "Effect of Sample Preparation and Excitation Conditions on the Single Molecule Spectroscopy of Conjugated Polymers," *J. Phys. Chem. B,* vol. 110, pp. 9739, 2006.

[316] J. D. Muller, F. A. Schabert, G. Boldt, and A. Engel, "Imaging Purple Membranes in Aqueous Solutions at Sub-Nanometer Resolution by Atomic Force Microscopy," *Biophys. J.,* vol. 68, p. 1681, 1995.

[317] H. Yamada, K. Kobayashi, T. Fukuma, Y. Hirata, T. Kajita, and K. Matsushige, "Molecular Resolution Imaging of Protein Molecules in Liquid Using Frequency Modulation Atomic Force Microscopy," *Appl. Phys. Express,* vol. 2, 2009.

[318] C. D. Cox, J. M. McCollum, M. S. Allen, R. D. Dar, and M. L. Simpson, "Using noise to probe and characterize gene circuits," *Proc. Natl. Acad. Sci.,* vol. 105, pp. 10809, 2008.

[319] C. D. Cox, J. M. McCollum, D. W. Austin, M. S. Allen, R. D. Dar, and M. L. Simpson, "Frequency domain analysis of noise in simple gene circuits," *Chaos: An Interdisciplinary Journal of Nonlinear Science,* vol. 16, pp. 026102, 2006.

[320] N. Vsevolodov, *Biomolecular Electronics: An Introduction Via Photosensitive Proteins* vol. 1 edn. Boston: Birkhäuser 1998.

[321] N. Arun, S. Mukhopadhyay, and K. S. Narayan, "Monitoring intermediate states of bacteriorhodopsin monolayers using near-field optical microscopy," *Appl. Opt.,* vol. 49, pp. 1131, 2010.

[322] T. He, N. Friedman, D. Cahen, and M. Sheves, "Bacteriorhodopsin Monolayers for Optoelectronics: Orientation and Photoelectric Response on Solid Supports," *Adv. Mater.,* vol. 17, pp. 1023, 2005.

[323] Y. Jin, T. Honig, I. Ron, N. Friedman, M. Sheves, and D. Cahen, "Bacteriorhodopsin as an electronic conduction medium for biomolecular electronics," *Chem. Soc. Rev.,* vol. 37, 2008.

[324] G. Varo and L. J. K., "Photoreactions of bacteriorhodopsin at acid pH," *Biophys. J. ,* vol. 56, p. 1143, 1989.

[325] M. Shibata, H. Yamashita, T. Uchihashi, H. Kandori, and T. Ando, "High-speed atomic force microscopy shows dynamic molecular processes in photoactivated bacteriorhodopsin," *Nat Nano,* vol. 5, pp. 208, 2010.

[326] J. H. Burroughes, D. D. C. Bradley, A. R. Brown, R. N. Marks, K. Mackay, R. H. Friend, P. L. Burns, and A. B. Holmes, "Light-emitting diodes based on conjugated polymers," *Nature,* vol. 347, pp. 539, 1990.

[327] Y. Ohmori, M. Uchida, K. Muro, and K. Yoshino, "Blue Electroluminescent Diodes Utilizing Poly(alkylfluorene)," *Jpn. J. Appl. Phys,* vol. 30, pp. L1941, 1991.

[328] G. Li, V. Shrotriya, J. Huang, Y. Yao, T. Moriarty, K. Emery, and Y. Yang, "High-efficiency solution processable polymer photovoltaic cells by self-organization of polymer blends," *Nat Mater,* vol. 4, pp. 864, 2005.

[329] P. Peumans, V. Bulovic, and S. R. Forrest, "Efficient, high-bandwidth organic multilayer photodetectors," *Appl. Phys. Lett.,* vol. 76, pp. 3855, 2000.

[330] T. Morita, V. Singh, S. Oku, S. Nagamatsu, W. Takashima, S. Hayase, and K. Kaneto, "Ambipolar Transport in Bilayer Organic Field-Effect Transistor Based on Poly(3-hexylthiophene) and Fullerene Derivatives," *Jpn. J. Appl. Phys.,* vol. 49, p. 041601, 2010.

[331] V. Singh, S. S. Pandey, W. Takashima, and K. Kaneto, "Role of Morphology on Photoluminescence Quenching and Depletion Width Formed at the Interface of Aluminum and Poly(3-alkylthiophene)," *Jpn. J. Appl. Phys.,* vol. 48, p. 061503, 2009.

[332] T. Mueller, F. Xia, and P. Avouris, "Graphene photodetectors for high-speed optical communications," *Nat Photon,* vol. 4, pp. 297, 2010.

[333] J. W. G. Wilder, L. C. Venema, A. G. Rinzler, R. E. Smalley, and C. Dekker, "Electronic structure of atomically resolved carbon nanotubes," *Nature,* vol. 391, pp. 59, 1998.

[334] W. Zhang, W. He, and X. Jing, "Preparation of a Stable Graphene Dispersion with High Concentration by Ultrasound," *J. Phys. Chem. B,* vol. 114, pp. 10368, 2010.

[335] G. Nordendorf, O. Kasdorf, H. Kitzerow, Y. Liang, X. Feng, and K. Müllen, "Liquid Crystal Addressing by Graphene Electrodes Made from Graphene Oxide," *Jpn. J. Appl. Phys.,* vol. 49, p. 100206, 2010.

[336] J. Wu, H. A. Becerril, Z. Bao, Z. Liu, Y. Chen, and P. Peumans, "Organic solar cells with solution-processed graphene transparent electrodes," *Appl. Phys. Lett.,* vol. 92, pp. 263302, 2008.

[337] K. S. Subrahmanyam, S. R. C. Vivekchand, A. Govindaraj, and C. N. R. Rao, "A study of graphenes prepared by different methods: characterization, properties and solubilization," *J. Mater. Chem.,* vol. 18, pp. 1517, 2008.

[338] J. Kim, L. J. Cote, F. Kim, and J. Huang, "Visualizing Graphene Based Sheets by Fluorescence Quenching Microscopy," *J. Am. Chem. Soc.,* vol. 132, pp. 260, 2009.

[339] Q. Liu, Z. Liu, X. Zhang, L. Yang, N. Zhang, G. Pan, S. Yin, Y. Chen, and J. Wei, "Polymer Photovoltaic Cells Based on Solution-Processable Graphene and P3HT," *Adv. Funct. Mater.,* vol. 19, pp. 894, 2009.

[340] Q. Liu, Z. Liu, X. Zhang, N. Zhang, L. Yang, S. Yin, and Y. Chen, "Organic photovoltaic cells based on an acceptor of soluble graphene," *Appl. Phys. Lett.,* vol. 92, pp. 223303, 2008.

[341] Z. Liu, D. He, Y. Wang, H. Wu, and J. Wang, "Graphene doping of P3HT:PCBM photovoltaic devices," *Synth. Metal.,* vol. 160, pp. 1036, 2010.

[342] Z. Liu, Q. Liu, Y. Huang, Y. Ma, S. Yin, X. Zhang, W. Sun, and Y. Chen, "Organic Photovoltaic Devices Based on a Novel Acceptor Material: Graphene," *Adv. Mater.,* vol. 20, pp. 3924, 2008.

[343] K. S. Subrahmanyam, R. Voggu, A. Govindaraj, and C. N. R. Rao, "A comparative Raman study of the interaction of electron donor and acceptor molecules with graphene prepared by different methods," *Chem. Phys. Lett.,* vol. 472, pp. 96, 2009.

[344] V. Rakesh and et al., "Effects of charge transfer interaction of graphene with electron donor and acceptor molecules examined using Raman spectroscopy and cognate techniques," *J. Phys.: Conden Mat.,* vol. 20, p. 472204, 2008.

[345] R. R. Nair, P. Blake, A. N. Grigorenko, K. S. Novoselov, T. J. Booth, T. Stauber, N. M. R. Peres, and A. K. Geim, "Fine Structure Constant Defines Visual Transparency of Graphene," *Science,* vol. 320, p. 1308, 2008.

[346] A. K. Geim, "Graphene: Status and Prospects," *Science,* vol. 324, pp. 1530, 2009.

[347] Manna A. K. and Pati S. K., "Tuning the Electronic Structure of Graphene by Molecular Charge Transfer: A Computational Study," *Chem. Asian J.,* vol. 4, pp. 855, 2009.

[348] R. C. Dunn, "Near-Field Scanning Optical Microscopy," *Chem. Rev.,* vol. 99, pp. 2891, 1999.

[349] A. J. Lewis, A. Ruseckas, O. P. M. Gaudin, G. R. Webster, P. L. Burn, and I. D. W. Samuel, "Singlet exciton diffusion in MEH-PPV films studied by exciton-exciton annihilation," *Org. Elect.,* vol. 7, pp. 452, 2006.

[350] G. Williams and P. V. Kamat, "Graphene Semiconductor Nanocomposites: Excited-State Interactions between ZnO Nanoparticles and Graphene Oxide " *Langmuir,* vol. 25, pp. 13869, 2009.

[351] R. S. Swathi and K. L. Sebastian, "Resonance energy transfer from a dye molecule to graphene," *J. Chem. Phys.,* vol. 129, pp. 054703, 2008.

[352] M. Rao, R. P. Ortiz, A. Facchetti, R. N. Marks, and K. S. Narayan, "Studies of Photogenerated Charge Carriers from Donor-Acceptor Interfaces in Organic Field Effect Transistors. Implications for Organic Solar Cells," *J.Phys. Chem. C.,* vol. 114, pp. 20609, 2010.

[353] H. Yan, Z. Chen, Y. Zheng, C. Newman, J. R. Quinn, F. Dotz, M. Kastler, and A. Facchetti, "A high-mobility electron-transporting polymer for printed transistors," *Nature,* vol. 457, pp. 679, 2009.